UNIVERSIDADE FEDERAL DO CEARÁ
CENTRO DE TECNOLOGIA
DEPARTAMENTO DE ENGENHARIA METALÚRGICA E DE MATERIAIS
PROGRAMA DE PÓS-GRADUAÇÃO EM ENGENHARIA E CIÊNCIA DE MATERIAIS

VITÓRIA MARIA RODRIGUES VASCONCELOS

POTENTIAL ENERGY SURFACE MAPPING OF ETHOXY-DIBENZALACETONE AND FULLERENE-BASED QUENCHERS FOR OPTOELECTRONICS

FORTALEZA
2025

VITÓRIA MARIA RODRIGUES VASCONCELOS

POTENTIAL ENERGY SURFACE MAPPING OF ETHOXY-DIBENZALACETONE AND FULLERENE-BASED QUENCHERS FOR OPTOELECTRONICS

Doctoral Thesis submitted to the Graduate Program in Materials Science and Engineering at the Federal University of Ceará in partial fulfillment of the requirements for the degree of Doctor in Materials Science and Engineering. Concentration area: Physical and Mechanical Properties of Materials.

Supervisor: Prof. Dr. Igor Frota de Vasconcelos

Supervisor: Prof. Dr. Eveline Matias Bezerra

FORTALEZA
2025

Dados Internacionais de Catalogação na Publicação
Universidade Federal do Ceará
Sistema de Bibliotecas
Gerada automaticamente pelo módulo Catalog, mediante os dados fornecidos pelo(a) autor(a)

V451p Vasconcelos, Vitória Maria Rodrigues.
Potential energy surface mapping of ethoxy-dibenzalacetone and fullerene-based quenchers for optoelectronics / Vitória Maria Rodrigues Vasconcelos. – 2025.
155 f. : il. color.

Tese (doutorado) – Universidade Federal do Ceará, Centro de Tecnologia, Programa de Pós-Graduação em Engenharia e Ciência de Materiais, Fortaleza, 2025.
Orientação: Prof. Dr. Igor Frota de Vasconcelos.
Coorientação: Profa. Dra. Eveline Matias Bezerra.

1. Potential energy surface. 2. Ethoxy-dibenzalacetone derivative. 3. Fullerene-based quenchers. 4. Static non-fluorescent complexes. 5. Organic/fullerene-based devices. I. Título.
CDD 620.11

VITÓRIA MARIA RODRIGUES VASCONCELOS

POTENTIAL ENERGY SURFACE MAPPING OF ETHOXY-DIBENZALACETONE AND FULLERENE-BASED QUENCHERS FOR OPTOELECTRONICS

Doctoral Thesis submitted to the Graduate Program in Materials Science and Engineering at the Federal University of Ceará in partial fulfillment of the requirements for the degree of Doctor in Materials Science and Engineering. Concentration area: Physical and Mechanical Properties of Materials.

Approval date: April 28, 2025

THESIS COMMITTEE

Prof. Dr. Igor Frota de Vasconcelos (Supervisor)
Universidade Federal do Ceará (UFC)

Prof. Dr. Eveline Matias Bezerra (Supervisor)
Universidade Federal Rural do Semi-Árido (UFERSA)

Prof. Dr. Filipe Matusalém de Souza
Instituto Tecnológico de Aeronáutica (ITA)

Prof. Dr. Roner Ferreira da Costa
Universidade Federal Rural do Semi-Árido (UFERSA)

Prof. Dr. Andrey Chaves
Universidade Federal do Ceará (UFC)

Prof. Dr. Pedro de Lima Neto
Universidade Federal do Ceará (UFC)

To my family and my beloved four-legged companions – Spyke, Luz, Ursinha, Sirene, and Margarida – for their unconditional love.

ACKNOWLEDGEMENTS

I am deeply grateful to God for the precious gift of life, for providing constant support in times of anguish, and for all the closed doors that served as an incentive to strengthen my resilience. I extend my sincere gratitude to my advisor, Prof. Dr. Igor Frota de Vasconcelos (UFC), for his confidence and guidance during my postgraduate studies and to my co-advisor, Prof. Dr. Eveline Matias Bezerra (UFERSA), whose support and encouragement were crucial during the most challenging moments of this journey.

My sincere thanks go to Prof. Dr. Valder Nogueira Freire (UFC) for providing the essential computational resources for this research and to Prof. Dr. Hélcio Silva dos Santos (UVA) for the chalcones that served as the basis for this thesis. I am also deeply grateful to Prof. Dr. Bruna Bueno Postacchini (UFOP) and Prof. Dr. Thiago Cazati (UFOP) for their invaluable support in experimental photophysical measurements, critical reviews, and contributions to my scientific development.

I sincerely thank the esteemed members of the examining committee, Prof. Dr. Pedro de Lima Neto (UFC), Prof. Dr. Andrey Chaves (UFC), Prof. Dr. Roner Ferreira da Costa (UFERSA), and Prof. Dr. Filipe Matusalém de Souza (ITA) for their valuable insights and constructive feedback. My gratitude extends to the Graduate Program in Materials Science and Engineering professors and staff at UFC, whose teachings and shared experiences greatly enriched my academic and personal journey.

A special acknowledgment to Prof. Dr. Mona Lisa Moura de Oliveira (UECE), who introduced me to scientific research and provided my first contact with scientific initiation. In addition, I extend my gratitude to the professors of the Department of Fundamental Chemistry (DQF) at the Federal University of Pernambuco (UFPE), especially Prof. Dr. Denys Ewerton da Silva Santos, Prof. Dr. Ricardo Luiz Longo, and Prof. Dr. Ivani Malvestiti, who contributed to this phase of my academic career.

I am deeply grateful to everyone who contributed, directly or indirectly, to this work. Finally, my eternal gratitude goes to my family – especially my parents, André and Inês; my brothers, Iury and André Júnior; and my love, Cleo – as well as to my beloved four-legged companions (Spyke, Luz, Ursinha, Sirene, and Margarida), whose unconditional love has been a constant source of strength, comfort, and inspiration.

I also dedicate a remembrance to my paternal grandparents, Maria do Carmo and Antônio Lisboa, and to my maternal grandparents, Francinete and Berilo – all *in memoriam* – for the moral and ethical values they taught me, a legacy of immeasurable richness that transcends material wealth.

This work was financed with the support of the Coordenação de Aperfeiçoamento de Pessoal de Nível Superior - Brazil (CAPES) - Financing Code 001.

“The task is not to see what has never been seen before, but to think what has never been thought before about what you see every day”.

(Erwin Schrödinger)

ABSTRACT

The photophysical properties of chromophores are influenced by their environment, which modulates both adiabatic and non-adiabatic energy dissipation mechanisms. This thesis explores the role of chemical reactivity descriptors and the potential energy surface (PES) in the fluorescence suppression of the ethoxy-dibenzalacetone derivative (DBAd) (1E,4E)-1,5-bis-(4-ethoxyphenyl)penta-1,4-dien-3-one by fullerene-based quenchers (C_{60} and $PC_{61}BM$). The quenching mechanism proceeds through static non-fluorescent complexes, as evidenced by the linearity of the Stern-Volmer curves and the unchanged excited-state lifetime (0.20 ns) with increasing quencher concentration. Förster resonance energy transfer (FRET) dominated in $PC_{61}BM$@DBAd due to its larger spectral overlap integral, leading to a Förster energy transfer rate constant (k_{FRET}) of 3.44×10^{12} s^{-1}, while photoinduced charge transfer prevailed in C_{60}@DBAd, thermodynamically driven by a charge-transfer driving force of -1.84 eV arising from HOMO-LUMO orbital alignment that favored charge transfer exciton (CTE) dissociation with binding energy estimated at approximately 2.29 ± 0.11 eV, as calculated by TD-DFT/PCM at the M06-2X/6-311+G(d,p) level of theory. PES analyses confirm the static ground-state complexes, with pronounced van der Waals interactions in $PC_{61}BM$@DBAd occurring at a short-range centroid-to-centroid distance of 4.92 Å. Thermodynamic calculations, performed at the DFT/BLYP-D2/DNP+ formalism, confirmed the spontaneity of complex formation, with Gibbs free energy values of -42.53 $\mathrm{kcal \cdot mol^{-1}}$ for C_{60}@DBAd and -51.91 $\mathrm{kcal \cdot mol^{-1}}$ for $PC_{61}BM$@DBAd. These findings reveal that DBAd effectively transfers the excitation energy and photoinduced charge to the fullerene acceptors by ultrafast non-radiative pathways at 5.0×10^{9} s^{-1}, emphasizing C_{60}@DBAd and $PC_{61}BM$@DBAd self-assemblies as alternative supramolecular complexes for optoelectronic applications, such as organic/fullerene-based devices for next-generation solar cells.

Keywords: Potential energy surface; Ethoxy-dibenzalacetone derivative; Fullerene-based quenchers; Static non-fluorescent complexes; Förster resonance energy transfer; Charge transfer exciton; Non-covalent interactions; Organic/fullerene-based devices.

RESUMO

As propriedades fotofísicas dos cromóforos são influenciadas por seu ambiente, que modula os mecanismos de dissipação de energia adiabáticos e não adiabáticos. Esta tese explora o papel dos descritores de reatividade química e da superfície de energia potencial (PES) na supressão da fluorescência do derivado de etoxi-dibenzalacetona (DBAd) (1E,4E)-1,5-bis(4-etoxifenil)penta-1,4-dien-3-ona por supressores baseados em fulereno (C_{60} e $PC_{61}BM$). O mecanismo de supressão ocorre por meio de complexos estáticos não fluorescentes, conforme evidenciado pela linearidade das curvas de Stern-Volmer e o tempo de vida do estado excitado inalterado ($0,20$ ns) com o aumento da concentração do supressor. A transferência de energia de ressonância de Förster (FRET) dominou em $PC_{61}BM$@DBAd devido à sua maior integral de sobreposição espectral, levando a uma constante de taxa de transferência de energia de Förster (k_{FRET}) de $3,44 \times 10^{12}$ s^{-1}, enquanto a transferência de carga fotoinduzida prevaleceu em C_{60}@DBAd, termodinamicamente conduzida por uma força motriz de transferência de carga de $-1,84$ eV decorrente do alinhamento dos orbitais HOMO-LUMO que favoreceu a dissociação do éxciton de transferência de carga (CTE), com energia de ligação estimada em aproximadamente $2,29 \pm 0,11$ eV, conforme calculado por TD-DFT/PCM no nível teórico M06-2X/6-311+G(d,p). As análises PES confirmam os complexos estáticos de estado fundamental, com interações de van der Waals pronunciadas em $PC_{61}BM$@DBAd ocorrendo a uma distância de curto alcance entre os centroides de $4,92$ Å. Cálculos termodinâmicos, realizados no formalismo DFT/BLYP-D2/DNP+, confirmaram a espontaneidade da formação dos complexos, com valores de energia livre de Gibbs de $-42,53$ $\mathrm{kcal \cdot mol^{-1}}$ para C_{60}@DBAd e $-51,91$ $\mathrm{kcal \cdot mol^{-1}}$ para $PC_{61}BM$@DBAd. Essas descobertas revelam que o DBAd transfere efetivamente a energia de excitação e a carga fotoinduzida para os aceptores de fulereno por vias não radiativas ultrarrápidas a $5,0 \times 10^{9}$ s^{-1}, enfatizando as automontagens C_{60}@DBAd e $PC_{61}BM$@DBAd como complexos supramoleculares alternativos para aplicações optoeletrônicas, como dispositivos orgânicos baseados em fulereno para células solares de próxima geração.

Palavras-chave: Superfície de energia potencial; Derivado de etoxi-dibenzalacetona; Supressores baseados em fulereno; Complexos estáticos não fluorescentes; Transferência de energia de ressonância de Förster; Éxciton de transferência de carga; Interações não covalentes; Dispositivos orgânicos/baseados em fulereno.

LIST OF FIGURES

LIST OF TABLES

LIST OF SYMBOLS

Λ	Thermal De Broglie wavelength
σ	Rotational symmetry number
$\theta_A, \theta_B, \theta_C$	Rotational temperatures associated with moments of inertia
θ_i	Characteristic vibrational temperature
ν_i	Vibrational frequency of normal mode i
m	Mass
k_B	Boltzmann's constant
T	Temperature
h	Planck's constant
$\hbar$	Reduced Planck's constant ($h/2\pi$)
V	System volume
q_{trans}	Translational partition function
q_{rot}	Rotational partition function
q_{vib}	Vibrational partition function
q_{elec}	Electronic partition function
Q	Molecular partition function
U	Internal energy
H	Enthalpy
S	Entropy
G	Gibbs free energy
C_p	Heat capacity at constant pressure
E_{ZPVE}	Zero-point vibrational energy

I_0, I	Initial and quenched fluorescence intensities
τ_0, τ	Initial and quenched excited-state lifetimes
K_{SV}	Stern-Volmer quenching constant
K_s	Static quenching binding constant
Φ_D	Fluorescence quantum yield of the donor
$J(\lambda)$	Spectral overlap integral
R_0	Förster radius
r	Distance between donor and acceptor
k_{FRET}	Förster energy transfer rate
ε	Molar absorption coefficient
$\mathrm{E}_{\mathrm{OPT}}$	Optical energy gap
E_{B}	Exciton binding energy
IP	Ionization potential
EA	Electron affinity
ΔG^0	Gibbs free energy under standard conditions
$\Delta G_{\mathrm{charge}}$	Charge transfer free energy
λ_{mt}	Reorganization energy (Marcus theory)
H_{mt}	Electronic coupling element (Marcus theory)
L_D	Exciton diffusion length
D	Exciton diffusion coefficient
Z	Geometric factor in exciton motion
η_{FRET}	Förster energy transfer efficiency
k_{DET}	Dexter energy transfer rate
$f(E_i, E_j)$	Boltzmann-weighted acceptance probability

LIST OF ABBREVIATIONS AND ACRONYMS

BLYP-D2	Becke-Lee-Yang-Parr functional with dispersion correction
CTE	Charge Transfer Exciton
DET	Dexter Energy Transfer
DFT	Density Functional Theory
DNP+	Double Numerical Basis Set with Polarization
DOS	Density of States
EA	Electron Affinity
FRET	Förster Resonance Energy Transfer
GGA	Generalized Gradient Approximation
HOMO	Highest Occupied Molecular Orbital
IP	Ionization Potential
IPES	Inverse Photoemission Spectroscopy
IR	Infrared Spectroscopy
IUPAC	International Union of Pure and Applied Chemistry
LUMO	Lowest Unoccupied Molecular Orbital
M06-2X	Meta-GGA Hybrid Functional
NAMD	Non-Adiabatic Molecular Dynamics
NMR	Nuclear Magnetic Resonance
PCM	Polarizable Continuum Model
PES	Potential Energy Surface
PL	Photoluminescence
SCF	Self-Consistent Field

SV	Stern-Volmer
TD-DFT	Time-Dependent Density Functional Theory
UFF	Universal Force Field
UPS	Ultraviolet Photoelectron Spectroscopy
UV-Vis	Ultraviolet-Visible Spectroscopy
XPS	X-ray Photoelectron Spectroscopy
ZPVE	Zero-Point Vibrational Energy

CONTENTS

1 INTRODUCTION

Climate change represents one of the most significant global challenges of the 21st century [1]. Scientific evidence indicates that changes on the planet are already irreversible [2, 3], compromising ecosystems and putting billions of people at risk. The climate crisis, caused mainly by anthropogenic emissions of greenhouse gases (GHG), has slowed global agricultural productivity, threatening food security, especially in economically vulnerable regions [4], impacted drinking water aquifers [5] and affected several other sectors, from maritime trade [6] to emergence of new epidemiological outbreaks [7].

According to the Copernicus Climate Change Service (C3S), January 2025 was the warmest on record globally, with an average surface air temperature of 13.23 °C, exceeding the 1991–2020 average by 0.73 °C and the pre-industrial levels (1850–1900) by 1.75 °C [8]. This milestone reinforces the unprecedented warming trend, with 18 of the past 19 months surpassing 1.5 °C above pre-industrial levels. Furthermore, 2024 was the hottest year ever recorded [8, 9], marking the first time that global temperatures remained above 1.55 °C throughout the entire year [10, 11]. Figure 1 shows the global mean temperature evolution for the 1850–2024 period.

Figure 1 – Global mean surface air temperature anomaly from 1850 to 2024, relative to the 1850–1900 pre-industrial average. The data highlight an unprecedented warming trend, with 2024 exceeding 1.5 °C above pre-industrial levels. Available at: <https://wmo.int/sites/default/files/2025-03/WMO-1368-2024_en.pdf>.

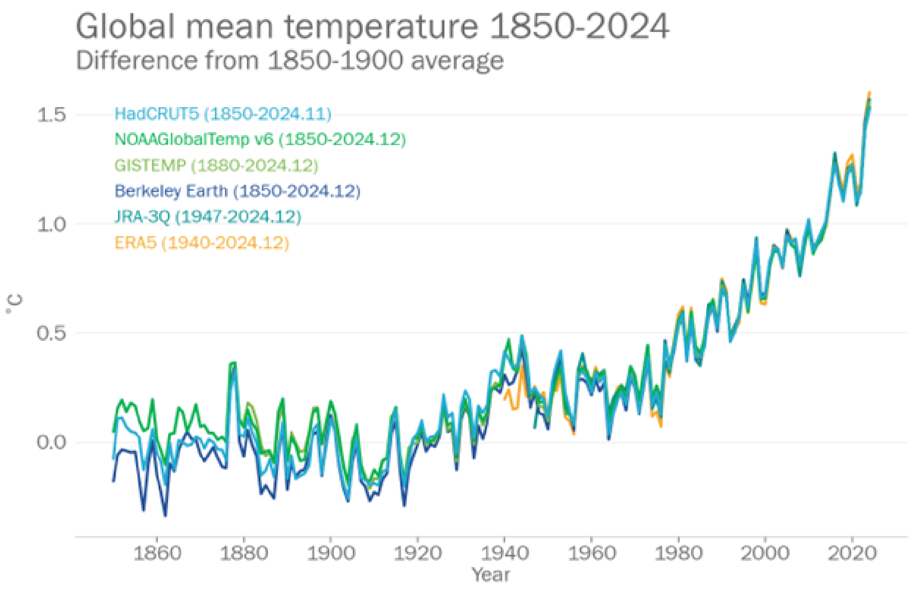

Source: World Meteorological Organization [12].

The rise in Earth's surface air temperature has increased water ocean temperatures, further amplified by the *El Niño* climate pattern [8]. This warming, which significantly exceeds values observed in previous years, contributed to the statistic conditions of 2024 [10, 13], a direct consequence of climate change and a harbinger of the planet's future conditions. Given the imminent risks associated with the unsafe rise in global temperature, it is crucial to adopt mitigation measures, mainly through a strategic sustainable transition in the energy sector.

Although the transition to renewable energy sources is a fundamental climate policy, these sources, such as biomass, photovoltaic solar, hydropower, and wind energy, are also vulnerable to climate change [14]. In the field of photovoltaic technology, flexible organic solar cells (OSCs), illustrated in Figure 2, have been around for a little over three decades [15–17]. In recent ten years, the energy efficiency of these devices has increased from less than 1% to about 20% [18–22] due to the development of new photoactive materials [23] and improvements in manufacturing techniques [24].

Figure 2 – Flexible organic solar cells: lighting today and preserving tomorrow.

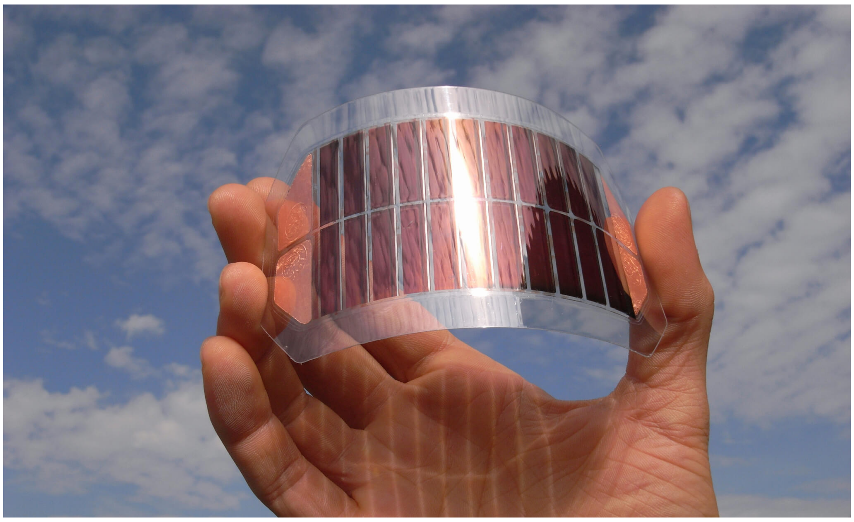

Source: Fraunhofer Institute for Solar Energy Systems (ISE) [25].

However, the efficiency of OSCs remains constrained by fundamental limitations, including energy losses due to thermalization, low charge carrier mobility [26], and the complex potential energy surface in the ground and excited states of the organic semiconductors [26–29]. These challenges are potentialized by morphological instabilities caused by the inherently low solubility of typical organic electronic materials, which restrict exciton dissociation and charge transport efficiency [30–33].

In OSCs, approximately 50% of the efficiency is lost in the recombination of charge carriers [34] due to the displacement of electronic states, weak intermolecular forces, and the low dielectric constant of organic semiconductors, which results in a low lifetime of excited states [35–39]. Thus, one way to optimize the efficiency in these devices consists of improving the interface between the deposited materials [40–42], maximizing the interfacial area and making it on a scale of the order of the exciton diffusion length [43, 44].

One strategy to improve the performance of these devices is among others, to increase the photoinduced charge transfer and excitation energy transfer with conformationally locked (rigid) sensitizing molecules, such as dibenzalacetone derivatives [45, 46] due to the controlling energy dissipation upon excitation; in systems with high configurational entropy, nonradiative relaxation processes dominate, leading to excited-state deactivation by molecular vibrational relaxation, resulting in ultrafast nonradiative fluorescence quenching [47].

In this work, although dibenzalacetone compounds have not yet been applied in commercial OSCs, we were motivated to investigate the ethoxy-dibenzalacetone derivative (DBAd), IUPAC[1] name (1E,4E)-1,5-bis(4-ethoxyphenyl)penta-1,4-dien-3-one [48], due to its facile synthesis by the Claisen-Schmidt condensation method, intense absorption in the near-UV-Vis region, and *s-trans* conformation, which can induce a adequate fluorescence quantum yield through electronic delocalization along the donor-acceptor-donor structure [49, 50]. Furthermore, its conjugated system can enhance π-π stacking and electronic interactions with fullerene-based acceptors already commonly used in OSCs, such as C_{60} and $PC_{61}BM$ compounds [51–53].

For this purpose, the singlet-singlet excited states and exciton energy (E_B) of DBAd were initially characterized using Time-Dependent Density Functional Theory (TD-DFT). Density Functional Theory (DFT) [54, 55] was employed for global chemical reactivity descriptors determination of DBAd, C_{60}, and $PC_{61}BM$, using the Generalized Gradient Approximation (GGA) with the BLYP exchange-correlation functional [56], enhanced by Grimme's dispersion correction (DFT-D) [57] and the double numerical polarization basis set (DNP+).

Finally, due to the computational cost of scanning the potential energy surface (PES) using first-principles approaches, the DFT calculations were complemented with classical molecular mechanics using the Universal Force Field (UFF) [58] of the Forcite module of the Biovia Materials Studio software package [59] to obtain the conformation that minimizes the energy of the DBAd-fullerene molecular complexes.

---

[1] International Union of Pure and Applied Chemistry

This computational protocol provides a molecular-level explanation for the experimentally fluorescence quenching of DBAd by fullerene-based quenchers (C_{60} and $PC_{61}BM$), indicating their potential as stable supramolecular complexes for organic/fullerene-based devices for next-generation solar cells. This work directly supports the United Nations Sustainable Development Goals (SDGs), especially Goal 7 (Affordable and Clean Energy) [60], by contributing to the development of more efficient solar energy technologies, and Goal 13 (Climate Action) [61], by promoting alternatives to fossil fuels and advancing clean, renewable energy solutions.

1.1 Objectives

The general objective of this thesis is to investigate the interaction mechanism between the ethoxy-dibenzalacetone derivative (DBAd) and fullerene compounds (C_{60} and $PC_{61}BM$) through molecular modeling methods and experimental photophysical measurements in order to evaluate the potential of these supramolecular complexes for application in organic solar cells (OSCs). In this context, the specific objectives are to:

(a) Compute the lowest-energy singlet-singlet excited states that constitute the UV-Vis absorption spectrum of DBAd, and determine corresponding exciton binding energy (E_B);

(b) Determine the lowest-energy conformers of the DBAd and fullerene compounds (C_{60} and $PC_{61}BM$) to obtain their optimized ground-state molecular geometries;

(c) Calculate global chemical reactivity descriptors to assess the contributions of highest occupied and lowest unoccupied molecular orbitals (HOMO and LUMO) in energy level alignment for photoinduced charge transfer;

(d) Scan the potential energy surface (PES) and calculate the intermolecular interaction parameters to determine the most stable supramolecular conformations;

(e) Experimentally characterize the photophysical properties of the supramolecular complexes C_{60}@DBAd and $PC_{61}BM$@DBAd in ethanol-toluene binary solution as a function of fullerene quencher concentration;

(f) Correlate the influence of the PES on the fluorescence quenching mechanism, Förster resonance energy transfer (FRET), and charge transfer exciton (CTE) of C_{60}@DBAd and $PC_{61}BM$@DBAd complexes;

(g) Propose a mechanistic interpretation of the quenching pathway based on stability of intermolecular interactions in order to assess the potential application of these complexes in organic/fullerene-based devices for next-generation solar cells.

2 STATE-OF-THE-ART REVIEW

The history of conductivity in organic compounds dates back to the turn of the 20th century with the study of photoconduction in anthracene, discovered by Pochettino and Sella [62, 63]. At that time, measurable dark conductivity and its dependence on the molten state were also reported, leading to various attempts to relate these phenomena to the recently discovered photoelectric effect by Einstein[1] [65, 66]. Volmer soon refuted these interpretations and demonstrated that photoconduction in anthracene occurred at approximately 3 eV [63, 67].

This energy value was significantly below the typical work function of solids (generally above 4 eV) and therefore insufficient to induce electron emission into the vacuum [68]. Consequently, photoconduction in anthracene arises from lower-energy optical excitation that promotes electrons from the highest occupied molecular orbital (HOMO) to the lowest unoccupied molecular orbital (LUMO), generating tightly Coulomb-bound electron-hole pairs (excitons), which can subsequently dissociate into free charge carriers that contribute to the electrical conductivity of the molecular crystal [69].

In the following decades, particularly between the 1920s and 1940s, several studies focused on organic dyes sought to elucidate how π-electron transfer between molecules plays a fundamental role in biological systems [70, 71]. In 1948, the temperature-dependent electrical conductivity of phthalocyanines was reported to follow an exponential behavior [72], reinforcing photoconduction as an intrinsic of specific molecular structures in organic compounds [62].

In 1976, scientists Hideki Shirakawa, Alan Heeger, and Alan MacDiarmid discovered that the electrical conductivity of polyacetylene could be enhanced by several orders of magnitude through electrochemical doping with halogen atoms [73, 74]. This pioneering work laid the foundation for the field of conducting polymers and was subsequently recognized with the Nobel Prize in Chemistry in the 2000s. Subsequently, in 1987, interest in the relationship between electronics and organic compounds gained prominence, especially with the development of the first organic light-emitting diode (OLED) device based on conjugated molecules by Ching Wan Tang and Steven Van Slyke [75].

Figure 3 illustrates the brief chronological evolution of electrical conductivity in organic compounds. These materials became known as organic semiconductors and constitute a class of molecular materials composed predominantly of carbon atoms in sp^2 hybridization, with

---

[1] The photoelectric effect was proposed by Albert Einstein in his 1905 paper in which he described light as composed of discrete particles called “photons” (quantum of light) [64]. This interpretation allowed the explanation of inconsistencies in classical physics, earning him the Nobel Prize in Physics in 1921.

non-hybridized p_z orbitals oriented perpendicularly to the molecular plane. These p_z orbitals overlap to form delocalized π and π^* molecular orbitals. Thus, organic semiconductors combine the electrical conductivity of inorganic semiconductors with the physicochemical properties of organic compounds [76, 77], widely employed in optoelectronic devices such as biological sensors [78–80], thermoelectric devices [81, 82], organic field-effect transistors (OFETs) [83, 84], and organic solar cells (OSCs) [85–87].

Figure 3 – Brief conductivity history of the organic compounds in a chronological timeline.

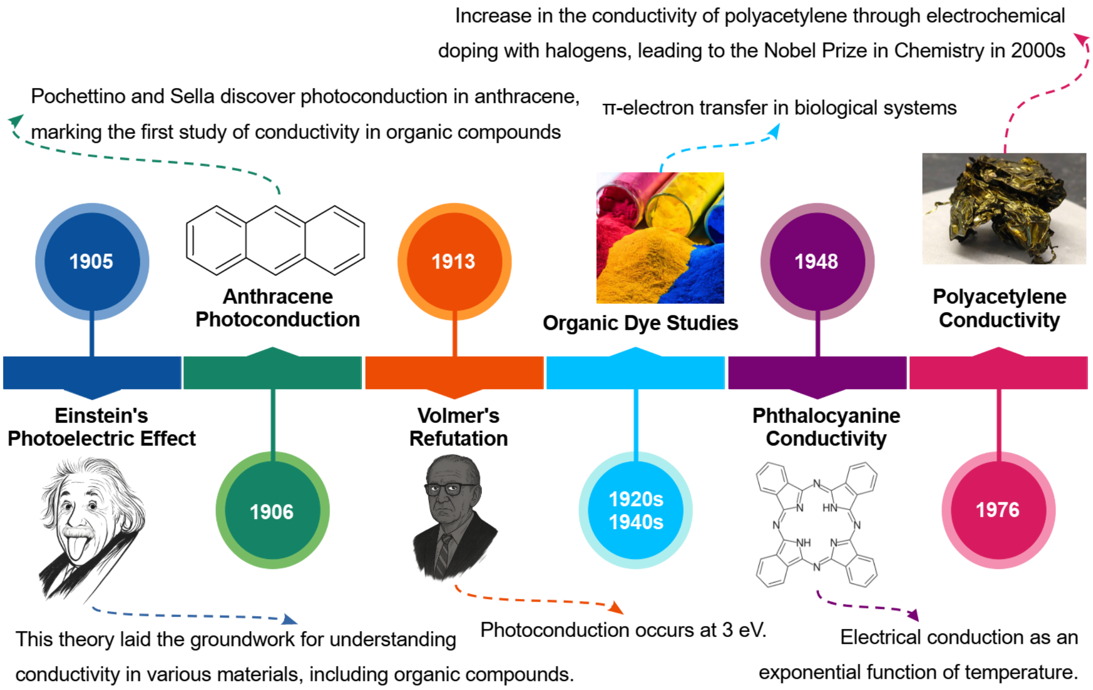

In these compounds, the overlap of the π orbitals promotes the delocalization of electrons in the conjugated system and produces a distribution of energy levels that resemble the band structures of inorganic semiconductors, whose highest occupied molecular orbital (HOMO) and lowest unoccupied molecular orbital (LUMO) represent the π and π^* orbitals, respectively, and are analogous to the valence and conduction bands [88].

According to Koopman's theorem [89], negative energies of the HOMO and LUMO orbitals indicate the chemical reactivity descriptors Ionization Potential (IP) and the Electron Affinity (EA) [90], respectively. The IP corresponds to the energy required to remove an electron from a neutral species, and EA is the energy released upon adding an electron to a neutral species. Thus, the fundamental gap (E_{fund}) corresponds to the subtraction value between the ionization potential and the electron affinity (E_{fund} = IP – EA).

The electronic transitions between the π and π^* orbitals can be optically accessed in the UV-visible region of the electromagnetic spectrum, preventing any significant concentration of charge carriers by thermal excitation at room temperature [76]. Consequently, photons energies in the range of 2 to 4 eV [91] promote the electronic transition to an excited state in the unoccupied/virtual orbital (LUMO), causing the creation of a positive charge carrier at the HOMO level, maintained by Coulomb interaction.

According to Brédas [90], the ground and lowest excited state energy difference correspond to the optical gap[2] ($E_{opt} = S_1 - S_0$). Typically, the optical gap is smaller than the fundamental gap because the electron remains electrostatically bound to the hole in the excited state, unlike the ionized state, where a free charge carrier is generated in the material [90]. Additionally, the difference between the fundamental gap and the optical gap indicates the binding energy of the electron-hole pair ($E_B = E_{fund} - E_{opt}$), called the exciton.

The E_{opt} can be estimated theoretically using Time-Dependent Density Functional Theory (TD-DFT) [95] by calculating the vertical excitation energy from the ground state (S_0) to the first singlet excited state (S_1), and experimentally by analyzing the optical absorption edge using the Tauc method [96]. The E_{fund} can be obtained experimentally by combining gas-phase ultraviolet photoelectron spectroscopy (UPS) and inverse photoemission spectroscopy (IPES), which provide ionization potential (IP) and the electron affinity (EA), respectively; and computationally by DFT-based calculations as an approximation the difference between the energy levels of the HOMO and the LUMO [90].

The accuracy of this approximation depends on the adopted exchange-correlation functional, especially on the fraction of the exact Hartree-Fock exchange incorporated. Hybrid functionals, which include a fraction of exact exchange, tend to reduce self-interaction errors and improve the description of frontier orbital energies [97]. However, even with hybrid functionals, the HOMO-LUMO gap generally underestimates the accurate E_{fund} due to the discontinuity of the exchange-correlation potential.

Long-range corrected (range-separated) hybrid functionals are particularly effective as they mitigate the delocalization error and improve the asymptotic behavior of the potential [98]. Thus, for accurate predictions of E_{opt}, E_{fund}, and E_B, careful selection and validation of the computational methodology are essential.

---

[2] Furthermore, the excited electronic state involves transitions to vibrational and rotational sublevels. According to Kasha's [92, 93] rule, fluorescence emission occurs predominantly from the lowest excited electronic state (S_1), regardless of which higher electronic state (S_n) was initially excited. Because the S_n rapidly relaxes by internal conversion to S_1 before emission, making fluorescence a process dominated by the first excited state [94].

In organic semiconductors, excitons generated within a single molecular unit are referred to as Frenkel excitons, characterized by strong electron-hole Coulombic binding and high spatial localization, which results in increased binding energy (E_B) [99, 100] due to the low dielectric constant of these materials. However, when the electron and hole become spatially separated across adjacent donor and acceptor molecular units at an interface, a charge-transfer exciton (CTE), also known as an exciplex, is formed [101].

These distinct excitons influence charge separation mechanisms in optoelectronic devices, such as organic solar cells (OSCs). Accordingly, organic semiconductor molecules and molecular crystals are divided between charge donor and acceptor materials, or even ambipolar, which can transport electrons and holes simultaneously [102]. In these devices, photoexcitation typically generates Frenkel excitons that must diffuse to a donor-acceptor interface, where they can form charge transfer excitons (CTEs). These CTEs facilitate the separation of charge carriers, a process essential for high OSCs efficiency [103].

The molecular conformation and driven electronic properties at the interface determine the CTEs and influence the reduction of E_B, making the electron and hole separate more easily into electric current for OSCs [104]. However, as the inherently low dielectric constant of organic semiconductors favors the prevalence of Frenkel excitons [76], the functionalization of these materials with polarizing auxochromes allows the manipulation of the molecular dipole moment, improving intermolecular interactions at the donor-acceptor interface. Therefore, increasing intermolecular interactions at the interface is a significant advantage in enhancing the performance of these optoelectronic devices.

2.1 Organic Solar Cells

Organic solar cells (OSCs) have attracted interest due to their processability, mechanical flexibility, low toxicity, and cost-effectiveness [105]. Historically, the first generation of OSCs emerged with the monolayer deposition of an organic semiconductor between two electrodes with different work functions (Φ) – defined as the difference between the vacuum (E_V) and Fermi (E_F) energies – and characterized by a power conversion efficiency (PCE) below 0.1% due to the annihilation of photogenerated excitons [106].

The second generation was represented by the bilayer structure of donor and acceptor electron materials [18], which still posed challenges for charge carrier diffusion and separation, also resulting in low-efficiency values [105, 107]. In this generation, copper phthalocyanine (donor) and perylene tetracarboxylic derivative (acceptor) were stacked as the active layer and produced a PCE of approximately 1%, as reported by Tang [18].

Significant advances were obtained by implementing bulk heterojunction (BHJ) structures, in which the donor and acceptor components were blended to maximize the interfacial region and enhance the exciton diffusion distance [44]. Since the implementation of BHJ in 1995, the efficiency has surged to 19.5% [108–111], making it attractive photovoltaic technology and marking the third generation of these devices. Figure 4 illustrates the evolution of OSCs generations over the decades.

Figure 4 – Representation of the evolution of organic solar cell (OSC) architectures: (a) First-generation single-layer device, (b) Second-generation bilayer device with separated donor and acceptor materials, and (c) Third-generation bulk heterojunction (BHJ) device, where donor and acceptor materials blended.

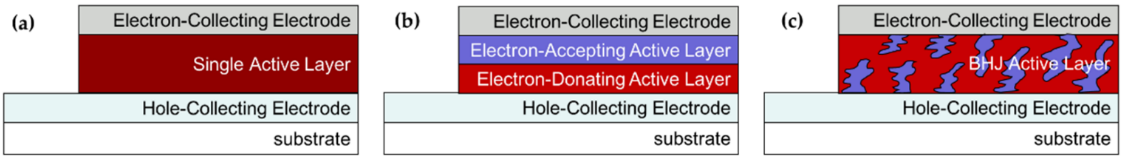

Source: Adapted from Zheng *et al.* [24].

Organic semiconductors as active layers play a crucial role in the efficiency of OSCs. These materials must exhibit high charge carrier mobility, well-aligned electronic energy levels, and nanoscale phase separation [26] because they facilitate light absorption and generation of electron-hole pairs, diffusion and dissociation of excitons at the donor-acceptor interface, and efficient transport of charge carriers to the respective electrodes [112, 113].

In OSCs, approximately 50% of the device efficiency is lost in the recombination of charge carriers [34]. Unlike inorganic semiconductors that have a high dielectric constant and delocalized degenerate states, in organic semiconductors, the excitons are highly localized and, therefore, have a high exciton binding energy (E_B) and a significant Coulomb barrier which results in a rapid decay of the excited state [35–39], typically at femtosecond time scale [114].

An alternative to increase the lifetime of these quasi-particles is to maximize the interfacial area in domains of the order of the exciton diffusion length ($\sim$ 10 nm) [39], since unlike inorganic semiconductors where charge carriers move in a periodic potential through strong covalent bonds [115], whose photon absorption results in nearly free particles due to the weak binding energy of Mott-Wannier excitons[3], organic interfaces typically are formed by non-covalent interactions, whose cohesion established by weak intermolecular van der Waals forces, hydrogen bonds or London dispersive forces [119].

According to Pope and Swenberg [100] and other authors [120–122], the energy required to dissociate an exciton in organic materials ranges from 0.5 to 1 eV. Under normal operating conditions, the device's thermal energy and electric field are insufficient to promote this dissociation. Instead, the difference in chemical potential between the organic semiconductors and compensations at the interfacial energy level plays a key role [123]. However, after dissociation, the electron and hole remain subject to a significant Coulomb attraction and, despite being structurally separated, remain in a bound state for a finite lifetime [124].

The Coulomb interaction remains significant until the electron-hole separation distance exceeds the Coulomb capture radius, also known as the Onsager radius, defined as the radius at which the Coulomb attraction is equal to the thermal energy ($\mathrm{k_B T}$) [125–127]. Thus, different molecular packing structures and diffusion in donor-acceptor materials influence the interaction between charge carriers.

Exciton diffusion can be described by Förster Resonance Energy Transfer (FRET) theory [128], in which the non-radiative transfer of electronic excitation energy occurs between molecules acting as oscillating dipoles through long-range Coulombic interactions. For conservation, the acceptor must possess an available electronic state such that the energy gained corresponds to the energy lost by the donor. Alternatively, exciton behavior may also be modeled by short-range mechanisms such as Dexter energy transfer [129], which involves electron exchange and requires orbital overlap, or by nonadiabatic dynamics methods such as surface hopping [47], which simulate the stochastic transitions between potential energy surfaces [130].

2.2 Charge transfer exciton

Analogous to massive particles, exciton transport can be described by a diffusional model due to the finite effective mass given by the sum of electron and hole effective mass [131]. In organic semiconductors, diffusion occurs from regions of high to low concentration, being characterized by the mean squared displacement (L_D), which quantifies the average diffusion length before radiative or non-radiative recombination [39], as described by the equation:

---

[3] Mott-Wannier excitons have a Bohr radius related to the relative motion of the electron and hole much larger than the lattice constant and present a small reduced mass, whose electron-hole attraction governed by the high dielectric constant ($\epsilon \sim 10$) [115–118].

$$L_D = \sqrt{ZD\tau} \tag{2.1}$$

where L_D is the mean squared exciton diffusion length (in Å), Z is the geometric factor associated with the exciton motion ($Z = 1, 2,$ or 3 for one-, two-, or three-dimensional diffusion, respectively), D is the diffusion coefficient (in $\mathrm{cm}^2 \cdot \mathrm{s}^{-1}$), and τ is the exciton lifetime in the excited state (in s).

The efficiency of exciton transport and dissociation at donor-acceptor interfaces is influenced by the distribution of electronic energy levels [39]. Due to the amorphous or semicrystalline nature of organic materials, energy levels exhibit Gaussian density of states, arising from conformational disorder and local variations in intermolecular interactions [132]. In this context, Förster and Dexter energy transfer mechanisms facilitate exciton hopping between conjugated delocalized, rendering this migration effectively diffusive [131, 133].

An electronically excited molecule can transfer energy to another by nonradiative processes, returning to the ground state while exciting the acceptor. The predominant mechanisms include Förster resonance energy transfer (FRET) [128], mediated by dipole-dipole interactions, and Dexter transfer, which involves short-range electron exchange enabled by wavefunction overlap [129]. Furthermore, FRET exhibits weak sensitivity to thermal variations, whereas the Dexter mechanism strongly depends on intermolecular proximity and energy barriers, making it more susceptible to temperature fluctuations [134, 135].

Moreover, surface hopping (SH) is a trajectory-based semiclassical method where electronic state populations evolve with classical nuclear motion [47]. This approach is particularly suitable for simulating nonradiative energy transfer involving electronic relaxation dynamics. Unlike potential energy surface (PES) approaches, electronic properties are computed in real-time along nuclear trajectories. Transition probabilities are estimated either within the local nonadiabatic interaction region or from propagated electronic wavefunction coefficients [136, 137].

2.2.1 Förster resonance energy transfer

Förster resonance energy transfer (FRET) is a nonradiative mechanism in which energy is transferred from an electronically excited donor molecule to an acceptor molecule by dipole-dipole interactions. This process is highly dependent on intermolecular distance (typically effective within 10 to 100 Å) and the spectral overlap between the donor's emission and the acceptor's absorption spectra [94], as illustrated in Figure 5.

Figure 5 – Schematic representation of Förster resonance energy transfer (FRET) within a biomacromolecule. The green region represents the donor site, where exciton diffusion occurs (purple arrow). The red region denotes the acceptor site, where fluorescence quenching takes place. The curved arrow (green-to-red gradient) illustrates the non-radiative energy transfer pathway from donor to acceptor.

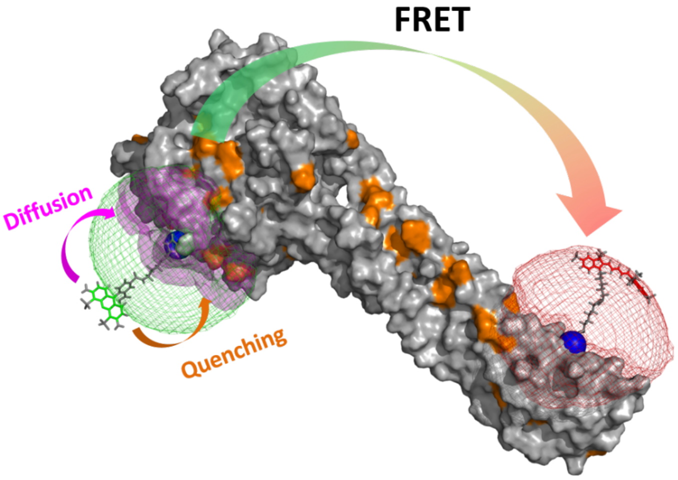

Source: Peulen *et al.* [138].

Physically, the FRET mechanism occurs without the actual transport of electrons and does not require direct orbital overlap between the donor and acceptor molecules. The FRET efficiency (η_{FRET}) can be expressed as:

$$\eta_{\text{FRET}} = \frac{R_0^6}{R_0^6 + r^6}\,, \tag{2.2}$$

where R_0 is the Förster radius and r is the distance between donor and acceptor. The R_0 is directly related to the spectral overlap integral, the relative orientation between the dipoles involved and the donor quantum yield, according to the equation:

$$R_0^6 = \frac{9000 \cdot \ln(10) \cdot \kappa^2 \cdot \; \Phi_{\text{D}} \cdot J(\lambda)}{128 \cdot \pi^5 \cdot n^4 \cdot N_A}\,, \tag{2.3}$$

where Φ_{D} is the fluorescence quantum yield of the donor, n the refractive index, κ^2 the dipole orientation factor, N_A is Avogadro's constant, and $J(\lambda)$ the overlap integral between the donor's normalized emission and the acceptor's molar absorptivity spectrum [131].

The FRET efficiency decays with the sixth power of the distance between the donor-acceptor centers (r) and the transfer rate (k_{FRET}) can be calculated by the expression:

$$k_{\text{FRET}} = \frac{1}{\tau_D} \left(\frac{R_0}{r} \right)^6 f(E_i, E_j) \ , \tag{2.4}$$

$$f(E_i, E_j) = \begin{cases} e^{-\frac{(E_j - E_i)}{k_B T}}, & \text{if } E_j > E_i, \\ 1, & \text{if } E_j \leq E_i. \end{cases} \tag{2.5}$$

where τ_D is the lifetime of the excited state of the donor in the absence of the acceptor, R_0 is the Förster radius (the donor-acceptor separation distance at which the transfer efficiency is 50%), and r is the center-to-center distance between the donor and acceptor. The function $f(E_i, E_j)$ is the Boltzmann-weighted acceptance probability, which accounts for the relative differences in the energy states i and j, commonly used in semiclassical and stochastic hopping models to incorporate thermal activation into transitions between electronic or vibronic states [139].

The equation (2.4), in the absence of the Boltzmann-weighted acceptance probability, describes energy transfer in discrete molecular systems, where the donor-acceptor interaction can be effectively modeled as a classical dipole-dipole coupling [140]. However, in disordered materials such as organic semiconductors, the statistical distribution of energy levels necessitates thermal modulation of the transfer rate, thereby justifying the incorporation of the probability factor $f(E_i, E_j)$ [141].

Furthermore, energy transfer generally occurs on timescales shorter than vibrational relaxation, allowing the structural configuration of the system to be considered fixed during the photoexcitation [142]. However, exceptions arise in systems with strong vibronic coupling, where vibrational redistribution influences the transfer rate [143, 144]. In such cases, generalized versions of Förster theory are more appropriate [130].

The efficiency of energy transfer is also strongly dependent on the type of exciton involved. Typically, only singlet excitons participate in the Förster mechanism, as this process preserves the total spin of the system. In contrast, triplet excitons, constrained by spin selection rules, predominantly follow the Dexter mechanism [145–147]. Although triplet excitons exhibit longer lifetimes, their lower diffusivity reduces the efficiency of energy transfer, leading to diffusion lengths comparable to those of singlet excitons [140].

Currently, several models have been proposed to describe charge transport and recombination mechanisms in organic solar cells (OSCs). Among them, Onsager's theory [127] describes the dissociation of charge pairs and bimolecular recombination in low-permittivity dielectric media. Monte Carlo-based methods, employing the Miller-Abrahams expression [148], are widely used to model charge mobility in disordered OSCs, accounting for hopping processes between localized states.

Additionally, Marcus theory [149, 150] describes a quantum-mechanical approach for electron transfer and charge recombination (both geminate and bimolecular) in organic semiconductors. This approach enables the direct calculation of recombination rates from the potential energy surfaces of the initial and final states, applying Fermi's Golden Rule [151] to determine the charge transfer rate constant, given by:

$$k = \frac{2\pi}{\hbar}|H_{mt}|^2 \frac{1}{\sqrt{4\pi\lambda_{mt}k_BT}} \exp\left[-\frac{(\Delta G^0 + \lambda_{mt})^2}{4\lambda_{mt}k_BT}\right] \tag{2.6}$$

where H_{mt} is the electronic coupling between the initial and final states, λ_{mt} is the reorganization energy associated with the donor-acceptor complex and its surrounding environment, and ΔG^0 is the standard Gibbs free energy change between the initial and final electronic states, typically determined from redox potential differences under standard conditions [152].

Förster resonance energy transfer directly impacting charge separation and recombination dynamics in optoelectronic devices [140, 153]. While conventional FRET models assume static dipole-dipole interactions, molecular reorganization and vibronic couplings introduce dynamic modulations that influence transfer efficiency [130, 141]. Understanding these effects is essential for optimizing energy transfer pathways, efficient light-harvesting and charge transport in next-generation organic photovoltaics [127, 149].

2.2.2 Dexter Energy Transfer and Surface Hopping Modeling

Dexter energy transfer (DET), also known as exchange-mediated energy transfer, is a short-range nonradiative mechanism that occurs by the exchange of electrons between adjacent donor and acceptor molecules [129]. Unlike Förster resonance energy transfer (FRET) [128], which is governed by long-range dipole-dipole interactions and typically involves singlet-singlet transitions, the Dexter mechanism requires direct wavefunction overlap and conserves the spin multiplicity, particularly relevant for triplet-triplet energy transfer [154, 155].

According to Dexter's original formulation based on Fermi's Golden Rule [129, 151], the rate of exchange-mediated energy transfer is given by

$$k_{\mathrm{DET}} = \frac{2\pi}{\hbar} |J_{\mathrm{ex}}|^2 \rho(E) = \frac{2\pi}{\hbar}\rho(E) \left| \int \Psi_f^* H \Psi_i \, d\tau \right|^2 \quad , \tag{2.7}$$

where J_{ex} is the exchange integral quantifying the orbital overlap between donor and acceptor wavefunctions mediated by the perturbation operator H, and $\rho(E)$ is the vibrational density of states at the transition energy. In practice, the k_{DET} is often approximated by an empirical expression that emphasizes the exponential decay with intermolecular distance:

$$k_{\mathrm{DET}} = KJe^{-2r/L} \quad , \tag{2.8}$$

where K is a constant that captures orbital interaction terms, J is an empirical prefactor related to donor-acceptor energy compatibility (not to be confused with the spectral overlap integral in Förster theory), r is the center-to-center distance, and L is the attenuation length related to the exponential decay of electronic overlap, typically approximated of 1 Å by the sum of the van der Waals radii of the donor and acceptor [152]; Given the exponential dependence, k_{DET} is efficient only when the r is typically within ≤ 1 nm [156], which implies that DET is predominant in molecular aggregates, crystalline phases, or supramolecular host-guest complexes [157].

Although DET is widely employed to describe short-range excitation energy transfer and can be rigorously described using Fermi's golden rule, the Dexter formalism assumes static orbital overlap (inherently time-independent), without resolving the underlying time-dependent nonadiabatic dynamics. In this context, surface hopping (SH) has been alternatively applied to simulate photoactive and optoelectronic materials [47]. The SH is a semiclassical trajectory-based approach in which nuclear motion is treated classically, while the electronic degrees of freedom evolve quantum mechanically according to nonadiabatic transition probabilities [139].

Within the SH modeling, two main strategies exist for computing electronic transition probabilities: (i) the global hopping probability, where transitions are evaluated after the system exits a nonadiabatic coupling region – exemplified by the Landau-Zener model [158, 159] commonly used for modeling avoided crossings in organic semiconductors; and (ii) the instantaneous hopping probability, as implemented in the Fewest Switches Surface Hopping (FSSH) algorithm, where the time-dependent Schrödinger equation is integrated at each time step to determine transition probabilities between adiabatic electronic states [139].

2.2.3 *Intermolecular Fluorescence Quenching Mechanisms*

The interaction between the potential energy surfaces (PES) of fluorescent molecules and suppressive agents can induce fluorescence quenching, which reveals local information about the fluorophore environment as well as the pathways of photoinduced charge and excitation energy transfer. Quenching is typically classified into two distinct mechanisms: dynamic (collisional) or static (ground-state complex formation), according to the Stern-Volmer kinetic model [67].

Dynamic fluorescence quenching occurs when fluorophore undergoes diffusion-controlled collisional deactivation by a quencher molecule [160]. This nonradiative phenomenon introduces an additional deactivation pathway, thereby increasing the total deactivation rate constant (k_T), which is inversely proportional to the excited state lifetime (τ), as expressed by:

$$\tau = \frac{1}{k_T} = \frac{1}{(k_r + k_{nr} + k_q[Q])} \quad , \tag{2.9}$$

where k_r is the radiative decay rate, k_{nr} is the nonradiative rate, and $k_q[Q]$ corresponds to the bimolecular quenching dependent on quencher concentration $[Q]$. The dynamic quenching is described by the classical Stern-Volmer model, which relates fluorescence intensity (I) and excited-state lifetime (τ) in the presence of a quencher at concentration $[Q]$, as follows:

$$\frac{I_0}{I} = \frac{\tau_0}{\tau} = 1 + K_{\mathrm{SV}}[Q] \ , \tag{2.10}$$

where I_0 and τ_0 correspond to the fluorophore's intensity and lifetime in the absence of the quencher, respectively, and K_{SV} is the Stern-Volmer constant, which is directly proportional to the bimolecular quenching rate constant (k_q) and the intrinsic excited-state lifetime, as follows:

$$K_{\mathrm{SV}} = k_q \tau_0 \ . \tag{2.11}$$

Dynamic quenching typically occurs in homogeneous solutions and depends on the diffusion between quencher and fluorophore [131, 160]. This classical model assumes that each collision can deactivate the excited state, reducing fluorescence intensity without affecting absorption. This behavior can be experimentally confirmed by the absence of new spectral bands and the reduction of the excited-state lifetime, as predicted by Eq. (2.11).

Static quenching occurs when the fluorophore forms a non-emissive ground-state complex with the quencher prior to photoexcitation, leading to nonradiative deactivation upon excitation [131, 161]. This mechanism is governed by an equilibrium association process, and the corresponding fluorescence intensity follows a modified Stern-Volmer equation:

$$\frac{I_0}{I} = 1 + K_s[Q] \ , \tag{2.12}$$

where K_s is the association (binding) constant for the formation of the ground-state donor-quencher complex. Unlike dynamic quenching, static quenching does not affect the excited-state lifetime, since the quenching occurs through complex formation before excitation. Experimentally, this behavior is typically confirmed by the unchanged excited-state lifetime and changes in the absorption spectrum indicative of complexation [162].

Furthermore, the temperature dependence of static quenching differs from that of dynamic quenching, as the formation of ground-state complexes is an exothermic process. Consequently, increasing the temperature destabilizes the donor-acceptor complex, thereby decreasing the quenching efficiency. In many molecular assemblies, fluorescence quenching arises from the coexistence of both mechanisms. In such cases, the Stern-Volmer behavior deviates from linearity due to the combined contributions of static complex formation and diffusion-controlled collisional interactions [163], as illustrated in Figure 6.

Figure 6 – Stern-Volmer plots as a function of quencher concentration ($[Q]$). The linear regime (blue line) denotes purely dynamic (collisional) or static (complexation) quenching. The upward curvature (red line) indicates combined quenching behavior, consistent with the modified Stern-Volmer relation: $I_0/I = \left(1 + k_q\tau_0[Q]\right)(1 + K_s[Q])$.

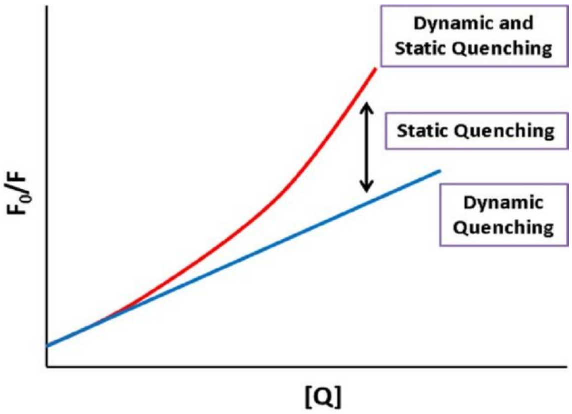

Source: Peulen *et al.* [138].

2.3 Dibenzalacetone Derivatives

Chalcone is a generic term referring to a class of synthetic and natural organic compounds that have a basic structure formed by two aromatic rings linked by a α,β-unsaturated conjugated double bond system, formally named 1,3-diaryl-2-propen-1-one [164–166], as shown in the Figure 7. Chalcones are commonly synthesized by Claisen-Schmidt condensation [164], a reaction involving the condensation between an aldehyde and a ketone (typically a benzaldehyde with acetophenone), catalyzed by an acidic or basic medium [167].

Figure 7 – Molecular structure of chalcone, illustrating two aromatic rings (labeled 1 to 6 and 1' to 6') connected by an α,β-unsaturated carbonyl system. Ring A corresponds to the acetophenone moiety, and ring B represents the aromatic aldehyde moiety. The conjugated system between the two rings plays a crucial role in the compound's electronic properties. In particular, the 4-position on ring B (para to the carbonyl group) is frequently functionalized with electron-donating or electron-withdrawing substituents, which modulate the molecule's photophysical and electronic behavior.

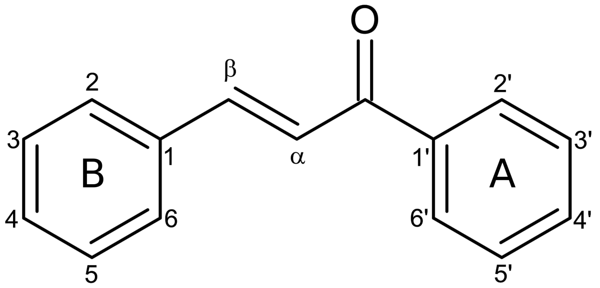

Source: Adapted from Zhuang *et al.* [165].

Stereochemically, chalcones can exist as E (from German, entgegen) or Z (from German, zusammen) isomers, with the Z isomer generally being less stable due to steric effects arising from the proximity of the aromatic rings to the carbonyl group [166]; see Figure 7. Furthermore, the conjugated enone provides a reactive structure for intramolecular cyclization that can lead to the formation of bioactive heterocycles, including flavones, flavanones, and aurones [166]. In particular, chalcones containing ortho-hydroxy substituents can cyclize under acidic or basic conditions to form flavanones, which may occur as racemic mixtures due to the formation of a stereocenter [168]. This has important implications, as stereochemistry can influence pharmacokinetic behavior and interactions with biomolecular targets.

Naturally, chalcones are biosynthesized in plant cells through the condensation of p-coumaroyl-CoA with malonyl-CoA, catalyzed by the enzyme chalcone synthase [169]. In addition to their natural biosynthesis, chalcones can be synthesized in various structural forms via Claisen-Schmidt condensation [170], Suzuki-Miyaura coupling [171], and Friedel-Crafts acylation [172], among others [165]. These synthetic chalcones are typically classified as conventional or hybrid derivatives, including bis-chalcones [165]. In these cases, the aromatic rings and the electrophilic α,β-unsaturated carbonyl group compose a delocalized π-system, which contributes to chemical reactivity, potential biological activity, and notable nonlinear optical activity [166, 173].

Bis-chalcones stand out among the main hybrid structures due to their extended conjugated system, resulting in compounds with potential pharmacological and optoelectronic applications [174–176]. These structures contain a symmetrical or asymmetrical dienone core linked to two aromatic rings, which can be substituted or unsubstituted, whose key feature is their ability to absorb energy in the near-ultraviolet-visible region [177]. Furthermore, from a synthetic perspective, there are no significant differences between the preparation of conventional chalcones and bis-chalcones, except for the requirement of two equivalents of aldehyde in the latter case [178].

In 1970, Tsukerman et al. [179] reported the luminescent study of the expanded conjugated system of compounds classified as para-dichalcones, whose experiments demonstrated that the introduction of electron-donating groups or the increase in conjugation caused a shift in absorption to the red region of the electromagnetic spectrum (red-shift) as a result of the decrease in the energy corresponding to the π–π^* transition, causing a notable increase in interest in the spectral properties of bis-chalcones. More recently, Vasconcelos et al. [50] investigated the electronic and optical properties of dibenzalacetone derivatives (DBAd), another bis-chalcones, emphasizing the role of substituents in modulating UV-Vis absorption properties. Functionalization with electron-donating and electron-withdrawing groups, such as ethoxy and chlorine, induces a significant red shift in absorption due to enhanced conjugation and hyperconjugation effects.

The interest in bis-chalcones such as DBAd compounds arises from their push-pull molecular structure, analogously illustrated in Figure 8, in which the carbonyl group acts as the acceptor fragment, while the substituents on the aromatic rings function as donors in the excited state [180]. In this context, substituted bis-chalcones satisfy key criteria for fluorescence activity, including structural rigidity, planarity, π-conjugated bonds, aromatic groups, and condensed rings [181]. Under specific conditions, molecules containing electron-donating and electron-withdrawing groups can induce internal charge transfer (ICT), leading to excited-state polarization and an increased Stokes shift.

Figure 8 – Schematic representation of a push-pull chalcone, where the electron-donating groups (in blue) and fluorescence-enhancing groups (in pink) are connected to an acceptor group (in red) through a conjugated chain. This structure facilitates charge transport and electronic coupling between the different regions of the molecule.

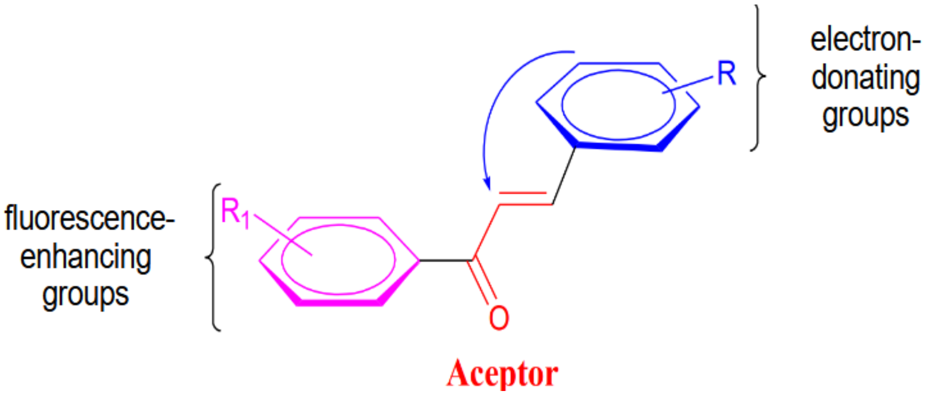

Source: Doroteio [182].

Zhou et al. [183] reported structural effects on the fluorescent properties of chalcones, highlighting that (i) a strong donor group in the 4-position of ring B (see Figure 7) is essential for fluorescence, (ii) the planar conformation of the chalcone, including both rings and the enone, is crucial, as sterically hindered compounds significantly reduce fluorescence quantum yield, (iii) weak donor and withdrawing groups positioned on ring A (see Figure 7) strongly influence the fluorescence quantum yield, (iv) intramolecular hydrogen interactions with the carbonyl fragment should avoided, and (v) an expanded conjugated system results in a red-shift. Moreover, the intensity and position of the absorption peaks are influenced by the molecular structure, varying with the nature and location of the functional groups present in the molecule.

3 EXCITED STATES AND EXCITON BINDING ENERGY

This chapter is structured into three main sections: (i) an overview of the ethoxy-dibenzalacetone derivative (DBAd) and the main properties of chalcones; (ii) a description of the theoretical and experimental methodologies to determine the excited electronic states of UV-Vis absorption spectrum and exciton binding energy of DBAd; and (iii) a comparative analysis of the results to evaluate the potential of DBAd for optoelectronic applications[1].

3.1 Introduction

Photophysical properties of small organic molecules are critical for optoelectronic, electrochemical, and biological applications [184–187]. The optical behavior of these compounds is governed by molecular architecture, whose extended conjugation and electron-donating or electron-withdrawing substitution modulate excited states and electronic transitions [188, 189]. Furthermore, solvatochromism can also significantly alter electronic density by polarization and solute-solvent intermolecular interactions. Consequently, accurate computational models are essential for predicting these electronic perturbations in the functional materials [190, 191].

Chalcones, generally non-luminescent due to intramolecular twisting and keto-enol tautomerism of the α,β-unsaturated ketone [192], exhibit derivatives with extensive π-electron delocalization and broad absorption in the ultraviolet-visible spectrum, such as dibenzalacetone derivatives [50]. These conjugated enones are typically synthesized by aldol condensation of diketones with aromatic aldehydes or dialdehydes with aromatic ketones [49, 174, 193–195]. “Chalcone” term refers to the core 1,3-diaryl-2-propen-1-one, an electrophilic unsaturated carbonyl unit conjugated to two aromatic rings [196].

In this chapter, singlet-singlet electronic transitions that compose the UV-Vis absorption spectrum of the ethoxy-dibenzalacetone derivative (DBAd) [(1E,4E)-1,5-bis(4-ethoxyphenyl)-penta-1,4-dien-3-one, $C_{21}H_{22}O_3$, PubChem CID 668155] [48], showed in Figure 9, were investigated in solvents of varying polarity. This research was motivated by the attractive properties of DBAd, including its facile synthesis by Claisen-Schmidt condensation method, intense absorption in the near-UV-Vis region, and *s-trans* conformation, which can induce a fluorescence quantum yield through electronic delocalization along the donor-acceptor-donor structure [49, 50].

---

[1] Part of the content of this chapter was previously published in: VASCONCELOS, V. M. R. et al. Red-shifted optical absorption induced by donor-acceptor-donor π-extended dibenzalacetone derivatives. **RSC Advances**, Royal Society of Chemistry, v. 15, p. 2416–2429, 2025. DOI: <https://doi.org/10.1039/d4ra07256a>

Figure 9 – Two-dimensional structure of ethoxy-dibenzalacetone derivative (DBAd, $C_{21}H_{22}O_3$). Carbon and hydrogen atoms are implicit; oxygen (red) is highlighted. The structure was generated using ChemCraft [197] program.

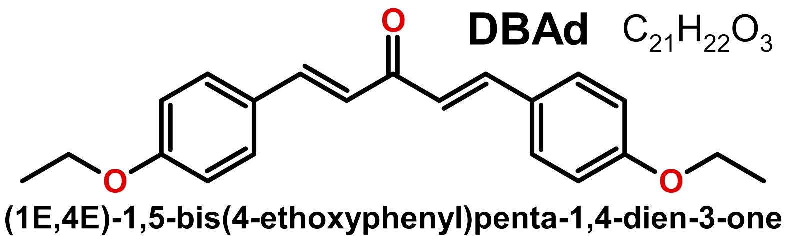

Density Functional Theory (DFT) [54, 55, 198] and Time-Dependent Density Functional Theory (TD-DFT) [199] with the Polarizable Continuum Model (PCM) at toluene ($\kappa_{\text{TOL}} = 2.37$), dichloromethane ($\kappa_{\text{DCM}} = 8.93$), and acetonitrile ($\kappa_{\text{ACN}} = 35.67$) were employed to determine the electronic structure of DBAd in ground and excited states, respectively, and corroborate with the experimental UV-Vis spectra. These electronic properties will be crucial for elucidating energy transfer and exciton dissociation at donor-fullerene interfaces.

3.2 Theoretical and Experimental Procedures

3.2.1 Sample measurements

The powder sample of the ethoxy-dibenzalacetone derivative (DBAd) was provided by the Department of Chemistry at the Universidade Estadual Vale do Acaraú (UVA), located in Sobral, Ceará, Brazil. The molecular structure of DBAd was confirmed by ^{1}H and ^{13}C nuclear magnetic resonance (NMR) spectroscopy, as shown in Figures 26 and 27 in Appendix 6. UV-Vis absorption spectra were recorded in toluene (TOL, $C_6H_5CH_3$), dichloromethane (DCM, CH_2Cl_2), and acetonitrile (ACN, CH_3CN) using a Shimadzu UV–1800 spectrophotometer at room temperature (25 °C) in quartz cuvettes with a 10 mm optical path length, over the wavelength range of 150 – 450 nm.

Stock solutions with concentrations on the order of 10^{-3} mol · L^{-1} were initially prepared of DBAd in each solvent, as detailed in Table 9 at Appendix 6. These solutions were homogenized using an ultrasonic bath for 5 min. The optical absorption spectra measurements of DBAd in each of the three solvents were conducted for five distinct concentrations in the range from an initial low (LC) concentration (0.5×10^{-5} mol · L^{-1}) to high (HC) concentration (3.5×10^{-5} mol · L^{-1}), obtained by dilution of the respective stock solutions.

According to the Beer-Lambert law, the molar absorption coefficient of DBAd was determined by linear regression analysis of the experimental data in the plot of absorbance at the maximum absorption wavelength as a function of concentration. The y-axis of the graph containing the optical absorption, which is usually acquired in arbitrary units, was corrected to $\mathrm{L \cdot mol^{-1} \cdot cm^{-1}}$, equivalently, $\mathrm{M^{-1} \cdot cm^{-1}}$; see obtained coefficients in the Table 10 at Appendix 6. Absorption data are finally reported as molar absorptivity (in $10^5\ \mathrm{L \cdot mol^{-1} \cdot cm^{-1}}$) as a function of wavelength (in nm).

Fourier-Transform Infrared (FT-IR) spectroscopy was performed for an experimental DBAd solid-state sample at room temperature using a Shimadzu IRTracer-100 spectrometer. The spectrum was acquired in transmittance mode over the range of $400 - 4000\ \mathrm{cm^{-1}}$, with a resolution of $4.0\ \mathrm{cm^{-1}}$. For sample preparation, the solid was finely ground in an agate mortar and pressed into a KBr pellet under a pressure of 80 kN using a hydraulic press.

3.2.2 *Theoretical calculations*

The structural model of the ethoxy-dibenzalacetone derivative (DBAd) was initially constructed using the ChemCraft [197] software. The optimal three-dimensional atomic arrangement was determined through conformational analysis. For this purpose, the Conformers module of the Biovia Materials Studio [200] package was employed, applying the Universal Force Field (UFF) [58] parameter set and a systematic grid-based scanning approach to explore the potential energy surface and identify the lowest-energy conformers.

Density Functional Theory (DFT) [54, 55, 198] calculations were performed on the most stable DBAd conformer. The M06-2X meta-hybrid exchange-correlation functional [201] and the 6-311+G(d,p) basis set were employed. Solvent effects were incorporated using the Polarizable Continuum Model (PCM) through the integral equation formalism variant (IEFPCM) [202] as the default Self-Consistent Reaction Field Theory (SCRF) approach. The calculations were carried out using the Gaussian 09 [203] software package considering three solvents: toluene ($\kappa_{\mathrm{TOL}} = 2.37$), dichloromethane ($\kappa_{\mathrm{DCM}} = 8.93$), and acetonitrile ($\kappa_{\mathrm{ACN}} = 35.67$), where κ denotes the dielectric constant.

Geometry optimizations were performed without constraints using the gradient method, ensuring a maximum force below $7 \times 10^{-5}\ \mathrm{Ha \cdot Bohr^{-1}}$ and an root-mean-square (RMS) force below $1 \times 10^{-5}\ \mathrm{Ha \cdot Bohr^{-1}}$, yielding geometries accurate to within 1×10^{-3} Å. Harmonic vibrational frequencies of the ground state were computed using analytical derivatives within the harmonic approximation in the Gaussian 09 [203] software at the same theoretical level (M06-2X/6-311+G(d,p)) employed for geometry optimizations. These frequencies do not include anharmonic corrections due to the absence of scaling factors for this functional and basis set combination in the Computational Chemistry Comparison and Benchmark Database (CCCBDB) [204]. All optimized structures for the ethoxy-dibenzalacetone derivative (DBAd) were confirmed as absolute minima based on the absence of imaginary vibrational modes.

Time-Dependent Density Functional Theory (TD-DFT) calculations, based on the Runge-Gross theorem and the time-dependent Kohn-Sham formulation [205–207], were employed to determine the 50 lowest-energy singlet-singlet vertical electronic transitions. The same functional and basis set used for geometry optimizations were applied, incorporating implicit solvent effects via the Integral Equation Formalism Polarizable Continuum Model (IEFPCM). The solvents – toluene (TOL, $\kappa_{\mathrm{TOL}} = 2.37$), dichloromethane (DCM, $\kappa_{\mathrm{DCM}} = 8.93$), and acetonitrile (ACN, $\kappa_{\mathrm{ACN}} = 35.67$) – were selected to assess solvatochromic effects on the electronic properties of DBAd.

Theoretical UV-Vis absorption spectra of DBAd were simulated by convoluting the vertical excitation energies and oscillator strengths obtained from TD-DFT/PCM/M06-2X/6-311+G(d,p) calculations, which each electronic transition was represented by a Gaussian distribution centered at the excitation energy (in eV), with a standard deviation (σ) of 0.283 eV, corresponding to a half-width at half-height (HWHH) of 0.333 eV or 2685.83 cm^{-1}. The absorption intensity of each band was scaled proportionally to the respective oscillator strength (f_i), which reflects the transition probability between electronic states and is directly related to the electric dipole transition moment [208].

This procedure follows the methodology described in the Gaussian 09 [203] software for simulating UV-Vis spectra (available at <https://gaussian.com/uvvisplot/>). The resulting total spectrum was obtained by summing the individual Gaussian profiles corresponding to each excitation, as expressed in:

$$\varepsilon(\tilde{\nu}) = \sum_{i=1}^{n} \varepsilon_i^{\max} \exp\left[-\frac{(\tilde{\nu}-\tilde{\nu}_i)^2}{2\sigma^2}\right] = \sum_{i=1}^{n} \frac{f_i}{\sigma\sqrt{2\pi}} \exp\left[-\frac{(\tilde{\nu}-\tilde{\nu}_i)^2}{2\sigma^2}\right], \tag{3.1}$$

where $\tilde{\nu}_i$ is the wavenumber of the i-th excitation (in cm^{-1}), σ is the standard deviation of the Gaussian function (also in cm^{-1}), f_i is the oscillator strength of the i-th transition (dimensionless), and $\varepsilon_i^{\max}$ is the maximum molar absorptivity, which is directly proportional to f_i. This approach allows for a direct comparison between theoretical and experimental UV-Vis spectra.

3.3 Results and Discussion

3.3.1 Molecular geometry optimization

The fundamental step in an *ab initio* computational procedure is determining the geometric parameters corresponding to the molecular geometry at the ground electronic state [209], as these parameters directly influence its electronic and vibrational properties. The bond lengths and angles calculated by DFT/PCM/M06-2X/6-311+G(d,p) methodology for the ethoxy-dibenzalacetone derivative (DBAd) are reported in Table 16 of the Appendix 6 and organized according to the atomic labeling scheme shown in Figure 10.

Figure 10 – Optimized molecular structures of the ethoxy-dibenzalacetone derivative (DBAd) obtained using the DFT method with the M06-2X functional and 6-311+G(d,p) basis set. Ball-and-stick representation depicts the superposition of DBAd conformations in toluene (TOL), dichloromethane (DCM), and acetonitrile (ACN), highlighting atom labels. Non-carbon atoms are color-coded by element type (oxygen in red and hydrogen in white). The figure was generated using PyMOL [210] (PyMOL Molecular Graphics System, available at <http://www.pymol.org>).

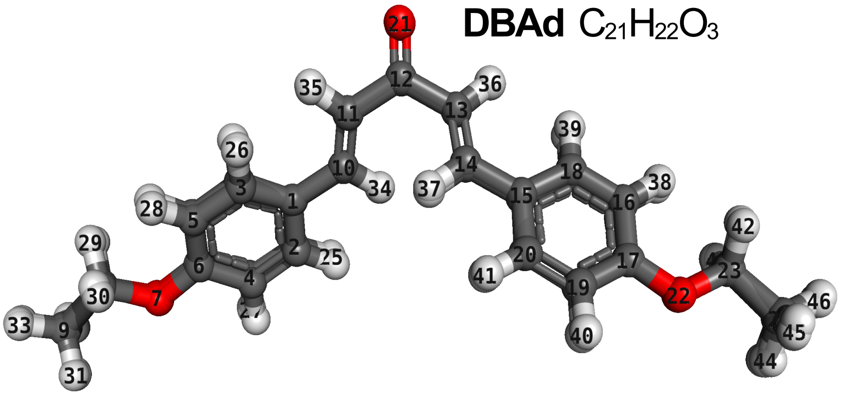

The geometry optimization confirmed that DBAd corresponds to a true minimum on the potential energy surface due to the absence of imaginary vibrational frequencies [211]. Furthermore, DBAd adopts a quasi-planar *s-trans* configuration across the enone fragment $O_{21}=C_{12}-C_{13}=C_{14}$, causing lower steric repulsion between the aryl and carbonyl groups and favoring π-extended conjugation throughout the molecule backbone [212, 213]. The crystallographic parameters for DBAd have been deposited at the Cambridge Crystallographic Data Centre (CCDC). They can be consulted using the 1015509 reference number [214].

Theoretical geometrical parameters obtained at the DFT/PCM/M06-2X/6-311+G(d,p) level were compared with the experimental single-crystal X-ray diffraction data of DBAd (CCDC 1015509) reported by Chantrapromma et al. [214]. Bond lengths such as C=O (1.222 Å), C−O (1.360 – 1.430 Å), C=C (1.314 – 1.326 Å), C−C (1.454 – 1.471 Å), and angular and torsional parameters were in good agreement with computed values, validating the accuracy of the theoretical approach employed; see Table 16 for comparison. Furthermore, it is important to note that the vibrational analysis performed here refers to the isolated DBAd molecule in solution and does not include phonon[2] calculations, restricted to the periodic molecular regime.

In Table 1, the vibrational signatures of the main infrared-active modes of the infrared bands for the ethoxy-dibenzalacetone derivative (DBAd) are presented. Experimental measurements were obtained in the solid state, while theoretical results were computed in toluene (TOL), dichloromethane (DCM), and acetonitrile (ACN) using the DFT/PCM/M06-2X/6-311+G(d,p) level of theory. DBAd exhibits an angular (non-planar) molecular geometry with 46 atoms and 132 normal vibrational modes. The molecular structure is classified in the monoclinic space group $P2_1/c$ (No. 14), following the Hermann-Mauguin notation [214].

Table 1 – Experimental and theoretical main wavenumbers (in cm^{-1}) for the ethoxy-dibenzalacetone derivative (DBAd, $C_{21}H_{22}O_3$). Experimental measurements were obtained from solid-state samples, while theoretical values were calculated using DFT/PCM/M06-2X/6-311+G(d,p) methodology.

	(C−H)sp^2	(C−H)sp^3	(C=O)	(C=C)	(C−C)	(C−O)
^{a}**Exp. (solid sample)**	3036	2883	1640	1568	1255	1167
^{b}**The. TOL**	3153 ± 117	3054 ± 171	1684 ± 44	1561 ± 7	1298 ± 43	1198 ± 31
^{b}**The. DCM**	3147 ± 111	3053 ± 170	1685 ± 45	1560 ± 8	1295 ± 40	1196 ± 29
^{b}**The. ACN**	3146 ± 110	3059 ± 176	1680 ± 40	1560 ± 8	1291 ± 36	1200 ± 33

^{a}Experimental wavenumbers obtained by second derivative-based method; ^{b}Theoretical harmonic vibrational wavenumbers (ω) calculated by DFT/PCM/M06-2X/6-311+G(d,p) methodology in toluene (κ_{TOL} = 2.37), dichloromethane (κ_{DCM} = 8.93), and acetonitrile (κ_{ACN} = 35.67); ± indicates the absolute deviation between calculated and experimental wavenumbers values.

---

[2] Phonons are quantized lattice vibrations that arise from the periodicity of crystalline solids and typically computed using plane-wave DFT methods with periodic boundary conditions [115], does not include isolated molecules.

In α,β-unsaturated ketones, the strong coupling between the C=C bond and the adjacent carbonyl group leads to π-electron delocalization by conjugation [215]. This effect decreases localized electron density, reducing bond force constants and shifting vibrational wavenumbers (in cm^{-1}) to lower values [216]. Consequently, the formation of chalcones is characterized by infrared absorption bands in the ranges 1650 a 1780 cm^{-1} for C=O, 1550 a 1650 cm^{-1} for C=C, and 800 a 1200 cm^{-1} for C−C, as indicated in Figure 11.

Figure 11 – Experimental and theoretical infrared (IR) spectra for ethoxy-dibenzalacetone derivative (DBAd). Panels shown (a) experimental solid-state spectrum, while theoretical harmonic spectra computed by DFT/PCM/M06-2X/6-311+G(d,p) using the implicit solvent model are presented for (b) toluene, TOL (ω_{TOL}, $\kappa_{\mathrm{TOL}} = 2.37$), (c) dichloromethane, DCM (ω_{DCM}, $\kappa_{\mathrm{DCM}} = 8.93$), and (d) acetonitrile, ACN (ω_{ACN}, $\kappa_{\mathrm{ACN}} = 35.67$). IR intensities given in arbitrary units (a.u.) as a function of wavenumber (in cm^{-1}) are presented in three spectral regions in increasing order of energy: 300–1450, 1450–2500, and 2550–3650 cm^{-1}. The experimental spectrum was converted from transmittance to absorbance by $2 - log(T)$. The ω unscaled theoretical spectra were convoluted with Gaussian functions with a full width at half maximum (FWHM) of 48.35 cm^{-1} for visualization.

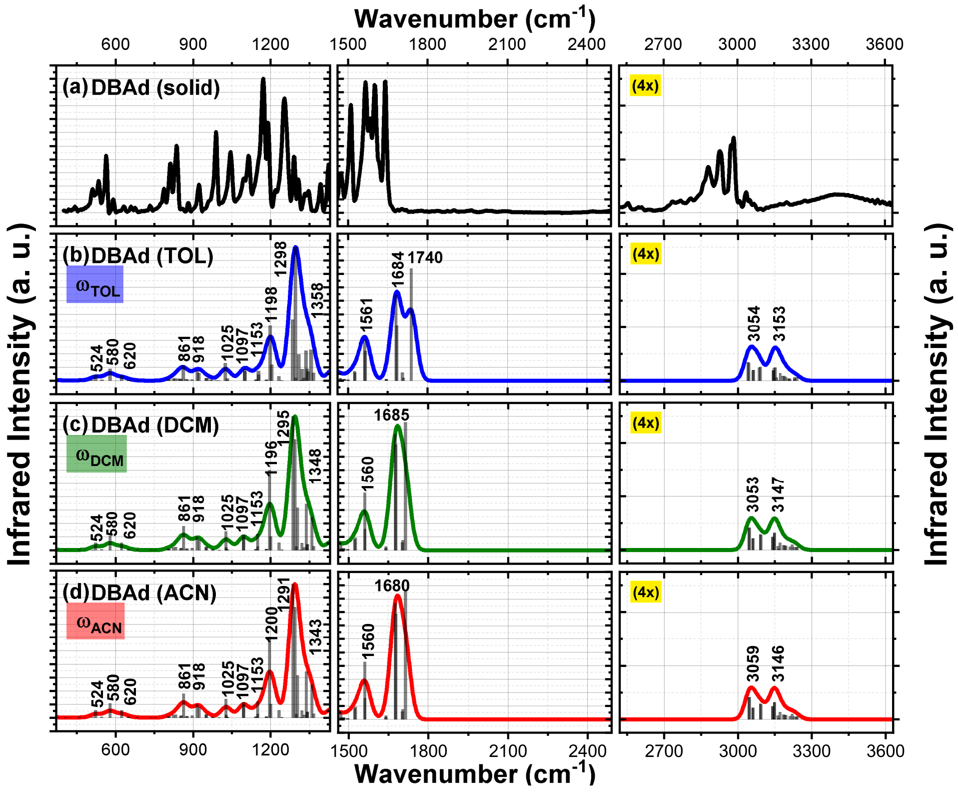

Theoretical C=O stretching wavenumbers for the α,β-unsaturated ketone group were calculated as 1684, 1685, and 1680 cm^{-1} in TOL, DCM, and ACN, respectively (see Table 1). These values are slightly shifted to lower wavenumbers relative to the typical carbonyl stretching due to enhanced conjugation in the enone ($O_{21}=C_{12}-C_{13}=C_{14}$ and $O_{21}=C_{12}-C_{11}=C_{10}$) fragment and the electron-donating effect of the ethoxy substituent [217].

The C=C stretching vibrations were observed at 1561, 1560, and 1560 cm^{-1} in the same solvents, consistent with conjugation-induced relative to isolated double bonds [218, 219]. The C–H stretching modes for the sp^2 carbons appear at 3153, 3147, and 3146 cm^{-1}, whereas sp^3 C–H stretches were found at 3054, 3053, and 3059 cm^{-1} in TOL, DCM, and ACN, respectively. The C–O stretching bands appeared in the range 1196 – 1200 cm^{-1}.

The experimental IR spectrum of DBAd in the solid state exhibits a strong C=O stretching band at 1640 cm^{-1}, consistent with theoretical predictions (see Table 1). The C=C stretching mode appears at 1568 cm^{-1}, and the C–O stretching band is observed at 1167 cm^{-1}. Additionally, absorption bands at 3036 cm^{-1} and 2883 cm^{-1} corresponds to the sp^2 and sp^3 C–H stretching vibrations from the ethoxy substituents, respectively.

DFT/PCM/M06-2X/6-311+G(d,p) overestimate vibrations compared to experimental data. This discrepancy arises due to the anharmonicity effects and the inherent approximations of quantum mechanical methods [220]. Furthermore, theoretical calculations consider a free-solvated molecule, whereas experimental data is performed on crystalline solid state, where intermolecular interactions and crystal packing effects influence vibrational modes [221].

The vibrational wavenumbers obtained in this study for the DBAd molecule exhibit good agreement with experimental FT-IR data reported by Chantrapromma et al. [214] for the same compound in crystalline form. Specifically, the experimental C=O stretching band was observed at 1640 cm^{-1} in our measurements and at 1670 cm^{-1} in the reference work. Similarly, the C=C stretching band appears at 1568 cm^{-1} in our solid-state data and 1602 cm^{-1} in Chantrapromma's results.

The C–O stretching mode was detected at 1167 cm^{-1} in our study, while the reference reported 1232 cm^{-1}. Additionally, the C–H stretching of the ethoxy sp^2 and sp^3 carbons were observed at 3036 and 2883 cm^{-1} in our data and at 2876 cm^{-1} in the literature. These discrepancies are within the expected variation due to differences in crystal packing effects, measurement conditions, and treatment of vibrational anharmonicity. Therefore, the comparison corroborates the vibrational assignments and theoretical predictions presented herein.

3.3.2 UV–Vis absorption spectra and HOMO–LUMO orbitals analysis

Experimental and theoretical UV-Vis absorption spectra of the ethoxy-dibenzalacetone derivative (DBAd) in toluene ($\kappa_{\text{TOL}} = 2.37$), dichloromethane ($\kappa_{\text{DCM}} = 8.93$), and acetonitrile ($\kappa_{\text{ACN}} = 35.67$) are presented in Figure 12. The UV-Vis spectra are expressed in terms of molar absorptivity ($\text{L} \cdot \text{mol}^{-1} \cdot \text{cm}^{-1}$) as a function of wavelength (nm) over the spectral range 150 a 450 nm. These solvents, commonly utilized in organic electronics [222, 223], exhibit an increasing dielectric constant and dipole moment (increasing in the order TOL < DCM < ACN), enabling assessment of solvatochromic effects on the electronic transitions of DBAd.

Figure 12 – (a) Experimental and (b) theoretical UV-Vis spectra obtained across a range of wavelengths from 150 a 450 nm, and (c) molar absorption coefficient in toluene ($\kappa_{\text{TOL}} = 2.37$), dichloromethane ($\kappa_{\text{DMC}} = 8.93$) and acetonitrile ($\kappa_{\text{ACN}} = 35.67$) by linear regression analysis of the experimental data of maximum absorption as a function of molar concentration, according to the Beer-Lambert law; see Table 10 in the Appendix 6; (d) theoretical oscillator strengths as a function of photon energy (in eV) for DBAd in TOL, DCM, and ACN.

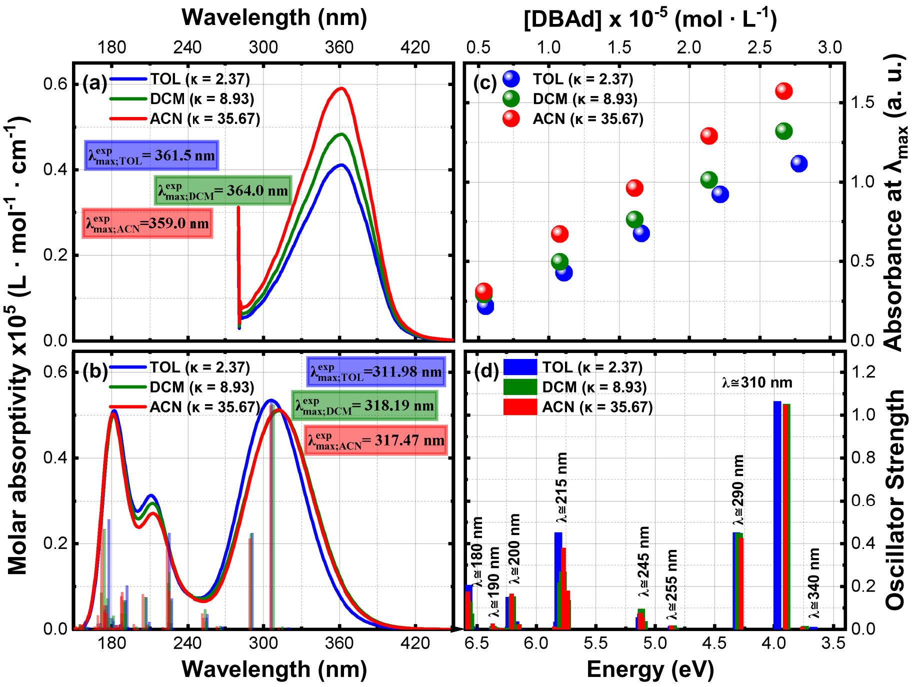

UV-Vis spectra were initially recorded in arbitrary units, as provided by default of the spectrophotometer. The absorbance data were converted into molar absorption coefficients (molar absorptivity) to enable direct comparison with theoretical results. This conversion was performed using linear regression of absorbance at the maximum absorption wavelength (λ_{max}) for varying concentrations of DBAd in TOL, DCM, and ACN, following the Beer-Lambert law [224, 225]. Figure 12 (b) shows the corresponding regression plot for DBAd.

TD-DFT/PCM/M06-2X/6-311+G(d,p) calculations were conducted as a function of oscillator strength (f_i), vertical excitation energy (E in eV), and transition probability between molecular orbitals (in %), as shown in Figure 12 (d). Table 2 presents the six lowest-energy electronic transitions of DBAd in the employed solvents. These transitions correspond to the most significant contributions to the observed absorption bands, providing insights into the electronic structure and solvatochromic behavior of DBAd. Table 15 in Appendix 6 expands each solvent's 10 lowest-energy excited states.

Table 2 – Excited states (ES), oscillator strength (f_i), and excitation energies (E in eV) for the six lowest-energy electronic transitions of the ethoxy-dibenzalacetone derivative (DBAd) in toluene (κ_{TOL} = 2.37), dichloromethane (κ_{DCM} = 8.93), and acetonitrile (κ_{ACN} = 35.67), calculated by TD-DFT/PCM/M06-2X/6-311+G(d,p) methodology.

	Toluene (κ_{TOL} = 2.37)				**Dichloromethane** (κ_{DCM} = 8.93)				**Acetonitrile** (κ_{ACN} = 35.67)			
ES	E (eV)	f_i	**Trans.**	(%)	E (eV)	f_i	**Trans.**	(%)	E (eV)	f_i	**Trans.**	(%)
1	3.67	0.011	H-4 ⟶ L	72.7	3.74	0.016	H-4 ⟶ L	73.5	3.76	0.011	H-4 ⟶ L	74.0
2	3.97	1.065	H ⟶ L	85.8	3.90	1.053	H ⟶ L	87.2	3.91	1.048	H ⟶ L	87.2
3	4.32	0.451	H-1 ⟶ L	82.7	4.30	0.449	H-1 ⟶ L	82.0	4.28	0.424	H-1 ⟶ L	85.5
4	4.85	0.013	H ⟶ L+1	23.7	4.83	0.005	H ⟶ L+1	35.5	4.85	0.002	H ⟶ L+1	30.7
5	4.86	0.015	H ⟶ L+3	24.6	4.85	0.018	H ⟶ L+2	27.7	4.86	0.017	H ⟶ L+2	27.2
6	5.12	0.073	H-1 ⟶ L+1	30.1	5.09	0.038	H ⟶ L+1	46.3	5.11	0.055	H ⟶ L+1	41.2

κ: dielectric constant of the solvent; H: Highest Occupied Molecular Orbital (HOMO), L: Lowest Unoccupied Molecular Orbital (LUMO); f_i: oscillator strength; Trans.: dominant electronic transition in terms of configuration interaction (CI) coefficient; %: configuration contribution in the excited-state wavefunction expansion.

According to the Franck-Condon principle, the maximum absorption peaks in UV-Vis spectra correspond to vertical electronic excitations from the ground state (S_0) to higher excited states (S_n) [226, 227]. The theoretical UV-Vis spectrum of the ethoxy-dibenzalacetone derivative (DBAd) (see Figure 12 (b)) exhibits three absorption bands centered at 190, 210, and 315 nm in the employed solvents. These bands correspond to $\pi - \pi^*$ and $n - \pi^*$ electronic transitions associated with the conjugated α, β-unsaturated ketone system and the aromatic rings.

However, due to inherent limitations in experimental measurements, such as instrumental setup, light source constraints, optical component efficiency, atmospheric interference, quartz cuvette transmission, and solvent absorption, only the lowest-energy absorption band was detectable in the experimental UV-Vis spectra of DBAd. The spectral cutoff point was 280 nm for onset of solvent absorption, as shown in Figure 12 (a).

The lowest-energy absorption band is characterized by absorption at a maximum wavelength ($\lambda^{\text{exp}}_{\text{max}}$) of 361.5, 364.0, and 359.0 nm for DBAd in the solvents TOL, DCM, and ACN, respectively, in good approximation to the calculated $\lambda^{\text{the}}_{\text{max}}$. These values are shown in Table 3. TD-DFT calculations predict the occurrence of a higher-probability electronic transition (allowed) at 311.98, 318.19, and 317.47 nm (3.97, 3.90, and 3.90 eV) for DBAd in TOL, DCM, and ACN, respectively, corresponding to the transition with the highest oscillator strength.

Table 3 – Comparative analysis of experimental and theoretical maximum wavelengths (λ_{max}, in nm) and molar absorption coefficients (ϵ_{max}, in 10^5 L · mol^{-1}· cm^{-1} or 10^5 M^{-1}· cm^{-1}) for the ethoxy-dibenzalacetone derivative (DBAd) in toluene (κ_{TOL} = 2.37), dichloromethane (κ_{DCM} = 8.93), and acetonitrile (κ_{ACN} = 35.67).

	[a]**Experimental**			[b]**Theoretical**			
Solvent	$\lambda^{\text{exp}}_{\text{max}}$ (nm)	$\epsilon^{\text{exp}}_{\text{max}}$ (10^5 M^{-1}·cm^{-1})	[g]$E^{\text{exp}}_{\text{opt}}$ (eV)	$\lambda^{\text{theo}}_{\text{max}}$ (nm)	$\epsilon^{\text{theo}}_{\text{max}}$ (10^5 M^{-1}·cm^{-1})	[h]$E^{\text{the}}_{\text{opt}}$ (eV)	[f] f_i
[c]TOL	361.5	0.405	3.15	311.98	0.535	3.97	1.065
[d]DMC	364.0	0.483	3.10	318.19	0.511	3.90	1.053
[e]ACN	359.0	0.596	3.15	317.47	0.512	3.91	1.048

[a]Experimental peak maxima and molar absorption coefficients determined using a second derivative-based method; [b]Theoretical values calculated using TD-DFT/PCM/M06-2X/6-311+G(d,p); [c]TOL, toluene (κ_{TOL} = 2.37); [d]DCM, dichloromethane (κ_{DCM} = 8.93); [e]ACN, acetonitrile (κ_{ACN} = 35.67); where κ is the dielectric constant for the solvent; [f] f_i, oscillator strength; [g]Experimental optical gap ($E^{\text{exp}}_{\text{opt}}$, in eV) determined using the Tauc plot method [96], which involves plotting (absorption coefficient x photon energy)$^{\gamma}$ in (eV · cm^{-1})$^{\gamma}$ against photon energy (in eV) to extrapolate the linear portion to the energy axis. Adopted $\gamma = 2$ considering indirect allowed transitions. Data expressed with one decimal place due to the resolution of the spectrophotometer; [h]Theoretical optical gap ($E^{\text{the}}_{\text{opt}}$, in eV) obtained from the second excited state (S_2) and selected due to its higher oscillator strength and HOMO$\longrightarrow$ LUMO transition probability, which indicates allowed electronic transitions [90].

This maximum absorption band corresponds mainly to the electronic excitation from the highest occupied molecular orbital (HOMO) to the lowest unoccupied molecular orbital (LUMO); see this transition between frontier orbitals corresponding to the second excited state energy in the Table 2. Figure 13 illustrate the symmetry of the molecular orbitals involved in the main electronic transitions of the first three lowest-energy excited states that compose the band centered at $\lambda_{\text{max}}^{\text{the}}$ in dichloromethane (κ_{DCM} = 8.93). The solvents toluene (κ_{TOL} = 2.37) and acetonitrile (κ_{ACN} = 35.67) involve similar frontier orbitals, and therefore are not repeated here.

Figure 13 – Molecular orbital energy diagram and isosurface representations of the ethoxy-dibenzalacetone derivative (DBAd) for the first three singlet excited states (DBAd-S1, S2, and S3) in dichloromethane (κ_{DCM} = 8.93), calculated by TD-DFT/PCM/M06-2X/6-311+G(d,p). Vertical excitations (grey lines) indicate the dominant electronic transitions between occupied (green horizontal lines) and unoccupied/virtual (violet horizontal lines) molecular orbitals. Frontier molecular orbitals are shown as isodensity surfaces with contour values of +0.015 (blue) and −0.015 (red).

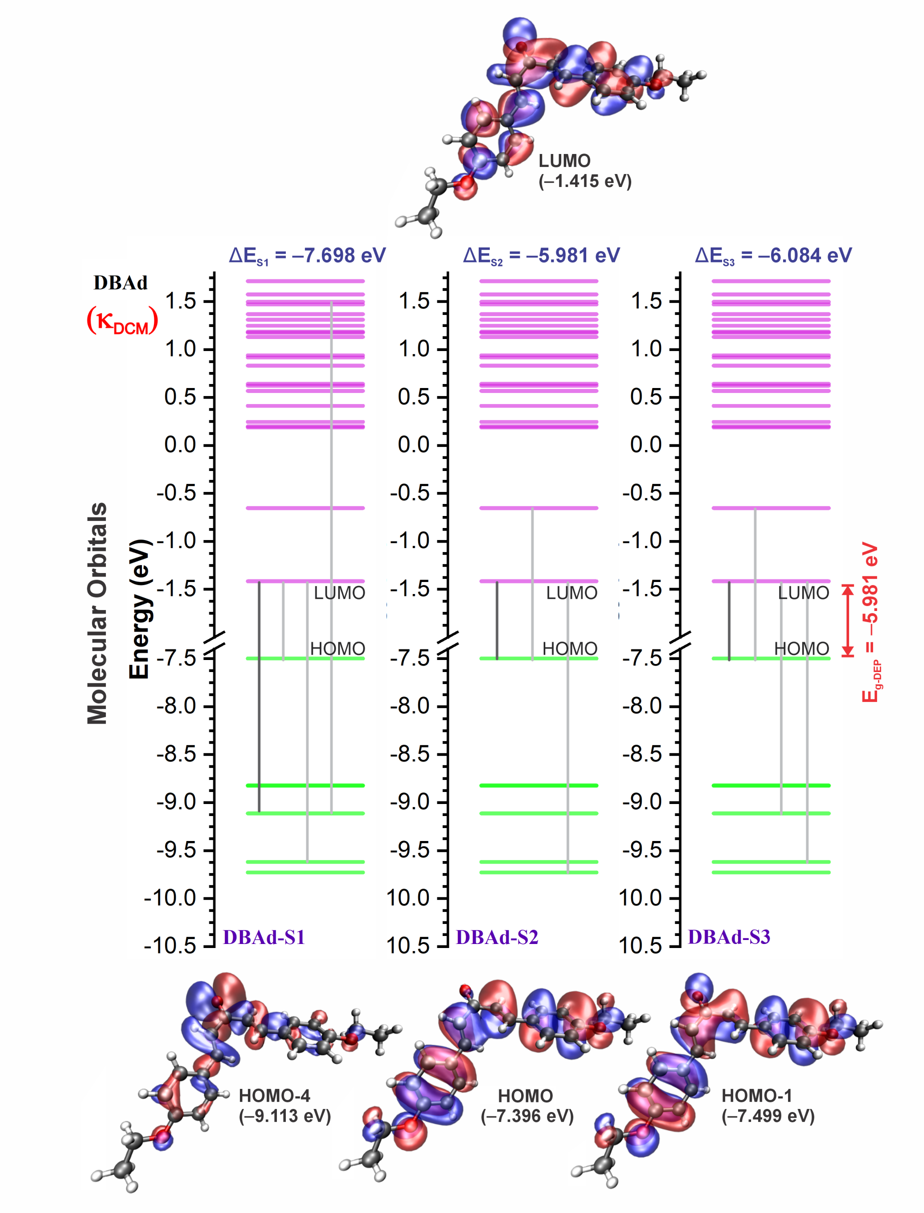

For a qualitative analysis of the experimental ($\mathrm{E}_{\mathrm{opt}}^{\mathrm{exp}}$) and theoretical ($\mathrm{E}_{\mathrm{opt}}^{\mathrm{the}}$) optical gap values, the Tauc method [96] to determine $\mathrm{E}_{\mathrm{opt}}^{\mathrm{exp}}$ and the energy of the second excited state (DBAd-S2) to quantify $\mathrm{E}_{\mathrm{opt}}^{\mathrm{the}}$ were employed. This assignment is justified since the optical gap corresponds to the energy of the lowest electronic transition accessible by photon absorption (typically from HOMO to LUMO) [90]. In this context, the first excited state (DBAd-S1) for DBAd was considered to be optically forbidden due to the symmetry of the involved molecular orbitals, leading to a low oscillator strength and transition H-4→L instead of HOMO→LUMO; see the first excited state for DBAd in Figure 13 and Table 2.

In general, $\mathrm{E}_{\mathrm{opt}}^{\mathrm{exp}}$ and $\mathrm{E}_{\mathrm{opt}}^{\mathrm{the}}$ decreases from toluene (TOL) to dichloromethane (DCM), consistent with the increase in solvent polarity. This behavior is attributed to the conjugation effect in α,β-unsaturated ketones, wherein π–π^* and n–π^* electronic transitions are shifted to longer wavelengths as a consequence of the reduced energy gap between electronic levels in chromophores by stabilization of the excited state by polar solvents [218, 228]. However, acetonitrile (ACN), despite its higher dielectric constant, does not strictly follow this trend.

The value of $\mathrm{E}_{\mathrm{opt}}^{\mathrm{exp}}$ in ACN equals that of TOL (3.15 eV), which can be attributed to the nature of the Tauc method, which is sensitive not only to the absorption onset (edge) but also to the absorption intensity [96, 229]. In this case, the increase in $\epsilon_{\mathrm{max}}^{\mathrm{exp}}$ in ACN compensates for the slight hypsochromic shift in $\lambda_{\mathrm{max}}^{\mathrm{exp}}$, maintaining the same optical gap as in TOL. Similarly, for the theoretical data, although $\epsilon_{\mathrm{max}}^{\mathrm{the}}$ increases slightly from DCM to ACN, the corresponding $\lambda_{\mathrm{max}}^{\mathrm{the}}$ shows a minor blue shift, which explains the subtle increase in $\mathrm{E}_{\mathrm{opt}}^{\mathrm{the}}$ from 3.90 eV (DCM) to 3.91 eV (ACN). Despite this deviation, the values remain within the same order of magnitude, indicating weak effects in aprotic solvents.

Furthermore, auxochromes containing unpaired electrons can induce bathochromic shifts by enhancing π-conjugation through $n \longrightarrow \pi^*$ interactions [230]. Consequently, the greater the number of nonbonding electrons interacting with unsaturated bonds, the stronger the bathochromic shift [231]. The excitation of n electrons in the π-extended chromophore leads to a partially electron-deficient excited atom, while the π system receives an electron in the π^* antibonding orbital [232]. This redistribution results in charge separation within the molecule, characterizing a charge transfer (CT) excited state [233], which can be influenced by solvents.

In DBAd, a small redshift is observed in $\lambda_{\mathrm{max}}^{\mathrm{the}}$ when transitioning from TOL (311.98 nm) to DCM (318.19 nm) and from TOL to ACN, suggesting moderate stabilization of the CT state due to increased solvent polarity. However, a hypsochromic shift is seen experimentally and theoretically in ACN (359.0 nm and 317.47 nm, respectively), deviating from the expected trend. In ACN, the ground state solvation stabilizes more than the excited state, leading to a blue shift in absorption maxima [202, 234].

Figure 12 and Table 3 indicate these solvent-dependent variations in $\lambda_{\max}^{\exp}$ and $\lambda_{\max}^{\text{the}}$. In addition to the contribution of nonbonding electrons of oxygen, hyperconjugation from the ethoxy group also influences the spectral shift by delocalizing electron density from the σ-orbitals of the C–H into the π-system (see Figure 13) [235]. This electronic interaction is captured by the Hartree-Fock exchange incorporated in the meta-hybrid M06-2X functional.

These results suggest that the DBAd exhibits low sensitivity to aprotic solvent polarity and demonstrates a satisfactory agreement between $\lambda_{\max}^{\exp}$ and $\lambda_{\max}^{\text{the}}$, with a theoretical-experimental difference ranging from 16%, 14%, and 13% for TOL, DCM, and ACN, respectively. Although the employed methodologies yielded a reasonable correlation, further studies with range-separated hybrid functionals, explicit and conductive solvation models, or vibrational reorganization energy calculations are necessary for a more comprehensive understanding.

3.3.3 Exciton binding energy

The exciton binding energy (E_B) is a fundamental parameter in the efficiency of optoelectronic materials. In π-conjugated systems, E_B arises from the difference between the fundamental gap (E_{fund}), determined by the ionization potential (IP) and electron affinity (EA), and the optical gap (E_{opt}), which corresponds to the vertical excitation energy from the ground (S_0) to the first singlet excited state (S_1) [90]. Typically, E_{opt} is smaller than E_{fund}, as the electron remains electrostatically bound to the hole in the excited state, unlike the ionized state, where a free charge carrier is generated in the material.

According to Koopman's [89] theorem, global chemical reactivity descriptors were computed using the DFT/PCM/M06-2X/6-311+G(d,p) methodology. As presented in Table 4, E_B of the ethoxy-dibenzalacetone derivative (DBAd) decreases with increasing solvent polarity, exhibiting values of 2.41, 2.24, and 2.21 eV in TOL, DCM, and ACN, respectively. Moreover, although the chemical potential (μ) becomes more negative with solvent polarity, indicating increased electronic stabilization, the electrophilicity index (ω) also rises due to the quadratic dependence on μ and the moderate variation in chemical hardness (η) [236, 237]. The rising ω and increasingly negative μ support the ambipolar character of DBAd, consistent with its donor-acceptor-donor structure.

Table 4 – Global chemical reactivity descriptors (in eV) calculated according to Koopman's [89] theorem for the ethoxy-dibenzalacetone derivative (DBAd, $C_{21}H_{22}O_3$) in toluene (TOL, $\kappa_{TOL} = 2.37$), dichloromethane (DCM, $\kappa_{DCM} = 8.93$), and acetonitrile (ACN, $\kappa_{ACN} = 35.67$) through DFT/PCM/M06-2X/6-311+G(d,p) level of theory.

	E_{HOMO}	E_{LUMO}	^{a}IP	^{b}EA	$^{c}E_{fund}$	$^{d}E_{B}$	$^{e}\omega$
TOL	−7.37	−1.29	7.37	1.29	6.08	2.41	28.47
DCM	−7.40	−1.42	7.40	1.42	5.98	2.24	29.02
ACN	−7.43	−1.46	7.43	1.46	5.97	2.21	29.53
^{f}Mean±SD	−7.40 ± 0.03	−1.39 ± 0.09	7.40 ± 0.03	1.39 ± 0.09	6.01 ± 0.06	2.29 ± 0.11	29.01 ± 0.53

^{a}Ionization potential (IP): IP $= -E_{HOMO}$ [89]; ^{b}Electron affinity (EA): EA $= -E_{LUMO}$ [89]; ^{c}Fundamental gap energy (E_{fund}): E_{fund} = IP − EA [90]; ^{d}Exciton binding energy (E_B): $E_B = E_{fund} - E_{opt}$ [90], where E_{opt} corresponds to $S_0 \rightarrow S_1$ excitation energy obtained by TD-DFT/PCM/M06-2X/6-311+G(d,p) (see Table 2); ^{e}Electrophilicity index (ω): $\omega = \mu^2/(2\eta)$ [237]; ^{f}Statistical mean and standard deviation (SD) computed from solvent-dependent values; *Electronegativity (χ): $\chi = -\mu = (\mathrm{IP} + \mathrm{EA})/2$ and Chemical potential (μ): $\mu = -\chi = -(\mathrm{IP} + \mathrm{EA})/2$ [238]; Chemical hardness (η): $\eta = (\mathrm{IP} - \mathrm{EA})/2$ and Chemical softness (S): $S = 1/\eta$ [198]; **Derived descriptors (not shown in table): Electronegativity (χ), chemical hardness (η), chemical softness (S), and chemical potential (μ) are 4.33, 4.41, and 4.45 eV; 3.04, 2.99, and 2.99 eV; 0.33, 0.33, and 0.34 eV^{-1}; and −4.33, −4.41, and −4.45 eV for TOL, DCM, and ACN, respectively; *** E_{HOMO} and E_{LUMO} obtained from DFT single-point calculations.

3.4 Final Considerations

This chapter investigated the excited states that compose the UV-Vis absorption spectrum and exciton binding energy (E_B) of the ethoxy-dibenzalacetone derivative (DBAd) using the TD-DFT/PCM/M06-2X/6-311+G(d,p) methodology to corroborate experimental measurements. The results confirmed that DBAd exhibits weak solvatochromic behavior, with bathochromic shifts influenced by an increase in solvent polarity (increasing from TOL to DCM). Theoretical-experimental discrepancies in λ_{max} were attributed to the limitations of implicit solvation models in capturing specific solute-solvent interactions. A key finding was also the systematic reduction in E_B with increasing solvent polarity, indicative of increased exciton dissociation efficiency in high dielectric medium. Furthermore, the presence of an extended π-conjugated system as well as hyperconjugative electron-donating effects of the ethoxy auxochrome contribute to charge transfer transitions, indicating the potential of DBAd as a donor and ambipolar molecule for applications in organic electronics. Subsequently, will explore the interactions of DBAd with fullerene quenchers to evaluate its distinct roles in photoinduced charge transfer and excitation energy transfer processes for next-generation optoelectronic devices.

4 GROUND-STATE NON-COVALENT INTERACTIONS

This chapter is divided into three main sections: (i) an overview of the influence of weak intermolecular forces in molecular organization, electronic coupling, and excitonic processes; (ii) a description of the theoretical approaches employed for geometry optimization, electronic structure analysis, and intermolecular interaction potential calculations, including Density Functional Theory (DFT) calculations for isolated molecules and classical molecular mechanics simulations using the Universal Force Field (UFF) to construct the potential energy surfaces (PES) of dibenzalacetone derivative (DBAd) interacting with fullerene compounds (C_{60} and $PC_{61}BM$); and (iii) a detailed analysis of the electronic and structural properties of the DBAd-fullerene complexes, emphasizing their impact on fluorescence quenching mechanisms, Förster resonance energy transfer (FRET), and photoinduced charge-transfer exciton. This chapter is based on the article entitled "Fluorescence quenching driven by PES-guided self-assembly of ethoxy-dibenzalacetone and fullerene-based quenchers", which is currently under peer review.

4.1 Introduction

Charge transfer exciton (CTE) dissociation into free charge carriers at donor-acceptor interfaces directly influences photocurrent generation in donor/fullerene-based bulk heterojunction organic solar cells [39, 153, 239]. Photoexcited electron-hole pairs bonded by Coulombic interaction, also known as Frenkel excitons, present limited diffusion lengths due to the low dielectric constant of organic semiconductors [35, 76], and radiatively annihilate through emitting photoluminescence, reducing the efficiency of organic photovoltaic devices [240]. However, understanding how the CTEs nonradiatively separate remains a long-standing challenge in both theoretical and experimental perspectives [241, 242].

Analogous to Marcus theory, in which electron transfer efficiency depends on the exchange integral between donor and acceptor wavefunctions – exchange interactions decay exponentially with increasing intermolecular distance – the dissociation of CTEs can be rationalized in a similar physical framework. The thermodynamic driving force for dissociation is to reduce the exciton binding energy (E_B) barrier through the enhanced coupling between donor-acceptor potential energy surfaces (PES) [243–247], and increased spectral overlap between donor emission and acceptor molar absorptivity by Förster resonance energy transfer (FRET), enabling excitons to migrate over 10 – 100 Å via nonradiative dipole-dipole coupling [135, 248].

Thermodynamically, the probability of charge separation is proportional to exp $\left(-\frac{\mathrm{E_B}}{k_\mathrm{B}T}\right)$ [249]. Consequently, CTE dissociation is limited when $\mathrm{E_B}$ exceeds thermal energy ($k_\mathrm{B}T$). In organic semiconductors, $\mathrm{E_B}$ is about 0.5 eV [107, 250], typically exceeds the thermal energy at room temperature (25 °C), and therefore optimizing donor-acceptor orbital overlap is essential to enhance CTE dissociation. Unlike the ionized state, where free charge carriers can transfer to the acceptor due to excess kinetic energy (hot carriers) [251], in the CTE state, the electron remains electrostatically bound to the hole, resulting in a low charge mobility [90].

Moreover, CTE dissociation depends on both the Onsager capture radius [127, 252, 253] and the short-range molecular order [254], as the composition of the donor-acceptor interface drives a favorable interaction force [104], which is critical to overcoming the $\mathrm{E_B}$ and preventing the trapping of minority charge carriers [255, 256]. However, noncovalent interactions predominantly dominate the interface in organic semiconductors, causing complex potential energy surfaces (PES) [47, 54, 55], critical in photoinduced processes [47].

Fazzi et al. [257] demonstrated that on-top orientations (stronger orbital overlap) promote high-energy charge transfer, while on-edge orientations induce low-energy charge transfer. Similarly, Benatto et al. [104] showed that the relative position of the acceptor to the donor molecule can significantly affect the dipole moment of the complex and the driving force for electron transfer. Therefore, the donor-acceptor PES is critical for CTE dissociation [258, 259]. Consequently, understanding how PES reduces exciton recombination losses through photoinduced charge and excitation energy transfer can enhance the performance of organic donor-fullerene solar cells.

In this chapter, chemical reactivity descriptors of the ethoxy-dibenzalacetone derivative (DBAd) (1E,4E)-1,5-bis(4-ethoxyphenyl)penta-1,4-dien-3-one and fullerene-based acceptors ($\mathrm{C_{60}}$ and $\mathrm{PC_{61}BM}$), as well as the potential energy surfaces (PES) of the supramolecular complexes DBAd@$\mathrm{C_{60}}$ and DBAd@$\mathrm{PC_{61}BM}$ were calculated to elucidate the fluorescence quenching mechanisms of DBAd. The strong interaction energy (ϵ) and short-range distance (r) observed for the DBAd-fullerene complexes indicate the formation of a stable donor-acceptor complex, confirming the static quenching revealed in fluorescence analysis. These findings suggest that the fullerene quencher is already adjacent to the DBAd at excitation, enabling efficient energy and charge transfer from DBAd (donor) to fullerenes (acceptor). Consequently, a non-fluorescent complex is formed, with an association constant (K_s) comparable to other non-covalently linked fullerene assemblies [260, 261].

4.2 Computational and Experimental Procedures

4.2.1 Molecular Geometry Optimization

The initial atomic coordinates for the (1E,4E)-1,5-bis(4-ethoxyphenyl)penta-1,4-dien-3-one ethoxy-dibenzalacetone derivative (DBAd) and the fullerene compounds (C_{60} and $PC_{61}BM$) were constructed using ChemCraft [197] and GaussView [262], respectively, as shown in Figure 14. Obtaining the lowest-energy conformers is crucial for accurate geometry optimization, as the spatial arrangement of atoms significantly affects molecular properties. To this end, the Conformers module of the Biovia Materials Studio [59] software package was employed, utilizing the Universal Force Field (UFF) [58] parameter set and the systematic grid scanning method.

Figure 14 – Two-dimensional chemical structure of the dibenzalacetone derivative (DBAd, $C_{21}H_{22}O_3$) and three-dimensional chemical structures of the fullerene compounds (C_{60} and $PC_{61}BM$, $C_{72}H_{14}O_2$) are presented prior to optimization. The carbon atoms of C_{60} and $PC_{61}BM$ are depicted in different colors (C_{60} in pink and $PC_{61}BM$ in purple). Carbon and hydrogen atoms are not explicitly shown. The figures were created using the ChemCraft program [197] (available at <https://www.chemcraftprog.com>), and the GaussView program [262] (available at <https://gaussian.com/gaussview6/>).

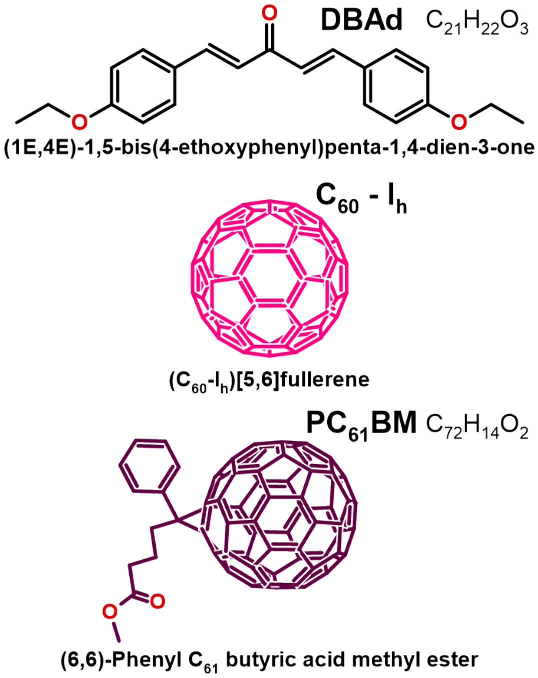

The conformational search was conducted with a van der Waals and vicinal radii scale factor of 0.4. Electrostatic and van der Waals interactions were calculated using an atom-based summation method with cubic spline truncation. An 18.5 Å cutoff distance and a 1 Å spline width were applied. Geometry optimizations used the Smart algorithm with convergence criteria of 2×10^{-5} $\mathrm{kcal \cdot mol^{-1}}$ for energy, 1×10^{-3} $\mathrm{kcal \cdot mol^{-1} \cdot \mathring{A}^{-1}}$ for force, and 1×10^{-5} Å for displacement. A maximum of 1000 iterations was set to systematically explore the conformational space of the potential energy surface.

Subsequently, Density Functional Theory (DFT) calculations [54, 55, 198] were performed on the most stable conformers of DBAd, C_{60}, and $PC_{61}BM$ using the $DMol^3$ module in the Biovia Materials Studio package [59]. These calculations employed the Generalized Gradient Approximation (GGA) with the BLYP exchange-correlation functional [56], complemented by Grimme's dispersion correction (DFT-D) [57] to account for van der Waals interactions.

The Kohn-Sham electronic orbitals were expanded using the double numerical polarization basis set (DNP+), with all-electron calculations and no pseudopotentials. The orbital cutoff radius was set to 3.7 Å, and the self-consistent field (SCF) convergence tolerance was set to 1×10^{-6} Ha using DIIS extrapolation. Geometry optimizations allowed up to 1000 iterations to ensure full convergence. The energy and gradient convergence tolerances were set to 1×10^{-5} Ha and 2×10^{-3} $\mathrm{Ha \cdot \mathring{A}^{-1}}$, respectively. All calculations were performed using unrestricted spin polarization to account for open-shell systems.

The geometry optimizations were unconstrained and used the gradient method, achieving a maximum force below 2×10^{-3} $\mathrm{Ha \cdot \mathring{A}^{-1}}$ and an RMS force less than 1×10^{-3} $\mathrm{Ha \cdot \mathring{A}^{-1}}$, ensuring geometries accurate to 5×10^{-3} Å. Harmonic vibrational frequencies of the ground state were calculated using analytical derivatives within the harmonic approximation in the $DMol^3$ module [59] at the same theoretical level as the geometry optimizations. All optimized structures were confirmed to be absolute minima by the absence of imaginary vibrational modes [263–265].

4.2.2 Potential Energy Surface (PES) Scanning

The potential energy surface (PES) scanning and non-covalent interaction energy calculations for the C_{60}@DBAd and $PC_{61}BM$@DBAd complexes were carried out using the Forcite module from the Biovia Materials Studio [59] software package. These calculations employed the Universal Force Field (UFF) [58] for energy evaluation and charge assignment. A non-periodic truncation approach was adopted, with van der Waals interactions calculated atom-by-atom and a buffer width of 0.5 Å to ensure convergence. The interaction energy for each complex was determined using the following equations:

$$E^{\text{interaction}}_{(\text{C}_{60}@\text{DBAd})} = E_{\text{C}_{60}@\text{DBAd}} - \left(E_{\text{C}_{60}} + E_{\text{DBAd}}\right) \ , \tag{4.1}$$

and,

$$E^{\text{interaction}}_{(\text{PC}_{61}\text{BM}@\text{DBAd})} = E_{\text{PC}_{61}\text{BM}@\text{DBAd}} - \left(E_{\text{PC}_{61}\text{BM}} + E_{\text{DBAd}}\right) \ , \tag{4.2}$$

where $E^{\text{interaction}}_{(\text{C}_{60}@\text{DBAd})}$ and $E^{\text{interaction}}_{(\text{PC}_{61}\text{BM}@\text{DBAd})}$ are the interaction energies of the C_{60}@DBAd and PC_{61}BM@DBAd, respectively, calculated as the difference between the total energy of the complex and the sum of the energies of their isolated components; and $E_{(\text{DBAd})}$, $E_{(\text{C}_{60})}$, and $E_{(\text{PC}_{61}\text{BM})}$ represent the energies of the DBAd, C_{60}, and PC_{61}BM isolated molecules, respectively.

Geometry optimizations were performed without constraints using a gradient-based method. The convergence criteria were defined as follows: the maximum gradient threshold was 2×10^{-3} Ha · Å^{-1}, energy variation was below 1×10^{-5} Ha, and atomic displacement was less than 5×10^{-3} Å. The Forcite module was set to ultrafine quality, with a maximum of 1000 charge iterations to ensure accurate charge assignment.

Rotational and translational configurations were systematically explored to map the PES, as illustrated in Figure 15. For the C_{60}@DBAd complex, due to the topological symmetry of C_{60}, only the DBAd molecule was rotated in 5° increments and translated up to 30 Å along each Cartesian axis to achieve a comprehensive spatial sweep. For the PC_{61}BM@DBAd complex, DBAd and PC_{61}BM were rotated in 5° and 40° increments, respectively, with DBAd translations performed along each Cartesian axis up to the same cutoff distance of 30 Å. Molecular centroids were recorded to calculate the intermolecular distance (r) and interaction energy (ϵ). Only conformations with interaction energies below -5.0 kcal · mol^{-1} were retained to reduce computational overhead.

To evaluate the force field efficiency and determine the separation distance at which the interaction potential between C_{60}@DBAd and PC_{61}BM@DBAd is zero, the Lennard-Jones (LJ) [266] and Mie [267] potentials were applied. In these models, the parameter σ defines the separation at which the potential energy is zero, indicating the balance point between attractive and repulsive forces [268], while ϵ represents the potential well depth, correlating with the interaction stability [269]. In the Mie model, the exponents $n = 6$ and $m = 12$ were initially adopted, analogous to the asymptotic behavior of the Lennard-Jones potential, preserving the description of van der Waals interactions: a repulsive term proportional to r^{-12} and an attractive term proportional to r^{-6} [270]. The LJ and Mie potentials are expressed as follows, respectively:

$$V(r)_{\mathrm{LJ}} = 4\epsilon\left[\left(\frac{\sigma}{r}\right)^{12} - \left(\frac{\sigma}{r}\right)^{6}\right] , \tag{4.3}$$

and,

$$V(r)_{\mathrm{Mie}} = \epsilon\left[\frac{n}{n-m}\left(\frac{n}{m}\right)^{\frac{m}{n-m}}\left(\frac{\sigma}{r}\right)^{n} - \frac{m}{n-m}\left(\frac{\sigma}{r}\right)^{m}\right] . \tag{4.4}$$

The PES mapping produced approximately 4,380 conformations for C_{60}@DBAd and 43,801 for $PC_{61}BM$@DBAd. This extensive exploration identified energetically favorable conformations and revealed active regions where phenomena such as chemical reactions, charge transfer, or energy transfer are most likely to occur [47, 271, 272].

Figure 15 – Schematic representation of the Potential Energy Surface (PES) calculation between the ethoxy-dibenzalacetone derivative (DBAd) and fullerene compounds (C_{60} and $PC_{61}BM$). (a) The initial Cartesian coordinates of DBAd (ba2) were rotated by the operator $\mathbf{R}(\theta_2)$ and translated by a displacement vector $\vec{r}$ to a cutoff distance of 30 Å relative to C_{60} (ba1), for the C_{60}@DBAd supramolecular complex. (b) For $PC_{61}BM$@DBAd, an additional rotation $\mathbf{R}(\theta_X, \theta_Y, \theta_Z)$ was applied to $PC_{61}BM$ (ba1) with translation of DBAd (ba2) to 30 Å cutoff distance. (c) The interaction energy was computed at each configuration yielding the PES.

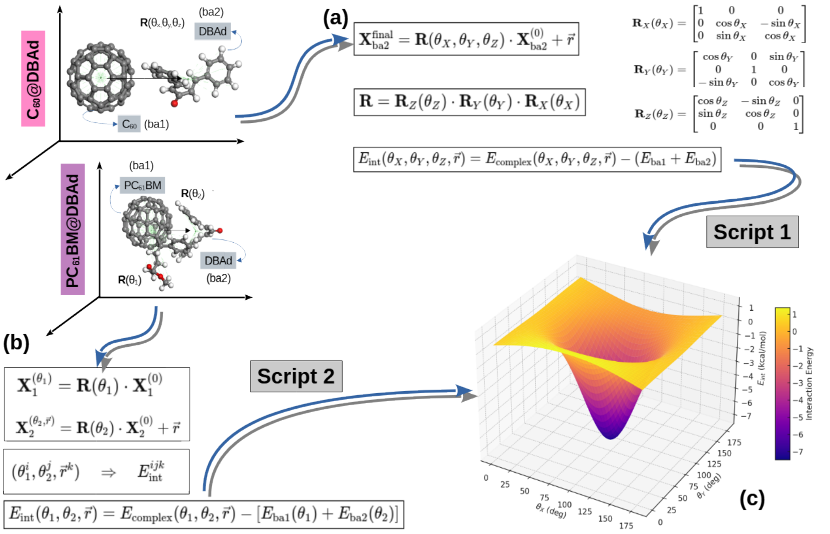

$$\mathbf{X}^{\mathrm{final}}_{\mathrm{ba2}} = \mathbf{R}(\theta_X, \theta_Y, \theta_Z) \cdot \mathbf{X}^{(0)}_{\mathrm{ba2}} + \vec{r}$$

$$\mathbf{R} = \mathbf{R}_Z(\theta_Z) \cdot \mathbf{R}_Y(\theta_Y) \cdot \mathbf{R}_X(\theta_X)$$

$$\mathbf{R}_X(\theta_X) = \begin{bmatrix} 1 & 0 & 0 \\ 0 & \cos\theta_X & -\sin\theta_X \\ 0 & \sin\theta_X & \cos\theta_X \end{bmatrix}$$

$$\mathbf{R}_Y(\theta_Y) = \begin{bmatrix} \cos\theta_Y & 0 & \sin\theta_Y \\ 0 & 1 & 0 \\ -\sin\theta_Y & 0 & \cos\theta_Y \end{bmatrix}$$

$$\mathbf{R}_Z(\theta_Z) = \begin{bmatrix} \cos\theta_Z & -\sin\theta_Z & 0 \\ \sin\theta_Z & \cos\theta_Z & 0 \\ 0 & 0 & 1 \end{bmatrix}$$

$$E_{\mathrm{int}}(\theta_X, \theta_Y, \theta_Z, \vec{r}) = E_{\mathrm{complex}}(\theta_X, \theta_Y, \theta_Z, \vec{r}) - (E_{\mathrm{ba1}} + E_{\mathrm{ba2}})$$

$$\mathbf{X}_1^{(\theta_1)} = \mathbf{R}(\theta_1) \cdot \mathbf{X}_1^{(0)}$$

$$\mathbf{X}_2^{(\theta_2, \vec{r})} = \mathbf{R}(\theta_2) \cdot \mathbf{X}_2^{(0)} + \vec{r}$$

$$(\theta_1^i, \theta_2^j, \vec{r}^k) \quad \Rightarrow \quad E_{\mathrm{int}}^{ijk}$$

$$E_{\mathrm{int}}(\theta_1, \theta_2, \vec{r}) = E_{\mathrm{complex}}(\theta_1, \theta_2, \vec{r}) - [E_{\mathrm{ba1}}(\theta_1) + E_{\mathrm{ba2}}(\theta_2)]$$

4.3 Statistical Thermodynamics of Dibenzalacetone-Fullerene Complexes

The thermodynamic properties of the lowest-energy supramolecular complexes C_{60}@DBAd and PC_{61}BM@DBAd, obtained by potential energy surface (PES) scanning with the Forcite module and the Universal Force Field (UFF) [58], were determined using Density Functional Theory (DFT) [54, 55, 198] within the ideal gas, rigid-rotor, and harmonic oscillator approximations. The DMol^3 module in the Biovia Materials Studio package [59] was employed to calculate macroscopic thermodynamic functions by analytical derivation from the molecular canonical partition function.

According to statistical thermodynamics, the molecular canonical partition function (Q) is factorized into translational (q_{trans}), rotational (q_{rot}), vibrational (q_{vib}), and electronic (q_{elec}) components under the Born-Oppenheimer approximation and the separability of the center-of-mass motion [273], as follows:

$$Q = q_{\text{trans}} \cdot q_{\text{rot}} \cdot q_{\text{vib}} \cdot q_{\text{elec}} \, . \tag{4.5}$$

The translational partition function, based on the free-particle approximation and valid for a monatomic or polyatomic molecule in the ideal gas phase, is expressed as:

$$q_{\text{trans}} = \left(\frac{2\pi m k_B T}{h^2} \right)^{\frac{3}{2}} V = \frac{V}{\Lambda^3} \, , \tag{4.6}$$

where m is the molecular mass, k_B is Boltzmann's constant, T is the absolute temperature, h is Planck's constant, V is the volume accessible to the center-of-mass motion of the molecule, and Λ is the thermal De Broglie wavelength, which quantifies the extent of the quantum mechanical wavefunction associated with the center-of-mass translational motion.

The classical approximation for the translational partition function is valid when Λ is much smaller than the system's characteristic length, ensuring that quantum effects are negligible. This condition is satisfied when the ratio Λ^3/V is sufficiently small, justifying the use of the Maxwell-Boltzmann distribution.

For a nonlinear molecule, the rotational partition function follows the rigid-rotor approximation:

$$q_{\text{rot}} = \frac{\pi^{1/2}}{\sigma} \left(\frac{T^3}{\theta_A \theta_B \theta_C} \right)^{\frac{1}{2}} \, , \tag{4.7}$$

where σ is the rotational symmetry number, and θ_A, θ_B, θ_C are the rotational temperatures associated with the moments of inertia I_A, I_B, and I_C, respectively. These rotational temperatures are defined as:

$$\theta_i = \frac{h^2}{8\pi^2 I_i k_B} , \tag{4.8}$$

for $i = A, B, C$. The rotational temperature θ_i describes the energy spacing between adjacent rotational energy levels, inversely proportional to the moment of inertia. The moments of inertia I_A, I_B, and I_C refer to the principal axes of rotation of the molecule, obtained from the diagonalization of the inertia tensor. For a linear molecule, the rotational partition function simplifies to $\frac{T}{\sigma\theta_r}$ or $\frac{k_B T}{\sigma h B}$, where $\theta_r = hB/k_B$ is the rotational temperature and B is the rotational constant defined by $\frac{h}{8\pi^2 Ic}$, with I being the moment of inertia and c the speed of light.

Within the harmonic oscillator approximation, the vibrational partition function is expressed as:

$$q_{\text{vib}} = \prod_{i=1}^{3N-6} \frac{e^{-\frac{\theta_i}{2T}}}{1 - e^{-\frac{\theta_i}{T}}} , \tag{4.9}$$

where N is the number of atoms in the molecule and $\theta_i = h\nu_i/k_B$ is the characteristic vibrational temperature corresponding to the i-th normal mode with frequency ν_i. The product operator considers $3N - 6$ vibrational degrees of freedom for a nonlinear molecule (or $3N - 5$ for a linear molecule) and incorporates the contribution of each quantized vibrational mode, treated as an independent quantum harmonic oscillator. Additionally, the denominator describes the thermal population of excited vibrational states according to the Boltzmann distribution, while the exponential factor in the numerator incorporates the zero-point energy (ZPE) contribution, which represents the lowest accessible energy level and persists at absolute zero temperature.

The electronic partition function is given by:

$$q_{\text{elec}} = g_0 + \sum_j g_j e^{-E_j/k_B T} , \tag{4.10}$$

where g_0 is the degeneracy of the electronic ground state, and g_j and E_j are the degeneracy and excitation energy (relative to the ground state) of the j-th excited state, respectively. At typical thermal energies ($k_B T$ is approximately 0.026 eV at 298 K), electronic excitation energies are usually much larger, causing the Boltzmann factors for excited states extremely small. Therefore, q_{elec} can be approximated by the ground-state degeneracy.

From the molecular canonical partition function (Q), the fundamental thermodynamic properties as internal energy (U), enthalpy (H), entropy (S), Gibbs free energy (G), and heat capacity at constant pressure (C_p) can be calculated according to classical statistical thermodynamics using the following expressions:

$$U = E_{\text{ZPE}}{}^{1} + k_B T^2 \left(\frac{\partial \ln Q}{\partial T} \right)_V \;, \tag{4.11}$$

$$H = U + PV \;, \tag{4.12}$$

$$S = k_B \left[\ln Q + T \left(\frac{\partial \ln Q}{\partial T} \right)_V \right] \;, \tag{4.13}$$

$$G = H - TS \;, \tag{4.14}$$

$$C_p = \left(\frac{\partial H}{\partial T} \right)_p \;. \tag{4.15}$$

Electronic structure calculations and thermodynamic functions were performed at the same theoretical level as the ground-state geometry optimizations. Density Functional Theory (DFT) was applied using the Becke-Lee-Yang-Parr (BLYP) exchange-correlation functional [56, 274], incorporating Grimme's empirical dispersion correction (DFT-D) [57] to account for long-range van der Waals interactions.

The self-consistent field (SCF) convergence criterion was set to 10^{-6} Ha to ensure numerical accuracy in energy. Harmonic vibrational frequencies were computed from the analytical Hessian matrix, enabling the evaluation of temperature-dependent thermodynamic properties [264, 275]. All thermodynamic functions were computed over a temperature range of $25 - 1000$ K in increments of 25 K. An all-electron numerical basis set (DNP+) was employed to accurately represent the electronic wavefunction, without the use of pseudopotentials.

---

[1] Although temperature-independent, E_{ZPE} contributes additively to U and H and is essential for obtaining physically significant thermodynamic values [265].

The Hessian matrix (H_{ij}) is defined as the matrix of second derivatives of the potential energy with respect to the nuclear Cartesian coordinates:

$$H_{ij} = \frac{\partial^2 E}{\partial x_i \partial x_j} \ . \tag{4.16}$$

Diagonalization of the mass-weighted Hessian yields the eigenvalues λ_i associated with the vibrational normal modes. These eigenvalues are related to the fundamental vibrational frequencies ν_i according to:

$$\nu_i = \frac{1}{2\pi}\sqrt{\frac{\lambda_i}{\mu_i}} \ , \tag{4.17}$$

where μ_i indicates the reduced mass associated with the i-th mode. The vibrational frequencies ν_i are then used to compute the characteristic vibrational temperatures:

$$\theta_i = \frac{h\nu_i}{k_B} \ , \tag{4.18}$$

which enter directly into the expression for the vibrational partition function under the harmonic oscillator approximation (see Equation 4.9). Therefore, the Hessian matrix provides the fundamental vibrational parameters required to evaluate q_{vib}, essential for calculating thermodynamic quantities that depend on vibrational motion, such as the internal energy (U), enthalpy (H), entropy (S), and heat capacity at constant pressure (C_p).

4.3.1 Samples Preparation and Spectroscopic Measurements

The molecular structure of ethoxy-dibenzalacetone derivative (DBAd) was confirmed by nuclear magnetic resonance (NMR) spectroscopy. The ^{1}H and ^{13}C NMR spectra, presented in Figures 26 and 27 of the Appendix 6, exhibits the expected chemical shifts for the compound: a singlet at 6.89 ppm (2H, $-CH{=}CH-$), multiple aromatic signals between 6.89 and 7.69 ppm (8H, Ar-H), a quartet at 4.05 ppm (4H, $-CH_2-$), and a triplet at 1.42 ppm (6H, $-CH_3$). The ^{13}C NMR spectrum exhibits resonance peaks at 188.9 ppm (C=O), 161.1–114.8 ppm (aromatic and vinyl carbons), and 63.7 and 14.9 ppm (ethoxy group). These signals are consistent with the expected DBAd molecular structure. The fullerene compounds (C_{60} and $PC_{61}BM$) were purchased from Sigma-Aldrich with analytical grade purity.

Fullerene compounds C_{60} and $PC_{61}BM$ are soluble in nonpolar solvents [276–279]. DBAd is soluble in polar and nonpolar solvents, such as ethanol and toluene. However, due to the absence of fluorescence signal observed for DBAd in toluene, a binary solvent mixture was used, consisting of 2000 µL of ethanol (EtOH, C_2H_6O) and 400 µL of toluene (TOL, $C_6H_5CH_3$). This combination optimized the solubility of all compounds, minimizing aggregation effects that could compromise spectroscopic measurements [280, 281]. Eventually, solvent mixtures are necessary to optimize the thermodynamic parameters of the solutions [282–284].

Initially, stock solutions of C_{60} and $PC_{61}BM$ at a concentration of 7.0×10^{-4} mol · L^{-1} were prepared in toluene, while DBAd solution was prepared at 1.68×10^{-5} mol · L^{-1} in ethanol. For the experiments, a fixed volume of 2000 µL of DBAd solution was used in each dilution standard, ensuring a constant concentration of 1.4×10^{-5} mol · L^{-1} of the DBAd. Incremental additions of C_{60} or $PC_{61}BM$ stock solutions yielded final concentrations ranging from a low concentration (LC) of 1.16×10^{-5} to a high concentration (HC) of 10.40×10^{-5} mol · L^{-1}; see Table 13 in the Appendix 6. All solutions were homogenized for 5 min in an ultrasonic bath.

UV-Vis absorption spectra for the LC to HC concentration range were recorded using a Shimadzu UV-Vis–1900i spectrophotometer at a room temperature (25 °C) and quartz cuvettes with an optical pathlength of 10 mm over a wavelength range of 280 to 480 nm. Steady-state fluorescence spectra were acquired using a Horiba Fluorolog spectrofluorometer equipped with a xenon lamp, operating in fast acquisition mode with a 0.2 nm sampling interval and 5/5 nm slit widths. DBAd was excited at maximum absorption wavelength (365 nm), and emission spectra were recorded from 300 to 700 nm.

Time-resolved fluorescence decays were measured using the time-correlated single-photon counting technique with a FluoTime 200 (PicoQuant). Excitation at 401 nm was provided by a pulsed diode laser with a repetition rate of 40 MHz. Lifetimes were obtained by fitting the fluorescence decay curves (with convoluted IRF-instrument response function) and the sum of exponentials using FluoFit® software and the plots of weighted residuals and reduced chi-square (χ^2) were used to accurately determine the quality of the fits during the analysis procedure.

Quenching effects were evaluated using Stern-Volmer plots to determine the extinction mechanism (dynamic or static) [285], based on the Stern-Volmer [286] equation:

$$\frac{I_0}{I} = 1 + K[Q] \tag{4.19}$$

where I_0 and I represent the fluorescence intensities of the fluorophore in the absence and presence of the quencher, respectively, K is the quenching constant, and $[Q]$ is the quencher concentration. For dynamic (collisional) quenching, K corresponds to the Stern-Volmer quenching constant (K_{SV}), defined as $K_{\mathrm{SV}} = k_{\mathrm{q}} \cdot \tau_0$, where k_{q} is the bimolecular quenching rate constant and τ_0 is the excited-state lifetime of the fluorophore in the absence of the quencher.

In this scenario, a decrease in excited-state lifetime is expected, as quenching introduces an additional depopulation pathway for the excited state. Since collisional quenching affects fluorescence intensity and lifetime equally, the ratio $\frac{I_0}{I}$ in Eq. (4.19) can replaced by $\frac{\tau_0}{\tau}$.

In contrast, static quenching arises from the formation of a nonfluorescent ground-state complex between the fluorophore and the quencher. In this case, quenching constant represents the association constant (K_{s}), and the lifetime of the uncomplexed fluorophore remains unchanged, which means that $\frac{\tau_0}{\tau} = 1$ [131, 161].

The charge transfer free energy ($\Delta\mathrm{G}_{\mathrm{charge}}$) was calculated using the Rehm-Weller [287] equation:

$$\Delta G_{\mathrm{charge}} = E_{\mathrm{ox}} - E_{\mathrm{red}} - E_{\mathrm{exc}} - \frac{e^2}{4\pi\epsilon_0\epsilon_r r} , \tag{4.20}$$

where E_{ox} is the oxidation potential of the donor (in eV), E_{red} is the reduction potential of the acceptor (in eV), and E_{exc} is the excitation energy of the singlet state of the donor (in eV); e is the elementary charge (1.602×10^{-19} C), ϵ_0 is the vacuum permittivity ($8.854 \times 10^{-12}\ \mathrm{F \cdot m^{-1}}$), ϵ_r is the relative dielectric constant of the binary solvents (dimensionless), and r is the average distance between the donor and the acceptor obtained by potential energy surface (PES) scanning.

The dielectric constants of pure ethanol and toluene under standard conditions were obtained from standard reference data [288]. The relative dielectric constant (ϵ_r) of the binary solvent mixture was calculated using a volume-fraction-weighted average as follows:

$$\epsilon_r = \phi_{\mathrm{EtOH}} \cdot \epsilon_{\mathrm{EtOH}} + \phi_{\mathrm{TOL}} \cdot \epsilon_{\mathrm{TOL}} , \tag{4.21}$$

where ϕ_{EtOH} and ϕ_{TOL} are the volume fractions of ethanol and toluene, respectively, and ϵ_{EtOH} and ϵ_{TOL} are their standard dielectric constants. For the experimental mixture used (2000 µL of ethanol and 400 µL of toluene), the volume fractions were ϕ_{EtOH} of 0.833 and ϕ_{TOL} of 0.167. This approach assumes ideal mixing behavior and is commonly applied to approximate the dielectric environment in binary solvents [234].

The Förster resonance energy transfer (FRET) mechanism was investigated to determine the non-radiative energy transfer rate constants (k_{FRET}) between the donor and acceptor molecules. The k_{FRET} was calculated using the Förster [128, 289] equation:

$$k_{\text{FRET}} = \frac{1}{\tau_D} \left(\frac{R_0}{r} \right)^6 , \tag{4.22}$$

where τ_D is the excited-state lifetime of the donor in the absence of the acceptor, R_0 is the Förster radius (the donor-acceptor separation distance at which the transfer efficiency is 50%), and r is the center-to-center distance between the donor and acceptor, calculated here by potential energy surface (PES) scanning.

The Förster radius (R_0, in Å) was determined using the following equation:

$$R_0 = 0.211 \left(\frac{\kappa^2 \cdot \Phi_D \cdot J(\lambda)}{n^4} \right)^{1/6} , \tag{4.23}$$

where κ^2 is the dipole orientation factor (ranging from 0 to 4, with an isotropic value of $2/3$ for freely rotating dipoles [131, 290]), Φ_D is the fluorescence quantum yield of the donor in ethanol at the absence of the acceptor, N_A is the Avogadro constant (6.022×10^{23} mol^{-1}), n is the refractive index for the ethanol-toluene mixture, and $J(\lambda)$ is the spectral overlap integral between the acceptor absorption spectrum and the area-normalized emission spectrum of the donor, defined as:

$$J(\lambda) \equiv \int_0^\infty F_D(\lambda) \varepsilon_A(\lambda) \lambda^4 d\lambda , \tag{4.24}$$

where $F_D(\lambda)$ is the normalized fluorescence emission spectrum of the donor, $\varepsilon_A(\lambda)$ is the molar extinction coefficient of the acceptor (in L · mol^{-1}· cm^{-1}), and λ is the wavelength (in nm) corresponding to the spectral overlap region between the donor emission and the acceptor absorption.

The refractive index of pure ethanol and toluene under standard conditions was obtained from standard references [288, 291, 292]. The relative refractive index (n) of the binary solvent mixture, required in Eq. (4.23), was estimated by a volume-fraction-weighted average:

$$n = \phi_{\text{EtOH}} \cdot n_{\text{EtOH}} + \phi_{\text{TOL}} \cdot n_{\text{TOL}} , \tag{4.25}$$

where ϕ_{EtOH} and ϕ_{TOL} are the volume fractions of ethanol and toluene, respectively, and n_{EtOH} and n_{TOL} are their standard refractive indices. For the experimental mixture used (2000 µL of ethanol and 400 µL of toluene), the resulting volume fractions were ϕ_{EtOH} of 0.833 and ϕ_{TOL} of 0.167. This mixing rule is adopted to approximate the optical properties of binary solvents, where n directly affects the Förster radius [94].

The FRET efficiency is quantitatively defined as:

$$\eta_{\mathrm{FRET}} = \frac{R_0^6}{R_0^6 + r^6}\,, \tag{4.26}$$

where η_{FRET} represents the fraction of energy transferred from the donor to the acceptor through dipole-dipole interactions [293]. Eq. (4.26) reveals the strong dependence of FRET efficiency with distance: as the donor-acceptor separation (r) decreases below the Förster radius (R_0), the energy transfer efficiency rapidly approaches unity ($\eta_{\mathrm{FRET}} \rightarrow 1.0$). Conversely, the efficiency diminishes significantly for distances greater than R_0, asymptotically approaching zero [131].

4.4 Results and Discussion

4.4.1 Structural and Electronic Properties

The bond lengths and angles of the ethoxy-dibenzalacetone derivative (DBAd) and fullerene compounds (C_{60} and $PC_{61}BM$) calculated using GGA-DFT/BLYP-D2/DNP+ methodology under non-periodic boundary conditions are presented in Table 17 in Appendix 6 and organized according to the atomic labeling scheme shown in Figure 16. Geometry optimizations confirmed that all structures correspond to true minima on the potential energy surface, as indicated by the absence of imaginary frequencies in the harmonic vibrational analysis.

Figure 17 shows the calculated Raman-active vibrational modes for the optimized structures of DBAd, C_{60}, and $PC_{61}BM$. In the fingerprint region, intense Raman bands at 1571 and 1626 cm^{-1} for DBAd are assigned to C=O stretching vibrations coupled with C=C stretching modes of the enone fragment. The delocalization induced by π-conjugation results in shifts to lower wavenumbers compared to saturated carbonyls, as also reported by Vasconcelos et al. [50]. The 650 – 850 cm^{-1} region corresponds to torsional modes and out-of-plane deformations of the aromatic (C=C and C–C) and ethoxy bonds, typical of planar π-conjugated compounds. C–H stretching modes of sp^3 and sp^2 hybridized carbons are observed between 2850 – 3150 cm^{-1}.

Figure 16 – Optimized structures of the ethoxy-dibenzalacetone derivative (DBAd) and fullerene compounds (C_{60} and $PC_{61}BM$) obtained by GGA/DFT/BLYP-D2/DNP+ level theory. The structures are represented in a ball-and-stick format with atom labels. The carbon atoms of C_{60} and $PC_{61}BM$ are depicted in different colors (C_{60} in pink and $PC_{61}BM$ in purple), while non-carbon atoms are colored according to their atom types (oxygen in red and hydrogen in light gray). The figure was created using PyMOL [210] (PyMOL Molecular Graphics System, available at <http://www.pymol.org>).

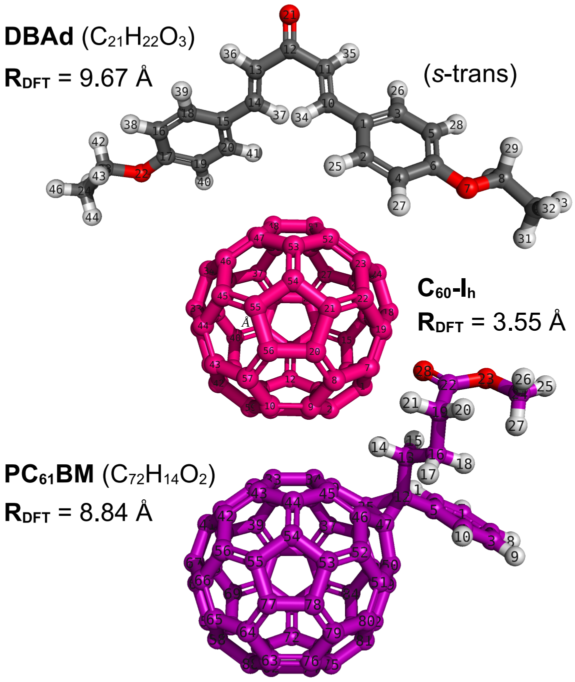

Oliveira et al. [49] reported the experimental Raman spectrum of trihydrated DBAd, in which the most intense bands appeared at 1569, 1584, and 1603 cm^{-1}, corresponding to conjugated C=O and C=C stretching vibrations. These values are in good agreement with the theoretical Raman bands calculated herein at 1571 and 1626 cm^{-1}, which also reflect strong π-conjugation effects in the enone fragment. Additional bands between 1272 – 1351 cm^{-1} in Oliveira's spectrum correspond to mixed in-plane bending modes δ(HCC) and ν(C–C) stretching modes in the aromatic rings and enone fragment.

Below 1200 cm^{-1}, the spectrum exhibits vibrational modes associated with torsional and out-of-plane deformations, including τ(HCCC) and γ(O–C=C), experimentally observed between 1098 – 878 cm^{-1}. High-frequency C–H stretching modes from vinyl (sp^2) and ethoxy (sp^3) groups appear at 2977 – 2862 cm^{-1}, although lower relative intensities. Table 5 summarizes the main Raman-active modes calculated herein by GGA/DFT/BLYP-D2/DNP+ for comparison.

Figure 17 – Theoretical Raman activity spectra for the optimized geometries of ethoxy-dibenzalacetone (DBAd), C_{60}, and $PC_{61}BM$, calculated at the GGA/DFT/BLYP-D2/DNP+ level theory. The Raman activities (in $Å^4 \cdot amu^{-1}$) versus wavenumber (in cm^{-1}) were plotted with 370 – 3630 cm^{-1} interval. The discrete spectral lines were convoluted using a Lorentzian function with a full width at half maximum (FWHM) of 30 cm^{-1}. Zoom factors (2× and 3×) were applied to improve visual amplification without modification in relative intensities.

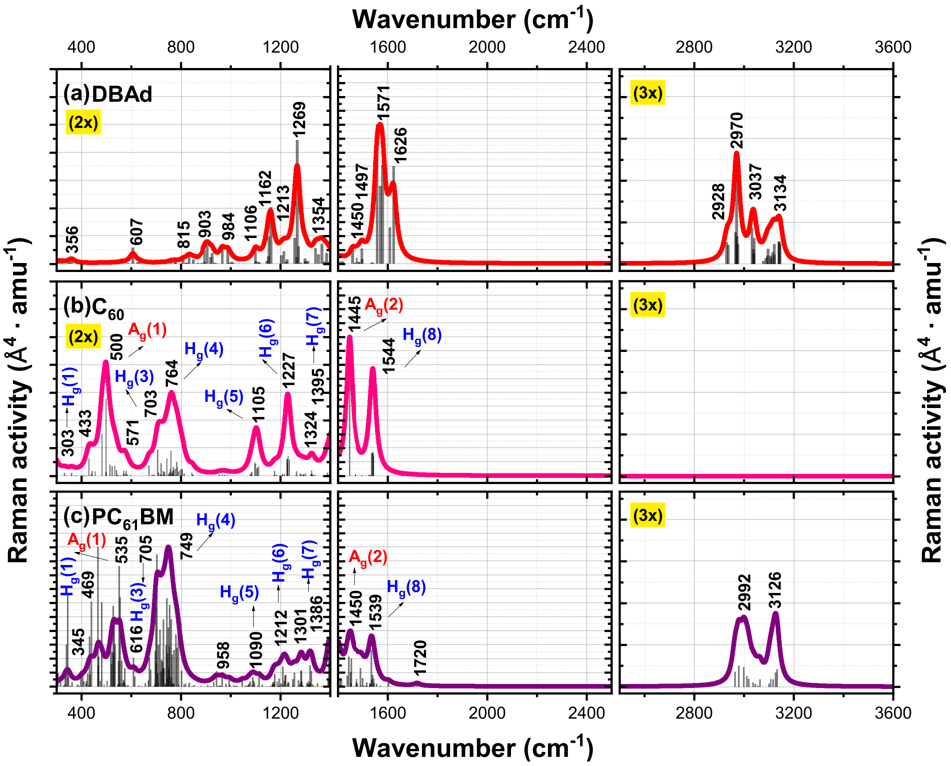

The experimental Raman spectrum of C_{60}, as reported in previous studies [294–296], is characterized by a limited number of intense and well-defined Raman-active modes, owing to the high icosahedral symmetry (I_h) of the C_{60}. Among the ten Raman-active modes, two possess A_g symmetry and eight belong to the H_g irreducible representation. The most prominent band is the breathing mode $A_g(2)$, located at approximately 1469 cm^{-1}, which is consistently reproduced in the calculated spectrum herein at roughly 1445 cm^{-1}.

In addition to the $A_g(2)$ breathing mode, the $H_g(8)$ tangential mode appears prominently in the experimental spectrum near 1578 cm^{-1} [295, 297], and is theoretically reproduced herein at 1535.7 cm^{-1}, showing good agreement within 42 cm^{-1} when considering the harmonic approximation. Similarly, the low-frequency $H_g(1)$ radial deformation mode is observed experimentally at approximately 272 cm^{-1} and is calculated here at 268.2 cm^{-1}.

The $A_g(1)$ mode associated with the symmetric pentagonal pinch motion is typically reported near 496 – 497 cm^{-1} [298]. The calculations herein yield a value of 497.7 cm^{-1}, corresponding to the experimental data with good precision [294, 297]. The $H_g(4)$ mode is calculated at 757.7 cm^{-1}, consistent with the experimental band at 759 cm^{-1}. The high-wavenumber $H_g(7)$ mode also shows satisfactory agreement, appearing at approximately 1395 cm^{-1}. These results confirm the capability of the DFT/BLYP-D2/DNP+ level of theory in reproduce high- and low-wavenumber vibrations of the non-degenerate (A_g) and degenerate (H_g) modes of the C_{60}-fullerene deformations; see Table 5.

Table 5 – Theoretical main Raman activity modes for the ethoxy-dibenzalacetone derivative (DBAd) and fullerene compounds (C_{60} and $PC_{61}BM$) obtained using the GGA-DFT/BLYP-D2/DNP+ methodology, determined analytically from the derivatives of the polarizability tensor with respect to nuclear displacements.

	DBAd		**C_{60}**		**$PC_{61}BM$**	
	$^a\omega_{DBAd}$	^{b}Raman act.	$^a\omega_{C_{60}}$	^{b}Raman act.	$^a\omega_{PC_{61}BM}$	^{b}Raman act.
C−C	–	–	268.2 ($H_g(1)$)	24.99	252.7 ($H_g(1)$)	29.14
C−C	–	–	497.7 ($A_g(1)$)	96.57	465.1 ($A_g(1)$)	403.48
C−C	–	–	757.7 ($H_g(4)$)	31.00	741.7 ($H_g(4)$)	468.24
C−O	1161.6	610.28	–	–	1166.1	10.64
C−C	1266.0	1331.51	1096.5 ($H_g(5)$)	16.43	1092.0 ($H_g(5)$)	46.84
C−C	–	–	1226.3 ($H_g(6)$)	21.35	1220.3 ($H_g(6)$)	112.14
C=C	1558.2	3005.93	1444.3 ($A_g(2)$)	349.28	1441.2 ($A_g(2)$)	364.19
C=O	1624.4	2096.90	–	–	1717.9	50.91
C−C	–	–	1535.7 ($H_g(8)$)	56.85	1540.5 ($H_g(8)$)	151.54
C−H sp^3	2970.3	782.97	–	–	2979.3	245.09
C−H sp^2	3139.5	156.93	–	–	3132.1	224.57

$^a\omega$: theoretical harmonic vibrational wavenumber (in cm^{-1}); ^{b}Raman act.: Raman activity expressed in Å^4· amu^{-1} (where amu indicates atomic mass unit) quantifies the capacity of a vibrational mode to induce molecular polarizability. The vibrational modes are classified according to irreducible representations in group theory notation, as follows: A_g for non-degenerate symmetric vibrational modes ($A_g(1)$ for radial breathing modes and $A_g(2)$ for pentagonal pinch), while H_g indicates degenerate modes, typically tangential and radial motions. The subscript g (gerade or even) denotes eigenvector symmetry under inversion operation [297]. The DBAd, C_{60}, and $PC_{61}BM$ molecules exhibit angular geometries with 132, 174, and 258 normal vibrational modes, respectively. These molecules are classified according to their crystallographic space groups: monoclinic $P2_1/c$ (No. 14) for DBAd, face-centered cubic $Fm\bar{3}m$ (No. 225) for C_{60}, and monoclinic $P2_1/n$ (No. 14) for $PC_{61}BM$, following the Hermann-Mauguin notation. The wavenumbers calculated by GGA-DFT/BLYP-D2/DNP+ methodology are in agreement with other works reported for Raman modes [49, 295, 297, 299].

The Raman spectrum of $PC_{61}BM$ exhibits greater complexity than C_{60} due to the reduction in molecular symmetry induced by functionalization at the [6,6]-bond with a phenyl-butyric acid methyl ester. This functionalization lowers the high C_{60}-I_h symmetry, eliminating degeneracies and activating previously silent or infrared-only active modes [297]. The experimental Raman spectrum of $PC_{61}BM$, as reported by Falke et al. [299], shows bands at approximately 531, 618, 741, 1092, and 1314 cm^{-1}, attributed to out-of-plane ring deformations and in-plane C – C stretching of the C_{60}-fullerene cage and side chain.

Figure 17 (c) shows intense bands at 535, 749, 1450, 1539, and 1720 cm^{-1}, consistent with assignments for C_{60}-fullerene cage [299]. Additionally, the C = O and C = C stretching vibrations at approximately 1720 and 1539 cm^{-1} correspond to the phenyl-butyric acid methyl ester. In the high-wavenumber region, modes at 2979.3 and 3132.1 cm^{-1} are consistent with aliphatic and aromatic C – H stretching vibrations, confirming the presence of the alkyl ester and phenyl. These values align with the literature, although with broader signatures typically attributed to vibrational mode coupling or structural disorder effects [297].

After geometry optimization of the DBAd, C_{60}, and $PC_{61}BM$, the Kohn-Sham orbitals were obtained by numerically solving the self-consistent field (SCF) equations using a real-space atom-centered basis set to evaluate the highest occupied molecular orbital (HOMO) and the lowest unoccupied molecular orbital (LUMO), which are fundamental descriptors of chemical reactivity and charge transfer propensity [55, 198, 300, 301]. Figure 18 shows the isosurfaces of HOMO and LUMO frontier orbitals, with yellow and blue regions denoting the positive and negative phases of the wavefunction, respectively [208, 302].

The isosurfaces reveal regions of high electron density, indicative of sites favorable for covalent and non-covalent interactions [57], which are critical to the donor-acceptor charge transfer process. In DBAd, electron delocalization extends along the *s-trans* conjugated molecular plane, whereas in C_{60} and $PC_{61}BM$, electronic density concentrates on the icosahedral surface. Additionally, $PC_{61}BM$ exhibits orbital overlap between the phenyl group and the fullerene cage, suggesting favorable π-π stacking interactions. These observations are consistent with previous studies [214, 303], including D'Avino et al. [304], who reported that functionalization in $PC_{61}BM$ induces electronic disorder that modulates the spatial distribution of HOMO and LUMO orbitals.

Table 6 shows the values of the HOMO and LUMO coefficients for DBAd and fullerene compounds (C_{60} and $PC_{61}BM$). The HOMO energy values indicate that DBAd predominantly behaves as an electron donor, with a value of −4.95 eV, which is higher than those of the

Figure 18 – Isosurfaces of the highest occupied molecular orbital (HOMO) and the lowest unoccupied molecular orbital (LUMO) for the ethoxy-dibenzalacetone derivative (DBAd) and fullerene compounds (C_{60} and $PC_{61}BM$), obtained using an isovalue of ±0.015. Yellow and blue surfaces denote the positive and negative phases of the wavefunction, respectively. The isosurfaces were generated using Materials Studio [59] (BIOVIA, Dassault Systèmes, available at <https://www.3ds.com/products-services/biovia/products/materials-studio/>).

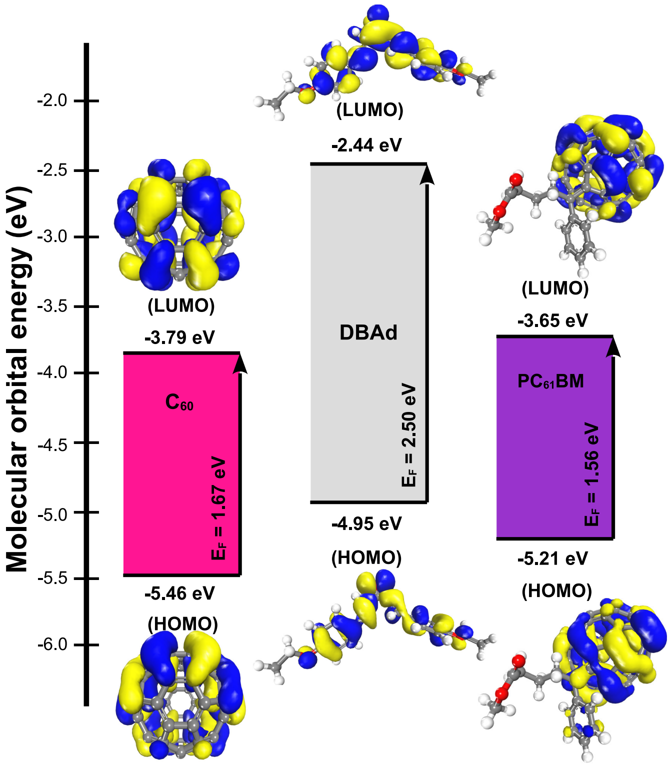

fullerene compounds C_{60} and $PC_{61}BM$ (−5.46 eV and −5.21 eV, respectively). This difference in HOMO levels suggests that DBAd has a greater propensity to donate electrons compared to the fullerenes [305, 306]. Furthermore, the LUMO energy of DBAd is significantly higher than those of C_{60} and $PC_{61}BM$, reflecting a higher energy barrier for electron acceptance [306]. These observations reinforce the role of fullerenes, with their lower LUMO values (−3.79 eV for C_{60} and −3.65 eV for $PC_{61}BM$), as efficient electron acceptors [304].

Sworakowski [307] experimentally determined the HOMO and LUMO levels of C_{60} at −6.37 eV and −3.99 eV, respectively, based on ultraviolet photoelectron spectroscopy (UPS) and inverse photoelectron spectroscopy (IPES). Shafiq et al. [308] reported that the electronic structure of $PC_{61}BM$ reveals HOMO and LUMO energy levels at −6.10 eV and −3.70 eV, respectively, in good agreement herein (see Table 6).

The energy difference ($\Delta E_{(\mathrm{HOMO_{DBAd}} \rightarrow \mathrm{LUMO_{C_{60}}})}$) between the HOMO of DBAd and the LUMO of C_{60} indicates a more thermodynamically favorable charge transfer of -1.16 eV compared to the $PC_{61}BM$, which has a $\Delta E_{(\mathrm{HOMO_{DBAd}} \rightarrow \mathrm{LUMO_{PC_{61}BM}})}$ of -1.30 eV [120]. This energetic difference is particularly relevant in molecular conformations where strong interactions occur between the icosahedral surface of C_{60} and the π-conjugated molecular plane of DBAd, enhancing electronic coupling and promoting efficient charge separation [303, 309].

The HOMO and LUMO orbital energies, as well as the theoretical fundamental gap (E_{fund}), are fundamental parameters in understanding charge transfer processes. E_{fund} is defined as the energy difference between the ionization potential (IP) and the electron affinity (EA) and can be approximated by the negative of the HOMO and LUMO energies, respectively, following Koopman's [89] theorem. These values are summarized in Table 6. Another critical parameter is the optical gap (E_{OPT}), which is typically smaller than E_{fund}. While E_{fund} describes ionized states, E_{OPT} is associated with electron-hole bound states, such as excitons [90, 310]. The DFT/BLYP-D2/DNP+ methodology employed herein describes only ground-state properties.

Table 6 – The highest occupied molecular orbital (HOMO), lowest unoccupied molecular orbital (LUMO), ionization potential (IP), electron affinity (EA), fundamental energy gap (E_{fund}), and experimental optical gap ($E^{\mathrm{exp}}_{\mathrm{OPT}}$) values for the ethoxy-dibenzalacetone derivative (DBAd) and the fullerene compounds (C_{60} and $PC_{61}BM$). These values provide information about the electronic structure, charge transfer properties and light absorption characteristics of the studied molecules.

	HOMO (eV)	**LUMO** (eV)	^{a}**IP (eV)**	^{b}**EA** (eV)	$^{c}\mathbf{E_{fund}}$ (eV)	$^{d}\mathbf{E^{exp}_{OPT}}$ (eV)
DBAd	-4.95	-2.44	4.95	2.44	2.50	2.9
C_{60}	-5.46	-3.79	5.46	3.79	1.67	3.5
$PC_{61}BM$	-5.21	-3.65	5.21	3.65	1.56	3.4

^{a}Ionization potential ($IP = -E_{\mathrm{HOMO}}$) is the energy required to remove an electron from the HOMO; ^{b}Electron affinity ($EA = -E_{\mathrm{LUMO}}$) is the energy released when an electron is added to the LUMO; $^{c}E_{\mathrm{fund}}$ is the fundamental gap ($E_F = IP - EA$); ^{d}Experimental optical gap ($E^{\mathrm{exp}}_{\mathrm{OPT}}$) determined using the Tauc plot method [96], which involves plotting (absorption coefficient vs. photon energy)$^{\gamma}$ in $(\mathrm{eV} \cdot \mathrm{cm}^{-1})^{\gamma}$ against photon energy (in eV) to extrapolate the linear portion to the energy axis; see Figure 29 in the Appendix 6. Adopted $\gamma = 2$ considering indirect allowed transitions. Data acquired in binary ethanol-toluene mixture and expressed with one decimal place due to the resolution of the spectrophotometer.

The difference in energy levels plays a critical role in charge carrier separation at the donor-acceptor interface and enhancing the open-circuit voltage (V_{OC}) in organic photovoltaic devices [311–313]. Although the fundamental band gap (E_{fund}) of DBAd is larger than those of the fullerenes, suggesting lower chemical reactivity, its ionization potential (IP) is lower than that of the fullerenes, implying that DBAd requires less energy to donate an electron.

Furthermore, the significantly higher electron affinity (EA) of the fullerene compounds underscores their strong ability to accept electrons, which is a critical factor for their effectiveness in organic optoelectronic devices [314]. The global chemical reactivity descriptors, ionization potential (IP), electron affinity (EA), and fundamental gap (E_{fund}) were estimated using Koopman's [89] theorem, with the results summarized in Table 6.

4.4.2 C_{60}@DBAd and $PC_{61}BM$@DBAd Intermolecular Interactions

Non-covalent interactions, including π-π stacking, van der Waals interactions (e.g., London dispersive forces), hydrogen bonding, and dipole-dipole interactions, play a crucial role in stabilizing supramolecular assemblies in both ground and excited states [315, 316]. In this study, non-bonded interactions were assessed at the molecular mechanics level using the Forcite module, with the Universal Force Field (UFF) [58] employed to parameterize equilibrium geometries and interaction potentials, based on ground-state structures previously optimized at the DFT/BLYP-D2/DNP+ level of theory.

Figure 19 presents the potential energy curves (ϵ in $\mathrm{kcal \cdot mol^{-1}}$), centroid-to-centroid distances (r in nm), and minimum-energy conformations mapped along each Cartesian coordinate (Figures 19 (a)–(f)). The interaction profiles were fitted using Lennard-Jones and Mie potentials to model the balance between attractive and repulsive contributions to the intermolecular potential. Following a similar procedure, Frazão et al. [317] and Hadad et al. [318] demonstrated the relevance of van der Waals and π-π interactions in stabilizing supramolecular assemblies, particularly in biologically active molecules and fullerene-based nanocarriers for drug delivery.

In the C_{60}@DBAd complex, the interaction energy along the x-axis is relatively weak, with a calculated value of $-6.81\ \mathrm{kcal \cdot mol^{-1}}$ at a centroid-to-centroid distance of 6.43 Å. This weaker interaction suggests limited π-π stacking and minimal overlap of van der Waals radii at this separation [57]; see the minimum-energy conformation mapped along the Cartesian x-coordinate in Figure 19 (a). The x-axis profile is characterized by longer interaction ranges, highlighting the predominance of weak but long-range attractive forces.

Figure 19 – Potential energy surface (PES) mapping between ethoxy-dibenzalacetone derivative (DBAd) and fullerene compounds (C_{60} and $PC_{61}BM$) using the Forcite module with Universal Force Field (UFF) [58] parametrization. The analytically calculated interaction energies were fitted using Lennard-Jones (LJ) and Mie potentials to describe the intermolecular potential profiles governing these supramolecular interactions. The plots illustrate the variation of interaction energy (in $\mathrm{kcal \cdot mol^{-1}}$) as a function of the centroid-to-centroid distance (r, in nm) between DBAd and C_{60} or $PC_{61}BM$. Additionally, the conformations corresponding to the minimum potential energy along each Cartesian axis are presented.

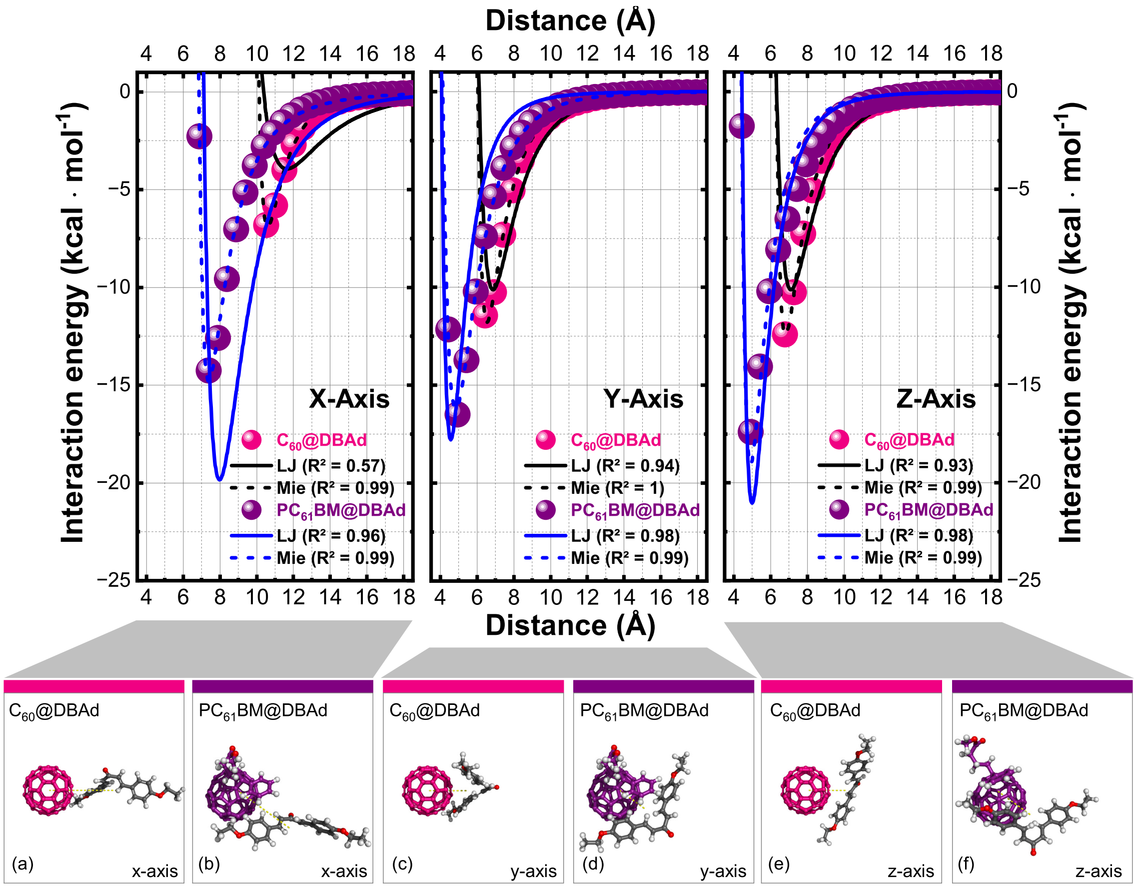

Conversely, the $PC_{61}BM$@DBAd complex exhibits a significantly stronger interaction along the x-axis, with a potential energy of $-14.25\ \mathrm{kcal \cdot mol^{-1}}$ occurring at a centroid-to-centroid distance of 7.39 Å. This enhanced binding affinity is attributed to the presence of the butyric acid methyl ester in $PC_{61}BM$, which reduces the icosahedral symmetry of the C_{60}-fullerene cage and introduces local asymmetries in the charge distribution [304, 319]. This functionalization also leads to a redistribution of the centroid of $PC_{61}BM$ and stronger non-covalent interactions with the conjugated molecular plane of DBAd.

The interactions along the y-axis exhibit energetically more favorable structural conformations. For the C_{60}@DBAd, an interaction energy of $-11.43\ \text{kcal} \cdot \text{mol}^{-1}$ is observed at a centroid-to-centroid distance of 6.43 Å. These values indicate favorable molecular docking, where the reduced intermolecular distance allows for more effective π-π interactions between the conjugated DBAd and the icosahedral surface of C_{60}. Similarly, the $PC_{61}BM$@DBAd complex exhibits an even stronger interaction, with a minimum energy of $-16.48\ \text{kcal} \cdot \text{mol}^{-1}$ at a centroid distance of 5.76 Å. This shorter centroid distance indicates enhanced spatial overlap and van der Waals contact between the DBAd and functionalized surface of $PC_{61}BM$ [306].

The enhanced short-range interactions along the y-axis suggest increased contributions from dispersive van der Waals forces and π-electron cloud overlap, which promote greater electronic delocalization at the DBAd-fullerene donor-acceptor interface [320]. Despite the reduced centroid-to-centroid distances, the predominant interaction motif is T-shaped rather than cofacial π-π stacking. This spatial arrangement minimizes electrostatic repulsion between the π-systems, stabilizes the complex through favorable quadrupole interactions [315, 321]. The interaction between topologies is particularly relevant for charge-transfer processes, as T-shaped geometries facilitate electronic coupling and promote ultrafast charge separation [322, 323].

Along the z-axis, the C_{60}@DBAd complex exhibits an interaction energy of $-12.41\ \text{kcal} \cdot \text{mol}^{-1}$ at a centroid-to-centroid distance of 6.78 Å. The $PC_{61}BM$@DBAd complex exhibits stronger binding of $-17.41\ \text{kcal} \cdot \text{mol}^{-1}$ at a slightly reduced centroid distance of 4.92 Å. Although this interaction energy exceeds the values observed along the x- and y-axes, the longer centroid distance for C_{60}@DBAd along the z-axis suggests a geometry characterized by dipole-dipole interactions involving the carbonyl group of DBAd and the fullerene surface, in addition to the orthogonal (T-shaped) non-covalent interactions [324]; see Figure 19 (e) and (f).

The interaction energy (ϵ) and centroid-to-centroid distance (r) corresponding to the lowest-energy conformations along each Cartesian axis are summarized in Table 7. The stronger ground-state non-covalent interactions in the $PC_{61}BM$@DBAd complex, relative to the C_{60}@DBAd, support the hypothesis that the ester functionalization of $PC_{61}BM$ enhances its non-covalent interaction potential. This functionalization breaks the high icosahedral symmetry of C_{60}-fullerene cage, introduces local dipoles, and enables stronger supramolecular association with the electron-rich and quasi-planar DBAd molecule. Conversely, the purely hydrophobic and symmetric nature of C_{60} limits interaction strength, as its π-delocalized cage offers weak nucleophilic character for non-covalent binding [325–327].

Although the intermolecular interactions were analyzed using classical force field-based calculations, it is indispensable to recognize that π-π stacking is generally weakened by inter-ring repulsive forces, especially at short distances [316, 321], something sensitively detected by the methodology used herein. Despite this limitation, the quasi-planar conjugated structure of DBAd still permits favorable T-shaped interactions with C_{60}, although these are less efficient compared to those involving $PC_{61}BM$. The enhanced molecular coupling and stronger non-covalent binding observed in the $PC_{61}BM$@DBAd complex further suggest that $PC_{61}BM$ can be a more effective fluorescence quencher [120, 328, 329]. This photophysical property will be discussed in greater detail in the next section.

Table 7 – Interaction parameters for the ethoxy-dibenzalacetone derivative (DBAd) with fullerene compounds (C_{60} and $PC_{61}BM$). The table presents the interaction energy (ϵ, in $\mathrm{kcal \cdot mol^{-1}}$), centroid-to-centroid distance (r, in Å), and total complex energy (E, in $\mathrm{kcal \cdot mol^{-1}}$) for the lowest-energy conformations along each Cartesian axis of the DBAd-fullerene complexes. These parameters provide insight into the non-covalent interactions responsible for the stability of the studied supramolecular complexes.

	$^{a}C_{60}$@DBAd			$^{b}PC_{61}BM$@DBAd		
^{c}Axis	ϵ ($\mathrm{kcal \cdot mol^{-1}}$)	r (Å)	E ($\mathrm{kcal \cdot mol^{-1}}$)	ϵ ($\mathrm{kcal \cdot mol^{-1}}$)	r (Å)	E ($\mathrm{kcal \cdot mol^{-1}}$)
X	−6.81	10.51	1144.09	−14.25	7.39	1405.34
Y	−11.43	6.43	1139.47	−16.48	5.76	1403.11
Z	−12.41	6.78	1138.49	−17.41	4.92	1402.19

^{a}Interaction parameters between ethoxy-dibenzalacetone derivative (DBAd) and C_{60}; ^{b}Interaction parameters between DBAd and $PC_{61}BM$; ^{c}The Cartesian axis values were derived from the lowest-energy conformations of the DBAd-fullerene. For $PC_{61}BM$, the values represent the optimal linear combination of axes, specifically: X of $PC_{61}BM$ with Y of DBAd for x-axis, Y of $PC_{61}BM$ with Y of DBAd for y-axis, and Z of $PC_{61}BM$ with Y of DBAd for z-axis; E ($\mathrm{kcal \cdot mol^{-1}}$) indicate total complex energy.

Benatto et al. [104] demonstrated that the position of C_{60} with respect to an electron-donor molecule affects the dipole moment, the energies of the charge transfer states, and the driving force for electron transfer. Moreover, lateral alkyl groups can act as “pincers”, guiding the diffusive motion of C_{60} toward the donor molecule. Investigations into phthalocyanine/fullerene heterojunctions, as emphasized by Rand et al. [330], highlight the importance of optimizing the donor-acceptor orientation to enhance critical photovoltaic conversion processes. Further studies corroborate the influence of molecular conformation on the efficiency of charge and energy transfer between donor and acceptor systems, thus supporting the interpretation of the results presented in this thesis [133, 331–333].

This study presents intrinsic limitations associated with molecular mechanics, including those arising from the Born-Oppenheimer approximation [334] and exclusive use of the Universal Force Field (UFF) [58]. Although UFF accounts for Coulomb interactions through the assignment of partial charges [58], these charges are fixed and generic, without electronic polarization or charge redistribution upon interaction [335]. This constraint affected the fitting accuracy when using the Lennard-Jones (LJ) potential, particularly in the short-range repulsion region [302]. In contrast, the Mie potential provided more consistent correlations for describing intermolecular forces, although overestimation cannot be entirely dismissed [336]; see as detailed fitted parameters for C_{60}@DBAd and $PC_{61}BM$@DBAd in Tables 11 and 12 in Appendix 6.

Nevertheless, the present results offer valuable estimates of the conformational stability of the C_{60}@DBAd and $PC_{61}BM$@DBAd complexes. The methodology employed herein is supported by the work of Coelho et al. [337], as well as by other related studies [317, 318]. To build on these findings, computational studies employing quantum chemical methods are recommended. Specifically, range-separated hybrid functionals (OT-RSH) should be employed to describe the long-range charge-transfer states in the C_{60}@DBAd and $PC_{61}BM$@DBAd systems, starting from the equilibrium conformations determined herein [338, 339].

4.4.3 Quenching Fluorescence and Excited-State Lifetime

UV-Vis absorption and fluorescence spectra of ethoxy-dibenzalacetone derivative (DBAd) in the presence of fullerene compounds (C_{60} and $PC_{61}BM$) suggest the interaction mechanisms governing these molecular systems [131, 161, 340]. Figures 20 (a) and (c) show the UV-Vis absorption spectra of the C_{60}@DBAd and $PC_{61}BM$@DBAd in ethanol-toluene binary mixtures, respectively. These spectra shows superposition of the absorption profile of DBAd (black curve), which exhibits a band centered at 365 nm, with the absorption bands of C_{60} and $PC_{61}BM$ (blue-gray curves), centered around 330 nm. The remaining colored spectra show the evolution of absorbance as a function of increasing concentrations of C_{60} and $PC_{61}BM$, while the DBAd concentration is kept constant at 1.4×10^{-5} mol $\cdot$ L^{-1}.

Figure 20 – (a) Experimental UV-Vis spectra of ethoxy-dibenzalacetone derivative (DBAd), C_{60}, and C_{60}@DBAd at concentrations ranging from low (LC) to high (HC) levels of fullerene. (b) The linear working range for C_{60}@DBAd shows the highest slope $(41,000 \pm 6,000)$, indicating rapid saturation of absorbance at concentrations above 4.63×10^{-5} mol $\cdot$ L^{-1}. (c) Experimental UV-Vis spectra of DBAd, $PC_{61}BM$, and $PC_{61}BM$@DBAd at varying concentrations from low (LC) to high (HC) levels of functionalized fullerene. (d) The linear working range for $PC_{61}BM$@DBAd exhibits the lowest slope $(33,000 \pm 400)$, highlighting the excellent solubility and dispersibility of $PC_{61}BM$@DBAd solutions in the ethanol-toluene mixture.

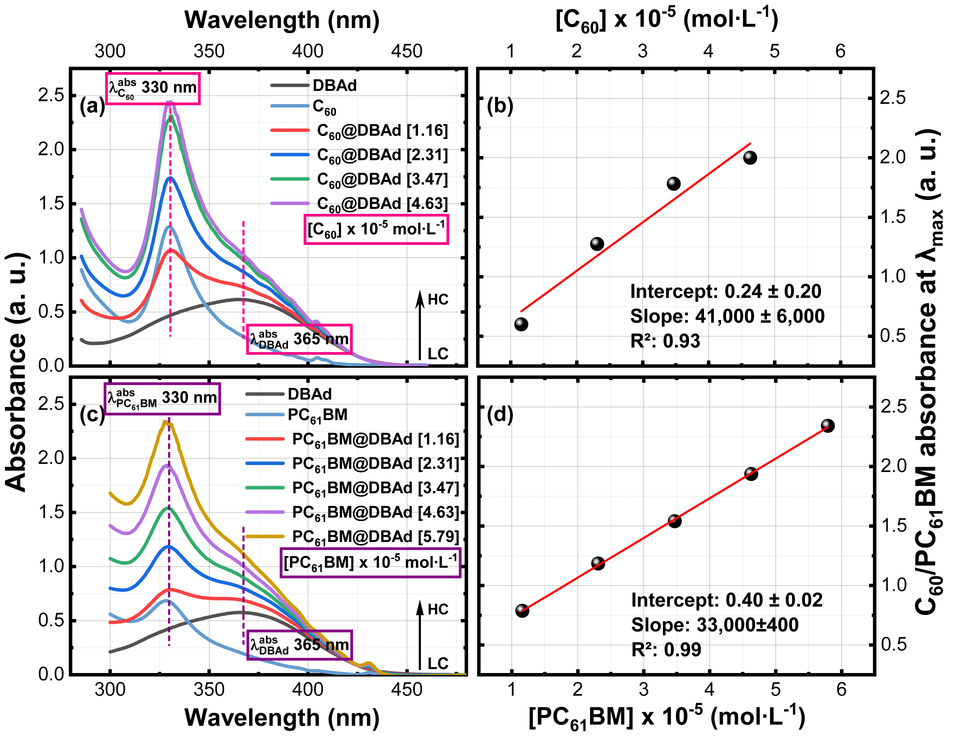

Figures 20 (b) and (d) define the linear dynamic range (LDR) for C_{60}@DBAd and $PC_{61}BM$@DBAd, considering concentrations from low (LC) to high (HC) levels of the fullerene compounds (C_{60} and $PC_{61}BM$). The presence of subtle shifts in the maximum absorption wavelength ($\lambda^{\text{abs}}_{\text{DBAd}}$) – see Figures 20 (a) and (c) – suggests a minor perturbation in the electronic environment of the DBAd chromophore arising from supramolecular association with C_{60} or $PC_{61}BM$ [131,341], in qualitative agreement with the stronger non-bonded interactions predicted by ground-state potential energy surface (PES) calculations; see Figure 19 and Table 7.

Additionally, no evidence of molecular aggregation was identified that could compromise the photophysical behavior of DBAd, except in the case of C_{60}@DBAd at concentrations above 3.47×10^{-5} mol · L^{-1}. At this concentration, the high optical density caused saturation in the absorption spectra, reflecting the lower solubility of C_{60} compared to functionalized $PC_{61}BM$ (see Figures 20 (b) and (d)), attributed to the hydrophobic surface of C_{60} [342], which impairs effective solvation and interaction with the DBAd chromophore [343–345]. Furthermore, C_{60} tends to self-associate by non-covalent autoaggregates, hindering its solubility [346, 347].

Figures 21 (a) and (c) display the steady-state fluorescence spectra of DBAd, recorded upon excitation at 365 nm, in binary ethanol-toluene mixtures containing C_{60}@DBAd and $PC_{61}BM$@DBAd, respectively. The spectra exhibit a linear decrease in DBAd emission as the concentrations of C_{60} and $PC_{61}BM$ progressively increase, indicating a quenching mechanism driven by molecular interactions between DBAd and the fullerene quenchers [348, 349].

Figure 21 – (a) Experimental emission spectra of ethoxy-dibenzalacetone derivative (DBAd) in the absence and presence of low (LC) to high (HC) concentration aliquots of C_{60}. (b) Stern-Volmer plot for C_{60}@DBAd with association constant (K_s) of 1.83×10^4 L · mol^{-1}, where aggregation effects cause minor deviations at higher concentrations. (c) Experimental emission spectra of DBAd in the absence and presence of low (LC) to high (HC) concentration aliquots of $PC_{61}BM$. (d) Stern-Volmer plot for $PC_{61}BM$@DBAd with association constant (K_s) of 2.27×10^4 L · mol^{-1}, confirming a linear quenching across the entire concentration range.

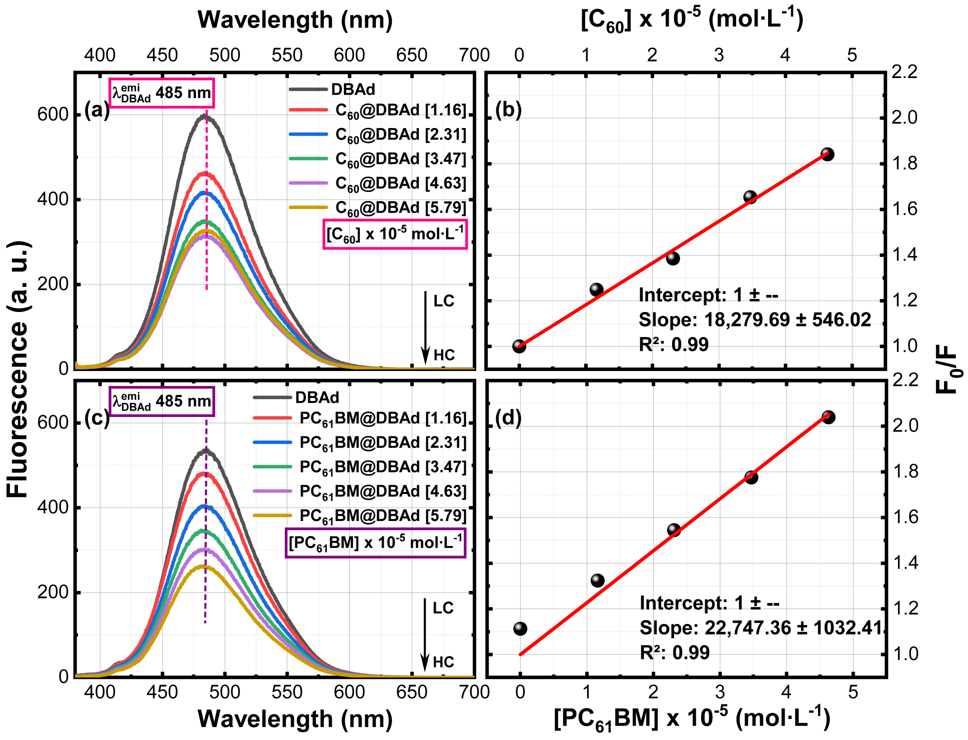

Notably, for C_{60} concentrations above 160 µL (4.63×10^{-5} mol · L^{-1}), the absorption spectra exhibited saturation due to excessive optical density, compromising the accuracy of photophysical measurements beyond this threshold and restricting the linear dynamic range. In contrast, the fluorescence response of the $PC_{61}BM$@DBAd confirms the absence of significant aggregation and underscores the superior solubility and dispersibility of this functionalized fullerene in the binary solvent mixture. Changes in the fluorescence profile at higher concentrations of C_{60} and $PC_{61}BM$ are presented in greater detail in Figure 28 of the Appendix 6.

A Stokes shift ($\Delta\tilde{\nu}$) of $6,778$ cm^{-1} was determined for DBAd in ethanol-toluene binary mixture, calculated as the difference between the wavenumbers corresponding to maximum absorption ($\lambda^{\text{abs}}_{\text{DBAd}}$ of 365 nm) and emission ($\lambda^{\text{emi}}_{\text{DBAd}}$ of 485 nm), consistent with dipolar electronic stabilization of the chromophore in the excited state due to the interactions with the binary solvent mixture [350, 351]. The fluorescence quantum yield of DBAd (Φ_{DBAd}) was estimated to be approximately 0.3% using comparative method with Coumarin 6 ($C_{20}H_{18}N_2O_2S$, PubChem CID 100334 [352]) in methanol (MetOH) as the reference standard under identical instrumental conditions [353] (see Fig. 31 in the Appendix 6), as follows:

$$\Phi_{\text{DBAd}} = \Phi_{\text{C6}} \cdot \frac{F_{\text{DBAd}}}{F_{\text{C6}}} \cdot \frac{f_{\text{C6}}}{f_{\text{DBAd}}} \cdot \left(\frac{n_{\text{EtOH}}}{n_{\text{MeOH}}}\right)^2 \quad , \tag{4.27}$$

where Φ_{DBAd} is the fluorescence quantum yield of the sample (DBAd), Φ_{C6} is the known quantum yield of Coumarin 6 (C6), F_{DBAd} and F_{C6} are the integrated fluorescence emission areas for DBAd and C6, respectively; $f_{\text{DBAd}} = 1 - 10^{-A}$ and $f_{\text{C6}} = 1 - 10^{-A}$ are the absorption factors for DBAd and C6, respectively, calculated from the absorbance (A) at the excitation wavelength; and n is the refractive index of the solvents. The refractive indices used were n_{EtOH} of 1.361 and n_{MeOH} of 1.329 [354]. The reference quantum yield for Coumarin 6 (Φ_{C6}) was taken as 0.7, in accordance with standard literature values [355].

Notably, the $\lambda^{\text{emi}}_{\text{DBAd}}$ remains invariant at 485 nm upon incremental addition of quenchers (C_{60} or $PC_{61}BM$), indicating that the quenching mechanism does not involve significant perturbation to the excited-state electronic structure of the chromophore [356] (see Figs. 21 (a) and (c)), implying that the emissive species correspond to non-complexed DBAd molecules, whereas the quenched population undergoes non-radiative deactivation by supramolecular ground-state association with the fullerene acceptors. Accordingly, non-covalent ground-state interactions govern the photoinduced charge transfer and excitation energy transfer of these complexes [131], particularly in $PC_{61}BM@DBAd$ owing to the thermodynamically stable short-range interactions, as supported by potential energy surface (PES) calculations; see Table 7.

Figures 21 (b) and (d) display the Stern-Volmer plots corresponding to the supramolecular complexes $C_{60}@DBAd$ and $PC_{61}BM@DBAd$ in the ethanol-toluene binary mixture. A linear fluorescence quenching relationship is observed across the entire concentration range analyzed for both $C_{60}@DBAd$ and $PC_{61}BM@DBAd$, as described by Eq. (4.19). This linearity suggests that the quenching occurs through a dynamic (collisional) or static mechanism, with the dominant pathway determined by fluorescence lifetime measurements [131, 163], since only dynamic quenching shortens the excited-state lifetime, whereas static quenching reduces fluorescence intensity without affecting the temporal decay kinetics.

The Stern-Volmer plots in Figures 21 (b) and (d) yield association constants (K_s) of 1.83×10^4 L · mol^{-1} for $C_{60}@DBAd$ and 2.27×10^4 L · mol^{-1} for $PC_{61}BM@DBAd$, extracted from the slopes of the linear fits, indicate strong supramolecular interactions between DBAd and the fullerenes, with a slightly higher binding affinity for the functionalized $PC_{61}BM$, as evidenced by the larger value of K_s. This experimental trend is in good agreement with theoretical predictions based on PES analyses (see Table 7), which reveal that the $PC_{61}BM@DBAd$ complex exhibits stronger ground-state non-covalent interactions compared to the $C_{60}@DBAd$.

The K_s values determined for the DBAd-fullerenes are consistent with those previously reported for non-covalently assembled donor-acceptor complexes. Ray et al. [260] reported K_s values of 6.50×10^3 L · mol^{-1} for $C_{60}@ZnPc$ and 2.22×10^4 L · mol^{-1} for $C_{70}@ZnPc$ of a designed zinc phthalocyanine (ZnPc) with C_{60} and C_{70} in toluene. Similarly, Ovchenkova et al. [261] also observed values for non-covalent donor-acceptor complexes based on (octakis−3,5−di−*tert*−butylphenoxy)phthalocyanine ($H_2Pc(3,5-\textit{tert}-BuPhO)_8$) with fullerenes ($C_{60}$ and C_{70}) whose bonding constants were 1.2×10^4 L · mol^{-1} for assemblies with C_{60} and 2.4×10^4 L · mol^{-1} for C_{70} [261].

Figure 22 presents time-resolved fluorescence decay curves for $C_{60}@DBAd$ and $PC_{61}BM@DBAd$, showing that the excited-state lifetime (τ) of DBAd remains constant at approximately 0.20 ns across all concentrations of the fullerene quenchers. The τ was obtained from monoexponential fitting (ExpDec1) of the fluorescence decays, acquired using the time-correlated single-photon counting (TCSPC) with laser excitation at 401 nm. The fitting was performed by convolution with the instrument response function (IRF) using FluoFit® software, and the quality of the fits assessed by the residual distribution and reduced chi-square (χ^2) values.

Figure 22 – Time-resolved fluorescence decay curves for the C_{60}@DBAd (left) and $PC_{61}BM$@DBAd (right) supramolecular complexes reveal consistent decay lifetimes of approximately 0.20 ns across all quencher concentrations. The absence of systematic variation in the decay lifetimes further supports that the fluorescence quenching mechanism is static due to ground-state supramolecular complex formation. The short-dashed red curves (ExpDec1) represent monoexponential fits to the fluorescence decay profiles, based on the function $I(t) = I_0 \exp\left(-\frac{t}{\tau}\right)$, where $I(t)$ is the fluorescence intensity at time t, I_0 is the initial intensity, and τ is the excited-state lifetime. The good agreement with the monoexponential model confirms the dominance of a single electronic relaxation pathway.

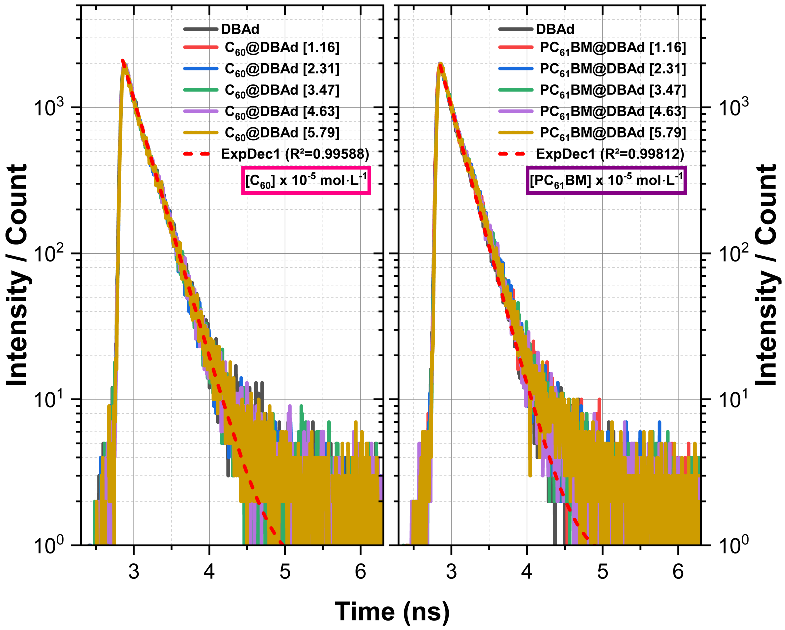

Time-resolved fluorescence decay and corresponding excited-state lifetimes of DBAd in the presence of increasing concentrations of fullerenes are shown in Figure 30 and summarized in Table 14 in Appendix 6. The invariance of the τ under increasing quencher concentrations indicates the absence of dynamic (collisional) quenching, supporting a static quenching mechanism as the predominant pathway. This interpretation is consistent with the PES calculations, which suggest the formation of strong non-bonded interactions in these supramolecular complexes (see Table 7 and Figure 19). Additionally, the excited-state lifetime decay's monoexponential fit (see ExpDec1 in Figure 22) confirms a single dominant electronic relaxation channel under the evaluated experimental conditions [94]. This model assumes a single dominant emissive species and a first-order unimolecular decay [357].

The radiative rate constant (k_r) of DBAd was estimated as 1.5×10^7 s^{-1} using the expression $k_r = \Phi_{\mathrm{DBAd}}/\tau_0$, whereas the non-radiative rate constant (k_{nr}) was substantially higher, at 5.0×10^9 s^{-1}, calculated using $k_{nr} = (1 - \Phi_{\mathrm{DBAd}})/\tau_0$ equation, where Φ_{DBAd} denotes the DBAd fluorescence quantum yield and τ_0 is the excited-state lifetime. The significantly larger non-radiative rate indicates that non-adiabatic deactivation pathways, such as internal conversion and potentially intersystem crossing, dominate the excited-state relaxation, further supported by the propensity of DBAd to undergo PES-guided supramolecular assembly with fullerene compounds (C_{60} and $PC_{61}BM$) [358–360].

Accordingly, the static fluorescence quenching observed upon incremental addition of fullerene quenchers suggests that non-radiative deactivation pathways occur on an ultrafast timescale [359]. These results indicate that supramolecular DBAd-fullerene complexes enable additional highly efficient excited-state deactivation channels, wherein the non-covalent interactions promote conformational stability at short-range distances. Moreover, the favorable electronic coupling between the frontier molecular orbitals (HOMO level of DBAd and the LUMO of the fullerene compounds) thermodynamically drives the photoinduced charge transfer [120, 321]. These also contribute to a reduction in the exciton binding energy (E_B), enhancing the probability of electron-hole dissociation into free charge carriers [361].

Ground-state PES indicated negative interaction energies of -12.41 $\mathrm{kcal \cdot mol^{-1}}$ for C_{60}@DBAd and -17.41 $\mathrm{kcal \cdot mol^{-1}}$ for $PC_{61}BM$@DBAd (see Table 7), equivalent to -0.54 eV and -0.76 eV, respectively, exceeding the E_B threshold of 0.5 to 1.0 eV, minimal required for ultrafast exciton dissociation in organic semiconductors, as estimated by Pope and Swenberg [100] and corroborated by other studies [120–122]. Notably, even with an E_B of approximately 2.29 ± 0.11 eV (see Table 4), which corresponds to an extremely low thermal dissociation probability on the order of 10^{-39}, the observed charge separation indicates that exciton dissociation can proceed via ultrafast non-thermal mechanisms driven by short-range donor-acceptor interactions [249].

The free energy of photoinduced charge transfer ($\Delta G_{\mathrm{charge}}$) was calculated using the Rehm-Weller equation (Eq. (4.20)), which incorporates the oxidation potential of the electron donor (DBAd), the reduction potential of the acceptors (C_{60} and $PC_{61}BM$), the relative dielectric constant of the ethanol-toluene binary solvent mixture (ϵ_r of 20.65, calculated via Eq. (4.21)), and the singlet excitation energy of the fluorophore, estimated herein from the optical gap determined through the Tauc method [96] (see $E_{\mathrm{OPT}}^{\mathrm{exp}}$ in Table 6). Conventionally, the Tauc plot is employed for π-conjugated organic materials to estimate the E_{OPT}^{exp} by extrapolating the linear portion of the absorption edge, associated with the onset of the lowest-energy dipole-allowed transition, which approximately corresponds to the vertical excitation from the electronic ground state (S_0) to the first singlet excited state (S_1) [362, 363].

The calculated ΔG_{charge} values were -1.84 eV for C_{60}@DBAd and -1.74 eV for $PC_{61}BM$@DBAd, indicating the thermodynamic driving force of the charge transfer mechanism, particularly for the C_{60}@DBAd complex, attributed to lower LUMO energy of C_{60}. Comparatively, Curcio et al. [364] reported less negative ΔG_{charge} values of -0.45 eV for C_{60}@DK1 and -0.41 eV for C_{60}@DK2, involving C_{60}-difluoroboron β-diketonate complexes. This difference arises because DBAd exhibits a higher-energy HOMO and a narrower HOMO-LUMO gap compared to the DK1 and DK2 derivatives, thereby enhancing the thermodynamic propensity for photoinduced charge transfer in the DBAd-based complexes.

According to Koopman's [89] theorem, the ionization potential (IP) and electron affinity (EA) of a molecule can be approximated, respectively, by the negative of the HOMO and LUMO energies. In the present thesis, these parameters are shown in Table 6 and were estimated using the GGA-DFT/BLYP-D2/DNP+ level of theory. However, this approximation is strictly valid only within the Hartree-Fock theory, as it neglects orbital relaxation and electron correlation effects. In the context of Kohn-Sham Density Functional Theory (DFT), particularly with Generalized Gradient Approximation (GGA) functionals, the HOMO and LUMO energies do not formally correspond to IP and EA due to self-interaction errors and the absence of derivative discontinuity in the exchange-correlation functional [365, 366].

Despite the known limitations of GGA functionals such as BLYP in accurately describing orbital energies, particularly due to the absence of Hartree-Fock exchange, the computed values herein showed good agreement with the literature and can still offer qualitative exploratory redox behavior. Furthermore, the experimental optical gap (E_{OPT}^{exp}) exhibits good agreement with the vertical excitation energy to the first singlet excited state (S_1), as obtained by Time-Dependent Density Functional Theory (TD-DFT) with Polarizable Continuum Model (PCM) solvation at the M06-2X/6-311+G(d,p) level [50]; see Table 2 in the Section 3.

The Förster energy transfer rate (k_{FRET}) for the C_{60}@DBAd and $PC_{61}BM$@DBAd supramolecular complexes were calculated using Eq. (4.22) [367, 368], based on experimental parameters including the excited-state lifetime of DBAd (τ_D of 0.20 ns), the Förster radius (R_0), and spectral overlap integral ($J(\lambda)$) for each complex at the respective fullerene quencher concentrations, obtained from Eqs (4.23) and (4.24), respectively. The calculations assumed an isotropic dipole orientation factor (κ) of $2/3$ and a refractive index (n) of 1.385 for the ethanol-toluene mixture, determined from Eq. (4.25). The $J(\lambda)$ values were computed from the overlap between the molar extinction coefficient (ε) spectra of the fullerene acceptors (C_{60} and $PC_{61}BM$) and the normalized fluorescence emission spectrum of the DBAd donor, as illustrated in Fig. 23. Table 8 summarizes the FRET parameters obtained for DBAd at increasing fullerene-quencher concentrations.

Figure 23 – Normalized molar extinction coefficient (ε, in $\mathrm{L \cdot mol^{-1} \cdot cm^{-1}}$) for fullerene compounds (C_{60} and $PC_{61}BM$), fluorescence emission spectra of DBAd (in arbitrary units), and corresponding spectral overlap integral ($J(\lambda)$, in $\mathrm{L \cdot mol^{-1} \cdot cm^{-1} \cdot nm^4}$) for C_{60}@DBAd and $PC_{61}BM$@DBAd supramolecular complexes. (a) The ϵ spectrum of C_{60} (in blue line) and fluorescence emission spectrum of DBAd (in red line) are displayed. (b) The ε spectrum of $PC_{61}BM$ (in blue line) and fluorescence emission spectrum of DBAd (in red line) are also shown. (c) The $J(\lambda)$ for the C_{60}@DBAd complex revealing lower interaction efficiency due to the smaller common area between the spectra. (d) The $J(\lambda)$ for the $PC_{61}BM$@DBAd indicates greater resonant energy transfer efficiency, as evidenced by the larger area of $J(\lambda)$.

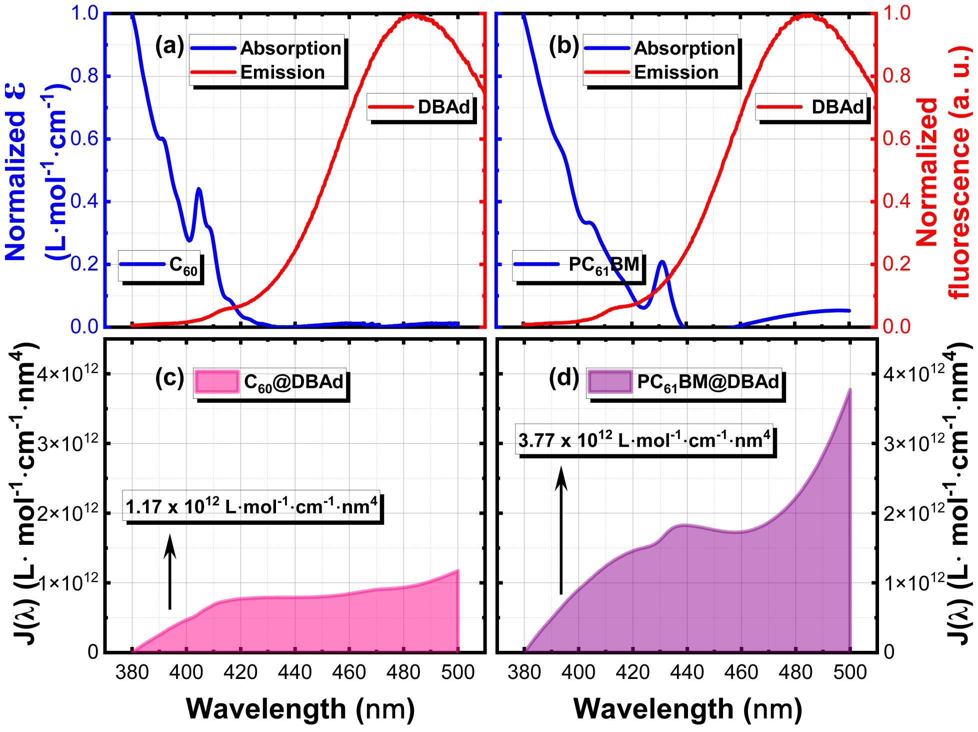

Table 8 – Förster resonance energy transfer (FRET) parameters for the ethoxy-dibenzalacetone derivative (DBAd) interacting with fullerene compounds (C_{60} and $PC_{61}BM$) at different quencher concentrations. The parameters include the spectral overlap integral ($J(\lambda)$, in $L \cdot mol^{-1} \cdot cm^{-1} \cdot nm^4$), Förster radius ($R_0$, in Å), Förster transfer rate (k_{FRET}, in s^{-1}), and dimensionless FRET efficiency (η_{FRET}).

	[C_{60}/$PC_{61}BM$]	$J(\lambda)$	R_0	k_{FRET}	η_{FRET}
C_{60}@DBAd	0.00	$(7.93 \pm 2.61) \times 10^{11}$	5.22 ± 0.59	–	–
	1.16	$(3.06 \pm 1.23) \times 10^{14}$	13.67 ± 2.04	$(4.11 \pm 1.95) \times 10^{11}$	0.97 ± 0.09
	2.31	$(1.56 \pm 0.62) \times 10^{14}$	12.22 ± 1.80	$(2.09 \pm 0.98) \times 10^{11}$	0.95 ± 0.10
	3.47	$(1.35 \pm 0.49) \times 10^{14}$	12.02 ± 1.61	$(1.82 \pm 0.79) \times 10^{11}$	0.95 ± 0.10
	4.63	$(1.54 \pm 0.50) \times 10^{14}$	12.37 ± 1.51	$(2.10 \pm 0.80) \times 10^{11}$	0.96 ± 0.09
	5.79	$(1.59 \pm 0.49) \times 10^{14}$	12.47 ± 1.45	$(2.17 \pm 0.77) \times 10^{11}$	0.96 ± 0.08
$PC_{61}BM$@DBAd	0.00	$(1.74 \pm 0.77) \times 10^{12}$	5.94 ± 0.73	–	–
	1.16	$(3.89 \pm 1.18) \times 10^{14}$	14.28 ± 1.78	$(3.44 \pm 1.29) \times 10^{12}$	0.99 ± 0.06
	2.31	$(1.94 \pm 0.59) \times 10^{14}$	12.74 ± 1.56	$(1.73 \pm 0.64) \times 10^{12}$	0.99 ± 0.07
	3.47	$(1.21 \pm 0.38) \times 10^{14}$	11.87 ± 1.43	$(1.13 \pm 0.41) \times 10^{12}$	0.99 ± 0.07
	4.63	$(7.76 \pm 2.54) \times 10^{13}$	11.13 ± 1.33	$(7.64 \pm 2.77) \times 10^{11}$	0.98 ± 0.07
	5.79	$(6.53 \pm 2.15) \times 10^{13}$	10.81 ± 1.31	$(6.42 \pm 2.34) \times 10^{11}$	0.98 ± 0.07

[*] A statistical treatment based on descriptive analysis was conducted to evaluate the FRET parameters at each quencher concentration. The reported values correspond to the arithmetic mean, with the standard deviation (SD) representing the dispersion across measurements. Additionally, the relative standard deviation (RSD) was calculated to assess the normalized variability of each parameter. Among the evaluated parameters, the spectral overlap integral $J(\lambda)$ exhibited a mean RSD of 34.54%, while the Förster radius R_0 showed lower variability (RSD of 12.61%). The Förster transfer rate constant (k_{FRET}) displayed the highest dispersion, with a mean RSD of 39.76%, whereas the FRET efficiency (η_{FRET}) presented the lowest variability (RSD of 11.22%), indicating that the energy transfer efficiency remains highly stable despite fluctuations in spectral and spatial parameters. [**] Notably, k_{FRET} and η_{FRET} are not reported at a quencher concentration of $0.00 \ mol \cdot L^{-1}$, as physical dipole-dipole coupling and, consequently, non-radiative energy transfer cannot occur in the absence of acceptor species. However, $J(\lambda)$ and R_0 remain physically meaningful under these conditions, since they are defined by the intrinsic spectral overlap between donor emission and acceptor absorption.

The higher Förster energy transfer rate constant (k_{FRET}) for the $PC_{61}BM$@DBAd complex (3.44×10^{12} s^{-1}) relative to that of C_{60}@DBAd (4.11×10^{11} s^{-1}), both evaluated at a quencher concentration of $1.16 \ mol \cdot L^{-1}$, indicates that FRET is the dominant quenching pathway for $PC_{61}BM$@DBAd assembly; see the full dataset of k_{FRET} values in Table 8. This result is further corroborated by the shorter donor-acceptor center-to-center distance of 4.92 Å and larger spectral overlap (as shown in Figure 23 (d)), both of which enhance the dipole-dipole coupling efficiency, thereby promoting the FRET rate constant increase. These values are in agreement with prior studies on coumarin-C_{60} dyads, in which Nascimento et al. [369] reported Förster radii around 33 Å and corresponding k_{FRET} values on the order of 6.0×10^{11} s^{-1} and 3.0×10^{12} s^{-1}, underscoring the ultrafast nature of energy transfer in these molecular assemblies.

Qaiser et al. [370] reported a Förster radius (R_0) of 34.1 Å for the C_{60}-coumarin C440, with a maximum energy transfer efficiency of 92.74% at the critical concentration for dimer formation, supporting the predominance of FRET as the main quenching pathway, and its dependence on the fullerene-acceptor concentration. Furthermore, Rybkin et al. [371] investigated fluorescence quenching in fullerene-fluorescein dyads and reported a Förster radius of 39.0 Å and a non-radiative energy and/or electron transfer rate from the excited electronic state (k_0) of 1.0×10^{13} s^{-1}, indicating highly efficient energy/electron transfer processes.

According to the data presented in the Table 8, the $PC_{61}BM@DBAd$ complex exhibits consistently larger k_{FRET} values across all fullerene-quencher concentrations than the $C_{60}@DBAd$, indicating an efficient non-radiative dipole-dipole channel. Notably, both $J(\lambda)$ and R_0 reaching maximum values at lower quencher concentrations ($1.16\ \mathrm{mol} \cdot \mathrm{L}^{-1}$) and subsequently decreasing at higher concentrations, specially in $PC_{61}BM@DBAd$, attributed to aggregation-induced spectral shifts, supramolecular conformational disorder, and a progressive loss of dipole orientation, which collectively diminish the effective spectral overlap and frontier orbital alignment necessary for optimal FRET. This behavior is consistent with the Qaiser et al. [370] reports, who demonstrated that FRET efficiency peaks near the dimerization threshold, beyond which excessive aggregation attenuates dipole-dipole coupling efficiency. Despite these variations in $J(\lambda)$, R_0, and k_{FRET}, the FRET efficiency (η_{FRET}) remains close to unity under all conditions, indicating that non-radiative Förster energy transfer dominates the excited-state deactivation pathways.

4.5 $C_{60}@DBAd$ and $PC_{61}BM@DBAd$ Thermodynamic and Electronic Properties

The zero-point vibrational energies (ZPVEs) for the optimized complexes were $460.70\ \mathrm{kcal} \cdot \mathrm{mol}^{-1}$ for $C_{60}@DBAd$ and $602.39\ \mathrm{kcal} \cdot \mathrm{mol}^{-1}$ for $PC_{61}BM@DBAd$, reflecting the vibrational contributions to the ground-state energy. However, the Hessian analysis showed seven and eight imaginary low frequencies for $C_{60}@DBAd$ and $PC_{61}BM@DBAd$, respectively, indicating that the obtained stationary points do not correspond to true minima. These results suggest the presence of transition states, higher-order saddle points, or numerical artifacts arising from the complexity of the classical potential energy surface (PES) [372].

Figure 24 shows temperature-dependent thermodynamic properties calculated by the DFT/BLYP-D2/DNP+ level of theory. The enthalpy (H) were 26.48 kcal $\cdot$ mol^{-1} for C_{60}@DBAd and 35.70 kcal $\cdot$ mol^{-1} for PC_{61}BM@DBAd, accompanied by positive entropy contributions (S) of 231.44 cal $\cdot$ mol $\cdot$ K^{-1} and 293.84 cal $\cdot$ mol $\cdot$ K^{-1}, respectively. The Gibbs free energy (G) were significantly negative, at -42.53 kcal $\cdot$ mol^{-1} for C_{60}@DBAd and -51.91 kcal $\cdot$ mol^{-1} for PC_{61}BM@DBAd, confirming the thermodynamic spontaneity of complex formation at 298.15 K.

Figure 24 – Temperature-dependent thermodynamic properties of the supramolecular complexes (a) C_{60}@DBAd and (b) PC_{61}BM@DBAd calculated by DFT/BLYP-D2/DNP+ level of theory. Entropy (■) and enthalpy (▲) exhibit a monotonic increase, while free energy (▼) decreases, indicating progressive thermodynamic destabilization at elevated temperatures. The heat capacity (●) stabilizes at high temperatures.

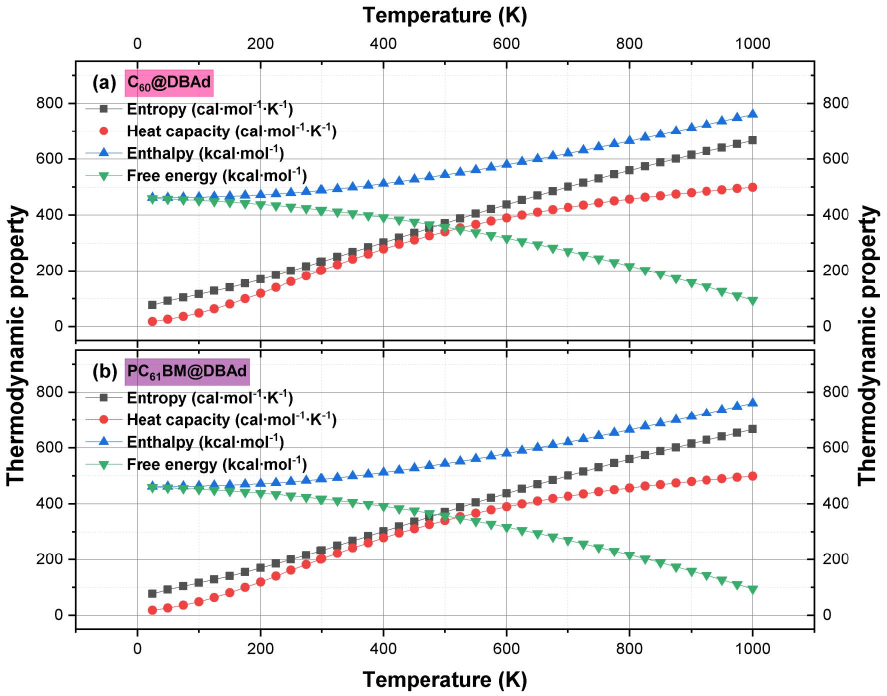

The Generalized Gradient Approximation (GGA) functional BLYP, employed herein with Grimme's dispersion correction (DFT-D2) for the calculation of thermodynamic and electronic properties of the C_{60}@DBAd and PC_{61}BM@DBAd complexes, is recognized for reasonable accuracy in predicting equilibrium geometries with weak non-covalent interactions [373]. However, BLYP underestimates binding energies due to the self-interaction errors and the absence of derivative discontinuity in the exchange-correlation potential [365, 374]. Consequently, the description of the electronic properties is qualitatively reliable but quantitatively inaccurate.

Despite these limitations, the more negative Gibbs free energy (G) observed in $PC_{61}BM$@DBAd complex indicates more spontaneity by stronger non-covalent interactions; in agreement with intermolecular potential values reported in Table 7. Furthermore, the highest occupied molecular orbital (HOMO) and the lowest unoccupied molecular orbital (LUMO) of the C_{60}@DBAd and $PC_{61}BM$@DBAd complexes were compared with those of the isolated molecules. For the unbound molecules, the HOMO energies were −4.95 eV for DBAd, −5.46 eV for C_{60}, and −5.21 eV for $PC_{61}BM$, while the corresponding LUMO levels were −2.44 eV, −3.79 eV, and −3.65 eV, respectively (see Table 6).

These values qualitatively yielded fundamental gaps (E_{fund}) of 2.50 eV for DBAd, 1.67 eV for C_{60}, and 1.56 eV for $PC_{61}BM$, in agreement with energy gaps reported in other works [50, 375–377]. Upon supramolecular complexation, the HOMO level of DBAd increased to −4.68 eV in C_{60}@DBAd and −4.66 eV in $PC_{61}BM$@DBAd, while the LUMO level decreased to −3.46 eV and −3.31 eV, respectively. Consequently, the HOMO-LUMO gap decreased to 1.22 eV in C_{60}@DBAd and 1.35 eV in $PC_{61}BM$@DBAd, qualitatively indicating a stabilization of the electronic density due to non-covalent interactions. Figure 25 illustrates the PES for the C_{60}@DBAd and $PC_{61}BM$@DBAd complexes, with isosurfaces (±0.015 isovalues) calculated using the DFT/BLYP-D2/DNP+ methodology.

This reduction in the fundamental gap (E_{fund}), compared at the same level of theory with that of their isolated molecules, suggests that the electronic delocalization between DBAd and the fullerene compounds can facilitate charge transfer, essential for optoelectronic applications. Additionally, the larger decrease in E_{fund} for C_{60}@DBAd compared to $PC_{61}BM$@DBAd indicates a potential stronger charge transfer interaction due to the lower LUMO energy of C_{60}@DBAd (−3.46 eV) compared to $PC_{61}BM$@DBAd (−3.31 eV) which implies a lower barrier for electron acceptance, favorable for exciton dissociation in organic photovoltaics [39].

Curcio et al. [364] investigated the photophysical properties of two difluoroboron flavanone-diketone derivatives interacting supramolecularly with C_{60} fullerene in toluene solution and spin-coated thin films. The frontier orbital energies and HOMO-LUMO gaps (ΔE) were computed using various exchange-correlation functionals (B3LYP, CAM-B3LYP, and PBE), yielding ΔE values of approximately 2.71 eV for C_{60}@DK1 and C_{60}@DK2 complexes. These values are comparable to the fundamental gap calculated herein for isolated DBAd (2.50 eV) but significantly higher than C_{60}@DBAd (1.22 eV) and $PC_{61}BM$@DBAd (1.35 eV), evaluated using the DFT/BLYP-D2/DNP+ methodology. This discrepancy may stem from the extended

Figure 25 – Potential energy surfaces of the lowest-energy conformations of the C_{60}@DBAd and PC_{61}BM@DBAd supramolecular complexes, calculated at the DFT/BLYP-D2/DNP+ level. The isosurfaces of the highest occupied molecular orbital (HOMO) and lowest unoccupied molecular orbital (LUMO) were determined using a value of ±0.015, with yellow and blue surfaces denoting the positive and negative phases of the molecular wavefunction, respectively. The isosurfaces were generated in Materials Studio [59] (BIOVIA, Dassault Systèmes, available at <https://www.3ds.com/products-services/biovia/products/materials-studio/>).

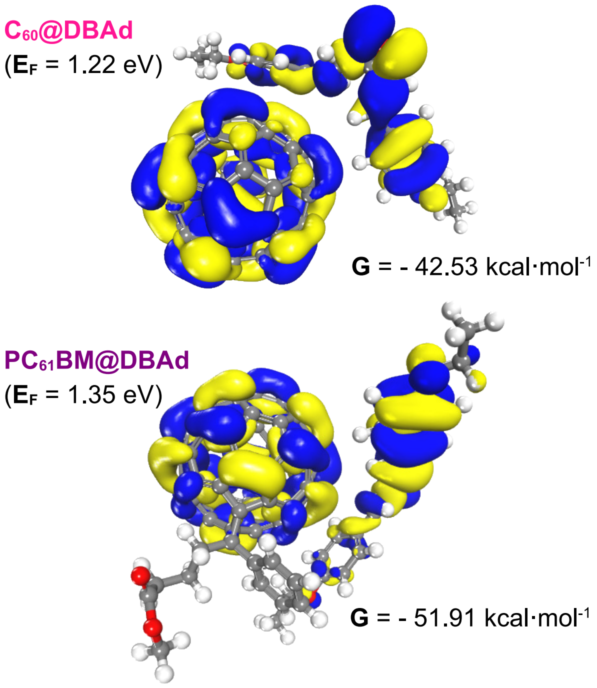

π-conjugation and planarity of the DBAd, which promotes stronger orbital delocalization and electronic coupling with the fullerene LUMO. Although the BLYP-D2 is appropriate for capturing weak non-covalent interactions, it is known to underestimate band gaps [365, 374], something partially corrected by Curcio et al. [364], incorporating a fraction of exact Hartree-Fock exchange.

Le et al. [378] employed isothermal titration calorimetry (ITC) experiments to obtain thermodynamic parameters for the formation of complexes between C_{60} and C_{70} fullerenes with the buckycatcher ($C_{60}H_{28}$) in a series of organic solvents at temperatures from 278 to 323 K. The results indicated that the supramolecular associations are enthalpy-driven with values ranging from -1.87 to -4.61 kcal · mol^{-1} for C_{60}@$C_{60}H_{28}$ and -1.97 to -3.76 kcal · mol^{-1} for C_{70}@$C_{60}H_{28}$; and entropy changes are slightly favorable or negligible with values ranging from -1.25 to 0.04 kcal · mol^{-1} for C_{60}@$C_{60}H_{28}$ and -2.04 to -0.29 kcal · mol^{-1} for C_{70}@$C_{60}H_{28}$

due to the reduction of translational and rotational degrees of freedom of the fullerene-guest. The Gibbs free energy change is more negative for $C_{70}@C_{60}H_{28}$, especially in toluene, indicating greater thermodynamic stability of this complex. This behavior confirms the exergonicity of complexation since non-covalent interactions lower the potential energy of the complexes.

Using the rigid rotor-harmonic oscillator model, Zhao and Truhlar [379] calculated the entropy contribution of the C_{60}@coranulene complex in the gas phase, yielding an association Gibbs free energy of approximately -6.7 kcal $\cdot$ mol^{-1}. Furthermore, supramolecular complexation in solution resulted in a considerable reduction in solvent-accessible surface area, reducing the exergonicity of the solvation. Similarly, Grimme [380] combined dispersion-corrected density functional theory (DFT-D3) with extended basis sets (triple-ζ and quadruple-ζ quality) to evaluate the solvation Gibbs free energy and the rotational and vibrational contributions to enthalpy and entropy based on harmonic frequency calculations. The study demonstrated that complexation energies in vacuum tend to overestimate binding affinity, and the inclusion of solvation effects and vibrational enthalpic-entropic corrections (especially from low-frequency modes) reduces the free energy of association by about 2 to 4.6 kcal $\cdot$ mol^{-1}.

The vibrational entropy contribution diverges as the vibrational frequency approaches zero [381, 382], which can introduce numerically incorrect binding free energies, especially in weakly bound noncovalent complexes, since low-frequency modes are common. In his study, Grimme [380] implemented a hybrid function in which a free-rotor entropy replaces the vibrational entropy via a switching function for low-frequency modes. However, computing numerically stable vibrational frequencies for these modes remains a challenge and may require manipulation of the Hessian matrix. Here, the vibrational entropies for C_{60}@DBAd and $PC_{61}BM$@DBAd were 143.88 cal $\cdot$ mol $\cdot$ K^{-1} and 204.84 cal $\cdot$ mol $\cdot$ K^{-1}, respectively, at DFT/BLYP-D2/DNP+ level of theory; see all dataset thermodynamic parameters in Table 18 of the Appendix 6.

Therefore, the thermodynamic parameters for C_{60}@DBAd and $PC_{61}BM$@DBAd should be interpreted considering the limitations of the harmonic approximation for supramolecular complexes in vacuum, arising from quasi-free translational and rotational motions, which contribute to an increase in the vibrational entropy and consequently a pronounced reduction in the Gibbs free energy. As evidenced by Grimme [380], this behavior is typical of supramolecular complexes without solvation corrections and the use of hybrid functions. Thus, the results presented in this thesis also reflect the need for future use of anharmonic corrections for a more realistic thermodynamic description.

4.6 Final Considerations

This thesis chapter investigates the influence of quantum chemical reactivity descriptors and the ground-state potential energy surface (PES) associated with the non-covalent interactions between the ethoxy-dibenzalacetone (DBAd) derivative and fullerene compounds (C_{60} and $PC_{61}BM$), to elucidate the photoinduced charge transfer and Förster resonance energy transfer (FRET). Specifically, the interaction energy (ϵ) and centroid-to-centroid distance (r) of the supramolecular complexes C_{60}@DBAd and $PC_{61}BM$@DBAd were evaluated and correlated with the efficiency of non-radiative quenching pathways in DBAd. Fluorescence deactivation occurs via a static quenching mechanism, consistent with the Born-Oppenheimer PES topology, which indicates the formation of thermodynamically stable supramolecular complexes.

Ground-state PES indicated negative interaction energies of -12.41 kcal $\cdot$ mol^{-1} for C_{60}@DBAd and -17.41 kcal $\cdot$ mol^{-1} for $PC_{61}BM$@DBAd, confirming the formation of stable donor-acceptor complexes, wherein static fluorescence quenching arises from the short-range distance of the fullerene quencher to the DBAd at the instant of photoexcitation. This close donor-acceptor proximity enables both efficient FRET and photoinduced charge transfer from DBAd to fullerenes, yielding non-emissive assemblies, as evidenced by the unchanged excited-state lifetime of DBAd, measured at approximately 0.20 ns, even under increasing concentrations of C_{60} and $PC_{61}BM$ quenchers.

Furthermore, $PC_{61}BM$@DBAd exhibits enhanced non-covalent interactions at short-range distances (4.92 Å) and larger spectral overlap integral, promoting increasing Förster transfer rate (k_{FRET}) at 3.44×10^{12} s^{-1}, while C_{60}@DBAd favors photoinduced charge transfer, with a driving force of -1.84 eV, attributed to the thermodynamically favorable HOMO-LUMO alignment. Thermodynamic calculations at DFT/BLYP-D2/DNP+ level of theory confirmed the spontaneity of complexes formation, with Gibbs free energy values of -42.53 kcal $\cdot$ mol^{-1} for C_{60}@DBAd and -51.91 kcal $\cdot$ mol^{-1} for $PC_{61}BM$@DBAd. Finally, these results indicate that efficient charge and energy transfer from DBAd to fullerenes could significantly enhance light harvesting and charge-transfer exciton (CTE) dissociation at the donor-acceptor interface of organic/fullerene-based devices, offering a strategic pathway to improve the performance of organic next-generation solar cells.

5 CONCLUSION

This thesis conducted a comprehensive investigation of the influence of non-covalent interactions between the potential energy surfaces (PES) of supramolecular complexes formed by ethoxy-dibenzalacetone derivative (DBAd) and fullerene compounds (C_{60} and $PC_{61}BM$) in the non-radiative suppression of fluorescence, observed in ethanol-toluene binary mixtures. The main conclusions are listed as follows:

(a) PES analysis indicates negative interaction energies in the ground state of $-12.41\ \mathrm{kcal\cdot mol^{-1}}$ for C_{60}@DBAd and $-17.41\ \mathrm{kcal\cdot mol^{-1}}$ for $PC_{61}BM$@DBAd, equivalent of -0.54 eV and -0.76 eV, respectively. These values exceed the exciton binding energy range (0.5 to 1.0 eV) typically required for charge separation in organic semiconductors, as estimated by Pope and Swenberg [100], and other authors [120–122];

(b) The spontaneous formation of these complexes was supported by significantly negative Gibbs free energies ($-42.53\ \mathrm{kcal\cdot mol^{-1}}$ for C_{60}@DBAd and $-51.91\ \mathrm{kcal\cdot mol^{-1}}$ for $PC_{61}BM$@DBAd), indicating thermodynamic favorability for supramolecular aggregation in the ground state [383, 384];

(c) The exciton binding energy (E_B) of DBAd was estimated, for the first time, under different dielectric environments, indicating a dependence of E_B on the solvent dielectric constant, consistent with dipolar stabilization of the excited state in polar media [120, 126]. The existence of a substantial E_B requires additional energy-level offsets at the donor-acceptor interface to drive exciton dissociation into free charge carriers, typically resulting in extra energy losses compared to inorganic and perovskite solar cells [249, 385];

(d) The fluorescence quenching was attributed to the formation of static ground-state non-emissive complexes. The spatial proximity of DBAd to the quenchers (C_{60} or $PC_{61}BM$) in the excited state facilitates non-radiative energy transfer by Förster resonance energy transfer (FRET) and charge transfer exciton (CTE) mechanisms at the interface, inhibiting photon emission by a fluorophore fraction. The literature supporting that stable interfacial conformation between donor and acceptor induces electrostatic stabilization that contributes to the reduction of the E_B, favoring exciton dissociation [120, 121].

Overall, the results identify C_{60}@DBAd and $PC_{61}BM$@DBAd as promising candidates for optoelectronic applications, particularly in third-generation organic solar cells. However, further computational and experimental studies are recommended, as outlined in the next section, to ensure their effective integration into practical organic photovoltaic devices.

6 FUTURE WORK PERSPECTIVES

This thesis establishes a theoretical and experimental procedure to investigate supramolecular complexes formed by the donor ethoxy-dibenzalacetone (DBAd) and fullerene-based acceptors, with potential applications in optoelectronic devices. The methodologies and results described herein can be extended to a broader class of donor-acceptor complexes and more profound investigations. Therefore, the following directions are proposed for future work:

(a) To apply Optimally Tuned Range-Separated Hybrid (OT-RSH) functional to each of the supramolecular complexes in equilibrium, to evaluate the delocalization and separation of charge, particularly in excitonic states. The OT-RSH function is effective in modeling long-range charge transfer interactions, as it separates short-range and long-range electron exchange contributions;

(b) To obtain benchmark ionization potential and electron affinity values for chemical reactivity descriptors using the finite-difference Self-Consistent Field method (ΔSCF), Equation-of-Motion Coupled-Cluster Singles and Doubles (EOM-CCSD), or Green's function with Coulomb interaction (GW), to accurate quasiparticle energies beyond Kohn-Sham orbital approximations;

(c) To investigate intermolecular interactions in a solvated environment through classical or quantum molecular dynamics simulations. Solvent effects can play a critical role in stabilizing or destabilizing non-covalent interactions, which may significantly alter the electronic properties of DBAd with fullerene compounds in realistic conditions;

(d) To extend the computational protocol to DBAd and related derivatives combined with electron-donating materials, such as conjugated polymers, to enhanced spectral overlap and improved exciton dissociation efficiency;

(e) To assess the influence of intermolecular interactions in the excited states non-equilibrium geometries by advanced quantum molecular dynamics to provide deeper insights into the mechanisms underlying these photophysical processes. The role of non-covalent interactions in excited states in modulating charge transfer processes, especially in organic solar cells, is often underestimated, and their inclusion could provide a deeper understanding of the photophysical behavior of these systems;

(f) To evaluate C_{60}@DBAd and $PC_{61}BM$@DBAd complexes using non-adiabatic molecular dynamics (NAMD), to elucidate the non-radiative decay pathways and their contribution to fluorescence quenching.

REFERENCES

[1] ABBASS, K.; QASIM, M. Z.; SONG, H.; MURSHED, M.; MAHMOOD, H.; YOUNIS, I. A review of the global climate change impacts, adaptation, and sustainable mitigation measures. **Environmental Science and Pollution Research**, Springer, v. 29, n. 28, p. 42539–42559, 2022.

[2] KIM, S.-K.; SHIN, J.; AN, S.-I.; KIM, H.-J.; IM, N.; XIE, S.-P.; KUG, J.-S.; YEH, S.-W. Widespread irreversible changes in surface temperature and precipitation in response to CO_2 forcing. **Nature Climate Change**, Springer Nature, v. 12, n. 9, p. 834–840, 2022.

[3] OH, J.-H.; KUG, J.-S.; AN, S.-I.; JIN, F.-F.; MCPHADEN, M. J.; SHIN, J. Emergent climate change patterns originating from deep ocean warming in climate mitigation scenarios. **Nature Climate Change**, Nature Publishing Group UK London, v. 14, n. 3, p. 260–266, 2024.

[4] ORTIZ-BOBEA, A.; AULT, T. R.; CARRILLO, C. M.; CHAMBERS, R. G.; LOBELL, D. B. Anthropogenic climate change has slowed global agricultural productivity growth. **Nature Climate Change**, Nature Publishing Group, v. 11, n. 4, p. 306–312, 2021.

[5] POKHREL, Y.; FELFELANI, F.; SATOH, Y.; BOULANGE, J.; BUREK, P.; GÄDEKE, A.; GERTEN, D.; GOSLING, S. N.; GRILLAKIS, M.; GUDMUNDSSON, L. *et al.* Global terrestrial water storage and drought severity under climate change. **Nature Climate Change**, Nature Publishing Group, v. 11, n. 3, p. 226–233, 2021.

[6] IZAGUIRRE, C.; LOSADA, I.; CAMUS, P.; VIGH, J.; STENEK, V. Climate change risk to global port operations. **Nature Climate Change**, Nature Publishing Group, v. 11, n. 1, p. 14–20, 2021.

[7] MORA, C.; MCKENZIE, T.; GAW, I. M.; DEAN, J. M.; HAMMERSTEIN, H. von; KNUDSON, T. A.; SETTER, R. O.; SMITH, C. Z.; WEBSTER, K. M.; PATZ, J. A. *et al.* Over half of known human pathogenic diseases can be aggravated by climate change. **Nature Climate Change**, Nature Publishing Group, v. 12, n. 9, p. 869–875, 2022.

[8] Copernicus Climate Change Service. **2024 is the first year to exceed 1.5°C above pre-industrial level**. Reading, UK: European Centre for Medium-Range Weather Forecasts (ECMWF), 2025. <https://climate.copernicus.eu/copernicus-2024-first-year-exceed-15degc-above-pre-industrial-level>. Accessed: 13th February 2025.

[9] MASSON-DELMOTTE, V.; ZHAI, P.; PÖRTNER, H.-O.; ROBERTS, D.; SKEA, J.; SHUKLA, P. R.; PIRANI, A.; MOUFOUMA-OKIA, W.; PÉAN, C.; PIDCOCK, R. *et al.* Global warming of 1.5º C. **An IPCC Special Report on the Impacts of Global Warming**, v. 1, n. 5, p. 43–50, 2018.

[10] BEVACQUA, E.; SCHLEUSSNER, C.-F.; ZSCHEISCHLER, J. A year above 1.5° C signals that earth is most probably within the 20-year period that will reach the paris agreement limit. **Nature Climate Change**, Nature Publishing Group, p. 1–4, 2025.

[11] TOLLEFSON, J. Earth breaches 1.5 °C climate limit for the first time: what does it mean? **Nature**, v. 637, n. 8047, p. 769–770, 2025.

[12] World Meteorological Organization. **State of the Global Climate 2024**. Geneva, Switzerland: WMO, 2025. Available at <https://wmo.int/sites/default/files/2025-03/WMO-1368-2024_en.pdf>. Accessed: 13th February 2025.

[13] MOREIRA, A. **Julho de 2023 deve ser o mês mais quente já registrado, apontam OMM e observatório europeu**. São Paulo, Brazil: G1 Globo, 2023. Available at <https://g1.globo.com/meio-ambiente/noticia/2023/07/27/julho-/de-2023-deve-ser-o-mes-mais-quente-ja-registrado-apontam-omm-e-observatorio-europeu.ghtml>. Accessed: 2nd August 2023.

[14] GERNAAT, D. E.; BOER, H. S. de; DAIOGLOU, V.; YALEW, S. G.; MÜLLER, C.; VUUREN, D. P. van. Climate change impacts on renewable energy supply. **Nature Climate Change**, Nature Publishing Group, v. 11, n. 2, p. 119–125, 2021.

[15] HOPPE, H.; SARICIFTCI, N. S. Organic solar cells: An overview. **Journal of Materials Research**, Cambridge University Press, v. 19, n. 7, p. 1924–1945, 2004.

[16] NELSON, J. Organic photovoltaic films. **Current Opinion in Solid State and Materials Science**, Elsevier, v. 6, n. 1, p. 87–95, 2002.

[17] CHAMBERLAIN, G. Organic solar cells: A review. **Solar Cells**, Elsevier, v. 8, n. 1, p. 47–83, 1983.

[18] TANG, C. W. Two-layer organic photovoltaic cell. **Applied Physics Letters**, American Institute of Physics, v. 48, n. 2, p. 183–185, 1986.

[19] CUI, Y.; YAO, H.; ZHANG, J.; XIAN, K.; ZHANG, T.; HONG, L.; WANG, Y.; XU, Y.; MA, K.; AN, C. *et al.* Single-junction organic photovoltaic cells with approaching 18% efficiency. **Advanced Materials**, Wiley Online Library, v. 32, n. 19, p. 1–7, 2020.

[20] ZHAN, L.; LI, S.; LAU, T.-K.; CUI, Y.; LU, X.; SHI, M.; LI, C.-Z.; LI, H.; HOU, J.; CHEN, H. Over 17% efficiency ternary organic solar cells enabled by two non-fullerene acceptors working in an alloy-like model. **Energy & Environmental Science**, Royal Society of Chemistry, v. 13, n. 2, p. 635–645, 2020.

[21] ZHAN, L.; LI, S.; LI, Y.; SUN, R.; MIN, J.; BI, Z.; MA, W.; CHEN, Z.; ZHOU, G.; ZHU, H. *et al.* Desired open-circuit voltage increase enables efficiencies approaching 19% in symmetric-asymmetric molecule ternary organic photovoltaics. **Joule**, Elsevier, v. 6, n. 3, p. 662–675, 2022.

[22] ZHU, L.; ZHANG, M.; XU, J.; LI, C.; YAN, J.; ZHOU, G.; ZHONG, W.; HAO, T.; SONG, J.; XUE, X. *et al.* Single-junction organic solar cells with over 19% efficiency enabled by a refined double-fibril network morphology. **Nature Materials**, Nature Publishing Group, v. 21, n. 6, p. 656–663, 2022.

[23] SUN, L.; FUKUDA, K.; SOMEYA, T. Recent progress in solution-processed flexible organic photovoltaics. **NPJ Flexible Electronics**, Nature Publishing Group, v. 6, n. 1, p. 1–14, 2022.

[24] ZHENG, Z.; WANG, J.; BI, P.; REN, J.; WANG, Y.; YANG, Y.; LIU, X.; ZHANG, S.; HOU, J. Tandem organic solar cell with 20.2% efficiency. **Joule**, Elsevier, v. 6, n. 1, p. 171–184, 2022.

[25] Fraunhofer Institute for Solar Energy Systems (ISE). **Organic Solar Cells and Modules - Fraunhofer ISE**. Freiburg, Germany: Fraunhofer ISE, 2023. Available at <https://www.ise.fraunhofer.de/en/business-areas/photovoltaics/perovskite-and-organic-photovoltaics/organic-solar-cells-and-modules.html>. Accessed: 8th November 2023.

[26] XUE, R.; ZHANG, J.; LI, Y.; LI, Y. Organic solar cell materials toward commercialization. **Small**, Wiley Online Library, v. 14, n. 41, p. 1–24, 2018.

[27] LEE, J.; PARK, S. A.; RYU, S. U.; CHUNG, D.; PARK, T.; SON, S. Y. Green-solvent-processable organic semiconductors and future directions for advanced organic electronics. **Journal of Materials Chemistry A**, Royal Society of Chemistry, v. 8, n. 41, p. 21455–21473, 2020.

[28] RAHMANUDIN, A.; MARCIAL-HERNANDEZ, R.; ZAMHURI, A.; WALTON, A. S.; TATE, D. J.; KHAN, R. U.; APHICHATPANICHAKUL, S.; FOSTER, A. B.; BROLL, S.; TURNER, M. L. Organic semiconductors processed from synthesis-to-device in water. **Advanced Science**, Wiley Online Library, v. 7, n. 21, p. 1–7, 2020.

[29] OKAMOTO, T.; YU, C. P.; MITSUI, C.; YAMAGISHI, M.; ISHII, H.; TAKEYA, J. Bent-shaped p-type small-molecule organic semiconductors: a molecular design strategy for next-generation practical applications. **Journal of the American Chemical Society**, ACS Publications, v. 142, n. 20, p. 9083–9096, 2020.

[30] YUN, D.-J.; YUN, Y.; LEE, J.; KIM, J.-Y.; CHUNG, J.; KIM, S. H.; KIM, Y.-S.; HEO, S.; PARK, J.-I.; KIM, K.-H. *et al.* In-depth investigation of the correlation between organic semiconductor orientation and energy-level alignment using in situ photoelectron spectroscopy. **ACS Applied Materials & Interfaces**, ACS Publications, v. 12, n. 45, p. 50628–50637, 2020.

[31] OPITZ, A.; FRISCH, J.; SCHLESINGER, R.; WILKE, A.; KOCH, N. Energy level alignment at interfaces in organic photovoltaic devices. **Journal of Electron Spectroscopy and Related Phenomena**, Elsevier, v. 190, p. 12–24, 2013.

[32] LEE, H.; CHO, S. W.; YI, Y. Interfacial electronic structure for high performance organic devices. **Current Applied Physics**, Elsevier, v. 16, n. 12, p. 1533–1549, 2016.

[33] CHEN, Q.; YE, F.; LAI, J.; DAI, P.; LU, S.; MA, C.; ZHAO, Y.; XIE, Y.; CHEN, L. Energy band alignment in operando inverted structure P3HT:PCBM organic solar cells. **Nano Energy**, Elsevier, v. 40, p. 454–461, 2017.

[34] WANG, K.; YI, C.; LIU, C.; HU, X.; CHUANG, S.; GONG, X. Effects of magnetic nanoparticles and external magnetostatic field on the bulk heterojunction polymer solar cells. **Scientific Reports**, Nature Publishing Group UK London, v. 5, n. 1, p. 1–9, 2015.

[35] KÖHLER, A.; SANTOS, D. D.; BELJONNE, D.; SHUAI, Z.; BRÉDAS, J.-L.; HOLMES, A. B.; KRAUS, A.; MÜLLEN, K.; FRIEND, R. H. Charge separation in localized and delocalized electronic states in polymeric semiconductors. **Nature**, Nature Publishing Group UK London, v. 392, n. 6679, p. 903–906, 1998.

[36] TORABI, S.; JAHANI, F.; SEVEREN, I. V.; KANIMOZHI, C.; PATIL, S.; HAVENITH, R. W.; CHIECHI, R. C.; LUTSEN, L.; VANDERZANDE, D. J.; CLEIJ, T. J. *et al.* Strategy for enhancing the dielectric constant of organic semiconductors without sacrificing charge carrier mobility and solubility. **Advanced Functional Materials**, Wiley Online Library, v. 25, n. 1, p. 150–157, 2015.

[37] LIU, X.; JEONG, K. S.; WILLIAMS, B. P.; VAKHSHOURI, K.; GUO, C.; HAN, K.; GOMEZ, E. D.; WANG, Q.; ASBURY, J. B. Tuning the dielectric properties of organic semiconductors via salt doping. **The Journal of Physical Chemistry B**, ACS Publications, v. 117, n. 49, p. 15866–15874, 2013.

[38] MUNTWILER, M.; YANG, Q.; TISDALE, W. A.; ZHU, X.-Y. Coulomb barrier for charge separation at an organic semiconductor interface. **Physical Review Letters**, APS, v. 101, n. 19, p. 1–4, 2008.

[39] MIKHNENKO, O. V.; BLOM, P. W.; NGUYEN, T.-Q. Exciton diffusion in organic semiconductors. **Energy & Environmental Science**, Royal Society of Chemistry, v. 8, n. 7, p. 1867–1888, 2015.

[40] MA, Y.-F.; ZHANG, Y.; ZHANG, H.-L. Solid additives in organic solar cells: progress and perspectives. **Journal of Materials Chemistry C**, Royal Society of Chemistry, v. 10, n. 7, p. 2364–2374, 2022.

[41] ZHU, L.; ZHANG, M.; ZHONG, W.; LENG, S.; ZHOU, G.; ZOU, Y.; SU, X.; DING, H.; GU, P.; LIU, F. *et al.* Progress and prospects of the morphology of non-fullerene acceptor based high-efficiency organic solar cells. **Energy & Environmental Science**, Royal Society of Chemistry, v. 14, n. 8, p. 4341–4357, 2021.

[42] LIU, Y.; ZHAO, J.; LI, Z.; MU, C.; MA, W.; HU, H.; JIANG, K.; LIN, H.; ADE, H.; YAN, H. Aggregation and morphology control enables multiple cases of high-efficiency polymer solar cells. **Nature Communications**, Nature Publishing Group UK London, v. 5, n. 1, p. 1–8, 2014.

[43] HALLS, J.; WALSH, C.; GREENHAM, N. C.; MARSEGLIA, E.; FRIEND, R. H.; MORATTI, S.; HOLMES, A. Efficient photodiodes from interpenetrating polymer networks. **Nature**, Springer, v. 376, p. 498–500, 1995.

[44] YU, G.; GAO, J.; HUMMELEN, J. C.; WUDL, F.; HEEGER, A. J. Polymer photovoltaic cells: enhanced efficiencies via a network of internal donor-acceptor heterojunctions. **Science**, American Association for the Advancement of Science, v. 270, n. 5243, p. 1789–1791, 1995.

[45] GUILLÉN-LÓPEZ, A.; DELESMA, C.; AMADOR-BEDOLLA, C.; ROBLES, M.; MUÑIZ, J. Electronic structure and nonlinear optical properties of organic photovoltaic systems with potential applications on solar cell devices: a DFT approach. **Theoretical Chemistry Accounts**, Springer, v. 137, p. 1–15, 2018.

[46] MAHMOOD, A.; TANG, A.; WANG, X.; ZHOU, E. First-principles theoretical designing of planar non-fullerene small molecular acceptors for organic solar cells: manipulation of noncovalent interactions. **Physical Chemistry Chemical Physics**, Royal Society of Chemistry, v. 21, n. 4, p. 2128–2139, 2019.

[47] TOLDO, J. M.; CASAL, M. T. D.; VENTURA, E.; MONTE, S. A. D.; BARBATTI, M. Surface hopping modeling of charge and energy transfer in active environments. **Physical Chemistry Chemical Physics**, Royal Society of Chemistry, v. 25, n. 12, p. 8293–8316, 2023.

[48] National Center for Biotechnology Information (NCBI). **(1E,4E)-1,5-bis(4-ethoxyphenyl)penta-1,4-dien-3-one**. Bethesda, MD, USA: PubChem Compound Database, 2024. <https://pubchem.ncbi.nlm.nih.gov/compound/668155>. Accessed: 15th July 2024.

[49] OLIVEIRA, M. M. de; NOGUEIRA, C. E.; ALMEIDA-NETO, F. W. Q.; SANTOS, H. S.; TEIXEIRA, A. M.; LIMA-NETO, P. de; MARINHO, E. S.; MORAES, M. O. de; PESSOA, C.; BARROS-NEPOMUCENO, F. W. A. Full spectroscopic characterization and cytotoxicity activity of synthetic dibenzalacetone derivatives. **Journal of Molecular Structure**, Elsevier, v. 1231, p. 1–11, 2021.

[50] VASCONCELOS, V. M.; POSTACCHINI, B. B.; SANTOS, H. S. dos; CAJAZEIRAS, F. F.; FREIRE, V. N.; JUNIOR, C. A.; PESSOA, C.; COSTA, R. F. da; VASCONCELOS, I. F.; BEZERRA, E. M. Red-shifted optical absorption induced by donor–acceptor–donor π-extended dibenzalacetone derivatives. **RSC Advances**, Royal Society of Chemistry, v. 15, n. 4, p. 2416–2429, 2025.

[51] LI, C.-Z.; YIP, H.-L.; JEN, A. K.-Y. Functional fullerenes for organic photovoltaics. **Journal of Materials Chemistry**, Royal Society of Chemistry, v. 22, n. 10, p. 4161–4177, 2012.

[52] DENG, L.-L.; XIE, S.-Y.; GAO, F. Fullerene-based materials for photovoltaic applications: Toward efficient, hysteresis-free, and stable perovskite solar cells. **Advanced Electronic Materials**, Wiley Online Library, v. 4, n. 10, p. 1–18, 2018.

[53] LIN, H.-S.; MATSUO, Y. Fullerenes in photovoltaics. In: KADISH, K.; RUOFF, R.; D'SOUZA, F. (Ed.). **Handbook of Fullerene Science and Technology**. Cham, Switzerland: Springer, 2022. p. 851–888.

[54] HOHENBERG, P.; KOHN, W. Inhomogeneous electron gas. **Physical Review**, v. 136, n. 3B, p. B864–B871, 1964.

[55] KOHN, W.; SHAM, L. J. Self-consistent equations including exchange and correlation effects. **Physical Review**, v. 140, n. 4A, p. A1133–A1138, 1965.

[56] BECKE, A. D. Density-functional exchange-energy approximation with correct asymptotic behavior. **Physical Review A**, v. 38, n. 6, p. 3098–3100, 1988.

[57] GRIMME, S. Semiempirical GGA-type density functional constructed with a long-range dispersion correction. **Journal of Computational Chemistry**, v. 27, n. 15, p. 1787–1799, 2006.

[58] RAPPÉ, A. K.; CASEWIT, C. J.; COLWELL, K. S.; GODDARD, W. A. I.; SKIFF, W. M. UFF, a full periodic table force field for molecular mechanics and molecular dynamics simulations. **Journal of the American Chemical Society**, v. 114, n. 25, p. 10024–10035, 1992.

[59] BIOVIA, Dassault Systèmes. **Discovery Studio Modeling Environment, Version 19.1**. San Diego, CA, USA: Dassault Systèmes BIOVIA, 2019. Available at <http://www.accelrys.com>. Accessed: 4th June 2024.

[60] NATIONS, U. **Goal 7: Ensure access to affordable, reliable, sustainable and modern energy for all**. New York, NY, USA: United Nations, 2015. Available at <https://sdgs.un.org/goals/goal7>. Accessed: 14th September 2024.

[61] NATIONS, U. **Goal 13: Take urgent action to combat climate change and its impacts**. New York, NY, USA: United Nations, 2015. Available at <https://sdgs.un.org/goals/goal13>. Accessed: 14th September 2024.

[62] JUSTER, N. J. **Organic Semiconductors**. Washington, DC, USA: ACS Publications, 1963.

[63] POCHETTINO, A.; SELLA, A. Photoelectric behavior of anthracene. **Acad. Lincei Rend**, v. 15, p. 355–363, 1906.

[64] EINSTEIN, A. Über einen die erzeugung und verwandlung des lichtes betreffenden heuristischen gesichtspunkt. **Annalen der Physik**, v. 322, n. 6, p. 132–148, 1905.

[65] HAAR, D. T. **The Old Quantum Theory**. Amsterdam, Netherlands: Elsevier, 2016.

[66] EINSTEIN, A. Zur theorie der lichterzeugung und lichtabsorption. **Annalen der Physik**, Wiley Online Library, v. 325, n. 6, p. 199–206, 1906.

[67] VOLMER, M. Different photoelectric phenomena in anthracene, their relation to one another, to fluorescence and to the formation of dianthracene. **Annalen der Physik**, v. 40, p. 775–96, 1913.

[68] MICHAELSON, H. B. The work function of the elements and its periodicity. **Journal of Applied Physics**, American Institute of Physics, v. 48, n. 11, p. 4729–4733, 1977.

[69] CHANCE, R.; BRAUN, C. Temperature dependence of intrinsic carrier generation in anthracene single crystals. **The Journal of Chemical Physics**, American Institute of Physics, v. 64, n. 9, p. 3573–3581, 1976.

[70] SMITH, R. A. **Semiconductors**. Cambridge, UK: Cambridge University Press, 1959.

[71] SZENT-GYÖRGYI, A. Towards a new biochemistry? **Science**, American Association for the Advancement of Science, v. 93, n. 2426, p. 609–611, 1941.

[72] HANNAY, N. B. (Ed.). **Semiconductors**. New York: Reinhold Publishing Corporation, 1959.

[73] CHIANG, C. K.; JR, C. F.; PARK, Y. W.; HEEGER, A. J.; SHIRAKAWA, H.; LOUIS, E. J.; GAU, S. C.; MACDIARMID, A. G. Electrical conductivity in doped polyacetylene. **Physical Review Letters**, APS, v. 39, n. 17, p. 1098–1101, 1977.

[74] SHIRAKAWA, H.; LOUIS, E. J.; MACDIARMID, A. G.; CHIANG, C. K.; HEEGER, A. J. Synthesis of electrically conducting organic polymers: halogen derivatives of polyacetylene,$(CH)_x$. **Journal of the Chemical Society, Chemical Communications**, Royal Society of Chemistry, n. 16, p. 578–580, 1977.

[75] TANG, C. W.; VANSLYKE, S. A. Organic electroluminescent diodes. **Applied Physics Letters**, American Institute of Physics, v. 51, n. 12, p. 913–915, 1987.

[76] KÖHLER, A.; BÄSSLER, H. **Electronic Processes in Organic Semiconductors: An Introduction**. Weinheim, Germany: John Wiley & Sons, 2015.

[77] POELKING, C. R. **The (Non-) Local Density of States of Electronic Excitations in Organic Semiconductors**. Cham, Switzerland: Springer, 2017.

[78] YU, C.; HE, J.-H.; CHENG, X.-F.; LIN, H.-Z.; YU, H.; LU, J.-M. An ion-in-conjugation-boosted organic semiconductor gas sensor operating at high temperature and immune to moisture. **Angewandte Chemie International Edition**, Wiley Online Library, v. 60, n. 28, p. 15328–15334, 2021.

[79] BORGES-GONZÁLEZ, J.; KOUSSEFF, C. J.; NIELSEN, C. B. Organic semiconductors for biological sensing. **Journal of Materials Chemistry C**, Royal Society of Chemistry, v. 7, n. 5, p. 1111–1130, 2019.

[80] ZANG, Y.; ZHANG, F.; HUANG, D.; GAO, X.; DI, C.-a.; ZHU, D. Flexible suspended gate organic thin-film transistors for ultra-sensitive pressure detection. **Nature Communications**, Nature Publishing Group UK London, v. 6, n. 1, p. 1–9, 2015.

[81] DAI, X.; MENG, Q.; ZHANG, F.; ZOU, Y.; DI, C.-a.; ZHU, D. Electronic structure engineering in organic thermoelectric materials. **Journal of Energy Chemistry**, Elsevier, v. 62, p. 204–219, 2021.

[82] DING, J.; LIU, Z.; ZHAO, W.; JIN, W.; XIANG, L.; WANG, Z.; ZENG, Y.; ZOU, Y.; ZHANG, F.; YI, Y. *et al.* Selenium-substituted diketopyrrolopyrrole polymer for high-performance p-type organic thermoelectric materials. **Angewandte Chemie International Edition**, Wiley Online Library, v. 58, n. 52, p. 18994–18999, 2019.

[83] WANG, Z.; CHEN, X.; YU, L.; GUO, S.; HU, Y.; HUANG, Y.; WANG, S.; QI, J.; HAN, C.; MA, X. *et al.* Polymer electrolyte dielectrics enable efficient exciton-polaron quenching in organic semiconductors for photostable organic transistors. **ACS Applied Materials & Interfaces**, ACS Publications, v. 14, n. 11, p. 13584–13592, 2022.

[84] KIM, J.; KIM, S. H.; AN, T. K.; PARK, S.; PARK, C. E. Highly stable fluorine-rich polymer treated dielectric surface for the preparation of solution-processed organic field-effect transistors. **Journal of Materials Chemistry C**, Royal Society of Chemistry, v. 1, n. 6, p. 1272–1278, 2013.

[85] CHEN, L. X. Organic solar cells: Recent progress and challenges. **ACS Energy Letters**, ACS Publications, v. 4, n. 10, p. 2537–2539, 2019.

[86] GAO, Y.; WU, Y.; LIU, Y.; LU, M.; YANG, L.; WANG, Y.; WILLIAM, W. Y.; BAI, X.; ZHANG, Y.; DAI, Q. Interface and grain boundary passivation for efficient and stable perovskite solar cells: The effect of terminal groups in hydrophobic fused benzothiadiazole-based organic semiconductors. **Nanoscale Horizons**, Royal Society of Chemistry, v. 5, n. 12, p. 1574–1585, 2020.

[87] HAINS, A. W.; LIANG, Z.; WOODHOUSE, M. A.; GREGG, B. A. Molecular semiconductors in organic photovoltaic cells. **Chemical Reviews**, ACS Publications, v. 110, n. 11, p. 6689–6735, 2010.

[88] CLAYDEN, J.; GREEVES, N.; WARREN, S. **Organic Chemistry**. Oxford, UK: Oxford University Press, 2012.

[89] KOOPMANS, T. Über die zuordnung von wellenfunktionen und eigenwerten zu den einzelnen elektronen eines atoms. **Physica**, Elsevier, v. 1, n. 1-6, p. 104–113, 1934.

[90] BREDAS, J.-L. Mind the gap! **Materials Horizons**, Royal Society of Chemistry, v. 1, n. 1, p. 17–19, 2014.

[91] HUMMEL, R. E. **Electrical Properties of Polymers, Ceramics, Dielectrics, and Amorphous Materials**. New York, NY, USA: Springer, 2001.

[92] KASHA, M. Characterization of electronic transitions in complex molecules. **Discussions of the Faraday Society**, Royal Society of Chemistry, v. 9, p. 14–19, 1950.

[93] KASHA, M.; RAWLS, H. R.; EL-BAYOUMI, M. A. The exciton model in molecular spectroscopy. **Pure and Applied Chemistry**, De Gruyter, v. 11, n. 3-4, p. 371–392, 1965.

[94] LAKOWICZ, J. R. **Principles of Fluorescence Spectroscopy**. 3. ed. New York, NY, USA: Springer, 2006.

[95] RUNGE, E.; GROSS, E. K. U. Density-functional theory for time-dependent systems. **Physical Review Letters**, American Physical Society, v. 52, p. 997–1000, Mar 1984.

[96] TAUC, J.; GRIGOROVICI, R.; VANCU, A. Optical properties and electronic structure of amorphous germanium. **Physica Status Solidi (b)**, Wiley Online Library, v. 15, n. 2, p. 627–637, 1966.

[97] ROPER, I. P.; BESLEY, N. A. The effect of basis set and exchange-correlation functional on time-dependent density functional theory calculations within the Tamm-Dancoff approximation of the x-ray emission spectroscopy of transition metal complexes. **The Journal of Chemical Physics**, AIP Publishing, v. 144, n. 11, p. 1–10, 2016.

[98] KÖRZDÖRFER, T.; SEARS, J. S.; SUTTON, C.; BRÉDAS, J.-L. Long-range corrected hybrid functionals for π-conjugated systems: Dependence of the range-separation parameter on conjugation length. **The Journal of Chemical Physics**, AIP Publishing, v. 135, n. 20, p. 1–6, 2011.

[99] FRENKEL, J. On the transformation of light into heat in solids. i. **Physical Review**, APS, v. 37, n. 1, p. 17–44, 1931.

[100] POPE, M.; SWENBERG, C. E. **Electronic Processes in Organic Crystals and Polymers**. New York, NY, USA: Oxford University Press, 1999.

[101] SARMA, M.; WONG, K.-T. Exciplex: an intermolecular charge-transfer approach for TADF. **ACS Applied Materials & Interfaces**, ACS Publications, v. 10, n. 23, p. 19279–19304, 2018.

[102] ZHANG, Y.; WANG, Y.; GAO, C.; NI, Z.; ZHANG, X.; HU, W.; DONG, H. Recent advances in n-type and ambipolar organic semiconductors and their multi-functional applications. **Chemical Society Reviews**, Royal Society of Chemistry, v. 52, n. 4, p. 1331–1381, 2023.

[103] HINRICHSEN, T. F.; CHAN, C. C.; MA, C.; PALEČEK, D.; GILLETT, A.; CHEN, S.; ZOU, X.; ZHANG, G.; YIP, H.-L.; WONG, K. S. *et al.* Long-lived and disorder-free charge transfer states enable endothermic charge separation in efficient non-fullerene organic solar cells. **Nature Communications**, Nature Publishing Group UK London, v. 11, n. 1, p. 1–10, 2020.

[104] BENATTO, L.; SOUSA, K. R. d. A.; KOEHLER, M. Driving force for exciton dissociation in organic solar cells: The influence of donor and acceptor relative orientation. **The Journal of Physical Chemistry C**, ACS Publications, v. 124, n. 25, p. 13580–13591, 2020.

[105] LI, Y.; HUANG, W.; ZHAO, D.; WANG, L.; JIAO, Z.; HUANG, Q.; WANG, P.; SUN, M.; YUAN, G. Recent progress in organic solar cells: a review on materials from acceptor to donor. **Molecules**, MDPI, v. 27, n. 6, p. 1–31, 2022.

[106] MARKS, R.; HALLS, J.; BRADLEY, D.; FRIEND, R.; HOLMES, A. The photovoltaic response in poly (p-phenylene vinylene) thin-film devices. **Journal of Physics: Condensed Matter**, IOP Publishing, v. 6, n. 7, p. 1379–1394, 1994.

[107] KNUPFER, M. Exciton binding energies in organic semiconductors. **Applied Physics A**, Springer, v. 77, p. 623–626, 2003.

[108] FU, J.; YANG, Q.; HUANG, P.; CHUNG, S.; CHO, K.; KAN, Z.; LIU, H.; LU, X.; LANG, Y.; LAI, H. *et al.* Rational molecular and device design enables organic solar cells approaching 20% efficiency. **Nature Communications**, Nature Publishing Group UK London, v. 15, n. 1, p. 1–10, 2024.

[109] LIU, Q.; JIANG, Y.; JIN, K.; QIN, J.; XU, J.; LI, W.; XIONG, J.; LIU, J.; XIAO, Z.; SUN, K. *et al.* 18% efficiency organic solar cells. **Science Bulletin**, v. 65, n. 4, p. 272–275, 2020.

[110] LIN, Y.; FIRDAUS, Y.; ISIKGOR, F. H.; NUGRAHA, M. I.; YENGEL, E.; HARRISON, G. T.; HALLANI, R.; EL-LABBAN, A.; FABER, H.; MA, C. *et al.* Self-assembled monolayer enables hole transport layer-free organic solar cells with 18% efficiency and improved operational stability. **ACS Energy Letters**, ACS Publications, v. 5, n. 9, p. 2935–2944, 2020.

[111] LIN, Y.; NUGRAHA, M. I.; FIRDAUS, Y.; SCACCABAROZZI, A. D.; ANIÉS, F.; EMWAS, A.-H.; YENGEL, E.; ZHENG, X.; LIU, J.; WAHYUDI, W. *et al.* A simple n-dopant derived from diquat boosts the efficiency of organic solar cells to 18.3%. **ACS Energy Letters**, ACS Publications, v. 5, n. 12, p. 3663–3671, 2020.

[112] XU, X.; ZHANG, G.; LI, Y.; PENG, Q. The recent progress of wide bandgap donor polymers towards non-fullerene organic solar cells. **Chinese Chemical Letters**, Elsevier, v. 30, n. 4, p. 809–825, 2019.

[113] DEY, S. Recent progress in molecular design of fused ring electron acceptors for organic solar cells. **Small**, Wiley Online Library, v. 15, n. 21, p. 1–38, 2019.

[114] KERSTING, R.; LEMMER, U.; MAHRT, R.; LEO, K.; KURZ, H.; BÄSSLER, H.; GÖBEL, E. Femtosecond energy relaxation in π-conjugated polymers. **Physical Review Letters**, APS, v. 70, n. 24, p. 3820–3823, 1993.

[115] KITTEL, C. **Introduction to Solid State Physics**. Hoboken, NJ, USA: John Wiley & Sons, Inc., 2005.

[116] BASSANI, F.; PARRAVICINI, G. P.; BALLINGER, R. A.; BIRMAN, J. L. **Electronic States and Optical Transitions in Solids**. New York, NY, USA: American Institute of Physics, 1976.

[117] BASSANI, G. F.; AGRANOVICH, V. M. **Electronic Excitations in Organic Based Nanostructures**. Amsterdam, Netherlands: Elsevier, 2003.

[118] COROPCEANU, V.; CHEN, X.-K.; WANG, T.; ZHENG, Z.; BRÉDAS, J.-L. Charge-transfer electronic states in organic solar cells. **Nature Reviews Materials**, Nature Publishing Group UK London, v. 4, n. 11, p. 689–707, 2019.

[119] GREGG, B. A.; HANNA, M. C. Comparing organic to inorganic photovoltaic cells: Theory, experiment, and simulation. **Journal of Applied Physics**, American Institute of Physics, v. 93, n. 6, p. 3605–3614, 2003.

[120] BRÉDAS, J.-L.; BELJONNE, D.; COROPCEANU, V.; CORNIL, J. Charge-transfer and energy-transfer processes in π-conjugated oligomers and polymers: a molecular picture. **Chemical Reviews**, ACS Publications, v. 104, n. 11, p. 4971–5004, 2004.

[121] DEIBEL, C.; STROBEL, T.; DYAKONOV, V. Role of the charge transfer state in organic donor–acceptor solar cells. **Advanced Materials**, Wiley Online Library, v. 22, n. 37, p. 4097–4111, 2010.

[122] GÉLINAS, S.; RAO, A.; KUMAR, A.; SMITH, S. L.; CHIN, A. W.; CLARK, J.; POLL, T. S. V. D.; BAZAN, G. C.; FRIEND, R. H. Ultrafast long-range charge separation in organic semiconductor photovoltaic diodes. **Science**, American Association for the Advancement of Science, v. 343, n. 6170, p. 512–516, 2014.

[123] GREGG, B. A. The photoconversion mechanism of excitonic solar cells. **MRS Bulletin**, Cambridge University Press, v. 30, n. 1, p. 20–22, 2005.

[124] BRAUN, C. L. Electric field assisted dissociation of charge transfer states as a mechanism of photocarrier production. **The Journal of Chemical Physics**, American Institute of Physics, v. 80, n. 9, p. 4157–4161, 1984.

[125] FERON, K.; ZHOU, X.; BELCHER, W.; DASTOOR, P. Exciton transport in organic semiconductors: Förster resonance energy transfer compared with a simple random walk. **Journal of Applied Physics**, AIP Publishing, v. 111, n. 4, p. 1–7, 2012.

[126] CLARKE, T. M.; DURRANT, J. R. Charge photogeneration in organic solar cells. **Chemical Reviews**, ACS Publications, v. 110, n. 11, p. 6736–6767, 2010.

[127] ONSAGER, L. Initial recombination of ions. **Physical Review**, American Physical Society, v. 54, n. 8, p. 554–557, 1938.

[128] FÖRSTER, T. Zwischenmolekulare energiewanderung und fluoreszenz. **Annalen der Physik**, Wiley Online Library, v. 437, n. 1-2, p. 55–75, 1948.

[129] DEXTER, D. L. A theory of sensitized luminescence in solids. **The Journal of Chemical Physics**, American Institute of Physics, v. 21, n. 5, p. 836–850, 1953.

[130] JANG, S.; JUNG, Y.; SILBEY, R. J. Nonequilibrium generalization of Förster–dexter theory for excitation energy transfer. **Chemical Physics**, Elsevier, v. 275, n. 1-3, p. 319–332, 2002.

[131] LAKOWICZ, J. R. **Principles of Fluorescence Spectroscopy**. New York, NY, USA: Springer Science & Business Media, 2013.

[132] BA, H. *et al.* Charge transport in disordered organic photoconductors. **Phys. Stat. Sol. B**, v. 175, p. 15–56, 1993.

[133] BRÉDAS, J.-L.; CALBERT, J. P.; FILHO, D. da S.; CORNIL, J. Organic semiconductors: A theoretical characterization of the basic parameters governing charge transport. **Proceedings of the National Academy of Sciences**, National Acad Sciences, v. 99, n. 9, p. 5804–5809, 2002.

[134] MANNA, B. Temperature dependence of resonance energy transfer in DCM doped anthracene nanoaggregates. **Journal of Luminescence**, Elsevier, v. 209, p. 379–386, 2019.

[135] LIU, Y.-X.; SUMMERS, M. A.; SCULLY, S. R.; MCGEHEE, M. D. Resonance energy transfer from organic chromophores to fullerene molecules. **Journal of Applied Physics**, AIP Publishing, v. 99, n. 9, p. 1–4, 2006.

[136] BELYAEV, A. K.; LEBEDEV, O. V. Nonadiabatic nuclear dynamics of atomic collisions based on branching classical trajectories. **Physical Review A**, APS, v. 84, n. 1, p. 1–4, 2011.

[137] BELYAEV, A. K.; LASSER, C.; TRIGILA, G. Landau–zener type surface hopping algorithms. **The Journal of Chemical Physics**, AIP Publishing, v. 140, n. 22, p. 1–10, 2014.

[138] PEULEN, T.-O.; OPANASYUK, O.; SEIDEL, C. A. Combining graphical and analytical methods with molecular simulations to analyze time-resolved FRET measurements of labeled macromolecules accurately. **The Journal of Physical Chemistry B**, ACS Publications, v. 121, n. 35, p. 8211–8241, 2017.

[139] TULLY, J. C. Molecular dynamics with electronic transitions. **The Journal of Chemical Physics**, v. 93, n. 2, p. 1061–1071, 1990.

[140] LUNT, R. R.; GIEBINK, N. C.; BELAK, A. A.; BENZIGER, J. B.; FORREST, S. R. Exciton diffusion lengths of organic semiconductor thin films measured by spectrally resolved photoluminescence quenching. **Journal of Applied Physics**, AIP Publishing, v. 105, n. 5, p. 1–7, 2009.

[141] BELJONNE, D.; CURUTCHET, C.; SCHOLES, G. D.; SILBEY, R. J. Beyond Förster resonance energy transfer in biological and nanoscale systems. **The Journal of Physical Chemistry B**, ACS Publications, v. 113, n. 19, p. 6583–6599, 2009.

[142] BACCHIOCCHI, C.; ZANNONI, C. Directional energy transfer in columnar liquid crystals: A computer-simulation study. **Physical Review E**, APS, v. 58, n. 3, p. 3237–3244, 1998.

[143] FEDCHENIA, I.; WESTLUND, P.-O. Influence of molecular reorientation on electronic energy transfer between a pair of mobile chromophores: The stochastic liouville equation combined with brownian dynamic simulation techniques. **Physical Review E**, APS, v. 50, n. 1, p. 555–565, 1994.

[144] FREDRICKSON, G. H. Concentration depolarization of fluorescence in the presence of molecular rotation. **The Journal of Chemical Physics**, American Institute of Physics, v. 88, n. 9, p. 5291–5299, 1988.

[145] SHAO, Y.; YANG, Y. Efficient organic heterojunction photovoltaic cells based on triplet materials. **Advanced Materials**, Wiley Online Library, v. 17, n. 23, p. 2841–2844, 2005.

[146] CHENG, X.; ICHIMURA, K.; FICHOU, D.; KOBAYASHI, T. Nanosecond time-resolved absorption spectra of thin films of α-conjugated thiophene oligomers. **Chemical Physics Letters**, Elsevier, v. 185, n. 3-4, p. 286–291, 1991.

[147] COOK, S.; OHKITA, H.; DURRANT, J. R.; KIM, Y.; BENSON-SMITH, J. J.; NELSON, J.; BRADLEY, D. D. Singlet exciton transfer and fullerene triplet formation in polymer-fullerene blend films. **Applied Physics Letters**, AIP Publishing, v. 89, n. 10, p. 1–3, 2006.

[148] MILLER, A.; ABRAHAMS, E. Impurity conduction at low concentrations. **Physical Review**, American Physical Society, v. 120, n. 3, p. 745–755, 1960.

[149] MARCUS, R. A. Chemical and electrochemical electron-transfer theory. **Annual Review of Physical Chemistry**, Annual Reviews, v. 15, n. 1, p. 155–196, 1964.

[150] MARCUS, R. A. On the theory of oxidation-reduction reactions involving electron transfer. i. **The Journal of Chemical Physics**, AIP Publishing, v. 24, n. 5, p. 966–978, 1956.

[151] SAKURAI, J. J.; NAPOLITANO, J. **Modern Quantum Mechanics**. 2nd. ed. Cambridge, UK: Cambridge University Press, 2017.

[152] BRYDEN, M. A.; MILLWARD, F.; LEE, O. S.; CORK, L.; GATHER, M. C.; STEFFEN, A.; ZYSMAN-COLMAN, E. Lessons learnt in photocatalysis–the influence of solvent polarity and the photostability of the photocatalyst. **Chemical Science**, Royal Society of Chemistry, v. 15, n. 10, p. 3741–3757, 2024.

[153] BLOM, P. W.; MIHAILETCHI, V. D.; KOSTER, L. J. A.; MARKOV, D. E. Device physics of polymer: fullerene bulk heterojunction solar cells. **Advanced Materials**, Wiley Online Library, v. 19, n. 12, p. 1551–1566, 2007.

[154] YABU, S.; SATO, H.; HIGASHI, M. Theoretical aspects of dexter-type excitation energy transfer for understanding optical phenomena on photosynthetic systems. **Chemical Physics Reviews**, AIP Publishing, v. 6, n. 1, p. 1–11, 2025.

[155] BALDO, M.; THOMPSON, M. E.; FORREST, S. High-efficiency fluorescent organic light-emitting devices using a phosphorescent sensitizer. **Nature**, Nature Publishing Group UK London, v. 403, n. 6771, p. 750–753, 2000.

[156] GAPONENKO, S. V.; DEMIR, H. V. Energy transfer processes. In: **Applied Nanophotonics**. [S.l.]: Cambridge University Press, 2018. cap. 7, p. 210–226.

[157] CHO, H.-H.; CONGRAVE, D. G.; GILLETT, A. J.; MONTANARO, S.; FRANCIS, H. E.; RIESGO-GONZALEZ, V.; YE, J.; CHOWDURY, R.; ZENG, W.; ETHERINGTON, M. K. *et al.* Suppression of dexter transfer by covalent encapsulation for efficient matrix-free narrowband deep blue hyperfluorescent oleds. **Nature Materials**, Nature Publishing Group UK London, v. 23, n. 4, p. 519–526, 2024.

[158] LANDAU, L. D. Zur theorie der energieübertragung ii. **Physikalische Zeitschrift der Sowjetunion**, v. 2, p. 46–51, 1932.

[159] ZENER, C. Non-adiabatic crossing of energy levels. **Proceedings of the Royal Society of London. Series A, Containing Papers of a Mathematical and Physical Character**, v. 137, n. 833, p. 696–702, 1932.

[160] SMOLUCHOWSKI, M. v. Versuch einer mathematischen theorie der koagulationskinetik kolloider lösungen. **Zeitschrift Für Physikalische Chemie**, De Gruyter Oldenbourg, v. 92, n. 1, p. 129–168, 1918.

[161] VALEUR, B.; BERBERAN-SANTOS, M. N. **Molecular fluorescence: principles and applications**. Weinheim, Germany: John Wiley & Sons, 2013.

[162] GENOVESE, D.; CINGOLANI, M.; RAMPAZZO, E.; PRODI, L.; ZACCHERONI, N. Static quenching upon adduct formation: a treatment without shortcuts and approximations. **Chemical Society Reviews**, Royal Society of Chemistry, v. 50, n. 15, p. 8414–8427, 2021.

[163] TANWAR, A. S.; PARUI, R.; GARAI, R.; CHANU, M. A.; IYER, P. K. Dual "static and dynamic" fluorescence quenching mechanisms based detection of TNT via a cationic conjugated polymer. **ACS Measurement Science Au**, ACS Publications, v. 2, n. 1, p. 23–30, 2021.

[164] SINGH, P.; ANAND, A.; KUMAR, V. Recent developments in biological activities of chalcones: A mini review. **European Journal of Medicinal Chemistry**, Elsevier, v. 85, p. 758–777, 2014.

[165] ZHUANG, C.; ZHANG, W.; SHENG, C.; ZHANG, W.; XING, C.; MIAO, Z. Chalcone: a privileged structure in medicinal chemistry. **Chemical Reviews**, ACS Publications, v. 117, n. 12, p. 7762–7810, 2017.

[166] RAMMOHAN, A.; REDDY, J. S.; SRAVYA, G.; RAO, C. N.; ZYRYANOV, G. V. Chalcone synthesis, properties and medicinal applications: a review. **Environmental Chemistry Letters**, Springer, v. 18, p. 433–458, 2020.

[167] SMITH, M. B. **March's Advanced Organic Chemistry: Reactions, Mechanisms, and Structure**. Hoboken, NJ, USA: John Wiley & Sons, 2020.

[168] GROTEWOLD, E. **The Science of Flavonoids**. New York, NY, USA: Springer, 2006.

[169] MORITA, H.; TAKAHASHI, Y.; NOGUCHI, H.; ABE, I. Enzymatic formation of unnatural aromatic polyketides by chalcone synthase. **Biochemical and Biophysical Research Communications**, Elsevier, v. 279, n. 1, p. 190–195, 2000.

[170] CALVINO, V.; PICALLO, M.; LÓPEZ-PEINADO, A.; MARTÍN-ARANDA, R.; DURÁN-VALLE, C. Ultrasound accelerated claisen–schmidt condensation: A green route to chalcones. **Applied Surface Science**, Elsevier, v. 252, n. 17, p. 6071–6074, 2006.

[171] BUSZEK, K. R.; BROWN, N. N-vinylpyridinium and-ammonium tetrafluoroborate salts: new electrophilic coupling partners for pd (0)-catalyzed suzuki cross-coupling reactions. **Organic Letters**, ACS Publications, v. 9, n. 4, p. 707–710, 2007.

[172] ZHOU, Y.; LI, X.; HOU, S.; XU, J. Facile synthesis of dihydrochalcones via the $AlCl_3$-promoted tandem friedel–crafts acylation and alkylation of arenes with 2-alkenoyl chlorides. **Journal of Molecular Catalysis A: Chemical**, Elsevier, v. 365, p. 203–211, 2012.

[173] ZAINURI, D. A.; RAZAK, I. A.; ARSHAD, S. Crystal structure and theoretical studies of two π-conjugated fused-ring chalcones:(e)-1-(anthracen-9-yl)-3-(9-ethyl-9h-carbazol-3-yl) prop-2-en-1-one and (e)-1-(anthracen-9-yl)-3-[4-(9h-carbazol-9-yl) phenyl] prop-2-en-1-one. **Acta Crystallographica Section E: Crystallographic Communications**, International Union of Crystallography, v. 74, n. 9, p. 1302–1308, 2018.

[174] PEREIRA, R.; SILVA, A. M.; RIBEIRO, D.; SILVA, V. L.; FERNANDES, E. Bis-chalcones: A review of synthetic methodologies and anti-inflammatory effects. **European Journal of Medicinal Chemistry**, Elsevier, v. 252, p. 1–22, 2023.

[175] SOWMYA, P.; PRAKASH, S.; JOSEPH, A. A bis-chalcone based colorimetric probe for the selective detection of bisulfite/sulfite anions: exploring surfactant promoted michael addition of anions to α, β-unsaturated ketones. **RSC Advances**, Royal Society of Chemistry, v. 13, n. 4, p. 2552–2560, 2023.

[176] ASIRI, A. M.; MARWANI, H. M.; ALAMRY, K. A.; AL-AMOUDI, M. S.; KHAN, S. A.; EL-DALY, S. A. Green synthesis, characterization, photophysical and electrochemical properties of bis-chalcones. **International Journal of Electrochemical Science**, Elsevier, v. 9, n. 2, p. 799–809, 2014.

[177] GOMES, M. N.; MURATOV, E. N.; PEREIRA, M.; PEIXOTO, J. C.; ROSSETO, L. P.; CRAVO, P. V.; ANDRADE, C. H.; NEVES, B. J. Chalcone derivatives: promising starting points for drug design. **Molecules**, MDPI, v. 22, n. 8, p. 1–25, 2017.

[178] GIACOLETTO, N.; DUMUR, F. Recent advances in bis-chalcone-based photoinitiators of polymerization: from mechanistic investigations to applications. **Molecules**, MDPI, v. 26, n. 11, p. 1–38, 2021.

[179] TSUKERMAN, S.; MASLENNIKOVA, V.; NIKITCHENKO, V.; LAVRUSHIN, V. Electronic spectra of isomeric para-dichalcones and para-dichalcone analogs. **Journal of Applied Spectroscopy**, Springer, v. 12, n. 1, p. 76–80, 1970.

[180] ALVIM, H. G.; FAGG, E. L.; OLIVEIRA, A. L. de; OLIVEIRA, H. C. de; FREITAS, S. M.; XAVIER, M.-A. E.; SOARES, T. A.; GOMES, A. F.; GOZZO, F. C.; SILVA, W. A. *et al.* Probing deep into the interaction of a fluorescent chalcone derivative and bovine serum albumin (bsa): an experimental and computational study. **Organic & Biomolecular Chemistry**, Royal Society of Chemistry, v. 11, n. 29, p. 4764–4777, 2013.

[181] PAVIA, D. L.; LAMPMAN, G. M.; KRIZ, G. S.; VYVYAN, J. R. **Introduction to Spectroscopy**. 5th. ed. Stamford, CT: Cengage Learning, 2015.

[182] DOROTEIO, N. L. **Synthesis of Symmetrical and Unsymmetrical Bis-Chalcone Analogs**. 88 p. Dissertação (Master's thesis) — University of Brasília, Institute of Chemistry, Graduate Program in Chemistry, 2016.

[183] ZHOU, B.; JIANG, P.; LU, J.; XING, C. Characterization of the fluorescence properties of 4-dialkylaminochalcones and investigation of the cytotoxic mechanism of chalcones. **Archiv der Pharmazie**, Wiley Online Library, v. 349, n. 7, p. 539–552, 2016.

[184] OSTROVERKHOVA, O. Organic optoelectronic materials: mechanisms and applications. **Chemical Reviews**, ACS Publications, v. 116, n. 22, p. 13279–13412, 2016.

[185] KUKHTA, N. A.; BRYCE, M. R. Dual emission in purely organic materials for optoelectronic applications. **Materials Horizons**, Royal Society of Chemistry, v. 8, n. 1, p. 33–55, 2021.

[186] HIRONO, A.; SAKAI, H.; KOCHI, S.; SATO, T.; HASOBE, T. Electrochemical properties and excited-state dynamics of azaperylene derivatives. **The Journal of Physical Chemistry B**, ACS Publications, v. 124, n. 44, p. 9921–9930, 2020.

[187] MELLADO, M.; SARIEGO-KLUGE, R.; VALDÉS-NAVARRO, F.; GONZÁLEZ, C.; SÁNCHEZ-GONZÁLEZ, R.; PIZARRO, N.; VILLENA, J.; JARA-GUTIERREZ, C.; CORDOVA, C.; BRAVO, M. A. *et al.* Synthesis of fluorescent chalcones, photophysical properties, quantitative structure-activity relationship and their biological application. **Spectrochimica Acta Part A: Molecular and Biomolecular Spectroscopy**, Elsevier, v. 291, p. 1–13, 2023.

[188] SHAFIQ, I.; KHALID, M.; MUNEER, M.; ASGHAR, M. A.; BABY, R.; AHMED, S.; AHAMAD, T.; MORAIS, S. F. de A.; BRAGA, A. A. The impact of structural modifications into benzodithiophene compounds on electronic and optical properties for organic solar cells. **Materials Chemistry and Physics**, Elsevier, v. 308, p. 1–13, 2023.

[189] MEHBOOB, M. Y.; HUSSAIN, R.; ADNAN, M.; IRSHAD, Z.; KHALID, M. Impact of π-linker modifications on the photovoltaic performance of rainbow-shaped acceptor molecules for high performance organic solar cell applications. **Physica B: Condensed Matter**, Elsevier, v. 625, p. 1–11, 2022.

[190] POOLE, C. F.; ATAPATTU, S. N. Recent advances for estimating environmental properties for small molecules from chromatographic measurements and the solvation parameter model. **Journal of Chromatography A**, Elsevier, v. 1687, p. 1–25, 2023.

[191] MENNUCCI, B. Modeling absorption and fluorescence solvatochromism with qm/classical approaches. **International Journal of Quantum Chemistry**, Wiley Online Library, v. 115, n. 18, p. 1202–1208, 2015.

[192] ESTEVES, C. I. C.; FONTES, L. F. B.; BORGES, A. F. N.; ROCHA, J.; SILVA, A. M. S.; GUIEU, S. Push-pulling induces the excited-state intramolecular proton transfer in 2′-aminochalcones. **Dyes and Pigments**, Elsevier, v. 202, p. 1–7, 2022.

[193] TAY, M. G.; TIONG, M. H.; CHIA, Y. Y.; KUAN, S. H. C.; LIU, Z.-Q. A way to improve luminescent efficiency of bis-chalcone derivatives. **Journal of Chemistry**, Wiley Online Library, v. 2016, n. 1, p. 1–8, 2016.

[194] MEZGEBE, K.; MELAKU, Y.; MULUGETA, E. Synthesis and pharmacological activities of chalcone and its derivatives bearing n-heterocyclic scaffolds: A review. **ACS Omega**, ACS Publications, v. 8, n. 22, p. 19194–19211, 2023.

[195] SILVA, A. A. da; MAIA, P. I. da S.; LOPES, C. D.; ALBUQUERQUE, S. de; VALLE, M. S. Synthesis, characterization and antichagasic evaluation of thiosemicarbazones prepared from chalcones and dibenzalacetones. **Journal of Molecular Structure**, Elsevier, v. 1232, p. 1–6, 2021.

[196] LIMA, E. M.; FERNANDO, L. M.; FELIX, L. P.; FILHO, A. A. de O.; NETO, A. N. C.; JR, R. T. M.; TELES, Y. C. First complete nmr data and theoretical study of an antimicrobial formylated dihydrochalcone from psidium guineense sw. **Natural Product Research**, Taylor & Francis, v. 36, n. 1, p. 419–423, 2021.

[197] Chemcraft. **Graphical Software for Visualization of Quantum Chemistry Computations**. Novosibirsk, Russia: Chemcraft Software, 2018. Available at <https://www.chemcraftprog.com>. Accessed: 4th June 2024.

[198] PARR, R. G.; YANG, W. **Density-Functional Theory of Atoms and Molecules**. New York: Oxford University Press, 1989.

[199] LAURENT, A. D.; JACQUEMIN, D. TD-DFT benchmarks: a review. **International Journal of Quantum Chemistry**, Wiley Online Library, v. 113, n. 17, p. 2019–2039, 2013.

[200] BIOVIA, D. S. Materials studio. **R2 (Dassault Systèmes BIOVIA, San Diego**, 2017.

[201] ZHAO, Y.; TRUHLAR, D. G. The m06 suite of density functionals for main group thermochemistry, thermochemical kinetics, noncovalent interactions, excited states, and transition elements: two new functionals and systematic testing of four m06-class functionals and 12 other functionals. **Theoretical Chemistry Accounts**, Springer, v. 120, p. 215–241, 2008.

[202] TOMASI, J.; MENNUCCI, B.; CAMMI, R. Quantum mechanical continuum solvation models. **Chemical Reviews**, ACS Publications, v. 105, n. 8, p. 2999–3094, 2005.

[203] FRISCH, M. J.; TRUCKS, G. W.; SCHLEGEL, H. B.; SCUSERIA, G. E.; ROBB, M. A.; CHEESEMAN, J. R.; SCALMANI, G.; BARONE, V.; PETERSSON, G. A.; NAKATSUJI, H.; LI, X.; CARICATO, M.; MARENICH, A. V.; BLOINO, J.; JANESKO, B. G.; GOMPERTS, R.;

MENNUCCI, B.; HRATCHIAN, H. P.; ORTIZ, J. V.; IZMAYLOV, A. F.; SONNENBERG, J. L.; WILLIAMS-YOUNG, D.; DING, F.; LIPPARINI, F.; EGIDI, F.; GOINGS, J.; PENG, B.; PETRONE, A.; HENDERSON, T.; RANASINGHE, D.; ZAKRZEWSKI, V. G.; GAO, J.; REGA, N.; ZHENG, G.; LIANG, W.; HADA, M.; EHARA, M.; TOYOTA, K.; FUKUDA, R.; HASEGAWA, J.; ISHIDA, M.; NAKAJIMA, T.; HONDA, Y.; KITAO, O.; NAKAI, H.; VREVEN, T.; THROSSELL, K.; MONTGOMERY Jr., J. A.; PERALTA, J. E.; OGLIARO, F.; BEARPARK, M. J.; HEYD, J. J.; BROTHERS, E. N.; KUDIN, K. N.; STAROVEROV, V. N.; KEITH, T. A.; KOBAYASHI, R.; NORMAND, J.; RAGHAVACHARI, K.; RENDELL, A. P.; BURANT, J. C.; IYENGAR, S. S.; TOMASI, J.; COSSI, M.; MILLAM, J. M.; KLENE, M.; ADAMO, C.; CAMMI, R.; OCHTERSKI, J. W.; MARTIN, R. L.; MOROKUMA, K.; FARKAS, O.; FORESMAN, J. B.; FOX, D. J. **Gaussian~09 Revision A.01**. 2009. Gaussian Inc. Wallingford CT.

[204] National Institute of Standards and Technology (NIST). **Computational Chemistry Comparison and Benchmark Database, NIST Standard Reference Database Number 101**. Gaithersburg, MD, USA: NIST, 2023. Available at <https://cccbdb.nist.gov>. Accessed: 12th May 2024.

[205] GROSS, a. E.; DOBSON, J.; PETERSILKA, M. Density functional theory of time-dependent phenomena. **Density Functional Theory II: Relativistic and Time Dependent Extensions**, Springer, p. 81–172, 2005.

[206] HERBERT, J. M. Density-functional theory for electronic excited states. In: MONARI, A.; LANZANI, G.; GONZáLEZ, L. (Ed.). **Theoretical and Computational Photochemistry**. Amsterdam: Elsevier, 2023. p. 69–118.

[207] TSUNEDA, T. Kohn–sham method. In: TSUNEDA, T. (Ed.). **Density Functional Theory in Quantum Chemistry**. Tokyo: Springer, 2014. p. 79–99.

[208] LEVINE, I. N. **Quantum Chemistry**. 6th. ed. Upper Saddle River, NJ: Pearson Prentice Hall, 2009.

[209] VONCI, M.; GIANSIRACUSA, M. J.; GABLE, R. W.; HEUVEL, W. Van den; LATHAM, K.; MOUBARAKI, B.; MURRAY, K. S.; YU, D.; MOLE, R. A.; SONCINI, A. *et al. Ab initio* calculations as a quantitative tool in the inelastic neutron scattering study of a single-molecule magnet analogue. **Chemical Communications**, Royal Society of Chemistry, v. 52, n. 10, p. 2091–2094, 2016.

[210] Schrödinger, LLC. **The PyMOL Molecular Graphics System, Version 1.8**. New York, NY, USA: Schrödinger, LLC, 2015. Available at <https://pymol.org/>. Accessed: 4th June 2024.

[211] PALLIKARA, I.; KAYASTHA, P.; SKELTON, J. M.; WHALLEY, L. D. The physical significance of imaginary phonon modes in crystals. **Electronic Structure**, IOP Publishing, v. 4, n. 3, p. 1–19, 2022.

[212] DABROWSKI, J.; KAMIENSKA-TRELA, K. Electronic spectra of. alpha.,. beta.-unsaturated carbonyl compounds. i. an evaluation of increments characteristic of changes in configuration (cis/trans) and conformation (s-cis/s-trans) based on direct observation of the isomerization of enamino aldehydes and ketones. **Journal of the American Chemical Society**, ACS Publications, v. 98, n. 10, p. 2826–2834, 1976.

[213] AKSÖZ, B. E.; ERTAN, R. Spectral properties of chalcones ii. **Fabad J. Pharm. Sci**, v. 37, n. 4, p. 205–216, 2012.

[214] CHANTRAPROMMA, S.; RUANWAS, P.; BOONNAK, N.; CHANTRAPROMMA, K.; FUN, H.-K. Synthesis, antityrosinase activity of curcumin analogues, and crystal structure of (1 e, 4E)-1, 5-bis (4-ethoxyphenyl) penta-1, 4-dien-3-one. **Crystallography Reports**, Springer, v. 61, p. 1081–1085, 2016.

[215] COSTA, P.; PILLI, R.; PINHEIRO, S.; BAKUZIS, P. **The Chemistry of Carbonyl Compounds and Derivatives**. Cambridge, UK: Royal Society of Chemistry, 2022.

[216] BARROW, G. M. Conjugation and the intensity of the infrared carbonyl band. **The Journal of Chemical Physics**, American Institute of Physics, v. 21, n. 11, p. 2008–2011, 1953.

[217] WANG, Y.-H.; ZOU, J.-W.; ZHANG, B.; LU, Y.-X.; JIN, H.-X.; YU, Q.-S. Enone–dienol tautomerism of but-2-enal and substituent effect: A theoretical study. **Journal of Molecular Structure: THEOCHEM**, Elsevier, v. 755, n. 1-3, p. 31–37, 2005.

[218] PAVIA, D. L.; LAMPMAN, G. M.; KRIZ, G. S.; VYVYAN, J. R. **Introduction to Spectroscopy**. 5th. ed. Stamford, CT: Cengage Learning, 2015.

[219] VDOVENKO, S. I.; GERUS, I. I.; ZHUK, Y. I.; KUKHAR, V. P.; PAGACZ-KOSTRZEWA, M.; WIERZEJEWSKA, M.; DANILIUC, C.-G. The conformational analysis of push-pull enaminones using ftir and nmr spectroscopy, and quantum chemical calculations. vi. β- n- methyl-aminovinyl trifluoromethyl ketone and α- methyl- β- n- methylaminovinyl trifluoromethyl ketone. **Journal of Molecular Structure**, Elsevier, v. 1128, p. 741–753, 2017.

[220] CORNATON, Y.; RINGHOLM, M.; LOUANT, O.; RUUD, K. Analytic calculations of anharmonic infrared and raman vibrational spectra. **Physical Chemistry Chemical Physics**, Royal Society of Chemistry, v. 18, n. 5, p. 4201–4215, 2016.

[221] HAOYU, S. Y.; FIEDLER, L. J.; ALECU, I.; TRUHLAR, D. G. Computational thermochemistry: Automated generation of scale factors for vibrational frequencies calculated by electronic structure model chemistries. **Computer Physics Communications**, Elsevier, v. 210, p. 132–138, 2017.

[222] DEL-OSO, J. A.; FRONTANA-URIBE, B. A.; MALDONADO, J.-L.; RIVERA, M.; TAPIA-TAPIA, M.; ROA-MORALES, G. Electrochemical deposition of poly [ethylene-dioxythiophene](pedot) films on ito electrodes for organic photovoltaic cells: control of morphology, thickness, and electronic properties. **Journal of Solid State Electrochemistry**, Springer, v. 22, p. 2025–2037, 2018.

[223] ZARZYCKI, P.; ZARZYCKA, M.; ŚLĄCZKA, M.; CLIFTON, V. Acetonitrile, the polarity chameleon. **Analytical and Bioanalytical Chemistry**, Springer, v. 397, p. 905–908, 2010.

[224] LAMBERT, J.-H. ***Photometria sive de mensura et gradibus luminis, colorum et umbrae***. Augsburg: Sumptibus Viduae Eberhardi Klett, 1760. Printed by Christophorus Petrus Detleffsen.

[225] BEER, A. Bestimmung der absorption des rothen lichts in farbigen flüssigkeiten. **Annalen der Physik**, Wiley-VCH, v. 162, n. 5, p. 78–88, 1852.

[226] RYBKIN, V. V. Franck–condon theory of quantum mechanochemistry. **The Journal of Physical Chemistry A**, ACS Publications, v. 121, n. 30, p. 5758–5762, 2017.

[227] HAZRA, A.; CHANG, H. H.; NOOIJEN, M. First principles simulation of the uv absorption spectrum of ethylene using the vertical franck-condon approach. **The Journal of Chemical Physics**, American Institute of Physics, v. 121, n. 5, p. 2125–2136, 2004.

[228] WOODWARD, R. B. Structure and the absorption spectra of α, β-unsaturated ketones. **Journal of the American Chemical Society**, ACS Publications, v. 63, n. 4, p. 1123–1126, 1941.

[229] CHOPRA, K.; MAJOR, S.; PANDYA, D. Transparent conductors—a status review. **Thin Solid Films**, Elsevier, v. 102, n. 1, p. 1–46, 1983.

[230] MIKHEEV, Y. A.; GUSEVA, L.; ERSHOV, Y. A. Origin of the coloration and structure of azobenzene chromogen. **Russian Journal of Physical Chemistry A**, Springer, v. 89, p. 2036–2050, 2015.

[231] MIZUGUCHI, J.; WOODEN, G. A large bathochromic shift from the solution to the solid state in 1, 4-diketo-3, 6-diphenyl-pyrrolo-[3, 4-c]-pyrrole. **Berichte der Bunsengesellschaft f"ur Physikalische Chemie**, Wiley Online Library, v. 95, n. 10, p. 1264–1274, 1991.

[232] WOLF, T.; MYHRE, R. H.; CRYAN, J.; CORIANI, S.; SQUIBB, R.; BATTISTONI, A.; BERRAH, N.; BOSTEDT, C.; BUCKSBAUM, P.; COSLOVICH, G. *et al.* Probing ultrafast π–π^*/n–π^* internal conversion in organic chromophores via k-edge resonant absorption. **Nature Communications**, Nature Publishing Group UK London, v. 8, n. 1, p. 1–7, 2017.

[233] GRABOWSKI, Z. R.; ROTKIEWICZ, K.; RETTIG, W. Structural changes accompanying intramolecular electron transfer: focus on twisted intramolecular charge-transfer states and structures. **Chemical Reviews**, ACS Publications, v. 103, n. 10, p. 3899–4032, 2003.

[234] REICHARDT, C.; WELTON, T. **Solvents and solvent effects in organic chemistry**. Weinheim, Germany: John Wiley & Sons, 2010.

[235] PITT, C. G. Hyperconjugation and its role in group iv chemistry. **Journal of Organometallic Chemistry**, Elsevier, v. 61, p. 49–70, 1973.

[236] PEARSON, R. G. Hard and soft acids and bases. **Journal of the American Chemical society**, ACS Publications, v. 85, n. 22, p. 3533–3539, 1963.

[237] PARR, R. G.; SZENTPÁLY, L. v.; LIU, S. Electrophilicity index. **Journal of the American Chemical Society**, ACS Publications, v. 121, n. 9, p. 1922–1924, 1999.

[238] PARR, R. G.; PEARSON, R. G. Absolute hardness: companion parameter to absolute electronegativity. **Journal of the American Chemical Society**, ACS Publications, v. 105, n. 26, p. 7512–7516, 1983.

[239] ZHU, L.; YI, Y.; WEI, Z. Exciton binding energies of nonfullerene small molecule acceptors: implication for exciton dissociation driving forces in organic solar cells. **The Journal of Physical Chemistry C**, ACS Publications, v. 122, n. 39, p. 22309–22316, 2018.

[240] TAMAI, Y. Charge generation in organic solar cells: Journey toward 20% power conversion efficiency: Special issue: Emerging investigators. **Aggregate**, Wiley Online Library, v. 3, n. 6, p. 1–29, 2022.

[241] WANG, Z.; SUN, C.; XU, X.; LIU, Y.; CHEN, Z.; YANG, Y. M.; ZHU, H. Long-range hot charge transfer exciton dissociation in an organic/2d semiconductor hybrid excitonic heterostructure. **Journal of the American Chemical Society**, ACS Publications, v. 145, n. 20, p. 11227–11235, 2023.

[242] GORENFLOT, J.; PAULKE, A.; PIERSIMONI, F.; WOLF, J.; KAN, Z.; CRUCIANI, F.; LABBAN, A. E.; NEHER, D.; BEAUJUGE, P. M.; LAQUAI, F. From recombination dynamics to device performance: quantifying the efficiency of exciton dissociation, charge separation, and extraction in bulk heterojunction solar cells with fluorine-substituted polymer donors. **Advanced Energy Materials**, Wiley Online Library, v. 8, n. 4, p. 1–12, 2018.

[243] EHRLICH, S.; MOELLMANN, J.; GRIMME, S. Dispersion-corrected density functional theory for aromatic interactions in complex systems. **Accounts of Chemical Research**, ACS Publications, v. 46, n. 4, p. 916–926, 2013.

[244] KRISTYÁN, S.; PULAY, P. Can (semi) local density functional theory account for the london dispersion forces? **Chemical Physics Letters**, Elsevier, v. 229, n. 3, p. 175–180, 1994.

[245] PÉREZ-JORDÁ, J.; BECKE, A. D. A density-functional study of van der waals forces: rare gas diatomics. **Chemical Physics Letters**, Elsevier, v. 233, n. 1-2, p. 134–137, 1995.

[246] MULLIKEN, R. S. Molecular compounds and their spectra. iii. the interaction of electron donors and acceptors. **The Journal of Physical Chemistry**, ACS Publications, v. 56, n. 7, p. 801–822, 1952.

[247] BLOCH, F. Zur theorie des ferromagnetismus. **Zeitschrift Für Physik**, Springer, v. 61, n. 3, p. 206–219, 1930.

[248] KOEPPE, R.; SARICIFTCI, N. Photoinduced charge and energy transfer involving fullerene derivatives. **Photochemical & Photobiological Sciences**, Springer, v. 5, n. 12, p. 1122–1131, 2006.

[249] ZHU, X.-Y.; YANG, Q.; MUNTWILER, M. Charge-transfer excitons at organic semiconductor surfaces and interfaces. **Accounts of Chemical Research**, ACS Publications, v. 42, n. 11, p. 1779–1787, 2009.

[250] SUGIE, A.; NAKANO, K.; TAJIMA, K.; OSAKA, I.; YOSHIDA, H. Dependence of exciton binding energy on bandgap of organic semiconductors. **The Journal of Physical Chemistry Letters**, ACS Publications, v. 14, n. 50, p. 11412–11420, 2023.

[251] CUNNINGHAM, P. D.; LANE, P. A.; MELINGER, J. S.; ESENTURK, O.; HEILWEIL, E. J. Probing charge transfer and hot carrier dynamics in organic solar cells with terahertz spectroscopy. In: ANWAR, M. F.; CROWE, T. W.; MANZUR, T. (Ed.). **Terahertz Physics, Devices, and Systems X: Advanced Applications in Industry and Defense**. Bellingham, WA, USA: SPIE, 2016. v. 9856, p. 98560Y.

[252] PELZER, K. M.; DARLING, S. B. Charge generation in organic photovoltaics: a review of theory and computation. **Molecular Systems Design & Engineering**, Royal Society of Chemistry, v. 1, n. 1, p. 10–24, 2016.

[253] FERON, K.; BELCHER, W. J.; FELL, C. J.; DASTOOR, P. C. Organic solar cells: understanding the role of Förster resonance energy transfer. **International Journal of Molecular**

Sciences, Molecular Diversity Preservation International (MDPI), v. 13, n. 12, p. 17019–17047, 2012.

[254] YAVUZ, I.; LOPEZ, S. A. Understanding dispersive charge-transport in crystalline organic-semiconductors. **Physical Chemistry Chemical Physics**, Royal Society of Chemistry, v. 19, n. 1, p. 231–236, 2017.

[255] WU, J.; LEE, J.; CHIN, Y.-C.; YAO, H.; CHA, H.; LUKE, J.; HOU, J.; KIM, J.-S.; DURRANT, J. R. Exceptionally low charge trapping enables highly efficient organic bulk heterojunction solar cells. **Energy & Environmental Science**, Royal Society of Chemistry, v. 13, n. 8, p. 2422–2430, 2020.

[256] HANEEF, H. F.; ZEIDELL, A. M.; JURCHESCU, O. D. Charge carrier traps in organic semiconductors: a review on the underlying physics and impact on electronic devices. **Journal of Materials Chemistry C**, Royal Society of Chemistry, v. 8, n. 3, p. 759–787, 2020.

[257] FAZZI, D.; BARBATTI, M.; THIEL, W. Hot and cold charge-transfer mechanisms in organic photovoltaics: insights into the excited states of donor/acceptor interfaces. **The Journal of Physical Chemistry Letters**, v. 8, n. 19, p. 4727–4734, 2017.

[258] CARSTEN, B.; SZARKO, J. M.; SON, H. J.; WANG, W.; LU, L.; HE, F.; ROLCZYNSKI, B. S.; LOU, S. J.; CHEN, L. X.; YU, L. Examining the effect of the dipole moment on charge separation in donor–acceptor polymers for organic photovoltaic applications. **Journal of the American Chemical Society**, ACS Publications, v. 133, n. 50, p. 20468–20475, 2011.

[259] BERNARDO, B.; CHEYNS, D.; VERREET, B.; SCHALLER, R. D.; RAND, B. P.; GIEBINK, N. C. Delocalization and dielectric screening of charge transfer states in organic photovoltaic cells. **Nature Communications**, Nature Publishing Group, v. 5, p. 1–7, 2014.

[260] RAY, A.; CHATTOPADHYAY, S.; BHATTACHARYA, S. Photophysical and theoretical insights on non-covalently linked fullerene–zinc phthalocyanine complexes. **Spectrochimica Acta Part A: Molecular and Biomolecular Spectroscopy**, Elsevier, v. 79, n. 5, p. 1435–1442, 2011.

[261] OVCHENKOVA, E. N.; BICHAN, N. G.; TSATURYAN, A. A.; LOMOVA, T. N. Non-covalent self-assembly of substituted phthalocyanine with C_{60}, C_{70}, and 9-phenylanthracene: spectroscopic insights and DFT calculations. **Tetrahedron**, Elsevier, p. 1–9, 2024.

[262] DENNINGTON, R.; KEITH, T. A.; MILLAM, J. M. **GaussView, Version 6.0**. Wallingford, CT, USA: Gaussian, Inc., 2019. Available at <https://gaussian.com/gaussview6/>. Accessed: 4th June 2024.

[263] FORESMAN, J. B.; FRISCH, A. **Exploring Chemistry with Electronic Structure Methods**. 2nd. ed. Pittsburgh, PA, USA: Gaussian, Inc., 1996.

[264] PULAY, P. *Ab initio* calculation of force constants and equilibrium geometries in polyatomic molecules. i. theory. **Molecular Physics**, v. 17, n. 2, p. 197–204, 1969.

[265] ATKINS, P. W.; FRIEDMAN, R. S. **Molecular quantum mechanics**. Oxford, UK: Oxford University Press, 2011.

[266] LENNARD, J.; JONES, I. On the determination of molecular fields.—i. from the variation of the viscosity of a gas with temperature. **Proceedings of the Royal Society of London. Series A, containing papers of a mathematical and physical character**, The Royal Society, v. 106, n. 738, p. 441–462, 1924.

[267] MIE, G. Beiträge zur optik trüber medien, speziell kolloidaler metallösungen. **Annalen der Physik**, Wiley Online Library, v. 330, n. 3, p. 377–445, 1908.

[268] JONES, J. E. On the determination of molecular fields.—ii. from the equation of state of a gas. **Proceedings of the Royal Society of London. Series A, Containing Papers of a Mathematical and Physical Character**, The Royal Society London, v. 106, n. 738, p. 463–477, 1924.

[269] WANG, X.; RAMÍREZ-HINESTROSA, S.; DOBNIKAR, J.; FRENKEL, D. The lennard-jones potential: when (not) to use it. **Physical Chemistry Chemical Physics**, Royal Society of Chemistry, v. 22, n. 19, p. 10624–10633, 2020.

[270] MOSCATO, P.; HAQUE, M. N. New alternatives to the lennard-jones potential. **Scientific Reports**, Nature Publishing Group UK London, v. 14, n. 1, p. 1–10, 2024.

[271] SCHLEGEL, H. B. Exploring potential energy surfaces for chemical reactions: An overview of some practical methods. **Journal of Computational Chemistry**, v. 24, n. 12, p. 1514–1527, 2003.

[272] TAJTI, A.; KOZMA, B.; SZALAY, P. G. Improved description of charge-transfer potential energy surfaces via spin-component-scaled cc2 and adc (2) methods. **Journal of Chemical Theory and Computation**, v. 17, n. 1, p. 439–449, 2020.

[273] MCQUARRIE, D. A. **Statistical Mechanics**. Sausalito, CA: University Science Books, 2000.

[274] LEE, C.; YANG, W.; PARR, R. G. Development of the colle-salvetti correlation-energy formula into a functional of the electron density. **Physical Review B**, v. 37, n. 2, p. 785–789, 1988.

[275] HERZBERG, G. Molecular spectra and molecular structure: Infrared and raman spectra of polyatomic molecules. **Van Nostrand Reinhold Company**, Princeton University Press, 1945.

[276] HUMMELEN, J. C.; KNIGHT, B. W.; LEPEQ, F.; WUDL, F.; YAO, J.; WILKINS, C. L. Preparation and characterization of fulleroid and methanofullerene derivatives. **The Journal of Organic Chemistry**, ACS Publications, v. 60, n. 3, p. 532–538, 1995.

[277] WANG, C. I.; HUA, C. C. Solubility of c60 and pcbm in organic solvents. **The Journal of Physical Chemistry B**, ACS Publications, v. 119, n. 45, p. 14496–14504, 2015.

[278] MARCUS, Y.; SMITH, A. L.; KOROBOV, M.; MIRAKYAN, A.; AVRAMENKO, N.; STUKALIN, E. Solubility of C_{60} fullerene. **The Journal of Physical Chemistry B**, ACS Publications, v. 105, n. 13, p. 2499–2506, 2001.

[279] RUOFF, R.; TSE, D. S.; MALHOTRA, R.; LORENTS, D. C. Solubility of fullerene (C_{60}) in a variety of solvents. **The Journal of Physical Chemistry**, ACS Publications, v. 97, n. 13, p. 3379–3383, 1993.

[280] KULKARNI, P. P.; JAFVERT, C. T. Solubility of C_{60} in solvent mixtures. **Environmental Science & Technology**, ACS Publications, v. 42, n. 3, p. 845–851, 2008.

[281] BARYSAITE, S.; CHMELIOV, J.; VALKUNAS, L.; GELZINIS, A. Concentration quenching of fluorescence decay kinetics of molecular systems. **The Journal of Physical Chemistry B**, ACS Publications, v. 128, n. 20, p. 4887–4897, 2024.

[282] GUEVARA-CARRION, G.; JANZEN, T.; MUÑOZ-MUÑOZ, Y. M.; VRABEC, J. Mutual diffusion of binary liquid mixtures containing methanol, ethanol, acetone, benzene, cyclohexane, toluene, and carbon tetrachloride. **The Journal of Chemical Physics**, AIP Publishing, v. 144, n. 12, p. 1–25, 2016.

[283] WOHLFARTH, C.; WOHLFARTH, C. Viscosity of the binary liquid mixture of ethanol and toluene. **Viscosity of Pure Organic Liquids and Binary Liquid Mixtures**, Springer, p. 836–836, 2017.

[284] PUROHIT, S.; SUTHAR, S. S.; VYAS, M.; BENIWAL, R. C. Studies on transport behaviour of a binary liquid mixture of ethanol and toluene at 298.15 K in terms of viscosity models. In: **AIP Conference Proceedings**. Melville, NY, USA: AIP Publishing, 2018. v. 1953, n. 1, p. 030152–1–030152–5.

[285] TAN, X.; CARAM, J. R. On the inadequacy of Stern–Volmer and FRET in describing quenching in binary donor–acceptor solutions. **The Journal of Chemical Physics**, AIP Publishing, v. 158, n. 20, p. 1–19, 2023.

[286] STERN, O.; VOLMER, M. Über die abklingungszeit der fluoreszenz. **Physikalische Zeitschrift**, Springer, v. 20, p. 183–188, 1919.

[287] REHM, D.; WELLER, A. Kinetics of fluorescence quenching by electron and H-atom transfer. **Israel Journal of Chemistry**, Wiley Online Library, v. 8, n. 2, p. 259–271, 1970.

[288] WOHLFARTH, C. **Static Dielectric Constants of Pure Liquids and Binary Liquid Mixtures**. Berlin, Heidelberg: Springer, 2017. v. 17B. 1–945 p. (Landolt-Börnstein - Group IV Physical Chemistry, v. 17B).

[289] MEER, B. W. van der. Förster theory. **FRET–Förster Resonance Energy Transfer**, Wiley Online Library, p. 23–62, 2013.

[290] VANDERMEER, B. W. Kappaphobia is the elephant in the fret room. **Methods and Applications in Fluorescence**, IOP Publishing, v. 8, n. 3, p. 030401–030405, 2020.

[291] National Center for Biotechnology Information (NCBI). **PubChem Compound Summary for CID 702, Ethanol**. Bethesda, MD, USA: PubChem Compound Database, 2025. Available at <https://pubchem.ncbi.nlm.nih.gov/compound/Ethanol#section=Odor-Threshold>. Accessed: 12th February 2025.

[292] National Center for Biotechnology Information (NCBI). **PubChem Compound Summary for CID 1140, Toluene**. Bethesda, MD, USA: PubChem Compound Database, 2025. Available at <https://pubchem.ncbi.nlm.nih.gov/compound/Toluene#section=Kovats-Retention-Index>. Accessed: 12th February 2025.

[293] BENATTO, L.; MESQUITA, O.; ROSA, J. L.; ROMAN, L. S.; KOEHLER, M.; CAPAZ, R. B.; CANDIOTTO, G. FRET–Calc: A free software and web server for Förster resonance energy transfer calculation. **Computer Physics Communications**, Elsevier, v. 287, p. 1–5, 2023.

[294] MEILUNAS, R.; CHANG, R.; LIU, S.; KAPPES, M. Infrared and Raman spectra of C_{60} and C_{70} solid films at room temperature. **NASA STI/Recon Technical Report N**, v. 91, p. 5128–5130, 1991.

[295] SCHETTINO, V.; PAGLIAI, M.; CIABINI, L.; CARDINI, G. The vibrational spectrum of fullerene C_{60}. **The Journal of Physical Chemistry A**, ACS Publications, v. 105, n. 50, p. 11192–11196, 2001.

[296] ZHIXUN, L.; YAN, F. Sers of gold/C_{60} and gold/C_{70} nano-clusters deposited on iron surface. **Vibrational spectroscopy**, Elsevier, v. 39, n. 2, p. 151–156, 2005.

[297] DRESSELHAUS, M. S.; DRESSELHAUS, G.; EKLUND, P. C. **Science of Fullerenes and Carbon Nanotubes: Their Properties and Applications**. San Diego, CA: Academic Press, 1996. 965 p.

[298] QIN, Y.; XU, J.; LIANG, Z.; TENG, H.; ZHAN, D.; XU, H. Raman spectroscopy of fullerenes: From C_{60} to functionalized derivatives. **Molecules**, MDPI, v. 30, n. 3, p. 1–28, 2025.

[299] FALKE, S.; ERAVUCHIRA, P.; MATERNY, A.; LIENAU, C. Raman spectroscopic identification of fullerene inclusions in polymer/fullerene blends. **Journal of Raman Spectroscopy**, Wiley Online Library, v. 42, n. 10, p. 1897–1900, 2011.

[300] BAERENDS, E.; GRITSENKO, O.; MEER, R. V. The Kohn–Sham gap, the fundamental gap and the optical gap: the physical meaning of occupied and virtual Kohn–Sham orbital energies. **Physical Chemistry Chemical Physics**, Royal Society of Chemistry, v. 15, n. 39, p. 16408–16425, 2013.

[301] SENET, P. Kohn-Sham orbital formulation of the chemical electronic responses, including the hardness. **The Journal of Chemical Physics**, AIP Publishing, v. 107, n. 7, p. 2516–2524, 1997.

[302] JENSEN, F. **Introduction to computational chemistry**. Chichester, UK: John Wiley & Sons, 2017.

[303] TAMURA, H.; TSUKADA, M. Role of intermolecular charge delocalization on electron transport in fullerene aggregates. **Physical Review B—Condensed Matter and Materials Physics**, APS, v. 85, n. 5, p. 1–8, 2012.

[304] D'AVINO, G.; OLIVIER, Y.; MUCCIOLI, L.; BELJONNE, D. Do charges delocalize over multiple molecules in fullerene derivatives? **Journal of Materials Chemistry C**, Royal Society of Chemistry, v. 4, n. 17, p. 3747–3756, 2016.

[305] HEEGER, A. J. Semiconducting polymers: the third generation. **Chemical Society Reviews**, Royal Society of Chemistry, v. 39, n. 7, p. 2354–2371, 2010.

[306] BRÉDAS, J.-L.; NORTON, J. E.; CORNIL, J.; COROPCEANU, V. Molecular understanding of organic solar cells: the challenges. **Accounts of Chemical Research**, ACS Publications, v. 42, n. 11, p. 1691–1699, 2009.

[307] SWORAKOWSKI, J. How accurate are energies of HOMO and LUMO levels in small-molecule organic semiconductors determined from cyclic voltammetry or optical spectroscopy? **Synthetic Metals**, Elsevier, v. 235, p. 125–130, 2018.

[308] SHAFIQ, A.; ADNAN, M.; HUSSAIN, R.; IRSHAD, Z.; FAROOQ, U.; MUHAMMAD, S. Molecular engineering of anthracene core-based hole-transporting materials for organic and perovskite photovoltaics. **ACS Omega**, ACS Publications, v. 8, n. 39, p. 35937–35955, 2023.

[309] KASTINEN, T.; FILHO, D. A. da S.; PAUNONEN, L.; LINARES, M.; JUNIOR, L. A. R.; CRAMARIUC, O.; HUKKA, T. I. Electronic couplings and rates of excited state charge transfer processes at poly (thiophene-co-quinoxaline)–$PC_{71}BM$ interfaces: two-versus multi-state treatments. **Physical Chemistry Chemical Physics**, Royal Society of Chemistry, v. 21, n. 46, p. 25606–25625, 2019.

[310] SHU, Y.; TRUHLAR, D. G. Relationships between orbital energies, optical and fundamental gaps, and exciton shifts in approximate density functional theory and quasiparticle theory. **Journal of Chemical Theory and Computation**, ACS Publications, v. 16, n. 7, p. 4337–4350, 2020.

[311] GONG, X.; TONG, M.; BRUNETTI, F. G.; SEO, J.; SUN, Y.; MOSES, D.; WUDL, F.; HEEGER, A. J. Bulk heterojunction solar cells with large open-circuit voltage: Electron transfer with small donor-acceptor energy offset. **Advanced Materials**, WILEY-VCH Verlag Weinheim, v. 23, n. 20, p. 2272–2277, 2011.

[312] STEVENS, M. A.; ARANGO, A. C. Open-circuit voltage exceeding the outermost HOMO–LUMO offset in cascade organic solar cells. **Organic Electronics**, Elsevier, v. 37, p. 80–84, 2016.

[313] HALLS, J. J.; FRIEND, R. H. **Organic photovoltaic devices**. London, UK: Imperial College Press, 2001.

[314] BRABEC, C. J.; CRAVINO, A.; MEISSNER, D.; SARICIFTCI, N. S.; FROMHERZ, T.; RISPENS, M. T.; SANCHEZ, L.; HUMMELEN, J. C. Origin of the open circuit voltage of plastic solar cells. **Advanced Functional Materials**, Wiley Online Library, v. 11, n. 5, p. 374–380, 2001.

[315] HUNTER, C. A.; SANDERS, J. K. The nature of π–π interactions. **Journal of the American Chemical Society**, ACS Publications, v. 112, n. 14, p. 5525–5534, 1990.

[316] GRIMME, S. Do special noncovalent π–π stacking interactions really exist? **Angewandte Chemie International Edition**, Wiley-VCH, v. 47, n. 18, p. 3430–3434, 2008.

[317] FRAZAO, N. F.; ALBUQUERQUE, E. L.; FULCO, U. L.; AZEVEDO, D. L.; MENDONÇA, G. L.; LIMA-NETO, P.; CAETANO, E. W.; SANTANA, J. V.; FREIRE, V. N. Four-level levodopa adsorption on C_{60} fullerene for transdermal and oral administration: a computational study. **RSC Advances**, Royal Society of Chemistry, v. 2, n. 22, p. 8306–8322, 2012.

[318] HADAD, A.; AZEVEDO, D. L.; CAETANO, E. W.; FREIRE, V. N.; MENDONCA, G. L.; NETO, P. L.; ALBUQUERQUE, E. L.; MARGIS, R.; GOTTFRIED, C. Two-level adsorption of ibuprofen on C_{60} fullerene for transdermal delivery: classical molecular dynamics and density functional theory computations. **The Journal of Physical Chemistry C**, ACS Publications, v. 115, n. 50, p. 24501–24511, 2011.

[319] ZHANG, K.; YU, H.; LIU, X.; DONG, Q.; WANG, Z.; WANG, Y.; CHEN, N.; ZHOU, Y.; SONG, B. Fullerenes and derivatives as electron transport materials in perovskite solar cells. **Science China Chemistry**, Springer, v. 60, p. 144–150, 2017.

[320] ZHANG, Y.-X.; FANG, J.; LI, W.; SHEN, Y.; CHEN, J.-D.; LI, Y.; GU, H.; PELIVANI, S.; ZHANG, M.; LI, Y. *et al.* Synergetic transparent electrode architecture for efficient non-fullerene flexible organic solar cells with> 12% efficiency. **ACS Nano**, ACS Publications, v. 13, n. 4, p. 4686–4694, 2019.

[321] TSUZUKI, S.; HONDA, K.; UCHIMARU, T.; MIKAMI, M.; TANABE, K. Origin of attraction and directionality of the π/π interaction: model chemistry calculations of benzene dimer interaction. **Journal of the American Chemical Society**, ACS Publications, v. 124, n. 1, p. 104–112, 2002.

[322] SCHOLES, G. D.; RUMBLES, G. Excitons in nanoscale systems. **Nature Materials**, Nature Publishing Group UK London, v. 5, n. 9, p. 683–696, 2006.

[323] DIMITRIEV, O. P. Dynamics of excitons in conjugated molecules and organic semiconductor systems. **Chemical Reviews**, ACS Publications, v. 122, n. 9, p. 8487–8593, 2022.

[324] TSUZUKI, S.; HONDA, K.; UCHIMARU, T.; MIKAMI, M.; TANABE, K. Origin of the attraction and directionality of the NH/π interaction: Comparison with OH/π and CH/π interactions. **Journal of the American Chemical Society**, ACS Publications, v. 122, n. 46, p. 11450–11458, 2000.

[325] BAKRY, R.; VALLANT, R. M.; HAQ, M. Najam-ul; RAINER, M.; SZABO, Z.; HUCK, C. W.; BONN, G. K. Medicinal applications of fullerenes. **International Journal of Nanomedicine**, Taylor & Francis, v. 2, n. 4, p. 639–649, 2007.

[326] ANDRIEVSKY, G. V.; KOSEVICH, M. V.; VOVK, M.; SHELKOVSKY, V. S.; VASHCHENKO, L. A. On the production of an aqueous colloidal solution of fullerenes. **Journal of the Chemical Society, Chemical Communications**, Royal Society of Chemistry, n. 12, p. 1281–1282, 1995.

[327] GULDI, D. M.; ILLESCAS, B. M.; ATIENZA, C. M.; WIELOPOLSKI, M.; MARTÍN, N. Fullerene for organic electronics. **Chemical Society Reviews**, Royal Society of Chemistry, v. 38, n. 6, p. 1587–1597, 2009.

[328] KÖHLER, A.; BÄSSLER, H. Triplet states in organic semiconductors. **Materials Science and Engineering: R: Reports**, Elsevier, v. 66, n. 4-6, p. 71–109, 2009.

[329] LI, Y. *et al.* Fullerene derivatives for efficient energy transfer and charge separation. **Journal of Physical Chemistry C**, American Chemical Society, v. 117, n. 7, p. 1493–1502, 2013.

[330] RAND, B. P.; CHEYNS, D.; VASSEUR, K.; GIEBINK, N. C.; MOTHY, S.; YI, Y.; COROPCEANU, V.; BELJONNE, D.; CORNIL, J.; BRÉDAS, J.-L. *et al.* The impact of molecular orientation on the photovoltaic properties of a phthalocyanine/fullerene heterojunction. **Advanced Functional Materials**, Wiley Online Library, v. 22, n. 14, p. 2987–2995, 2012.

[331] SHAVEZ, M.; MAHAPATRA, S. Influence of molecular orientation on photovoltaic performance in double donor with fullerene and non-fullerene acceptor-based heterojunctions. **Physical Chemistry Chemical Physics**, Royal Society of Chemistry, v. 24, n. 19, p. 11726–11736, 2022.

[332] TROISI, A.; ORLANDI, G. Dynamics of the intermolecular transfer integral in crystalline organic semiconductors. **The Journal of Physical Chemistry A**, ACS Publications, v. 110, n. 11, p. 4065–4070, 2006.

[333] COROPCEANU, V.; CORNIL, J.; FILHO, D. A. da S.; OLIVIER, Y.; SILBEY, R.; BRÉDAS, J.-L. Charge transport in organic semiconductors. **Chemical Reviews**, ACS Publications, v. 107, n. 4, p. 926–952, 2007.

[334] WORTH, G. A.; BURGHARDT, I. Chemistry without the Born–Oppenheimer approximation. **Philosophical Transactions of the Royal Society A: Mathematical, Physical and Engineering Sciences**, Royal Society Publishing, v. 378, n. 2184, p. 1–5, 2020.

[335] CERDA, J. J. e. a. Charge transfer and non-coulombic effects in molecular interactions. **Chemical Physics Letters**, Elsevier, v. 318, p. 153–160, 2000.

[336] MIE, G. Zur kinetischen theorie der einatomigen körper. **Annalen der Physik**, Wiley Online Library, v. 316, n. 8, p. 657–697, 1903.

[337] COELHO, M. M.; BEZERRA, E. M.; COSTA, R. F. da; ALVARENGA, É. C. de; FREIRE, V. N.; CARVALHO, C. R.; PESSOA, C.; ALBUQUERQUE, E. L.; COSTA, R. A. In silico description of the adsorption of cell signaling pathway proteins ovalbumin, glutathione, lc3, tlr4, asc pycard, pi3k and nf-kβ on 7.0 nm gold nanoparticles: obtaining their lennard-jones-like potentials through docking and molecular mechanics. **RSC Advances**, Royal Society of Chemistry, v. 13, n. 50, p. 35493–35499, 2023.

[338] KRETZ, B.; EGGER, D. A. Accurate non-adiabatic couplings from optimally tuned range-separated hybrid functionals. **The Journal of Chemical Physics**, AIP Publishing, v. 157, n. 10, p. 101104–1–101104–6, 2022.

[339] YANG, Y.; PROKOPIOU, G.; QIU, T.; SCHANKLER, A. M.; RAPPE, A. M.; KRONIK, L.; JR, R. A. D. Range-separated hybrid functional pseudopotentials. **Physical Review B**, APS, v. 108, n. 16, p. 1–9, 2023.

[340] MOCZ, G.; ROSS, J. A. Fluorescence techniques in analysis of protein–ligand interactions. In: GOHLKE, H. (Ed.). **Protein-Ligand Interactions: Methods and Applications**. Berlin, Heidelberg: Springer, 2013. p. 169–210.

[341] TOMIN, V. I. Physical principles behind spectroscopic response of organic fluorophores to intermolecular interactions. **Advanced Fluorescence Reporters in Chemistry and Biology I: Fundamentals and Molecular Design**, Springer, p. 189–223, 2010.

[342] LI, J.; CHEN, M.; ZHOU, S.; LI, H.; HAO, J. Self-assembly of fullerene C_{60}-based amphiphiles in solutions. **Chemical Society Reviews**, Royal Society of Chemistry, v. 51, n. 8, p. 3226–3242, 2022.

[343] LIU, Y.-Z.; CHEN, Y.-N.; SUN, Q. The dependence of hydrophobic interactions on the shape of solute surface. **Molecules**, MDPI, v. 29, n. 11, p. 1–22, 2024.

[344] ATHAWALE, M. V.; JAMADAGNI, S. N.; GARDE, S. How hydrophobic hydration responds to solute size and attractions: Theory and simulations. **The Journal of Chemical Physics**, AIP Publishing, v. 131, n. 11, p. 115102–1–115102–9, 2009.

[345] IKEDA, A. Water-soluble fullerenes using solubilizing agents, and their applications. **Journal of Inclusion Phenomena and Macrocyclic Chemistry**, Springer, v. 77, p. 49–65, 2013.

[346] REDDY, C.; YU, Z. G.; ZHANG, Y.-W. Two-dimensional van der waals C_{60} molecular crystal. **Scientific Reports**, Nature Publishing Group UK London, v. 5, n. 1, p. 1–7, 2015.

[347] SABIROV, D. S.; ORI, O.; TUKHBATULLINA, A. A.; SHEPELEVICH, I. S. Covalently bonded fullerene nano-aggregates $(C_{60})_n$: Digitalizing their energy–topology–symmetry. **Symmetry**, MDPI, v. 13, n. 10, p. 1–13, 2021.

[348] NAYAK, S.; RAY, A.; BHATTACHARYA, S. Size selective supramolecular interaction upon molecular complexation of a designed porphyrin with C_{60} and C_{70} in solution. **Journal of Molecular Liquids**, Elsevier, v. 321, p. 1–14, 2021.

[349] ELISTRATOVA, M. A.; KOROLEVA, M. O.; ZAKHAROVA, I. B. Fluorescence quenching of tetraphenylporphyrin-fullerene molecular complexes. **International Youth Conference on Electronics, Telecommunications and Information Technologies**, Springer, p. 247–253, 2020.

[350] MATHEW, E.; JOE, I. H. Solvent dependent nonlinear optical properties of benzodioxol chalcone: An elucidation of spectroscopic, DFT, solvatochromism and z-scan technique. **Journal of Molecular Liquids**, Elsevier, v. 392, p. 1–6, 2023.

[351] MATHEW, E.; JOE, I. H.; HARSHITHA, K.; SAROJINI, B. Augmenting the effect of solvents on optical nonlinearity by spectroscopic, DFT, solvatochromism and z-scan studies of push-pull chalcone: (2E)-1-(4-ethoxyphenyl)-3-(4-methoxyphenyl) prop-2-en-1-one. **Spectrochimica Acta Part A: Molecular and Biomolecular Spectroscopy**, Elsevier, v. 293, p. 1–13, 2024.

[352] National Center for Biotechnology Information (NCBI). **PubChem Compound Summary for CID 5315457, Coumarin 6**. 2024. <https://pubchem.ncbi.nlm.nih.gov/compound/Coumarin-6>. Accessed: June 10, 2025.

[353] BROUWER, A. M. Standards for photoluminescence quantum yield measurements in solution. **Pure and Applied Chemistry**, v. 83, n. 12, p. 2213–2228, 2011.

[354] HAYNES, W. M. **CRC Handbook of Chemistry and Physics**. 95th. ed. Boca Raton, FL: CRC Press, 2014. ISBN 978-1-4822-0867-2. Disponível em: <https://www.routledge.com/CRC-Handbook-of-Chemistry-and-Physics-95th-Edition/Haynes/p/book/9781482208672>.

[355] RAIKAR, U.; RENUKA, C.; NADAF, Y.; MULIMANI, B.; KARGUPPIKAR, A.; SOUDAGAR, M. Solvent effects on the absorption and fluorescence spectra of coumarins 6 and 7 molecules: Determination of ground and excited state dipole moment. **Spectrochimica Acta Part A: Molecular and Biomolecular Spectroscopy**, Elsevier, v. 65, n. 3-4, p. 673–677, 2006.

[356] ALBANI, J. R. **Structure and Dynamics of Macromolecules: Absorption and Fluorescence Studies**. Amsterdam, Netherlands: Elsevier, 2011.

[357] VALEUR, B.; BERBERAN-SANTOS, M. N. A brief history of fluorescence and phosphorescence before the emergence of quantum theory. **Journal of Chemical Education**, ACS Publications, v. 88, n. 6, p. 731–738, 2011.

[358] NELSON, T. R.; WHITE, A. J.; BJORGAARD, J. A.; SIFAIN, A. E.; ZHANG, Y.; NEBGEN, B.; FERNANDEZ-ALBERTI, S.; MOZYRSKY, D.; ROITBERG, A. E.; TRETIAK, S. Non-adiabatic excited-state molecular dynamics: Theory and applications for modeling photophysics in extended molecular materials. **Chemical Reviews**, ACS Publications, v. 120, n. 4, p. 2215–2287, 2020.

[359] EFTINK, M. R.; GHIRON, C. A. Fluorescence quenching studies with proteins. **Analytical Biochemistry**, Elsevier, v. 114, n. 2, p. 199–227, 1981.

[360] BELJONNE, D.; YAMAGATA, H.; BRÉDAS, J.; SPANO, F.; OLIVIER, Y. Charge-transfer excitations steer the davydov splitting and mediate singlet exciton fission in pentacene. **Physical Review Letters**, APS, v. 110, n. 22, p. 226402–1–226402–5, 2013.

[361] KIMBER, P.; PLASSER, F. Energy component analysis for electronically excited states of molecules: why the lowest excited state is not always the HOMO/LUMO transition. **Journal of Chemical Theory and Computation**, ACS Publications, v. 19, n. 8, p. 2340–2352, 2023.

[362] ZIRZLMEIER, J.; SCHRETTL, S.; BRAUER, J. C.; CONTAL, E.; VANNAY, L.; BRÉMOND, É.; JAHNKE, E.; GULDI, D. M.; CORMINBOEUF, C.; TYKWINSKI, R. R. *et al.* Optical gap and fundamental gap of oligoynes and carbyne. **Nature Communications**, Nature Publishing Group UK London, v. 11, n. 1, p. 1–10, 2020.

[363] JOHANNES, A. Z.; PINGAK, R. K.; BUKIT, M. Tauc plot software: Calculating energy gap values of organic materials based on ultraviolet-visible absorbance spectrum. In: **IOP Conference Series: Materials Science and Engineering**. Bristol, UK: IOP Publishing, 2020. v. 823, n. 1, p. 1–8.

[364] CURCIO, S. F.; CARVALHO, G. L.; PAEZ, E. B. A.; NEME, N. P.; VALASKI, R.; MATOS, M. J.; TAYLOR, J. G.; CAZATI, T. Exploring photophysical behavior and fullerene-induced quenching in difluoroboron flavanone β-diketonates for application in organic electronic devices: Experimental and theoretical analysis. **Materials Today Communications**, Elsevier, v. 41, p. 1–13, 2024.

[365] PERDEW, J. P.; PARR, R. G.; LEVY, M.; BALDUZ, J. L. Density-functional theory for fractional particle number: Derivative discontinuities of the energy. **Physical Review Letters**, American Physical Society, v. 49, n. 23, p. 1691–1694, 1982.

[366] GRIMME, S. Accurate description of van der waals complexes by density functional theory including empirical corrections. **Journal of Computational Chemistry**, Wiley Online Library, v. 25, n. 12, p. 1463–1473, 2004.

[367] MASTERS, B. Paths to Förster's resonance energy transfer (FRET) theory. **The European Physical Journal H**, Springer, v. 39, p. 87–139, 2014.

[368] GOVOROV, A.; DEMIR, H. V. *et al.* **Understanding and Modeling Förster-type Resonance Energy Transfer (FRET)**. Cham, Switzerland: Springer, 2017.

[369] NASCIMENTO, S.; FEDOROV, A.; BRITES, M. J.; BERBERAN-SANTOS, M. N. New coumarin-[60] fullerene dyads connected by an alkynyl linkage: Synthesis and fluorescence studies. evidence for efficient singlet–singlet energy transfer. **Dyes and Pigments**, Elsevier, v. 114, p. 158–165, 2015.

[370] QAISER, D.; KHAN, M. S.; SINGH, R.; KHAN, Z. H.; CHAWLA, S. Förster's resonance energy transfer between fullerene C_{60} and coumarin C440. **Spectrochimica Acta Part A: Molecular and Biomolecular Spectroscopy**, Elsevier, v. 77, n. 5, p. 1065–1068, 2010.

[371] RYBKIN, A. Y.; BELIK, A. Y.; KRAEVAYA, O.; KHAKINA, E.; ZHILENKOV, A.; GORYACHEV, N.; VOLYNIUK, D.; GRAZULEVICIUS, J.; TROSHIN, P.; KOTELNIKOV, A. Covalently linked water-soluble fullerene–fluorescein dyads as highly efficient photosensitizers: Synthesis, photophysical properties and photochemical action. **Dyes and Pigments**, Elsevier, v. 160, p. 457–466, 2019.

[372] HENKELMAN, G.; JÓHANNESSON, G.; JÓNSSON, H. Methods for finding saddle points and minimum energy paths. **Theoretical Methods in Condensed Phase Chemistry**, Springer, p. 269–302, 2002.

[373] TASINATO, N.; GRIMME, S. Unveiling the non-covalent interactions of molecular homodimers by dispersion-corrected DFT calculations and collision-induced broadening of ro-vibrational transitions: application to $(CH_2F_2)_2$ and $(SO_2)_2$. **Physical Chemistry Chemical Physics**, Royal Society of Chemistry, v. 17, n. 8, p. 5659–5669, 2015.

[374] COHEN, A. J.; MORI-SÁNCHEZ, P.; YANG, W. Insights into current limitations of density functional theory. **Science**, American Association for the Advancement of Science, v. 321, n. 5890, p. 792–794, 2008.

[375] NOH, S.; YANG, J.; KIM, S.; LEE, C.; KIM, J.-Y. Investigation into the thermal annealing effect on the photovoltaic properties of organic solar cells based on CuPc/C_{60} heterojunctions. **Journal of the Korean Physical Society**, The Korean Physical Society, v. 52, n. 2, p. 505–510, 2008.

[376] KHLAIFIA, D.; MASSUYEAU, F.; EWELS, C. P.; DUVAIL, J.-L.; FAULQUES, E.; ALIMI, K. DFT modeling of novel donor-acceptor (D-A) molecules incorporating 3-hexylthiophene (3HT) for bulk heterojunction solar cells. **ChemistrySelect**, Wiley Online Library, v. 2, n. 31, p. 10082–10090, 2017.

[377] SATHIYAN, G.; SIVA, G.; SIVAKUMAR, E.; PRAKASH, J.; SWART, H. C.; SAKTHIVEL, P. Synthesis and studies of carbazole-based donor polymer for organic solar cell applications. **Colloid and Polymer Science**, Springer, v. 296, p. 1193–1203, 2018.

[378] LE, V. H.; YANNEY, M.; MCGUIRE, M.; SYGULA, A.; LEWIS, E. A. Thermodynamics of host–guest interactions between fullerenes and a buckycatcher. **The Journal of Physical Chemistry B**, ACS Publications, v. 118, n. 41, p. 11956–11964, 2014.

[379] ZHAO, Y.; TRUHLAR, D. G. Computational characterization and modeling of buckyball tweezers: density functional study of concave–convex π–π interactions. **Physical Chemistry Chemical Physics**, Royal Society of Chemistry, v. 10, n. 19, p. 2813–2818, 2008.

[380] GRIMME, S. Supramolecular binding thermodynamics by dispersion-corrected density functional theory. **Chemistry–A European Journal**, Wiley Online Library, v. 18, n. 32, p. 9955–9964, 2012.

[381] VELMISKINA, J. A.; MALYSHEV, V. I.; GERASIMOV, I. S.; MEDVEDEV, M. G. Least popular vibrational entropy model provides the best accuracy and robustness. **The Journal of Chemical Physics**, AIP Publishing, v. 162, n. 12, p. 1–10, 2025.

[382] RIBEIRO, R. F.; MARENICH, A. V.; CRAMER, C. J.; TRUHLAR, D. G. Use of solution-phase vibrational frequencies in continuum models for the free energy of solvation. **The Journal of Physical Chemistry B**, ACS Publications, v. 115, n. 49, p. 14556–14562, 2011.

[383] STEED, J. W.; ATWOOD, J. L. **Supramolecular Chemistry**. Chichester, UK: John Wiley & Sons, 2022.

[384] DIEDERICH, F.; STANG, P. J. **Templated Organic Synthesis**. Weinheim, Germany: John Wiley & Sons, 2008.

[385] BRAUN, S.; SALANECK, W. R.; FAHLMAN, M. Energy-level alignment at organic/metal and organic/organic interfaces. **Advanced Materials**, Wiley Online Library, v. 21, n. 14-15, p. 1450–1472, 2009.

APPENDIX A – SUPPLEMENTARY INFORMATION

Figure 26 – ^{1}H NMR spectrum of (1E,4E)-1,5-bis(4-ethoxyphenyl)penta-1,4-dien-3-one dibenzalacetone derivative (DBAd), recorded in $CDCl_3$ at 300 MHz.

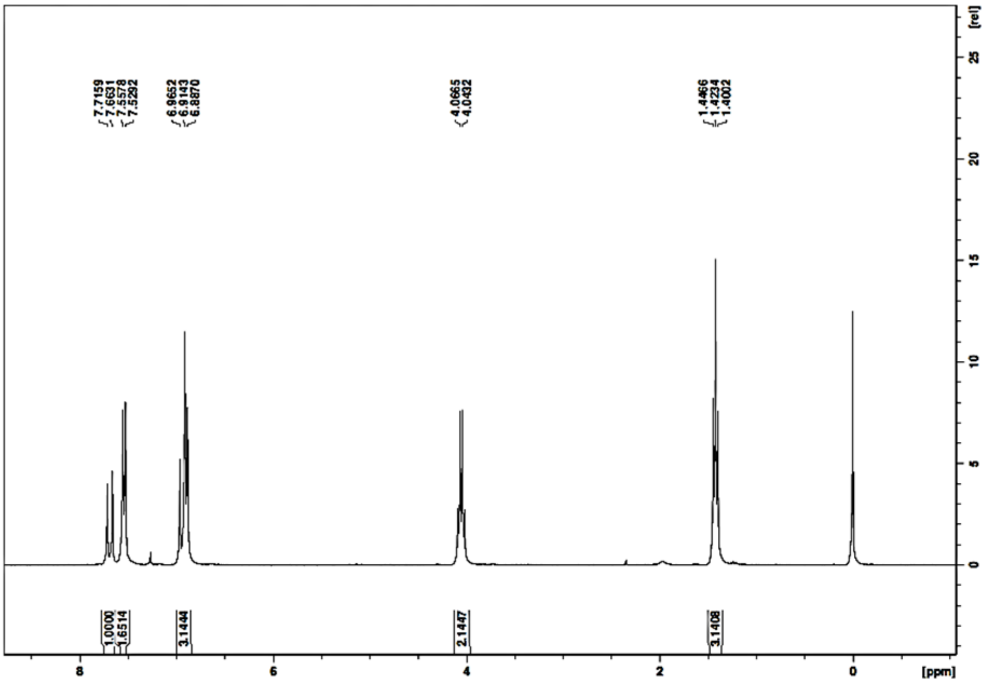

Figure 27 – ^{13}C NMR spectrum of (1E,4E)-1,5-bis(4-ethoxyphenyl)penta-1,4-dien-3-one dibenzalacetone derivative (DBAd), recorded in $CDCl_3$ at 125 MHz.

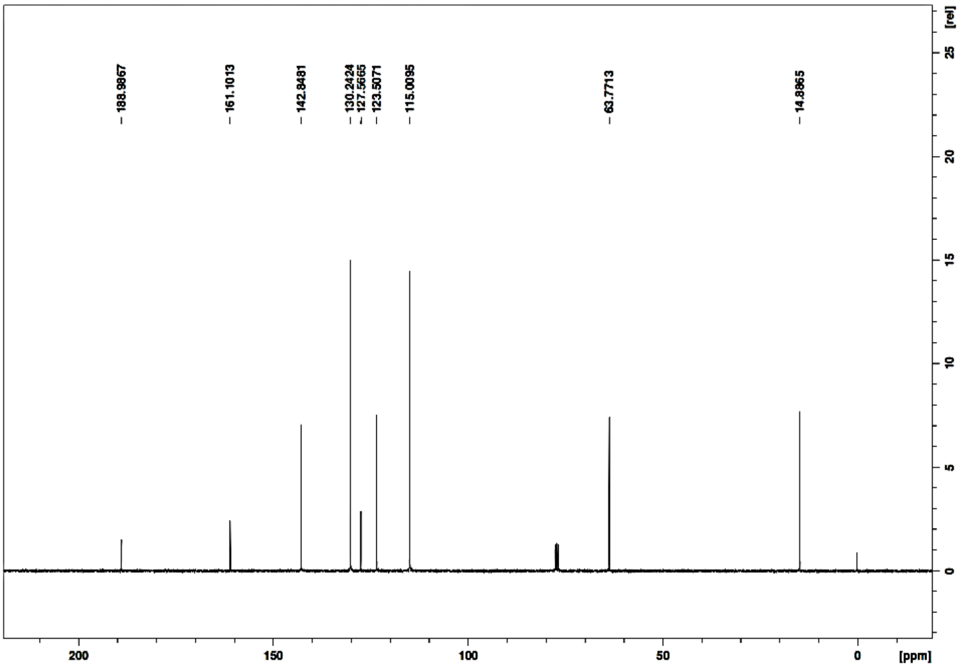

Figure 28 – (a) UV-Vis absorption spectra of C_{60}@DBAd complexes at increasing C_{60} concentrations. (b) Fluorescence emission spectra of C_{60}@DBAd under excitation at $\lambda^{\mathrm{emi}}_{\mathrm{DBAd}}$ of 365 nm, showing progressive fluorescence quenching with increasing C_{60} concentration. (c) UV-Vis absorption spectra of DBAd at increasing $PC_{61}BM$ concentrations. (d) Fluorescence emission spectra of $PC_{61}BM$@DBAd under the same excitation conditions ($\lambda^{\mathrm{emi}}_{\mathrm{DBAd}}$ of 365 nm) also exhibit pronounced quenching behavior as a function of $PC_{61}BM$ concentration.

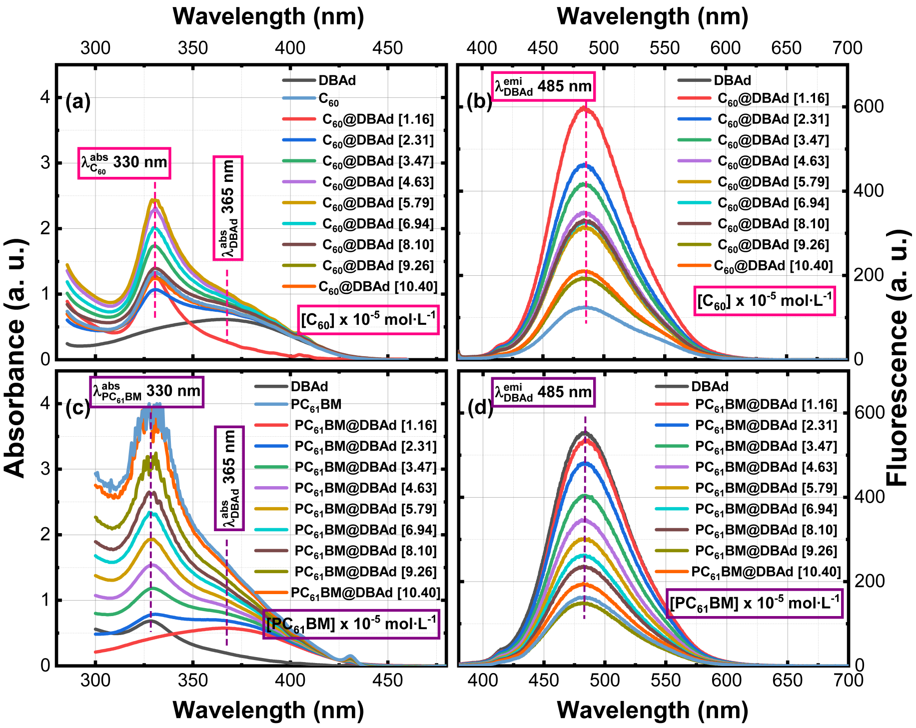

Table 9 – Molar concentrations of the ethoxy-dibenzalacetone derivative (DBAd) in toluene (TOL), dichloromethane (DCM), and acetonitrile (ACN) solvents. The stock solutions were prepared at a concentration of 1.6×10^{-3} mol · L^{-1} and subsequently diluted to obtain the corresponding working solutions, with uncertainties in the last digit.

	Stock solution (mol · L^{-1})	**Working solution concentrations** ($\times 10^{-5}$mol · L^{-1})				
		1st	2nd	3rd	4th	5th
DBAd	1.6×10^{-3}	0.53(4)	1.07(6)	1.62(9)	2.17(9)	2.72(9)

[a] Toluene ($\kappa_{\mathrm{TOL}} = 2.37$); [b] Dichloromethane ($\kappa_{\mathrm{DCM}} = 8.93$); [c] Acetonitrile ($\kappa_{\mathrm{ACN}} = 35.67$).

Table 10 – Molar absorption coefficients (ε, in $\times 10^4$ $\mathrm{L \cdot mol^{-1} \cdot cm^{-1}}$) of the ethoxy-dibenzalacetone derivative (DBAd) in toluene (TOL), dichloromethane (DCM), and acetonitrile (ACN), obtained from Beer-Lambert linear regression fits. Reported values correspond to the slope of the absorbance versus concentration plot, with standard uncertainties given in parentheses, which affect the last digit.

	Molar absorption coefficient (ε, in $\times 10^4$ $\mathrm{L \cdot mol^{-1} \cdot cm^{-1}}$)		
	[a]**Toluene** (κ_{TOL} = 2.37)	[b]**Dichloromethane** (κ_{DCM} = 8.93)	[c]**Acetonitrile** (κ_{ACN} = 35.67)
DBAd	4.05(4)	4.83(7)	5.96(5)

[a] Toluene (κ_{TOL} = 2.37); [b] Dichloromethane (κ_{DCM} = 8.93); [c] Acetonitrile (κ_{ACN} = 35.67).

Figure 29 – Experimental optical band gap ($\mathrm{E_{OPT}^{exp}}$) determination using Tauc plots for (a) the ethoxy-dibenzalacetone derivative (DBAd), (b) $\mathrm{C_{60}}$, and (c) $\mathrm{PC_{61}BM}$. The plots show the linear extrapolation of $(\alpha h\nu)^2$ as a function of the photon energy ($h\nu$), assuming $\gamma = 2$ for indirect allowed electronic transitions. The intersection of the linear fit with the photon energy axis (highlighted regions) corresponds to the estimated $\mathrm{E_{OPT}^{exp}}$.

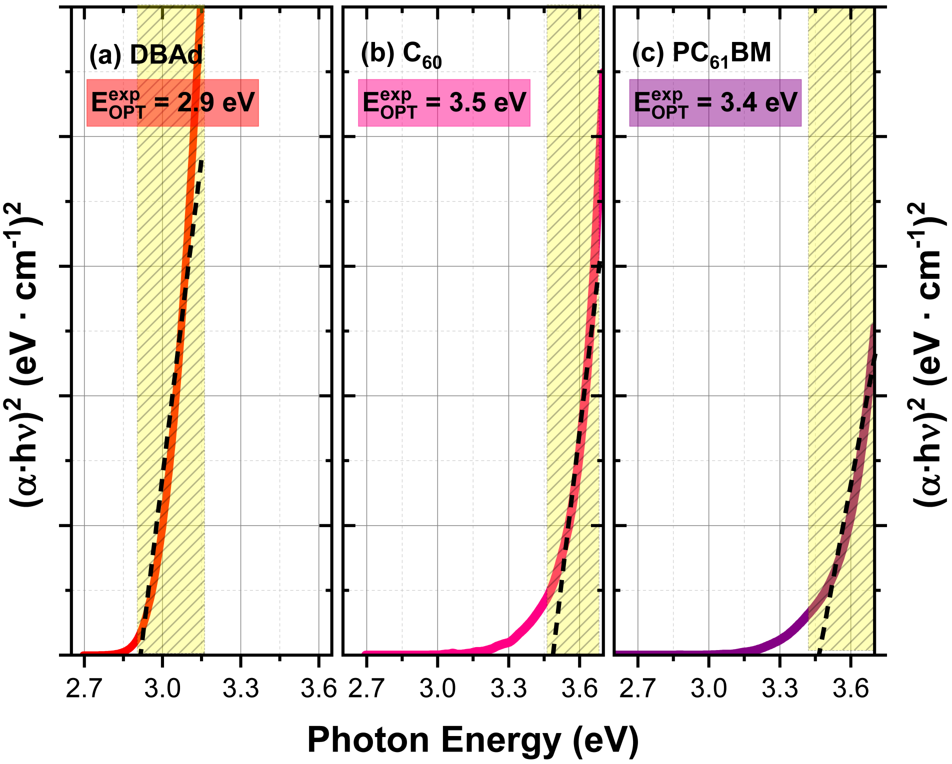

Table 11 – Lennard-Jones potential parameters fitted for ethoxy-dibenzalacetone derivative (DBAd) interacting with fullerene compounds (C_{60} and $PC_{61}BM$). The interaction energy (ϵ), centroid distance (r), and zero-potential separation (σ) are reported for each Cartesian direction, highlighting the most stable configurations. The coefficient of determination (R^2) quantifies the regression accuracy for each interaction.

		Lennard-Jones Parameters			
	Axis	$^{a}\epsilon$ (kcal · mol^{-1})	^{b}r (Å)	$^{c}\sigma$ (Å)	R^2
C_{60}@DBAd	X	−3.93 ± 0.57	10.51	10.37 ± 0.08	0.57
	Y	−10.12 ± 0.41	6.43	6.12 ± 0.01	0.94
	Z	−10.12 ± 0.38	6.78	6.34 ± 0.01	0.93
$PC_{61}BM$@DBAd	X	−19.84 ± 1.88	7.39	7.11 ± 0.03	0.96
	Y	−17.01 ± 0.33	5.76	4.94 ± 0.00	0.98
	Z	−23.56 ± 1.33	5.80	5.40 ± 0.02	0.98

[a] ϵ: Interaction energy between the DBAd and fullerene compounds (C_{60} or $PC_{61}BM$).

[b] r: Centroid distance between the DBAd and fullerene compounds (C_{60} or $PC_{61}BM$).

[c] σ: Equilibrium separation where the potential between two molecules is zero.

Table 12 – Mie potential parameters fitted for ethoxy-dibenzalacetone derivative (DBAd) interacting with fullerene compounds (C_{60} and $PC_{61}BM$). The interaction energy (ϵ), centroid distance (r), equilibrium separation (σ), and adjusted Mie exponents (n, m) are reported for the most stable configurations. The coefficient of determination (R^2) indicates the regression accuracy for each interaction.

		Mie Parameters					
	Axis	$^{a}\epsilon$ (kcal · mol^{-1})	^{b}r (Å)	$^{c}\sigma$ (Å)	^{d}n	^{d}m	R^2
C_{60}@DBAd	X	15.71 ± 0.11	10.51	10.14 ± 7.06E^{-4}	44.99 ± 0.39	9.26 ± 0.04	0.99
	Y	30.93 ± 0.03	6.43	6.05 ± 8.94E^{-5}	22.42 ± 0.03	6.02 ± 0.00	1.00
	Z	31.52 ± 0.09	6.78	6.32 ± 1.37E^{-4}	24.29 ± 0.09	6.13 ± 0.01	0.99
$PC_{61}BM$@DBAd	X	33.99 ± 0.52	7.39	6.86 ± 0.00E^{0}	26.26 ± 0.19	5.54 ± 0.07	0.99
	Y	88.81 ± 2.66	5.76	4.97 ± 6.46E^{-4}	8.79 ± 0.15	6.35 ± 0.10	0.99
	Z	39.44 ± 0.68	5.80	5.28 ± 0.00E^{0}	21.24 ± 0.16	4.42 ± 0.06	0.99

[a] ϵ: Interaction energy between the DBAd and fullerene compounds (C_{60} or $PC_{61}BM$).

[b] r: Centroid distance between the DBAd and fullerene compounds (C_{60} or $PC_{61}BM$).

[c] σ: Equilibrium separation where the potential energy between two molecules is zero.

[d] m and n: Mie exponents representing the repulsive and attractive components of the potential, respectively.

Table 13 – Concentration profiles of (1E,4E)-1,5-bis(4-ethoxyphenyl)penta-1,4-dien-3-one ethoxy-dibenzalacetone derivative (DBAd) and fullerene compounds (C_{60} and $PC_{61}BM$) in ethanol-toluene binary mixtures. Measurements were conducted at 25 °C.

Toluene Volume	**Initial Volume**		**Final Concentration**	
(µL)	[a]**[C_{60}/PC_{61}BM]** (µL)	[b]**[DBAd]** (µL)	**[C_{60}/PC_{61}BM]** ($mol \cdot L^{-1}$)	**[DBAd]** ($mol \cdot L^{-1}$)
400	0	2000	0.00	1.4×10^{-5}
360	40	2000	1.16×10^{-5}	1.4×10^{-5}
320	80	2000	2.31×10^{-5}	1.4×10^{-5}
280	120	2000	3.47×10^{-5}	1.4×10^{-5}
240	160	2000	4.63×10^{-5}	1.4×10^{-5}
200	200	2000	5.79×10^{-5}	1.4×10^{-5}
160	240	2000	6.94×10^{-5}	1.4×10^{-5}
120	280	2000	8.10×10^{-5}	1.4×10^{-5}
80	320	2000	9.26×10^{-5}	1.4×10^{-5}
40	360	2000	10.40×10^{-5}	1.4×10^{-5}

[a] [C_{60}/PC_{61}BM]: initial concentration in toluene solvent at 7.0×10^{-4} $mol \cdot L^{-1}$;

[b] [DBAd]: initial concentration in ethanol solvent at 1.68×10^{-5} $mol \cdot L^{-1}$.

Figure 30 – Fluorescence decay profiles with monoexponential fits (ExpDec1) of the excited state of dibenzalacetone derivative (DBAd) in C_{60}@DBAd (left) and PC_{61}BM@DBAd (right) at varying fullerene-quenchers concentrations.

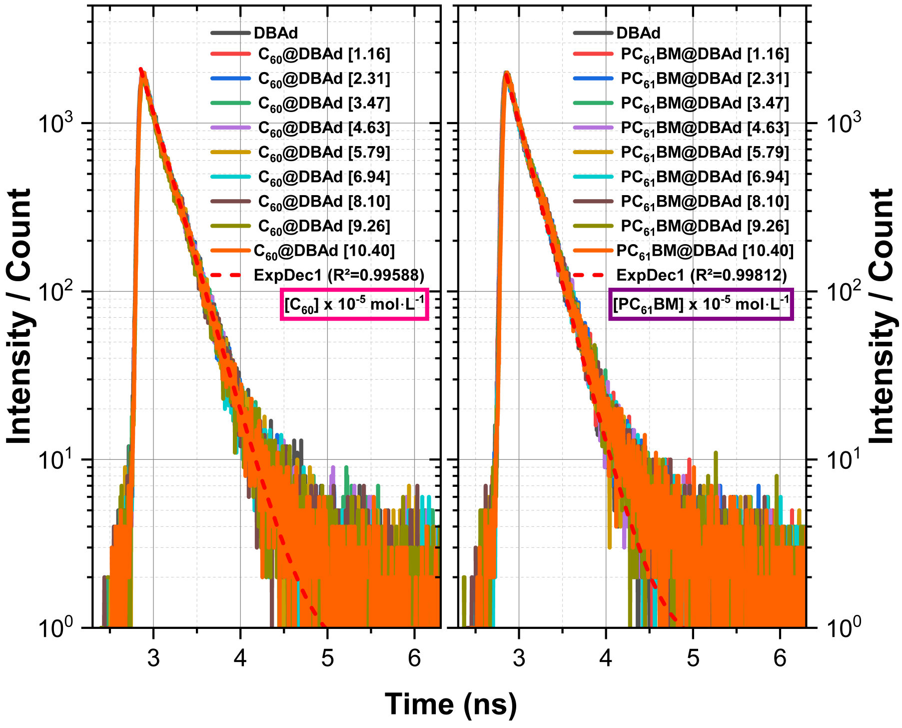

Table 14 – Excited-state lifetimes (τ, in ns) of ethoxy-dibenzalacetone derivative (DBAd) in ethanol-toluene mixture with different concentrations of C_{60} and $PC_{61}BM$.

Molar Concentration of C_{60} and $PC_{61}BM$ ($\times 10^{-5}$ mol $\cdot$ L^{-1})	[a]**Excited-State Lifetime** (ns)	
	C_{60}@DBAd	$PC_{61}BM$@DBAd
0.00	0.205 ± 0.002	0.199 ± 0.002
1.16	0.202 ± 0.002	0.206 ± 0.002
2.31	0.199 ± 0.002	0.207 ± 0.002
3.47	0.199 ± 0.002	0.206 ± 0.002
4.63	0.201 ± 0.002	0.202 ± 0.002
5.79	0.196 ± 0.002	0.203 ± 0.002
6.94	0.198 ± 0.002	0.204 ± 0.002
8.10	0.196 ± 0.002	0.202 ± 0.002
9.26	0.197 ± 0.002	0.199 ± 0.002
10.40	0.199 ± 0.002	0.196 ± 0.002

[a] τ: Excited-state lifetime of DBAd in ethanol-toluene binary mixtures with varying concentrations of C_{60} and $PC_{61}BM$, determined by time-correlated single-photon counting (TCSPC) with deconvolution of the instrument response function (IRF) and chi-square (χ^2) minimization.

Table 16 – Optimized geometric parameters (bond length and bond angles) for the ethoxy-dibenzalacetone derivative (DBAd, $C_{21}H_{22}O_3$) calculated by TD-DFT/PCM/M06-2X/6-311+G(d,p) in toluene (TOL, κ_{TOL} = 2.37), dichloromethane (DCM, κ_{DCM} = 8.93), and acetonitrile (ACN, κ_{ACN} = 35.67).

Toluene (κ_{TOL} = 2.37)				**Dichloromethane** (κ_{DCM} = 8.93)				**Acetonitrile** (κ_{ACN} = 35.67)			
Lig.	Å	Lig.	°	Lig.	Å	Lig.	°	Lig.	Å	Lig.	°
1 – 2	1.403	2 – 1 – 3	117.8	1 – 2	1.403	2 – 1 – 3	117.8	1 – 2	1.403	2 – 1 – 3	117.9
1 – 3	1.397	2 – 1 – 10	119.2	1 – 3	1.398	2 – 1 – 10	118.9	1 – 3	1.398	2 – 1 – 10	119.1
1 – 10	1.466	1 – 2 – 4	121.4	1 – 10	1.465	1 – 2 – 4	121.4	1 – 10	1.465	1 – 2 – 4	121.3
2 – 4	1.382	1 – 2 – 25	119.3	2 – 4	1.382	1 – 2 – 25	119.3	2 – 4	1.383	1 – 2 – 25	119.3
2 – 25	1.085	3 – 1 – 10	123.0	2 – 25	1.085	3 – 1 – 10	123.3	2 – 25	1.085	3 – 1 – 10	122.9
3 – 5	1.389	1 – 3 – 5	121.6	3 – 5	1.389	1 – 3 – 5	121.5	3 – 5	1.389	1 – 3 – 5	121.5
3 – 26	1.084	1 – 3 – 26	119.9	3 – 26	1.084	1 – 3 – 26	120.2	3 – 26	1.084	1 – 3 – 26	120.1
4 – 6	1.398	1 – 10 – 11	126.4	4 – 6	1.399	1 – 10 – 11	126.8	4 – 6	1.399	1 – 10 – 11	126.2
4 – 27	1.083	1 – 10 – 34	115.2	4 – 27	1.083	1 – 10 – 34	114.8	4 – 27	1.083	1 – 10 – 34	115.2
5 – 6	1.398	4 – 2 – 25	119.3	5 – 6	1.399	4 – 2 – 25	119.3	5 – 6	1.399	4 – 2 – 25	119.4

Continued on next page

Table 16 – Continued

Toluene (κ_{TOL} = 2.37)				**Dichloromethane** (κ_{DCM} = 8.93)				**Acetonitrile** (κ_{ACN} = 35.674)			
Lig.	Å	Lig.	°	Lig.	Å	Lig.	°	Lig.	Å	Lig.	°
5 – 28	1.081	2 – 4 – 6	120.0	5 – 28	1.081	2 – 4 – 6	120.0	5 – 28	1.081	2 – 4 – 6	120.0
6 – 7	1.353	2 – 4 – 27	121.4	6 – 7	1.352	2 – 4 – 27	121.3	6 – 7	1.352	2 – 4 – 27	121.2
7 – 8	1.425	5 – 3 – 26	118.5	7 – 8	1.428	5 – 3 – 26	118.3	7 – 8	1.429	5 – 3 – 26	118.4
8 – 9	1.512	3 – 5 – 6	119.6	8 – 9	1.512	3 – 5 – 6	119.7	8 – 9	1.512	3 – 5 – 6	119.6
8 – 29	1.095	3 – 5 – 28	119.2	8 – 29	1.095	3 – 5 – 28	119.2	8 – 29	1.095	3 – 5 – 28	119.2
8 – 30	1.096	6 – 4 – 27	118.6	8 – 30	1.095	6 – 4 – 27	118.8	8 – 30	1.095	6 – 4 – 27	118.8
9 – 31	1.091	4 – 6 – 5	119.6	9 – 31	1.091	4 – 6 – 5	119.6	9 – 31	1.091	4 – 6 – 5	119.6
9 – 32	1.091	4 – 6 – 7	116.1	9 – 32	1.091	4 – 6 – 7	116.1	9 – 32	1.091	4 – 6 – 7	116.1
9 – 33	1.091	6 – 5 – 28	121.1	9 – 33	1.091	6 – 5 – 28	121.1	9 – 33	1.091	6 – 5 – 28	121.2
10 – 11	1.340	5 – 6 – 7	124.3	10 – 11	1.342	5 – 6 – 7	124.3	10 – 11	1.342	5 – 6 – 7	124.3
10 – 34	1.087	6 – 7 – 8	118.4	10 – 34	1.087	6 – 7 – 8	118.4	10 – 34	1.087	6 – 7 – 8	118.4
11 – 12	1.483	7 – 8 – 9	107.4	11 – 12	1.480	7 – 8 – 9	107.4	11 – 12	1.479	7 – 8 – 9	107.4
11 – 35	1.085	7 – 8 – 29	109.4	11 – 35	1.085	7 – 8 – 29	109.3	11 – 35	1.086	7 – 8 – 29	109.3
12 – 13	1.482	7 – 8 – 30	109.3	12 – 13	1.480	7 – 8 – 30	109.3	12 – 13	1.478	7 – 8 – 30	109.3
12 – 21	1.221	9 – 8 – 29	111.1	12 – 21	1.225	9 – 8 – 29	111.1	12 – 21	1.226	9 – 8 – 29	111.1
13 – 14	1.341	9 – 8 – 30	111.1	13 – 14	1.342	9 – 8 – 30	111.1	13 – 14	1.342	9 – 8 – 30	111.1
13 – 36	1.085	8 – 9 – 31	110.4	13 – 36	1.086	8 – 9 – 31	110.5	13 – 36	1.086	8 – 9 – 31	110.5
14 – 15	1.465	8 – 9 – 32	110.4	14 – 15	1.465	8 – 9 – 32	110.5	14 – 15	1.464	8 – 9 – 32	110.6
14 – 37	1.087	8 – 9 – 33	109.9	14 – 37	1.087	8 – 9 – 33	109.7	14 – 37	1.087	8 – 9 – 33	109.7
15 – 18	1.397	29 – 8 – 30	108.5	15 – 18	1.398	29 – 8 – 30	108.6	15 – 18	1.398	29 – 8 – 30	108.6
15 – 20	1.403	31 – 9 – 32	108.7	15 – 20	1.404	31 – 9 – 32	108.8	15 – 20	1.403	31 – 9 – 32	108.9
16 – 17	1.399	31 – 9 – 33	108.7	16 – 17	1.399	31 – 9 – 33	108.6	16 – 17	1.399	31 – 9 – 33	108.6
16 – 18	1.389	32 – 9 – 33	108.6	16 – 18	1.389	32 – 9 – 33	108.6	16 – 18	1.389	32 – 9 – 33	108.6
16 – 38	1.081	11 – 10 – 34	118.4	16 – 38	1.081	11 – 10 – 34	118.4	16 – 38	1.081	11 – 10 – 34	118.6
17 – 19	1.398	10 – 11 – 12	124.2	17 – 19	1.399	10 – 11 – 12	124.2	17 – 19	1.399	10 – 11 – 12	124.1
17 – 22	1.352	10 – 11 – 35	121.4	17 – 22	1.352	10 – 11 – 35	121.6	17 – 22	1.352	10 – 11 – 35	121.3
18 – 39	1.084	12 – 11 – 35	113.9	18 – 39	1.084	12 – 11 – 35	113.9	18 – 39	1.084	12 – 11 – 35	114.1
19 – 20	1.382	11 – 12 – 13	121.2	19 – 20	1.382	11 – 12 – 13	121.4	19 – 20	1.382	11 – 12 – 13	121.4
19 – 40	1.083	11 – 12 – 21	119.4	19 – 40	1.083	11 – 12 – 21	119.3	19 – 40	1.083	11 – 12 – 21	119.3
20 – 41	1.085	13 – 12 – 21	119.4	20 – 41	1.085	13 – 12 – 21	119.3	20 – 41	1.085	13 – 12 – 21	119.3
22 – 23	1.425	12 – 13 – 14	124.3	22 – 23	1.428	12 – 13 – 14	124.3	22 – 23	1.429	12 – 13 – 14	124.2
23 – 24	1.512	12 – 13 – 36	113.6	23 – 24	1.512	12 – 13 – 36	113.8	23 – 24	1.511	12 – 13 – 36	113.9
23 – 42	1.096	14 – 13 – 36	121.7	23 – 42	1.095	14 – 13 – 36	121.6	23 – 42	1.095	14 – 13 – 36	121.4
23 – 43	1.095	13 – 14 – 15	126.9	23 – 43	1.095	13 – 14 – 15	126.8	23 – 43	1.095	13 – 14 – 15	126.5

Continued on next page

Table 16 – Continued

Toluene ($\kappa_{\textbf{TOL}}$ = 2.37)				**Dichloromethane** ($\kappa_{\textbf{DCM}}$ = 8.93)				**Acetonitrile** ($\kappa_{\textbf{ACN}}$ = 35.674)			
Lig.	Å	Lig.	°	Lig.	Å	Lig.	°	Lig.	Å	Lig.	°
24 – 44	1.091	13 – 14 – 37	118.3	24 – 44	1.091	13 – 14 – 37	118.4	24 – 44	1.091	13 – 14 – 37	118.5
24 – 45	1.091	15 – 14 – 37	114.8	24 – 45	1.091	15 – 14 – 37	114.8	24 – 45	1.091	15 – 14 – 37	114.9
24 – 46	1.091	14 – 15 – 18	123.4	24 – 46	1.091	14 – 15 – 18	123.4	24 – 46	1.091	14 – 15 – 18	123.3
–	–	14 – 15 – 20	118.9	–	–	14 – 15 – 20	118.8	–	–	14 – 15 – 20	118.8
–	–	18 – 15 – 20	117.8	–	–	18 – 15 – 20	117.8	–	–	18 – 15 – 20	117.9
–	–	15 – 18 – 16	121.6	–	–	15 – 18 – 16	121.6	–	–	15 – 18 – 16	121.5
–	–	15 – 18 – 39	120.1	–	–	15 – 18 – 39	120.2	–	–	15 – 18 – 39	120.2
–	–	15 – 20 – 19	121.5	–	–	15 – 20 – 19	121.4	–	–	15 – 20 – 19	121.4
–	–	15 – 20 – 41	119.2	–	–	15 – 20 – 41	119.3	–	–	15 – 20 – 41	119.2
–	–	17 – 16 – 18	119.7	–	–	17 – 16 – 18	119.6	–	–	17 – 16 – 18	119.6
–	–	17 – 16 – 38	121.1	–	–	17 – 16 – 38	121.1	–	–	17 – 16 – 38	121.1
–	–	16 – 17 – 19	119.6	–	–	16 – 17 – 19	119.6	–	–	16 – 17 – 19	119.6
–	–	16 – 17 – 22	124.4	–	–	16 – 17 – 22	124.3	–	–	16 – 17 – 22	124.3
–	–	18 – 16 – 38	119.2	–	–	18 – 16 – 38	119.2	–	–	18 – 16 – 38	119.2
–	–	16 – 18 – 39	118.3	–	–	16 – 18 – 39	118.2	–	–	16 – 18 – 39	118.3
–	–	19 – 17 – 22	116.0	–	–	19 – 17 – 22	116.1	–	–	19 – 17 – 22	116.1
–	–	17 – 19 – 20	120.0	–	–	17 – 19 – 20	120.0	–	–	17 – 19 – 20	120.0
–	–	17 – 19 – 40	118.6	–	–	17 – 19 – 40	118.7	–	–	17 – 19 – 40	118.8
–	–	17 – 22 – 23	118.5	–	–	17 – 22 – 23	118.5	–	–	17 – 22 – 23	118.5
–	–	20 – 19 – 40	121.5	–	–	20 – 19 – 40	121.3	–	–	20 – 19 – 40	121.3
–	–	19 – 20 – 41	119.3	–	–	19 – 20 – 41	119.3	–	–	19 – 20 – 41	119.4
–	–	22 – 23 – 24	107.4	–	–	22 – 23 – 24	107.4	–	–	22 – 23 – 24	107.5
–	–	22 – 23 – 42	109.3	–	–	22 – 23 – 42	109.3	–	–	22 – 23 – 42	109.2
–	–	22 – 23 – 43	109.4	–	–	22 – 23 – 43	109.4	–	–	22 – 23 – 43	109.4
–	–	24 – 23 – 42	111.1	–	–	24 – 23 – 42	111.1	–	–	24 – 23 – 42	111.0
–	–	24 – 23 – 43	111.1	–	–	24 – 23 – 43	111.1	–	–	24 – 23 – 43	111.1
–	–	23 – 24 – 44	110.4	–	–	23 – 24 – 44	110.5	–	–	23 – 24 – 44	110.8
–	–	23 – 24 – 45	110.4	–	–	23 – 24 – 45	110.5	–	–	23 – 24 – 45	110.5
–	–	23 – 24 – 46	109.9	–	–	23 – 24 – 46	109.7	–	–	23 – 24 – 46	109.6
–	–	42 – 23 – 43	108.5	–	–	42 – 23 – 43	108.6	–	–	42 – 23 – 43	108.5
–	–	44 – 24 – 45	108.7	–	–	44 – 24 – 45	108.8	–	–	44 – 24 – 45	108.8
–	–	44 – 24 – 46	108.7	–	–	44 – 24 – 46	108.6	–	–	44 – 24 – 46	108.6
–	–	45 – 24 – 46	108.6	–	–	45 – 24 – 46	108.6	–	–	45 – 24 – 46	108.5

Table 15 – Excited state (ES), energies (E in eV), oscillator strengths (O Str), vertical transition, and propability (%) of ethoxy-dibenzalacetona derivative (DBAd) calculated at TD-DFT/PCM/M06-2X/6-311+G(d,p) in toluene (TOL, $\kappa_{\mathrm{TOL}} = 2.37$), dichloromethane (DCM, $\kappa_{\mathrm{DCM}} = 8.93$), and acetonitrile (ACN, $\kappa_{\mathrm{ACN}} = 35.67$).

	Toluene (κ_{TOL} = 2.37)				**Dichloromethane** (κ_{DCM} = 8.93)				**Acetonitrile** (κ_{ACN} = 35.67)			
ES	E (eV)	^{c}**O Str**	**Trans.**	^{d}(%)	E (eV)	^{c}**O Str**	**Trans.**	^{d}(%)	E (eV)	^{c}**O Str**	**Trans.**	^{d}(%)
1	3.67	0.011	H-4 ⟶ L	72.7	3.74	0.016	H-4 ⟶ L	73.5	3.76	0.011	H-4 ⟶ L	74.0
			H-1 ⟶ L	3.6			H-1 ⟶ L	5.3			H-5 ⟶ L	5.1
			H-4 ⟶ L+16	3.52			H-5 ⟶ L	3.7			H-1 ⟶ L	3.5
			H-5 ⟶ L	2.7			H-4 ⟶ L+19	3.3			H-4 ⟶ L+19	2.4
			H-2 ⟶ L	2.6								
			H-4 ⟶ L+19	2.3								
2	3.97	1.065	H ⟶ L	85.5	3.90	1.053	H ⟶ L	87.2	3.91	1.048	H ⟶ L	87.2
			H-1 ⟶ L+1	10.5			H-1 ⟶ L+1	8.9			H-1 ⟶ L+1	8.6
			H-6 ⟶ L	2.3			H-6 ⟶ L	2.4			H-6 ⟶ L	2.5
3	4.32	0.451	H-1 ⟶ L	82.7	4.30	0.449	H-1 ⟶ L	82.0	4.28	0.424	H-1 ⟶ L	85.5
			H ⟶ L+1	10.4			H ⟶ L+1	9.5			H ⟶ L+1	7.5
			H-4 ⟶ L	2.6			H-4 ⟶ L	3.6			H-5 ⟶ L	2.3
							H-5 ⟶ L	2.2			H-4 ⟶ L	2.2
4	4.85	0.013	H ⟶ L+1	23.7	4.83	0.005	H ⟶ L+1	35.5	4.85	0.002	H ⟶ L+1	30.7
			H-1 ⟶ L+3	14.4			H-1 ⟶ L+2	20.6			H-1 ⟶ L+2	22.1
			H ⟶ L+4	13.7			H-2 ⟶ L	9.0			H ⟶ L+3	14.7
			H-3 ⟶ L	8.8			H ⟶ L+3	8.2			H-2 ⟶ L	6.9
			H-3 ⟶ L+1	6.3			H ⟶ L+4	7.6			H-3 ⟶ L	5.7
			H-1 ⟶ L+1	5.5			H-3 ⟶ L+1	5.6			H-3 ⟶ L+1	5.1
			H-1 ⟶ L+4	4.6			H-1 ⟶ L	5.4			H-1 ⟶ L	3.8
			H ⟶ L+2	4.2							H ⟶ L+4	2.6
			H-1 ⟶ L	4.2								
			H ⟶ L+3	3.4								
5	4.86	0.015	H ⟶ L+3	24.6	4.85	0.018	H ⟶ L+2	27.7	4.86	0.017	H ⟶ L+2	27.2
			H-1 ⟶ L+1	20.6			H-1 ⟶ L+1	27.3			H-1 ⟶ L+1	24.2
			H-1 ⟶ L+3	9.4			H-3 ⟶ L	11.1			H-1 ⟶ L+3	14.9
			H-1 ⟶ L+4	9.3			H-1 ⟶ L+3	8.6			H-3 ⟶ L	9.1
			H-2 ⟶ L	7.7			H-1 ⟶ L+4	7.5			H-2 ⟶ L+1	5.9
			H-2 ⟶ L+1	6.9			H-2 ⟶ L+1	6.7			H-2 ⟶ L	5.0
			H ⟶ L+1	5.6			H ⟶ L	2.7			H ⟶ L	2.4
			H-3 ⟶ L	2.6							H-1 ⟶ L+4	2.3
			H ⟶ L	2.5								
6	5.12	0.073	H-1 ⟶ L+1	30.1	5.09	0.038	H ⟶ L+1	46.3	5.11	0.055	H ⟶ L+1	41.2
			H ⟶ L+1	23.5			H-2 ⟶ L	14.6			H-2 ⟶ L	13.3
			H-2 ⟶ L	9.7			H ⟶ L+3	7.4			H-1 ⟶ L+1	11.4
			H-2 ⟶ L+1	4.0			H ⟶ L+4	6.3			H ⟶ L+3	8.5
			H-1 ⟶ L+4	3.9			H-3 ⟶ L+1	6.0			H-2 ⟶ L+1	4.2
			H ⟶ L+3	3.9			H-1 ⟶ L+2	5.3			H-1 ⟶ L+2	2.9
			H ⟶ L+4	3.8			H-1 ⟶ L	2.8			H-1 ⟶ L+3	2.2
			H-1 ⟶ L+3	3.8							H-1 ⟶ L	2.0
			H ⟶ L	2.9								
			H-1 ⟶ L	2.0								
7	5.13	0.056	H ⟶ L+1	28.2	5.12	0.096	H-1 ⟶ L+1	55.2	5.13	0.075	H-1 ⟶ L+1	47.1
			H-1 ⟶ L+1	25.1			H-3 ⟶ L	11.4			H-3 ⟶ L	12.9
			H-3 ⟶ L	11.3			H-1 ⟶ L+3	4.8			H ⟶ L+1	11.2
			H ⟶ L+4	6.4			H-1 ⟶ L+4	4.6			H-1 ⟶ L+3	5.0
			H-1 ⟶ L+4	4.6			H ⟶ L+2	4.5			H-3 ⟶ L+1	3.4
			H-3 ⟶ L+1	4.5			H ⟶ L	4.3			H ⟶ L	3.3
			H ⟶ L	2.3			H-2 ⟶ L+1	4.0			H ⟶ L+2	2.7
8	5.75	0.006	H ⟶ L+2	54.7	5.74	0.136	H-3 ⟶ L	47.2	5.74	0.180	H-3 ⟶ L	37.1
			H-1 ⟶ L+5	15.5			H ⟶ L+2	20.7			H ⟶ L+2	20.8
			H ⟶ L+4	7.0			H-2 ⟶ L+1	8.3			H-2 ⟶ L	15.2
			H-3 ⟶ L	2.8			H-1 ⟶ L+3	6.9			H-1 ⟶ L+3	11.9
			H-1 ⟶ L+4	2.8			H-1 ⟶ L+4	6.7			H-2 ⟶ L+1	5.3
			H-1 ⟶ L+2	2.4			H-2 ⟶ L	4.4			H-1 ⟶ L+4	3.2
			H-1 ⟶ L+9	2.2							H-3 ⟶ L+1	2.3
9	5.77	0.147	H-3 ⟶ L	28.0	5.78	0.269	H ⟶ L+3	38.6	5.77	0.380	H-2 ⟶ L	38.1
			H ⟶ L+3	15.3			H-2 ⟶ L	31.8			H ⟶ L+3	19.0
			H-2 ⟶ L	13.5			H-1 ⟶ L+2	8.0			H-1 ⟶ L+2	16.1
			H-2 ⟶ L+1	10.6			H-1 ⟶ L+5	6.9			H-3 ⟶ L	14.8
			H-4 ⟶ L+1	9.8			H-3 ⟶ L+1	3.9			H-3 ⟶ L+1	3.4
			H-1 ⟶ L+4	7.9			H-3 ⟶ L	2.3			H ⟶ L+4	2.3
			H-3 ⟶ L+1	3.2							H-2 ⟶ L+1	2.3
10	5.78	0.032	H-1 ⟶ L+2	47.7	5.79	0.218	H ⟶ L+4	43.2	5.81	0.007	H ⟶ L+4	55.5
			H ⟶ L+5	24.2			H-2 ⟶ L	16.7			H-1 ⟶ L+5	18.2
			H-1 ⟶ L+4	5.9			H-1 ⟶ L+5	10.5			H ⟶ L+3	10.2
			H ⟶ L+2	3.1			H-1 ⟶ L+2	8.0				
			H ⟶ L+9	2.7			H ⟶ L+3	7.1				
			H-3 ⟶ L	2.1			H-3 ⟶ L	2.4				
							H-3 ⟶ L+1	2.3				

${}^{a}\kappa$, is the dielectric constant for the solvent; ^{b}H=HOMO, L=LUMO. ^{c}O Str, oscillator strength; ^{d}Probability;

Figure 31 – UV-Vis absorption (black curves) and fluorescence emission (blue curves) spectra (in absolute units) for ethoxy-dibenzalacetone (DBAd) and Coumarin 6 (C6) used as standard reference in the DBAd fluorescence quantum yield (Φ_{DBAd}) determination. The absorbance spectra were recorded with maximum absorption bands observed at 365 nm for $\lambda_{\text{abs}}^{\text{DBAd}}$ and 455 nm for $\lambda_{\text{abs}}^{\text{C6}}$. Emission spectra were acquired under the same instrumental conditions with maxima at 485 nm for $\lambda_{\text{em}}^{\text{DBAd}}$ and 503 nm for $\lambda_{\text{em}}^{\text{C6}}$. The Φ_{DBAd} was calculated by comparison to C6 using Eq. (4.27).

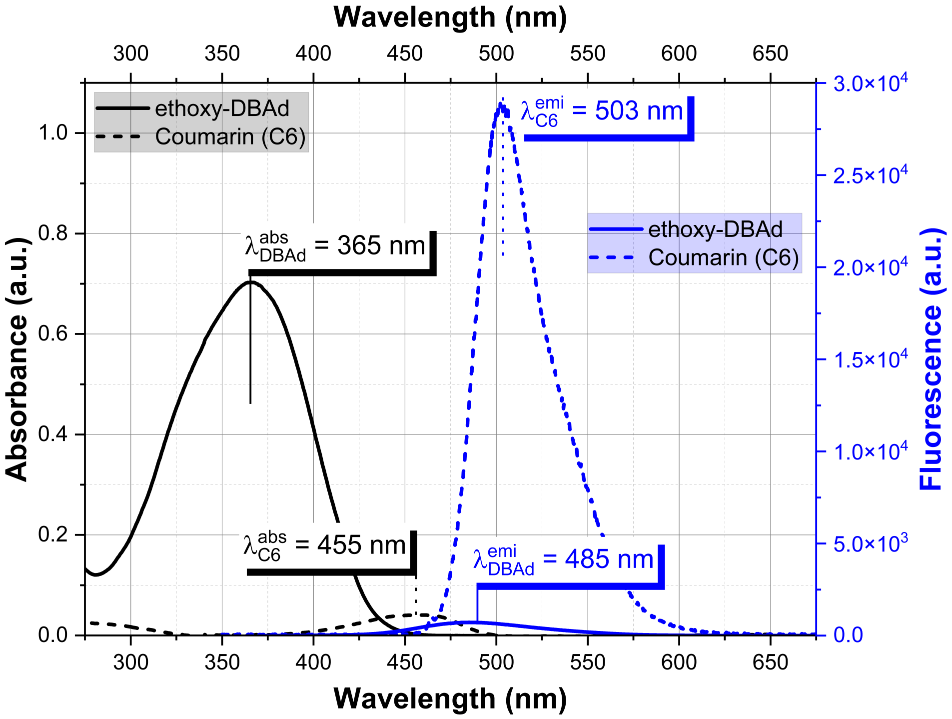

Table 17 – GGA-DFT/BLYP-D2/DNP+ optimized geometric parameters (bond lengths and bond angles) for (1E,4E)-1,5-bis(4-ethoxyphenyl)penta-1,4-dien-3-one ethoxy-dibenzalacetone derivative (DBAd) and fullerene compounds (C_{60} and $PC_{61}BM$). The atom labels are presented in Figure 16.

DBAd				**C_{60}**				**$PC_{61}BM$**			
Lig.	Å	Lig.	°	Lig.	Å	Lig.	°	Lig.	Å	Lig.	°
1-2	1.401	2-1-3	117.6	1-2	1.401	2-1-6	120.0	1-2	1.401	2-1-6	120.0
1-3	1.410	2-1-10	119.3	1-6	1.398	2-1-7	120.1	1-6	1.398	2-1-7	120.1
1-10	1.460	1-2-4	121.6	1-7	1.089	1-2-3	119.9	1-7	1.089	1-2-3	119.9

Continued on next page

Table 17 – Continued

DBAd				**C_{60}**				**$PC_{61}BM$**			
Lig.	Å	Lig.	°	Lig.	Å	Lig.	°	Lig.	Å	Lig.	°
2-4	1.389	1-2-25	118.7	2-3	1.401	1-2-9	108.0	2-3	1.401	1-2-8	120.0
2-25	1.090	3-1-10	123.1	2-9	1.454	6-1-7	119.9	2-8	1.089	6-1-7	119.9
3-5	1.395	1-3-5	121.5	3-4	1.398	1-6-5	120.2	3-4	1.398	1-6-5	120.2
3-26	1.089	1-3-26	119.6	3-11	1.454	1-6-17	120.0	3-9	1.090	1-6-11	120.7
4-6	1.407	1-10-11	126.8	4-5	1.399	1-7-8	108.0	4-5	1.399	3-2-8	120.1
4-27	1.088	1-10-34	115.3	4-12	1.454	1-7-19	120.0	4-10	1.089	2-3-4	119.9
5-6	1.400	4-2-25	119.7	5-6	1.400	3-2-9	120.0	5-6	1.400	2-3-9	120.2
5-28	1.086	2-4-6	119.8	5-15	1.454	2-3-4	119.9	5-12	1.500	4-3-9	119.9
6-7	1.373	2-4-27	121.3	6-17	1.454	2-3-11	120.0	6-11	1.089	3-4-5	120.2
7-8	1.452	5-3-26	118.9	7-8	1.452	2-9-8	108.0	12-13	1.521	3-4-10	120.5
8-9	1.523	3-5-6	119.8	7-19	1.399	2-9-10	120.0	12-35	1.497	5-4-10	119.3
8-29	1.101	3-5-28	119.7	8-9	1.523	4-3-11	108.0	12-47	1.498	4-5-6	119.8
8-30	1.101	6-4-27	118.9	8-20	1.399	3-4-5	120.2	13-14	1.095	4-5-12	120.5
9-31	1.097	4-6-5	119.7	9-10	1.399	3-4-12	108.0	13-15	1.096	6-5-12	119.7
9-32	1.098	4-6-7	115.6	10-57	1.454	3-11-29	108.0	13-16	1.531	5-6-11	119.2
9-33	1.099	6-5-28	120.5	10-59	1.454	3-11-59	120.0	16-17	1.099	5-12-13	114.8
10-11	1.355	5-6-7	124.7	11-29	1.454	5-4-12	120.0	16-18	1.098	5-12-35	115.5
10-34	1.091	6-7-8	117.8	11-59	1.399	4-5-6	119.8	16-19	1.549	5-12-47	116.0
11-12	1.478	7-8-9	107.5	12-13	1.521	4-5-15	120.0	19-20	1.097	13-12-35	116.7
11-35	1.090	7-8-29	109.3	12-29	1.454	4-12-13	120.0	19-21	1.096	13-12-47	116.1
12-13	1.521	7-8-30	108.6	13-14	1.095	4-12-29	108.0	19-22	1.526	12-13-14	110.2
12-21	1.246	9-8-29	111.4	13-39	1.454	6-5-15	108.0	22-23	1.377	12-13-15	108.2
13-14	1.095	9-8-30	111.5	14-15	1.460	5-6-17	108.0	22-28	1.216	12-13-16	110.9
13-36	1.090	8-9-31	110.4	14-28	1.454	5-15-14	120.0	23-24	1.454	35-12-47	70.7

Continued on next page

Table 17 – Continued

DBAd				**C_{60}**				**$PC_{61}BM$**			
Lig.	Å	Lig.	°	Lig.	Å	Lig.	°	Lig.	Å	Lig.	°
14-15	1.460	8-9-32	110.8	15-16	1.454	5-15-16	108.0	24-25	1.095	12-35-29	127.7
14-37	1.091	8-9-33	109.4	16-17	1.099	6-17-16	108.0	24-26	1.099	12-35-36	125.8
15-18	1.410	29-8-30	108.5	16-26	1.399	6-17-18	120.0	24-27	1.097	12-47-46	127.0
15-20	1.416	31-9-32	108.8	17-18	1.399	8-7-19	120.0	29-30	1.447	12-47-50	126.3
16-17	1.099	31-9-33	108.7	18-19	1.454	7-8-9	107.5	29-34	1.390	14-13-15	107.2
16-18	1.098	32-9-33	108.8	18-24	1.454	7-8-20	120.0	29-35	1.478	14-13-16	109.5
16-38	1.086	11-10-34	117.9	19-22	1.526	7-19-18	120.0	30-31	1.397	15-13-16	110.8
17-19	1.407	10-11-12	124.1	20-21	1.454	7-19-22	120.0	30-37	1.450	13-16-17	108.7
17-22	1.374	10-11-35	120.8	20-56	1.454	9-8-20	120.0	31-32	1.445	13-16-18	109.2
18-39	1.089	12-11-35	114.5	21-22	1.399	8-9-10	120.0	31-39	1.455	13-16-19	112.0
19-20	1.097	11-12-13	120.5	21-54	1.454	8-20-21	120.0	32-33	1.402	17-16-18	107.5
19-40	1.089	11-12-21	119.8	22-23	1.377	8-20-56	120.0	32-40	1.452	17-16-19	108.5
20-41	1.090	13-12-21	119.8	23-24	1.454	9-10-57	120.0	33-34	1.453	18-16-19	110.7
22-23	1.377	12-13-14	110.2	23-52	1.399	9-10-59	120.0	33-43	1.451	16-19-20	109.6
23-24	1.454	12-13-36	114.5	24-25	1.095	57-10-59	108.0	34-45	1.474	16-19-21	109.1
23-42	1.101	14-13-36	120.8	25-26	1.454	10-57-43	108.0	35-36	1.476	16-19-22	110.5
23-43	1.101	13-14-15	126.8	25-50	1.454	10-57-56	120.0	36-37	1.447	20-19-21	108.6
24-44	1.097	13-14-37	117.9	26-27	1.454	10-59-11	120.0	36-48	1.389	20-19-22	112.7
24-45	1.098	15-14-37	115.3	27-28	1.399	10-59-42	108.0	37-38	1.397	21-19-22	106.2
24-46	1.099	14-15-18	123.1	27-49	1.454	29-11-59	120.0	38-85	1.446	19-22-23	119.2
-	-	14-15-20	119.3	28-38	1.454	11-29-12	108.0	38-87	1.455	19-22-28	122.6
-	-	18-15-20	117.6	29-58	1.399	11-29-58	120.0	39-57	1.452	23-22-28	118.0
-	-	15-18-16	121.5	30-31	1.397	11-59-42	120.0	39-87	1.398	22-23-24	120.2
-	-	15-18-39	119.6	30-37	1.450	13-12-29	120.0	40-41	1.397	23-24-25	105.2

Continued on next page

Table 17 – Continued

DBAd				**C_{60}**				**$PC_{61}BM$**			
Lig.	Å	Lig.	°	Lig.	Å	Lig.	°	Lig.	Å	Lig.	°
-	-	15-20-19	121.6	30-60	1.454	12-13-14	110.2	40-57	1.456	23-24-26	110.6
-	-	15-20-41	118.7	31-32	1.445	12-13-39	120.0	41-42	1.452	23-24-27	111.1
-	-	17-16-18	107.5	31-40	1.454	12-29-58	120.0	41-67	1.451	25-24-26	109.7
-	-	17-16-38	120.5	32-33	1.402	14-13-39	108.0	42-43	1.402	25-24-27	110.0
-	-	16-17-19	119.7	32-41	1.454	13-14-15	126.8	42-56	1.453	26-24-27	110.2
-	-	16-17-22	124.7	33-34	1.453	13-14-28	108.0	43-44	1.449	30-29-34	119.6
-	-	18-16-38	119.7	33-44	1.454	13-39-38	108.0	44-45	1.458	30-29-35	107.8
-	-	16-18-39	118.9	34-46	1.454	13-39-40	120.0	44-54	1.402	29-30-31	121.3
-	-	19-17-22	115.6	34-60	1.399	15-14-28	120.0	45-46	1.391	29-30-37	108.3
-	-	17-19-20	119.8	35-36	1.476	14-15-16	120.0	46-47	1.475	34-29-35	123.4
-	-	17-19-40	118.9	35-48	1.399	14-28-27	120.0	46-52	1.451	29-34-33	119.3
-	-	17-22-23	117.8	35-60	1.454	14-28-38	108.0	47-50	1.476	29-34-45	121.8
-	-	20-19-40	121.3	36-37	1.447	15-16-17	108.0	48-49	1.471	29-35-36	105.9
-	-	19-20-41	119.7	36-49	1.399	15-16-26	120.0	48-84	1.457	31-30-37	120.1
-	-	22-23-24	120.2	37-38	1.397	17-16-26	120.0	49-50	1.388	30-31-32	119.1
-	-	22-23-42	109.3	38-39	1.454	16-17-18	120.0	49-82	1.456	30-31-39	120.0
-	-	22-23-43	108.6	39-40	1.399	16-26-25	120.0	50-51	1.443	30-37-36	108.3
-	-	24-23-42	111.4	40-58	1.454	16-26-27	120.0	51-52	1.450	30-37-38	119.9
-	-	24-23-43	111.5	41-42	1.452	17-18-19	120.0	51-80	1.397	32-31-39	108.4
-	-	23-24-44	110.4	41-58	1.454	17-18-24	120.0	52-53	1.396	31-32-33	119.6
-	-	23-24-45	110.8	42-43	1.399	19-18-24	108.0	53-54	1.446	31-32-40	107.9
-	-	23-24-46	109.4	42-59	1.454	18-19-22	108.0	53-78	1.454	31-39-57	107.7
-	-	42-23-43	108.5	43-44	1.449	18-24-23	108.0	54-55	1.454	31-39-87	119.9
-	-	44-24-45	108.8	43-57	1.454	18-24-25	120.0	55-56	1.398	33-32-40	120.2

Continued on next page

Table 17 – Continued

DBAd				**C_{60}**				**$PC_{61}BM$**			
Lig.	Å	Lig.	°	Lig.	Å	Lig.	°	Lig.	Å	Lig.	°
-	-	44-24-46	108.7	44-45	1.458	19-22-21	120.0	55-77	1.456	32-33-34	120.8
-	-	45-24-46	108.8	45-46	1.391	19-22-23	119.2	56-66	1.453	32-33-43	119.6
-	-	-	-	45-55	1.399	21-20-56	108.0	57-86	1.398	32-40-41	120.0
-	-	-	-	46-47	1.475	20-21-22	120.0	58-59	1.398	32-40-57	108.0
-	-	-	-	47-48	1.454	20-21-54	108.0	58-65	1.454	34-33-43	108.5
-	-	-	-	47-53	1.454	20-56-55	108.0	58-88	1.455	33-34-45	107.5
-	-	-	-	48-51	1.454	20-56-57	120.0	59-60	1.456	33-43-42	120.4
-	-	-	-	49-50	1.388	22-21-54	120.0	59-68	1.388	33-43-44	108.2
-	-	-	-	50-51	1.443	21-22-23	120.0	60-61	1.443	34-45-44	107.4
-	-	-	-	51-52	1.450	21-54-53	120.0	60-69	1.453	34-45-46	122.0
-	-	-	-	52-53	1.396	21-54-55	108.0	61-62	1.455	35-36-37	107.9
-	-	-	-	53-54	1.446	22-23-24	120.2	61-72	1.452	35-36-48	123.9
-	-	-	-	54-55	1.454	22-23-52	120.0	62-74	1.451	37-36-48	119.8
-	-	-	-	55-56	1.398	24-23-52	120.0	62-88	1.399	36-37-38	121.5
-	-	-	-	56-57	1.399	23-24-25	105.2	63-64	1.455	36-48-49	122.0
-	-	-	-	-	-	23-52-51	120.0	63-76	1.399	36-48-84	118.9
-	-	-	-	-	-	23-52-53	120.0	63-88	1.453	37-38-85	119.1
-	-	-	-	-	-	24-25-26	120.0	64-65	1.455	37-38-87	120.2
-	-	-	-	-	-	24-25-50	120.0	64-77	1.399	85-38-87	108.6
-	-	-	-	-	-	26-25-50	108.0	65-66	1.399	38-85-71	107.8
-	-	-	-	-	-	25-26-27	108.0	66-67	1.454	38-85-84	119.4
-	-	-	-	-	-	25-50-49	108.0	67-68	1.399	38-87-39	119.9
-	-	-	-	-	-	25-50-51	120.0	68-86	1.451	38-87-70	107.5
-	-	-	-	-	-	26-27-28	120.0	69-70	1.399	57-39-87	120.1

Continued on next page

Table 17 – Continued

DBAd				**C_{60}**				**$PC_{61}BM$**			
Lig.	Å	Lig.	°	Lig.	Å	Lig.	°	Lig.	Å	Lig.	°
-	-	-	-	-	-	26-27-49	108.0	69-86	1.455	39-57-40	108.0
-	-	-	-	-	-	28-27-49	120.0	70-71	1.456	39-57-86	119.9
-	-	-	-	-	-	27-28-38	120.0	70-87	1.452	39-87-70	120.1
-	-	-	-	-	-	27-49-36	120.0	71-72	1.398	41-40-57	120.0
-	-	-	-	-	-	27-49-50	108.0	71-85	1.454	40-41-42	120.1
-	-	-	-	-	-	28-38-37	120.0	72-73	1.452	40-41-67	120.1
-	-	-	-	-	-	28-38-39	108.0	73-74	1.455	40-57-86	119.9
-	-	-	-	-	-	29-58-40	120.0	73-83	1.399	42-41-67	108.0
-	-	-	-	-	-	29-58-41	120.0	74-75	1.398	41-42-43	119.8
-	-	-	-	-	-	31-30-37	120.1	75-76	1.455	41-42-56	108.1
-	-	-	-	-	-	31-30-60	120.0	75-81	1.453	41-67-66	108.1
-	-	-	-	-	-	30-31-32	119.1	76-79	1.455	41-67-68	119.1
-	-	-	-	-	-	30-31-40	120.0	77-78	1.454	43-42-56	120.1
-	-	-	-	-	-	37-30-60	108.0	78-79	1.397	42-43-44	120.3
-	-	-	-	-	-	30-37-36	108.3	79-80	1.453	42-56-55	119.8
-	-	-	-	-	-	30-37-38	119.9	80-81	1.446	42-56-66	108.0
-	-	-	-	-	-	30-60-34	120.0	81-82	1.402	43-44-45	108.4
-	-	-	-	-	-	30-60-35	108.0	82-83	1.450	43-44-54	119.5
-	-	-	-	-	-	32-31-40	108.0	83-84	1.450	45-44-54	120.9
-	-	-	-	-	-	31-32-33	119.6	84-85	1.403	44-45-46	119.2
-	-	-	-	-	-	31-32-41	108.0	-	-	44-54-53	119.6
-	-	-	-	-	-	31-40-39	120.0	-	-	44-54-55	120.2
-	-	-	-	-	-	31-40-58	108.0	-	-	45-46-47	123.7
-	-	-	-	-	-	33-32-41	120.0	-	-	45-46-52	119.6

Continued on next page

Table 17 – Continued

DBAd				**C_{60}**				**$PC_{61}BM$**			
Lig.	Å	Lig.	°	Lig.	Å	Lig.	°	Lig.	Å	Lig.	°
-	-	-	-	-	-	32-33-34	120.8	-	-	47-46-52	107.8
-	-	-	-	-	-	32-33-44	120.0	-	-	46-47-50	105.9
-	-	-	-	-	-	32-41-42	120.0	-	-	46-52-51	108.1
-	-	-	-	-	-	32-41-58	108.0	-	-	46-52-53	121.3
-	-	-	-	-	-	34-33-44	108.0	-	-	47-50-49	123.5
-	-	-	-	-	-	33-34-46	108.0	-	-	47-50-51	108.0
-	-	-	-	-	-	33-34-60	120.0	-	-	49-48-84	107.5
-	-	-	-	-	-	33-44-43	120.0	-	-	48-49-50	121.6
-	-	-	-	-	-	33-44-45	108.0	-	-	48-49-82	107.5
-	-	-	-	-	-	46-34-60	120.0	-	-	48-84-83	108.4
-	-	-	-	-	-	34-46-45	108.0	-	-	48-84-85	121.2
-	-	-	-	-	-	34-46-47	120.0	-	-	50-49-82	119.0
-	-	-	-	-	-	34-60-35	120.0	-	-	49-50-51	120.0
-	-	-	-	-	-	36-35-48	120.0	-	-	49-82-81	121.0
-	-	-	-	-	-	36-35-60	108.0	-	-	49-82-83	108.5
-	-	-	-	-	-	35-36-37	107.9	-	-	50-51-52	108.4
-	-	-	-	-	-	35-36-49	120.0	-	-	50-51-80	121.2
-	-	-	-	-	-	48-35-60	120.0	-	-	52-51-80	120.2
-	-	-	-	-	-	35-48-47	120.0	-	-	51-52-53	119.8
-	-	-	-	-	-	35-48-51	120.0	-	-	51-80-79	120.0
-	-	-	-	-	-	37-36-49	120.0	-	-	51-80-81	119.2
-	-	-	-	-	-	36-37-38	121.5	-	-	52-53-54	119.3
-	-	-	-	-	-	36-49-50	120.0	-	-	52-53-78	120.1
-	-	-	-	-	-	37-38-39	120.0	-	-	54-53-78	108.6

Continued on next page

Table 17 – Continued

DBAd				**C_{60}**				**PC_{61}BM**			
Lig.	Å	Lig.	°	Lig.	Å	Lig.	°	Lig.	Å	Lig.	°
-	-	-	-	-	-	38-39-40	120.0	-	-	53-54-55	107.8
-	-	-	-	-	-	39-40-58	120.0	-	-	53-78-77	107.6
-	-	-	-	-	-	40-58-41	108.0	-	-	53-78-79	120.0
-	-	-	-	-	-	42-41-58	120.0	-	-	54-55-56	120.0
-	-	-	-	-	-	41-42-43	119.8	-	-	54-55-77	108.0
-	-	-	-	-	-	41-42-59	120.0	-	-	56-55-77	119.8
-	-	-	-	-	-	43-42-59	108.0	-	-	55-56-66	120.3
-	-	-	-	-	-	42-43-44	120.3	-	-	55-77-64	119.9
-	-	-	-	-	-	42-43-57	108.0	-	-	55-77-78	108.0
-	-	-	-	-	-	44-43-57	120.0	-	-	56-66-65	120.0
-	-	-	-	-	-	43-44-45	108.4	-	-	56-66-67	107.9
-	-	-	-	-	-	43-57-56	120.0	-	-	57-86-68	120.1
-	-	-	-	-	-	44-45-46	119.2	-	-	57-86-69	120.0
-	-	-	-	-	-	44-45-55	120.0	-	-	59-58-65	120.0
-	-	-	-	-	-	46-45-55	120.0	-	-	59-58-88	120.1
-	-	-	-	-	-	45-46-47	123.7	-	-	58-59-60	119.9
-	-	-	-	-	-	45-55-54	120.0	-	-	58-59-68	119.9
-	-	-	-	-	-	45-55-56	120.0	-	-	65-58-88	108.0
-	-	-	-	-	-	46-47-48	120.0	-	-	58-65-64	108.0
-	-	-	-	-	-	46-47-53	120.0	-	-	58-65-66	120.1
-	-	-	-	-	-	48-47-53	108.0	-	-	58-88-62	120.1
-	-	-	-	-	-	47-48-51	108.0	-	-	58-88-63	107.9
-	-	-	-	-	-	47-53-52	108.0	-	-	60-59-68	108.0
-	-	-	-	-	-	47-53-54	120.0	-	-	59-60-61	120.0

Continued on next page

Table 17 – Continued

DBAd				**C_{60}**				**PC$_{61}$BM**			
Lig.	Å	Lig.	°	Lig.	Å	Lig.	°	Lig.	Å	Lig.	°
-	-	-	-	-	-	48-51-50	120.0	-	-	59-60-69	108.0
-	-	-	-	-	-	48-51-52	108.0	-	-	59-68-67	120.2
-	-	-	-	-	-	49-50-51	120.0	-	-	59-68-86	107.9
-	-	-	-	-	-	50-51-52	108.4	-	-	61-60-69	108.4
-	-	-	-	-	-	51-52-53	119.8	-	-	60-61-62	120.1
-	-	-	-	-	-	52-53-54	119.3	-	-	60-61-72	119.3
-	-	-	-	-	-	53-54-55	107.8	-	-	60-69-70	107.8
-	-	-	-	-	-	54-55-56	120.0	-	-	60-69-86	107.9
-	-	-	-	-	-	55-56-57	120.0	-	-	62-61-72	108.0
-	-	-	-	-	-	-	-	-	-	61-62-74	108.0
-	-	-	-	-	-	-	-	-	-	61-62-88	119.9
-	-	-	-	-	-	-	-	-	-	61-72-71	119.9
-	-	-	-	-	-	-	-	-	-	61-72-73	108.0
-	-	-	-	-	-	-	-	-	-	74-62-88	120.1
-	-	-	-	-	-	-	-	-	-	62-74-73	108.0
-	-	-	-	-	-	-	-	-	-	62-74-75	120.0
-	-	-	-	-	-	-	-	-	-	62-88-63	120.0
-	-	-	-	-	-	-	-	-	-	64-63-76	120.0
-	-	-	-	-	-	-	-	-	-	64-63-88	108.1
-	-	-	-	-	-	-	-	-	-	63-64-65	107.9
-	-	-	-	-	-	-	-	-	-	63-64-77	119.9
-	-	-	-	-	-	-	-	-	-	76-63-88	120.0
-	-	-	-	-	-	-	-	-	-	63-76-75	119.9
-	-	-	-	-	-	-	-	-	-	63-76-79	119.9

Continued on next page

Table 17 – Continued

DBAd				**C_{60}**				**$PC_{61}BM$**			
Lig.	Å	Lig.	°	Lig.	Å	Lig.	°	Lig.	Å	Lig.	°
-	-	-	-	-	-	-	-	-	-	65-64-77	120.2
-	-	-	-	-	-	-	-	-	-	64-65-66	119.8
-	-	-	-	-	-	-	-	-	-	64-77-78	120.1
-	-	-	-	-	-	-	-	-	-	65-66-67	120.0
-	-	-	-	-	-	-	-	-	-	66-67-68	119.8
-	-	-	-	-	-	-	-	-	-	67-68-86	120.0
-	-	-	-	-	-	-	-	-	-	68-86-69	108.2
-	-	-	-	-	-	-	-	-	-	70-69-86	120.0
-	-	-	-	-	-	-	-	-	-	69-70-71	119.8
-	-	-	-	-	-	-	-	-	-	69-70-87	119.8
-	-	-	-	-	-	-	-	-	-	71-70-87	108.1
-	-	-	-	-	-	-	-	-	-	70-71-72	120.1
-	-	-	-	-	-	-	-	-	-	70-71-85	107.9
-	-	-	-	-	-	-	-	-	-	72-71-85	119.8
-	-	-	-	-	-	-	-	-	-	71-72-73	120.0
-	-	-	-	-	-	-	-	-	-	71-85-84	120.4
-	-	-	-	-	-	-	-	-	-	72-73-74	108.0
-	-	-	-	-	-	-	-	-	-	72-73-83	120.0
-	-	-	-	-	-	-	-	-	-	74-73-83	120.0
-	-	-	-	-	-	-	-	-	-	73-74-75	119.9
-	-	-	-	-	-	-	-	-	-	73-83-82	120.2
-	-	-	-	-	-	-	-	-	-	73-83-84	120.4
-	-	-	-	-	-	-	-	-	-	74-75-76	120.0
-	-	-	-	-	-	-	-	-	-	74-75-81	119.9

Continued on next page

Table 17 – Continued

DBAd				**C_{60}**				**$PC_{61}BM$**			
Lig.	Å	Lig.	°	Lig.	Å	Lig.	°	Lig.	Å	Lig.	°
-	-	-	-	-	-	-	-	-	-	76-75-81	108.1
-	-	-	-	-	-	-	-	-	-	75-76-79	107.9
-	-	-	-	-	-	-	-	-	-	75-81-80	107.8
-	-	-	-	-	-	-	-	-	-	75-81-82	120.3
-	-	-	-	-	-	-	-	-	-	76-79-78	120.1
-	-	-	-	-	-	-	-	-	-	76-79-80	107.7
-	-	-	-	-	-	-	-	-	-	77-78-79	120.0
-	-	-	-	-	-	-	-	-	-	78-79-80	119.9
-	-	-	-	-	-	-	-	-	-	79-80-81	108.5
-	-	-	-	-	-	-	-	-	-	80-81-82	119.5
-	-	-	-	-	-	-	-	-	-	81-82-83	119.7
-	-	-	-	-	-	-	-	-	-	82-83-84	108.1
-	-	-	-	-	-	-	-	-	-	83-84-85	119.4

Table 18 – Statistical thermodynamic parameters for the supramolecular complexes C_{60}@DBAd and $PC_{61}BM$@DBAd at 298.15 K and 1 atm, calculated using the rigid rotor-harmonic oscillator model at the DFT/BLYP-D2/DNP+ level of theory. Enthalpy (H), entropy (S), and heat capacity (C_p) are reported according to their translational (trans), rotational (rot), and vibrational (vib) contributions.

	H (kcal · mol^{-1})			**S** (cal · mol^{-1} · K^{-1})			C_p (cal · mol^{-1}·K^{-1})		
	$H_{\text{trans}} + H_{\text{rot}}$	H_{vib}[a]	H_{total}[b]	$S_{\text{trans}} + S_{\text{rot}}$	S_{vib}	S_{total}	$C_{p,\text{trans}}$	$C_{p,\text{rot}}$	$C_{p,\text{vib}}$
C_{60}@DBAd	1.778	24.107	26.477	87.566	143.875	231.441	4.968	2.981	192.628
$PC_{61}BM$@DBAd	1.778	33.327	35.697	88.997	204.839	293.837	4.968	2.981	250.353

[a] H_{vib} excludes zero-point vibrational energy (ZPVE);

[b] $H_{\text{total}} = H_{\text{trans}} + H_{\text{rot}} + H_{\text{vib}} + H_{pV}$, with $H_{pV} = 0.592$ kcal · mol^{-1} for both complexes.

APPENDIX B – LIST OF PUBLICATIONS

This appendix presents the scientific publications authored or co-authored during the period of doctoral research, comprising peer-reviewed articles, book chapters, and conference proceedings:

1. **Vasconcelos, V. M. R.**; Postacchini, B. B.; Santos, H. S.; Cajazeiras, F. F. M.; Freire, V. N.; Alves Junior, C.; Pessoa, C.; Costa, R. F.; Vasconcelos, I. F.; Bezerra, E. M. Red-shifted optical absorption induced by donor-acceptor-donor π-extended dibenzalacetone derivatives. **RSC Advances**, v. 15, p. 2416–2429, 2025.
2. Pereira, M. S.; **Vasconcelos, V. M. R.**; Palacio, M. P. S.; Oliveira, F. G. S.; Santos, L. P. M.; Vasconcelos, D. L. M.; Freire, P. T. C.; Vasconcelos, I. F. Characterization of $CoFe_2O_4$, $NiFe_2O_4$, and $ZnFe_2O_4$ nanoparticles synthesized by a proteic sol-gel method. **Journal of Superconductivity and Novel Magnetism**, v. 34, p. 2845–2853, 2021.
3. Moreira, F. S.; Sarmento, J. S.; Nascimento, L. M.; Palacio, M. P. S.; Garcia, P. H. N.; Alves, R. S. G.; Santos, V. S.; **Vasconcelos, V. M. R.**; Nogueira, R. E. F. Q. Os avanços na técnica de sinterização a frio: redução no consumo de energia e otimização na fabricação de cerâmicas funcionais. In: Lara, N. (Org.). **Engenharia de Materiais: Materializando o Futuro**. 1. ed. São Paulo: Pimenta Cultural, 2022, p. 69–89.
4. **Vasconcelos, V. M. R.**; Bezerra, E. M.; Postacchini, B. B.; Costa, R. F.; Freire, V. N.; Santos, H. S.; Vasconcelos, I. F. Influence of solvatochromism on the optical absorption spectrum of the chalcone-based derivative dicinnamalacetone: a PCM/TD-DFT approach. In: 25th CBECiMat, 2024, Fortaleza, CE. *Livro do Evento*, 2024. v. 1.
5. Bampoky, N. A.; Vasconcelos, I. F.; Santos, L. P. M.; **Vasconcelos, V. M. R.** Synthesis and characterization of cobalt ferrite obtained by the protein sol-gel method and its application as an electrocatalyst in water electrolysis. In: 25th CBECiMat, 2024, Fortaleza, CE. *Livro do Evento*, 2024. v. 1.
6. **Vasconcelos, V. M. R.**; Mendes, F. R. S.; Santos, H. S.; Costa, R. F.; Alves Junior, C.; Freire, V. N.; Bezerra, E. M.; Vasconcelos, I. F. Theoretical and experimental investigation of gap energy dependence with the increase of π-conjugated system in bis-chalcones. In: XXI B-MRS Meeting, 2023, Maceió, AL. *Proceedings*, 2023.
7. **Vasconcelos, V. M. R.**; Costa, R. F.; Alves Junior, C.; Freire, V. N.; Bezerra, E. M.; Vasconcelos, I. F. Classical molecular mechanics approach to the intermolecular interaction potential between $P3HT{:}PC_{61}BM$ complex. In: XXI B-MRS Meeting, 2023, Maceió, AL.

Proceedings, 2023.

8. Santos, G. P. B.; **Vasconcelos, V. M. R.**; Vasconcelos, I. F.; Medeiros, S. L. S. Ultrasound-assisted surface modification of $CoFe_2O_4$ magnetic nanoparticles: colloidal stability improvement by anionic polyelectrolyte and surfactants. In: 4th ICAIC and 4th IMMSEM, Maranhão, 2023.